



UNIVERSIDADE D
COIMBRA

Patricio Gustavo Riofrío Villena

**PROPRIEDADES MECÂNICAS E
COMPORTAMENTO À FADIGA DE CHAPAS
DE AÇO HSLA SOLDADAS POR LASER**

Tese no âmbito do Doutoramento em Engenharia Mecânica na Especialidade de Integridade Estrutural orientada pelos Professores Doutor José António Martins Ferreira e Doutor Carlos Alexandre Bento Capela e apresentada ao Departamento de Engenharia Mecânica da Faculdade de Ciências e Tecnologia da Universidade de Coimbra

Julho de 2021



UNIVERSIDADE D
COIMBRA

FCTUC FACULDADE DE CIÊNCIAS
E TECNOLOGIA
UNIVERSIDADE DE COIMBRA

DEPARTAMENTO DE
ENGENHARIA MECÂNICA

Fatigue Behaviour and Mechanical Properties of Thin Laser Welded HSLA Steel

Thesis submitted for obtaining the degree of Doctor of Philosophy in
Mechanical Engineering in Structural Integrity Specialty.

Author

Patricio Gustavo Riofrío Villena

Supervisors:

José António Martins Ferreira

Full Professor of the University of Coimbra

Carlos Alexandre Bento Capela

Coordinate Professor of the Polytechnic Institute of Leiria

Coimbra, 2021

"A little learning is a dangerous thing;
drink deep, or taste not the Pierian spring:
there shallow draughts intoxicate the brain,
and drinking largely sobers us again."

Alexander Pope, *An Essay on Criticism*, 1709.

To my mother and maternal grandparents †

ACKNOWLEDGEMENTS

I would like to express my gratitude, in particular, to my supervisors, Professors José António Martins Ferreira and Carlos Alexandre Bento Capela, for their constant guidance and support throughout the investigation carried out. Their advice and suggestions were very important to the project.

I would also like to extend my thanks to Professor Amílcar Ramalho, for his support and guidance in various tests in the mechanical testing laboratory.

I offer my sincere thanks to Dr. Joel de Jesus, Dr. Luís Vilhena, Dr. Carlos Leitão and Dr. José da Costa for their help in my fatigue, tensile and microhardness experiments; to Dr. António Batista for measuring the residual stresses in the welding specimens and to Mr. Fernando Bernardes for assisting in various specimen preparation work.

I also thank Professor Marta Oliveira for her guidance in the doctoral program.

I acknowledge the financial support from Universidad de las Fuerzas Armadas-ESPE with the PhD scholarship, as well as the support provided by Mr. Mário Da Costa Martins and Mr. Fernando Meireles of the Orthopedia Médica company where laser welding was done.

Thanks to my mother, cousin Alberto, uncles and family for their love and constant encouragement during this difficult period brought by the coronavirus pandemic.

A special thanks to Lili Tamayo who, with her love and constant companionship, has made this period away from my country short and pleasant.

Abstract

The present research focuses on the fatigue behaviour and mechanical properties of a laser welded thin high-strength low-alloy (HSLA) steel. Under a maximum laser power of 2 kW, single pass and double pass butt welded joints were developed by autogenous laser welding (ALW) on 3 mm thick Strenx® 700MCE steel. This steel has a minimum yield strength at 700 MPa and its typical applications include elements and parts of trailer, trucks, crane, cars and wagon. This work aims to understand the effect of weld bead geometry, imperfections and local properties such as microstructure, hardness and residual stresses in the fatigue strength, fatigue lives and tensile strength of the butt welded joints. It also sought to establish the laser welding parameters for the development of single pass ALW as well as to determine their influence on the main factors that affect fatigue behaviour and mechanical properties.

Design of experiments and analysis of variance (ANOVA) was used to establish and validate the effect of the welding parameters on the weld bead geometry. Extensive experimental work was carried out, including, among others: the welding of two sets of butt joints in addition to previous tests; the determination of S-N curves, fatigue crack growth rate (FCGR) curves and residual stresses for four welded series and the base metal (BM). The finite element method (FEM) was used in order to determine the stress concentration factor (SCF). The main novel contributions achieved by the research carried out include:

(1) Determination of the effect of the main laser welding parameters on the weld bead geometry in low ranges of laser power (1-2 kW), welding speed (1.5-2.5 m/min) and heat inputs (20-80 J/mm);

(2) Development of single pass ALW with B quality level according to the ISO 13919-1 welding quality standard, with a detailed description of imperfections including undercuts and porosity distributions and faithful geometric modeling of weld bead profiles either real or based on average dimensions for a better determination of SCFs by FEM.

(3) Understanding the effects of laser welding parameters on main factors that influence fatigue behaviour and the mechanical properties of the HSLA steel. A low HI in the heat-affected zone (HAZ) and fusion zone (FZ) where fatigue cracks started and propagated, achieves the following positive effects: smaller width of these zones, bainitic microstructure that retards the growth of cracks, high hardness in the FZ and less softening in the HAZ, low residual tensile stresses and even residual compressive stresses in the center of the FZ, however it also causes a slight increase in porosity and underfill.

(4) Understanding the influence of the main factors on fatigue behaviour and mechanical properties of the HSLA steel. It was demonstrated that in the fatigue limit assessment, where the crack initiation period prevails, the stress-concentrating approach and the consideration of the local properties of hardness and residual stress and an appropriate SCF that reflects the weld bead profile, achieves a close estimate of the fatigue limits thus explaining the small differences between the welded joints.

(5) The application of the crack propagation approach, assuming an initial crack size and appropriate FCGRs at high stress levels to joints welded with thin plates where the fatigue life is strongly influenced by the quantity, size and location of crack-like imperfections which determines the formation of characteristic surface cracks leading to neglect the crack initiation period.

Keywords Fatigue, HSLA steel, Laser welding, Mechanical properties

Resumo

O presente trabalho estuda o comportamento à fadiga e as propriedades mecânicas de chapas finas de aço de baixa liga e alta resistência, soldadas a laser. Usando uma potência máxima do laser de 2 kW, as juntas são soldadas de topo a topo com uma só passagem e dupla passagem, em aço Strenx® 700MCE de 3 mm de espessura. Esse aço tem limite de escoamento mínimo de 700 MPa e suas aplicações típicas são elementos e peças de reboques, camiões, guindastes, carros e vagões.

O trabalho visa compreender o efeito da geometria do cordão de solda, imperfeições e propriedades locais como microestrutura, dureza e tensões residuais na resistência à fadiga, vida à fadiga e resistência à tração das juntas soldadas de topo. Pretende-se também estabelecer os parâmetros da soldadura a laser autógena de passe único e determinar sua influência nos principais fatores que afetam o comportamento à fadiga e as propriedades mecânicas.

Plano de experimento e análise de variância foram usados para estabelecer e validar o efeito dos parâmetros de soldadura na geometria do cordão de solda. Foi realizado um extenso trabalho experimental que incluiu: a soldadura de dois conjuntos de juntas de topo em adição aos testes anteriores; a determinação das curvas S-N, a obtenção de curvas da velocidade de crescimento de fendas por fadiga e tensões residuais para quatro séries soldadas e o metal base, entre outras. O método dos elementos finitos foi utilizado na determinação do fator de concentração de tensão. As principais contribuições do trabalho realizado, são:

(1) Determinação do efeito dos principais parâmetros de soldadura a laser na geometria do cordão para baixas faixas de potência do laser (1-2 kW), velocidade de soldadura (1,5-2,5 m / min) e entradas de calor (20-80 J / mm).

(2) Desenvolvimento do procedimento de soldadura a laser autógena de passagem única com nível de qualidade B de acordo com a norma de qualidade ISO 13919-1, com a descrição detalhada de imperfeições, incluindo defeitos na raiz do cordão e

distribuições de porosidade e modelação geométrica dos perfis de cordão de soldadura, reais ou, baseados em dimensões médias para uma melhor determinação dos fatores de concentração de tensão pelo método dos elementos finitos.

(3) Compreender o efeito dos parâmetros de soldadura a laser nos principais fatores que influenciam o comportamento à fadiga e as propriedades mecânicas. Uma entrada de calor baixa, na zona afetada pelo calor e na zona de fusão onde as fissuras de fadiga se iniciam e propagam, produz os seguintes efeitos positivos: menor largura dessas zonas, microestrutura bainítica que retarda o crescimento das fendas, alta dureza na zona de fusão e menos amaciamento na zona afetada pelo calor, baixas tensões residuais de tração e até tensões compressivas residuais no centro da zona de fusão. No entanto, também causa um ligeiro aumento da porosidade e falta de enchimento.

(4) Analisar a influência dos principais fatores de soldadura no comportamento à fadiga e nas propriedades mecânicas do aço de baixa liga de alta resistência. Foi demonstrado que na avaliação da tensão limite de fadiga, onde o período de iniciação da fenda prevalece, a abordagem baseada na concentração de tensão e na consideração das propriedades locais de dureza e tensão residual conduz a uma estimativa adequada dos limites de fadiga, permitindo explicar as pequenas diferenças entre as juntas soldadas.

(5) A aplicação da abordagem baseada na propagação de fendas, assumindo um tamanho de fenda inicial e taxas de crescimento de fenda de fadiga apropriadas em altos níveis de tensão para juntas soldadas de chapa fina, onde a vida à fadiga é fortemente influenciada pela quantidade, tamanho e localização de fissuras ou imperfeições que determinam a formação de fissuras superficiais características que reduzem o período de iniciação da fenda.

Palavras-chave: Aço HSLA, Fadiga, Propriedades mecânicas, Soldadura laser

Table of Contents

Table of Contents	vi
List of figures	xi
List of tables	xvi
List of publications.....	xviii
Abbreviations	xix
Nomenclature	xxi
Chapter 1: Introduction	1
1.1. Research background and motivation.....	1
1.2. Aim and objectives	3
1.2.1. Aim.....	3
1.2.2. Objectives.....	3
1.3. Scientific and technological challenges.....	4
1.4. Thesis structure.....	4
1.5. References	5
Chapter 2: Literature review	7
2.1. High strength steels overview.....	7
2.2. Strenx® 700MCE steel.....	9
2.3. Laser welding	11
2.3.1. Laser optics and beam quality	12
2.3.2. Disk Laser	14
2.3.3. Operation modes	15
2.3.4. Laser Welding Parameters	17
2.3.5. Effect of Laser Welding Parameters on Weld Geometry.....	18
2.3.6. Effect of Laser Welding Parameters on Imperfections	20
2.3.7. Modelling and Optimization in laser welding.....	24
2.3.8. Laser welding of high strength steels	26
2.3.8.1. Effect on microstructure and hardness.....	27
2.3.8.2. Effect on tensile strength and ductility	31

2.3.9. Laser welding of S700MC steel	33
2.4. Residual stress in high strength steels laser welded	33
2.5. Fatigue in Welded Joints.....	36
2.5.1. S-N curve of welded joints	38
2.5.2. Fatigue strength of high strength steels	39
2.5.3. Effect of the weld quality.	41
2.5.4. Effect of the weld bead geometry and residual stresses	43
2.5.5. Fatigue of S700MC steels	45
2.6. Fatigue crack growth	45
2.6.1. Crack closure phenomenon	47
2.6.2. Factors that affect the fatigue crack propagation.....	47
2.7. Fatigue strength assessment.....	49
2.7.1. Fatigue limit assessment.....	51
2.7.2. Crack propagation approach.....	52
2.8. References.....	55
 Chapter 3: Interactions of the process parameters and mechanical properties of laser butt welds in thin high strength low alloy steel plates.....	 61
3.1. Introduction.....	62
3.2. Material and experimental procedures.....	65
3.2.1. Material.....	65
3.2.2. Laser welding	66
3.2.3. Weld bead geometry, microstructure, and mechanical properties.....	68
3.3. Results and discussion	69
3.3.1. Appearance, section geometry, and defects of the weld bead.....	69
3.3.2. Effects of the laser parameters on the penetration and width of HAZ and FZ..	73
3.3.2.1. Effect of surface and edge condition.....	74
3.3.2.2. Effect of the heat input.....	75
3.3.3. Weld bead optimization.....	77
3.3.4. Macrostructure and microstructure.....	78
3.3.5. Microhardness	80

3.3.6. Mechanical properties and fracture analysis	81
3.4. Conclusions	84
3.5. References	85
Chapter 4: Imperfections and Modelling of the Weld Bead Profile of Laser Butt Joints in HSLA Steel Thin Plate	87
4.1. Introduction	88
4.2. Materials and Methods	91
4.2.1. Material and Laser Welding	91
4.2.2. Measurement of Weld Bead Geometry and Imperfections	93
4.3. Results and discussion	95
4.3.1. Welding Bead Geometry	95
4.3.2. Profile Modelling	98
4.3.3. Imperfections.....	100
4.3.3.1. Porosity	100
4.3.3.2. Undercuts	102
4.3.3.3. Variation of the Underfill along the Weld Axis.....	104
4.3.4. Evaluation of Imperfections	105
4.3.5. Analysis of Variance	108
4.4. Conclusions	111
4.5. References	112
Chapter 5: Fatigue performance of thin laser butt welds in HSLA steel	115
5.1. Introduction	116
5.2. Material and procedures	118
5.2.1. Material and laser welding	118
5.2.2. Fatigue testing and analysis.....	120
5.2.3. Measurement of residual stresses	121
5.3. Results and discussion	122
5.3.1. S-N curves	122
5.3.2. Fatigue failure modes	124
5.3.3. Effect of weld bead geometry and imperfections.....	128
5.3.4. Effect of top side and bottom side in the fatigue strength.....	131

5.3.5.	Fatigue limit assessment.....	133	
5.3.5.1.	Local Properties: microstructure and hardness	133	
5.3.5.2.	Residual Stresses	135	
5.3.5.3.	Fatigue limit evaluation.....	136	
5.3.6.	Fatigue limit predictions.....	139	
5.4.	Conclusions	142	
5.5.	References.....	143	
Chapter 6: Influence of local properties on fatigue crack growth of laser butt welds in thin plates of high-strength low-alloy steel			145
6.1.	Introduction.....	146	
6.2.	Materials and Methods.....	148	
6.3.	Results and discussion	151	
6.3.1.1.	Welded defects and hardness	151	
6.3.2.	S-N curves	153	
6.3.3.	Fatigue crack growth	154	
6.3.4.	Crack opening displacement and crack closure.....	155	
6.3.5.	Effect of Imperfections at high stress levels.....	159	
6.3.6.	Fatigue lives predictions.....	162	
6.4.	Conclusions.....	166	
6.5.	References.....	167	
Chapter 7: Conclusions and Future Work			171
7.1.	Conclusions.....	171	
7.1.1.	Laser Welding, weld profile and imperfections	172	
7.1.2.	Microstructure, hardness, residuals stresses and tensile strength.....	173	
7.1.3	Fatigue behaviour	174	
7.2.	Future Work.....	176	
7.2.1.	Toughness and formability properties	176	
7.2.2.	Comparative studies with conventional welding processes	176	
7.2.3.	Improvement of welding quality through laser welding parameters’ optimization techniques.....	177	

7.2.4. Using conduction mode or increasing laser power to improve the weld profile	177
7.2.5. Small crack behaviour	178
7.2.6. Predictions of the S-N curves	178

List of figures

Figure 2.1 Location of HSS in the space elongation-tensile strength [2].....	7
Figure 2.2 Diagram carbon-carbon equivalent [22].	11
Figure 2.3 A laser welding application (a) [25] and ALW weld bead (b) [26].	12
Figure 2.4 Schemes of the laser optical system a) and irradiance distribution in space b), adapted from [27]	13
Figure 2.5 Schemes of disk laser systems [30, 32].	15
Figure 2.6 Scheme of laser welding operating modes, adapted from [36].	16
Figure 2.7 Penetration depth as function of power (a) and of welding speed (b) [33].	18
Figure 2.8 Welding speed and defocusing effects in the weld bead [50].	21
Figure 2.9 Defects of the system A produced as function of welding speed [57].	22
Figure 2.10 Sound welds windows in space depth-welding speed (a) [49] and welding speed-power (b) [45].	23
Figure 2.11 Wed bead cross sections for different power laser (kW), 6 (a), 6.2 (b), 6.7 (c) and 6.5 (d) [42].	25
Figure 2.12 Microstructures of steel S700 in ALW, BM (a), HAZ (b) and FZ (c) adapted from [26].	27
Figure 2.13 Micro-hardness of steels S700 [26].	27
Figure 2.14 Evolution of microstructure in DP steels; BM (left)-HAZ (center)-FZ (right); (a)-(b)-(c) DP600 and (d)-(e)-(f) DP980 [67].	28
Figure 2.15 Hardness profiles of the dual phase steels DP600 (a) and DP980 (b) [67].	29
Figure 2.16 Microstructures in HAZ for high heat input ($t_{8/5} = 20$ s, left) and low heat input ($t_{8/5} = 5$ s, right) for S700MC-1 steel (a) and (b) and S700MC-2 steel (c) and (d), respectively.	30
Figure 2.17 Microstructures of steel S700MC for three cooling times [15].	30

Figure 2.18 Residual stress distributions in laser welding (a) modified form [73], and in various welding processes (b) [26].....	35
Figure 2.19 Sketch of remote stress (σ) and local stresses (σ_k) in imperfections.	37
Figure 2.20 S-N curves for welded joint and similar non-welded elements [79].	39
Figure 2.21 S-N curves for AHSS: DP600 and DP980 (a) [67] and DP440, DP590 and MS (b) [87].....	40
Figure 2.22 Hardness profiles obtained in processes: GMAW (a) [87] and in laser (b) [48].	41
Figure 2.23 Aspect of the machined and non-machined weld toe (a) and fatigue strength (b) [104].	44
Figure 2.24 Sketch of fatigue crack growth rate diagram.	46
Figure 2.25 Curve $da/dN - \Delta K$ and microstructures characteristics, adapted from [116]...	48
Figure 2.26 Residual stresses due to welding consumables (a) and FCGR for JIS SPV490 steel (b) [119].	49
Figure 2.27 Scheme with three types of surface cracks.	53
Figure 2.28 Scheme with sizes of semi-elliptical crack (a) and aspect ratio $a/c-a/t$ for two types of cracks (b).	53
Figure 3.1 Microstructure of the base material: (a) optical microscopy; (b) SEM micrograph.	66
Figure 3.2 Schemes of (a) location of specimens and pieces in the weld sample and (b) measurements made on the cross section of the weld bead	68
Figure 3.3 Appearance, section geometry, and defects of weld beads for samples 14, 1, 13, 12, and 9.	72
Figure 3.4 Appearance, section geometry, and defects of weld beads for samples 4, 7, 10, 2, and 6.	72
Figure 3.5 Appearance, section geometry, and defects of weld beads for samples 11, 3, 5, and 8.	73

Figure 3.6 Penetration depth D and width W in function of: (a) welding speed, (b) power, (c) focus diameter, and (d) focus position.	74
Figure 3.7 Effect of the surface-edge condition: (a) gap difference between conditions C1 and C3 (C2, C4); (b) penetration depth D	75
Figure 3.8 Penetration depth D (a), and width W (b), in function of heat input (HI).	76
Figure 3.9 Appearance, section geometry, and defects of weld beads for samples 18, 19, and 20.	77
Figure 3.10 Macrostructure and microstructure of the welded sample # 4: (a) optical microscopy and SEM micrographs of: (b) FG-HAZ, (c) CG-HAZ, and (d) FZ.	78
Figure 3.11 SEM micrographs of the FZ showing microstructures for the samples: # 11 (a)–(b); #12 (c)–(d); and # 14 (e)–(f).	79
Figure 3.12 Microhardness of several samples.	81
Figure 3.13 Stress–strain curves of several samples and base metal (BM).....	82
Figure 3.14 Fracture surface of the tensile specimens: (a) sample # 9 and (b) sample #12.	83
Figure 4.1 Schemes of: (a) the welded sample; (b) the weld bead with designations of typical imperfections and zones produced by welding.....	94
Figure 4.2 Appearance of the weld beads for welded series: profiles (above); macrographs (below).....	95
Figure 4.3 Sketch of the idealized profiles and their geometrical parameters: (a) t-profile; (b) b-profile.	96
Figure 4.4 Examples of profiles: real, model and average model for S1, S2, S3 and S5 series (Y-axis and X-axis in mm).	99
Figure 4.5 Distribution (a) and appearance (b) of porosity for the welded series.	101
Figure 4.6 Distributions of undercut parameters for the set of series: (a) depth; (b) radius.	103
Figure 4.7 Appearance of weld roots and undercuts for S1, S2 and S3 series: (a) captured by profilometer; (b) photograph	103

Figure 4.8 Variation of height of the profiles (Y-axis in μm) along the weld axis (X-axis in mm) in places of underfill for S1, S2, S3 and S5 series.....	105
Figure 4.9 SCFs for undercuts and profiles and porosity percentage of S1, S2, S3 and S5 series.....	107
Figure 4.10 Plots of the residuals for width W: (a) normal probability; (b) residuals vs HI.	109
Figure 4.11 (a) Interaction in the factorial experiment; (b) width W in the function of the Heat Input.....	110
Figure 5.1 a) Sketch of plates for the welding and location of specimens, b) dimensions of specimens used in fatigue tests.....	120
Figure 5.2 S-N data for all welded series and BM.	122
Figure 5.3 S-N curves of each series.....	123
Figure 5.4 Failure modes distributions found in the specimens of the welded series and sketches of starts and paths on their cross-sections.....	127
Figure 5.5 Weld profile models of the welded series and details of meshing used in FEM.	129
Figure 5.6 Stress distribution in bottom side of the welded series: a) S3 and b) S5.....	130
Figure 5.7 S-N curves for S1 and S2 series in two conditions: as-welded and bottom side-removed.....	131
Figure 5.8 Fatigue lives of specimens at 600 MPa in various conditions.....	132
Figure 5.9 Fatigue initiation sites in the microstructure for underfill, undercuts and weld toe.	134
Figure 5.10 Microhardness profiles in S1 and S5 series.	135
Figure 5.11 Residual stresses profiles in fatigue specimens.	136
Figure 5.12 Fatigue failure points of specimens and modified Goodman lines.....	138
Figure 6.1 Specimens geometry used in FCGR tests, dimensions in mm.	150
Figure 6.2 Cross-sections macrographs of the welded series.....	151

Figure 6.3 Metallographic and morphologic analyses. a) S1 series macrograph, b) Metallographic analysis and underfill defect, c) toe of weld root, d) un-dercut defect.....	152
Figure 6.4 S-N curves.....	153
Figure 6.5 Fatigue crack growth rate at Paris regime. a) S1 series, b) S3 series, c) S2 series and d) S5 series.....	155
Figure 6.6 ΔP -COD example curves of each welded series and BM.....	156
Figure 6.7 Fatigue crack growth rate at Paris regime. a) $da/dN - \Delta K$ and b) $da/dN - \Delta K_{eff}$.	158
Figure 6.8 Fractured surfaces of specimens at 600 MPa.....	161
Figure 6.9 Fatigue failure modes with details and corresponding types of cracks. a) extended crack, b) semi-elliptical multicracks c) semi-elliptical crack and d) corner crack.....	164

List of tables

Table 2.1 Chemical composition (%).....	9
Table 2.2 Tensile mechanical properties.....	9
Table 2.3 General characteristics of available laser equipment.	15
Table 2.4 Welding parameters used in various works.	19
Table 2.5 Mechanical properties of Docol 1200M welds [46].	32
Table 2.6 Mechanical properties of TRIP welds [46].	32
Table 3.1 Chemical composition of the base metal.	66
Table 3.2 Tensile mechanical properties of the base metal.....	66
Table 3.3 Welding parameters used in the experimental work.	67
Table 3.4 Laser equipment characteristics.	67
Table 3.5 Sample set results.	70
Table 3.6 Mechanical properties, microhardness, width, and heat input of samples.....	83
Table 4.1 Chemical composition of the base metal.	91
Table 4.2 Tensile mechanical properties of the base metal.....	91
Table 4.3 Welding parameters used in the experimental work.	92
Table 4.4 Geometrical parameters of the welded series.....	97
Table 4.5 Means of macrographs features	98
Table 4.6 Porosity features of welded series.....	101
Table 4.7 Parameters of the undercut geometry.....	102
Table 4.8 Evaluation of the weld quality of the welded series.	106
Table 4.9 Data for width W.....	108
Table 4.10 ANOVA table for width W.....	108
Table 4.11 ANOVA table for factorial design applied to width W.	110
Table 5.1 Chemical composition of the base metal.	118

Table 5.2 Tensile mechanical properties of the base metal.	118
Table 5.3 Welding parameters used in the experimental work.	119
Table 5.4 S-N curves parameters and fatigue limits.....	124
Table 5.5 Failure modes features.....	125
Table 5.6 SCFs and mean geometric parameters of imperfections.	129
Table 5.7 Correlation between ratios of SCFs and fatigue strengths.	132
Table 5.8 Data for fatigue strength assessment based on the modified Goodman line.	137
Table 5.9 Fatigue limit predictions.....	140
Table 5.10 Data and parameters for prediction of fatigue limits.....	141
Table 6.1 Chemical composition of the base metal.....	148
Table 6.2 Welding parameters used in the experimental work.	149
Table 6.3 S-N curves parameters and fatigue limits.....	154
Table 6.4 A, n parameters of the FCGR ¹ curves in function of ΔK_{eff}	158
Table 6.5 Data and parameters for the estimation of the fatigue life.	166
Table 6.6 Data and parameters for the predictions of the fatigue life.	166

List of publications

1. **Patricio G. Riofrío**, Carlos A. Capela, José A.M. Ferreira and Amílcar Ramalho. *Interactions of the process parameters and mechanical properties of laser butt welds in thin high strength low alloy steel plates*. **Proc. Inst. Mech. Eng. Part L: J. Materials: Design and Applications**. 234 (5) (2020) 665-680, [doi:10.1177/1464420720910442](https://doi.org/10.1177/1464420720910442).
2. **Patricio G. Riofrío**, José A. M. Ferreira and Carlos A. Capela. *Imperfections and modelling of the weld bead profile of laser butt joints in HSLA steel thin plate*. **Metals**. 11 (151) (2021), [doi: 10.3390/met11010151](https://doi.org/10.3390/met11010151).
3. **Patricio G. Riofrío**, F. V. Antunes, J.A.M. Ferreira, C. Capela, A.C. Batista. *Fatigue performance of thin laser butt welds in HSLA steel*. **Metals**. Submitted.
4. **Patricio G. Riofrío**, Joel de Jesus, José A. M. Ferreira and Carlos Capela. *Influence of local properties on fatigue crack growth of laser butt welds in thin plates of high-strength low-alloy steel*. **Applied Sciences**. Submitted.

Abbreviations

AHSS	Advanced high strength steels
ALW	Autogenous laser welding
ANN	Artificial neural networks
ANOVA	Analysis of variance
ASMT	American Society for Testing and Materials
BM	Base metal
BPNN	back-propagation neural network
BPP	Beam parameter product
CCT	Continuous cooling temperature
CE	Carbon equivalent
CG	Coarse grain
CG-HAZ	Coarse-grain heat-affected zone
COD	Crack opening displacement
D	Penetration depth
DoE	Design of experiments
EDM	Electrical discharge machining
FAT	Fatigue class curve
FCG	Fatigue crack growth
FCGR	Fatigue crack growth rate
FEM	Finite element method
FG	Fine grain
FG-HAZ	Fine-grain heat-affected zone
FM	Failure mode
FZ	Fusion zone
GA	Genetic algorithm
GHG	Greenhouse emissions gas
GMAW	Gas metal arc welding
GTAW	Gas tungsten arc welding
HAZ	Heat-affected zone
HI	Heat input

HSLA	High-strength low-alloy
HSS	High strength steels
HV	Vickers hardness
IIW	International Institute of Welding
ISO	International Organization for Standardization
NDT	Nondestructive testing
NGLW	Narrow gap laser welding
OFAT	One-factor-at-a-time
PWHT	Post-welding heat treated
Q&T	Quenching and tempering process
RSM	Response surface methodology
SCF	Stress concentration factor
SD	Standard deviation
SEM	Scanning electron microscopy
SIF	Stress intensity factor
SIFR	Stress intensity factor range
TMCP	Thermomechanical control process
W	Width of fusion zone and heat-affected zone.
XRD	X-ray diffraction

Nomenclature

a	crack size (mm)
a^*	material strength parameter in Peterson expression (mm)
a_f	final crack depth (mm)
a_i	initial crack depth (mm)
a/c	crack aspect ratio
a/t	crack depth/thickness ratio
\sqrt{Area}	Murakami's area parameter (μm)
A, A^*	Paris law parameters
b	segment length in t-profile (mm)
BPP	Beam Parameter Product
c	crack width (mm)
c_i	initial crack with (mm)
c_f	final crack width (mm)
C	S-N curve parameter
CE	carbon equivalent
da/dN	fatigue crack growth rate (mm/cycle)
f	maximum projected area of pores (%)
f_l	focus depth (focus length) (mm)
f_d	focus diameter (waist diameter or spot diameter) (μm)
f_p	focus position (mm)
F_f, F_c	focal lengths (mm)
hc	excess weld metal depth (mm)
hb	excessive penetration depth (mm)
he	linear misalignment (mm)
hi	underfill depth (mm)
hp	maximum dimension for single pore (mm)
hu	undercut depth (mm)
HI	heat input (J/mm)
HV	Vickers hardness

lc	affected weld length in combined porosity (mm)
lb	width of b-profile (mm)
lt	width of t-profile (mm)
K	stress intensity factor (MPa m ^{1/2})
K_t	stress concentration factor
K_f	effective stress concentration factor
K_{tu}	stress concentration factor in undercut
K_{tw}	stress concentration factor in excess weld
M^2	beam factor
M_k	local geometry correction factor
m	S-N curve slope
n_G	Goodman criteria factor
n, n^*	Paris law parameters
N	number of cycles (cycles)
I	irradiance (W/cm ²)
P	laser power (kW)
q	notch sensitivity factor
r	toe radius in b-profile (mm)
ru	undercut radius (mm)
R	stress ratio
S_e	fatigue limit (MPa)
S_{ut}	tensile ultimate strength (MPa)
sc	semi-chord length (mm)
sr	segment radius length (mm)
t	thickness (mm)
$t_{8/5}$	cooling times (s)
v	welding speed (m/min)
Y	geometry factor of element cracked
α	Murakami's factor
δ	angle in t-profile (°)
Δa	crack size increment (mm)

ΔK_{th}	stress intensity range threshold value (MPa m ^{1/2})
ΔK_c	stress intensity range limit value (MPa m ^{1/2})
ΔK	stress intensity range (MPa m ^{1/2})
ΔS_{op}	crack opening stress range (MPa)
ΔK_{eff}	effective stress intensity range (MPa m ^{1/2})
ΔP	tension load range (N)
Δl_p	length for linear porosity (mm)
$\Delta \sigma$	nominal stress range (MPa)
θ	weld toe angle (°)
ρ	notch radius (mm)
σ	remote stress (MPa)
σ_a	nominal alternating (amplitude) stress (MPa)
σ_m	nominal mean stress (MPa)
σ_w	fatigue limit according Murakami's expression (MPa)
φ	notch groove angle (°)
ψ	divergence angle (°)
\emptyset	fiber diameter (μm)
\mathfrak{R}^2	coefficient of determination

Chapter 1: Introduction

1.1. Research background and motivation

Current challenges such as weight reduction and environmental protection in mechanical constructions seem feasible with the use of high strength steels (HSS), thin plates and advantageous welding processes. The automotive sector may be the most visible case that has shown significant savings in weight, cost and reduction of greenhouse gas emissions due to the replacement of lower strength steels with high strength steels in several of its thin components, some of which are welded by laser [1].

Due to the appropriate combination of mechanical properties and weldability, high-strength low-alloy (HSLA) steels are used in a variety of applications such as automotive, structural, oil and gas pipelines, pressure vessels, shipbuilding and offshore structures [2-4]. Thermomechanical control process (TMCP) has allowed the development of HSLA steels by increasing mechanical strength while retaining toughness and weldability [5]. HSLA steels with yield strengths above 1000 MPa are available, however the welding process limits their exploitation.

The deterioration of the mechanical properties in welded components that used high-strength HSLA steels and conventional welding processes is generally attributed to the high heat input, which produces changes in the microstructure, residual stresses, distortions and weld bead imperfections [6, 7]. This has led to a search for solutions that are productively efficient and take advantage of the high strength of steels.

Laser welding is gaining more applications due to the improvement in laser technology and the advantages of laser welding over conventional process. The key feature of laser welding is its high power density that allows depth penetration with a lower heat input, high cooling rate and a narrow heat-affected zone (HAZ) [8, 9]. Although these characteristics are propitious for the welding of HSLA steels, laser welding also poses challenges due to process sensitivity in keyhole mode and because there are several welding parameters that must be adjusted to obtain sound welds with appropriate mechanical properties.

There is a large number of studies about the effect of laser welding parameters in the weld geometry and imperfections for various materials as well as those that report the mechanical properties obtained under specific welding conditions. In HSLA steels, welds free of defects or tensile mechanical properties equal or similar to the base metal (BM) have been reported [10, 11], however, this is not the case regarding fatigue strength, where large reductions are commonly reported in the as-welded condition; additionally, the fatigue limit seems practically constant despite increasing the mechanical strength of the steel [12, 13].

While the fatigue behaviour of welds has been widely studied, there are still gaps in knowledge due to the complexity of the subject. The weld quality, the residual stresses, the material and the thickness effects have been pointed out as the main factors that influence the fatigue behaviour of the welded joints [14]. On the other hand, the use of steel plates with a thickness of less than 5 mm is limited, however, in the literature there is a great interest in investigating the fatigue strength of welded joints with thin steel plates and slender components as well as considering weld beads' real geometry and local properties [15-17].

Strenx® 700MCE steel is a HSLA steel with low carbon content, minimum yield strength of 700 MPa and an elongation of 10-12% and, according to the manufacturer, is a hot-rolled structural steel made for cold forming, designed for stronger and lighter structures with good weldability [18]. The typical applications are elements and parts of trailer, trucks, crane, cars and wagons [19]. As an example, in trailer chassis applications, the replacement of S335 steel grade by Strenx® S700MC steel could produce a saving in weight of 30 % [20].

There are few works where Strenx® S700MCE steel or similar ones are laser welded and those do not consider the fatigue behaviour in thin plates, taking into account local properties such as residual stress, hardness, weld imperfections and crack growth rate. On the other hand, laser welding works at low laser powers in keyhole mode are scarce. Thus, there are knowledge gaps and data shortages on this type of steels that must be identified and covered in order to contribute to the development of solutions in welded joints in a way that tends to weight reduction and environment protection.

1.2. Aim and objectives

1.2.1. Aim

The present research focuses on the fatigue behaviour and mechanical properties of a thin HSLA steel welded by laser. The aim is to understand the effect of weld bead geometry, imperfections, hardness and residual stresses in fatigue strength, fatigue life and tensile strength of laser welded butt joints in Strenx® 700 MCE steel, 3 mm thick. It is also sought to establish relationships between the factors that affect fatigue behaviour and the laser welding parameters, as well as the effect of the latter in the development of butt welded joints with a single pass.

1.2.2. Objectives

- To develop the laser welding for butt joints single pass autogenous obtaining acceptable weld bead using low laser power.
- To obtain a set of butt joints with differences in the main factors that affect fatigue behaviour for further study and to determine the weld quality, imperfection size distributions and weld profiles.
- To establish relationships between the laser welding parameters and microstructure, weld bead geometry, imperfections and residual stresses.
- To understand the effect of local properties in the fatigue crack growth rate of the laser welded butt joints.
- To understand the effect of weld bead profile, imperfections, hardness and residual stresses in the tensile strength, fatigue strength and fatigue life of the laser welded butt joints.

1.3. Scientific and technological challenges

The low laser power (2 kW) of the laser equipment available limits the laser power-welding speed space for the search of sound weld beads with a penetration of 3 mm and in keyhole mode. Therefore, obtaining welds with acceptable quality poses as a first challenge and understanding the complex phenomenon of fatigue in a thin element considering its main factors constitutes the second challenge of this work.

1.4. Thesis structure

Chapter 2 comprises the literature review of this thesis, its purpose being to establish the frame of reference and identify knowledge gaps in relation to laser welding and high-strength thin-gauge steels' fatigue behaviour. Emphasis is placed on the relationships between laser welding parameters and the main factors influencing the mechanical properties and fatigue behaviour.

In Chapter 3, a single pass autogenous laser welding is developed to weld 3mm thick Strenx® 700 MCE HSLA steel. Using a one-factor-at-a-time strategy, the effect of the main laser welding parameters on the weld bead geometry was determined, as well as the influence on imperfections. A set of welding parameters for a suitable weld bead were identified. Microstructure and mechanical properties (hardness and tensile strength) as a function of heat input were established and discussed.

In Chapter 4, a 2² factorial experimental design based on laser power and welding speed was conceived in order to obtain four butt joints with different heat inputs, hardness and imperfections. One of the joints was welded with the parameters that produced an adequate weld bead from Chapter 3, with the addition of a double-welded joint. The previously mentioned obtained butt welded joints will be used in the study of fatigue behaviour in the following chapters. With the imperfections and weld profile being influencing factors in fatigue strength, these two aspects were described in detail, having the weld quality level also been evaluated according to the ISO 13919-1 standard. The analysis

of variance (ANOVA) was applied to the weld geometry to validate the effect of the laser welding parameters.

The experimental results of four butt-welded joints' S-N curves are analyzed and discussed in Chapter 5. The influence of weld profile, imperfections, residual stress and hardness on the fatigue behaviour at low stress levels through the stress-concentrating effect were explained. The welded series' fatigue limits were predicted through the stress-concentrating effect and by the relationship proposed by Murakami.

In Chapter 6, the fatigue crack growth in the fusion zone (FZ) and in the HAZ for four welded series was studied. Paris' Law parameters considering the effect of the crack closure were obtained. The fracture analysis of fatigue specimens at high stress levels served to make estimates and predictions by the fracture mechanics approach to welded joints' fatigue lives.

Finally, general conclusions and future work are presented in Chapter 7.

1.5. References

- [1] World Auto Steel, "Advanced High-Strength Steels, Application Guidelines Version 6.0," April 2017. [Online]. Available: <https://www.worldautosteel.org/download-ahss-guidelines-6-0-free/>. [Accessed 1 February 2019].
- [2] C. I. García, "High strength low alloyed (HSLA) steels," in *Automotive Steels*, London, Elsevier Ltd, 2017, pp. 145-166.
- [3] A. Ilić, L. Ivanović, D. Josifović and V. Lazić, "Advantages of High Strength Steels Applications in Mechanical Constructions," in *The 7th International Symposium KOD, Balantofured*, 2012.
- [4] ASM International, *ASM Handbook*, Ohio: ASM, 1993, pp. 193-202.
- [5] W. Yan, L. Zhu, W. Sha, Y. Shan and K. Yang, "Change of tensile behavior of a high-strength low-alloy steel with tempering temperature," *Materials Science and Engineering A*, vol. 517, pp. 369-374, 2009.
- [6] E. Gyasi and P. Kah, "Structural Integrity Analysis of the Usability of High Strength Steels (HSS)," *Advanced Materials Science*, vol. 46, pp. 39-52, 2016.
- [7] T. Mohandas, G. Reddy and B. Kumar, "Heat-affected zone softening in high-strength low-alloy steels," *Journal of Materials Processing Technology* 88, pp. 284-294, 1999.
- [8] J. Górka, "Assessment of the Weldability of T-Welded Joints in 10 mm Thick TMCP Steel Using Laser Beam," *Materials*, vol. 11, no. 1192, pp. 1-16, 2018.
- [9] A. Jayanthi, K. Venkataramanan and K. Kumar, "Laser Beams A Novel Tool for Welding: A Review," *IOSR Journal of Applied Physics*, vol. 8, no. 6, pp. 8-26, 2016.
- [10] J. Górka and A. Ozgowicz, "Structure and Properties of Laser-Beam-Welded Joints of Low-Alloy High-Strength Steel DOCOL 1200M with a Martensitic Structure," *Materials and Technology*, vol. 52, no. 2, pp. 189-193, 2018.
- [11] W. Guo, D. Crowther, J. Francis, A. Thompson, Z. Liu and L. Li, "Microstructure and mechanical properties of autogenous laser welded S960 high strength steel," *Materials & Design*, vol. 85, p. 534-548, 2015.

- [12] D. Parkes, W. Xu, D. Westerbaan, S. Nayak, Y. Zhou, F. Goodwin, S. Bhole and D. Chen, "Microstructure and fatigue properties of fiber laser welded dissimilar joints between high strength low alloy and dual-phase steels," *Materials and Design*, vol. 51, pp. 665-675, 2013.
- [13] N. Farabi, D. Chen and Y. Zhou, "Fatigue properties of laser welded dual-phase steel joints," *Procedia Engineering*, vol. 2, p. 835-843, 2010.
- [14] S. J. Maddox, *Fatigue strength of welded structures*, Cambridge: Abington Publishing, 2002.
- [15] I. Lillemäe, S. Liinalampi, H. Remes, A. Itävuo and A. Niemelä, "Fatigue strength of thin laser-hybrid welded full-scale deck structure," *International Journal of Fatigue*, vol. 95, pp. 282-292, 2017.
- [16] H. Remes, J. Romanoff, I. Lillemäe, D. Frank, S. Liinalampi, P. Lehto and P. Varsta, "Factors affecting the fatigue strength of thin-plates in large structures," *International Journal of Fatigue*, vol. 101, pp. 397-407, 2017.
- [17] P. Kucharczyk, M. Madia, U. Zerbst, B. Schork, P. Gerwien and S. Münstermann, "Fracture-mechanics based prediction of the fatigue strength of weldments. Material aspects," *Engineering Fracture Mechanics*, vol. 198, pp. 79-102, 2018.
- [18] SSAB, "www.ssab.com," SSAB, 20 April 2017. [Online]. Available: [https://www.ssab.com /api/sitecore/Datasheet/GetDocument?productId=961589BF607D44A6869FCC20CDC8D0D2&language=en](https://www.ssab.com/api/sitecore/Datasheet/GetDocument?productId=961589BF607D44A6869FCC20CDC8D0D2&language=en). [Accessed 1 February 2019].
- [19] M. Mazur and R. Ulewicz, "Analysis of strength and fatigue properties of construction materials for manufacturing the parts of semi-trailers," *Applied Engineering Letters*, vol. 2, no. 1, pp. 32-37, 2017.
- [20] SSAB, "www.ssab.com," 2015. [Online]. Available: https://www.ssab.fi/-/media/Files/EN/Strenx/240en-Trailer-Design-Guideline-V3-2014_Confetti.pdf. [Accessed 2 January 2019].

Chapter 2: Literature review

2.1. High strength steels overview

The high strength steels (HSS) term refers to steels that exceed a certain level of strength. Although this value is generally not explicitly defined in some works and design guides, in the European Standard Eurocode 3 it has been established as 460 MPa [1]. Currently the previous level has been widely exceeded by a variety of steels as can be seen in Figure 2.1, where especially steels with automotive applications such as advanced high strength steels (AHSS), high-strength low-alloy (HSLA) steels and other type of steels are located in the elongation-tensile strength space.

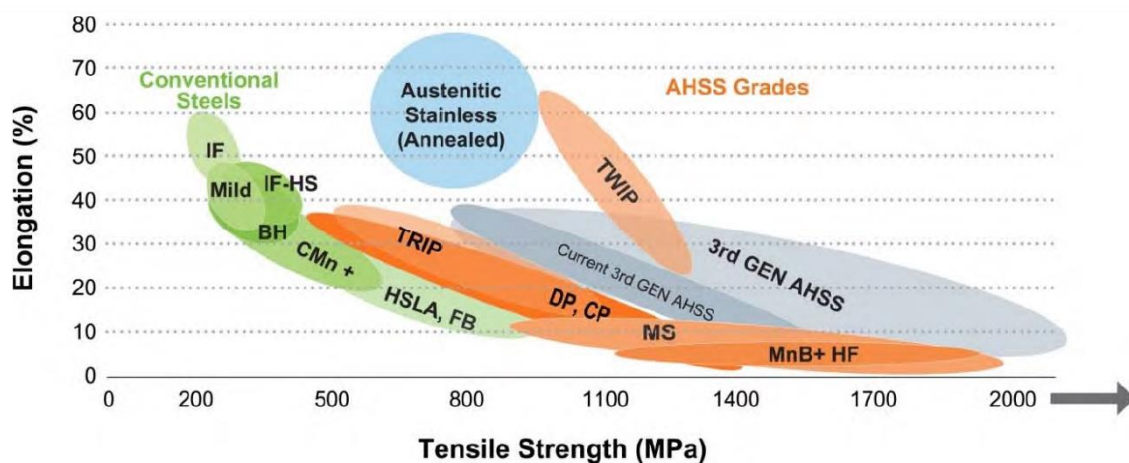


Figure 2.1 Location of HSS in the space elongation-tensile strength [2].

The production of HSS with increasing tensile strength has allowed considerable reductions in weight and cost and environmental benefits. For example, Hulka et al. [3] showed a case where under tension loads, the plate thickness was reduced 60% when S960 steel was used instead of S355 steel, Nowacki et al. [4] presented a chart with various savings (in thickness, weight, time and others) that exceeded 70% in comparisons between the use of S335 and S1100QL, meanwhile, He et al. [5], in a case study that estimates various environmental benefits from the use of AHSS instead of common steels, it is shown for example that the replacement of 50% of the vehicle body results in 185.6 kg CO₂eq reduction in cradle-to-gate greenhouse emissions gas (GHG) per vehicle.

The key factor in the production of current HSS has been attributed mainly to thermo-mechanical controlled processing (TMCP) although quenching and tempering processes (Q&T) are also used. TMCP is a sophisticated combination of well-defined deformation operations and heat treatments in a single stage to control the microstructure of steels for to produce multiphase steels [6]. This technology is used to produce both HSLA steels and AHSS.

Unlike AHSS, HSLA steels have a broader spectrum of applications such as automotive, structural, oil and gas pipelines, lifting, shipbuilding, pressure vessels, farm machinery and industrial equipment [1, 7, 8]. HSLA steels are classified as microalloyed steels, have low carbon content and with a varied chemical composition. The good combination of properties such as tensile strength, toughness and weldability is mainly based on a fine grain size, low carbon content and the precipitation strengthening of vanadium, niobium and titanium, although other elements can strengthening by solid-solution or improve the hardenability and the resistance to atmospheric corrosion [8, 9].

More demanding or additional requirements in several of the industries that have used HSLA steels are being covered by new solutions aimed to weight reduction and enhance specific properties according to the application. For example, in a reactor pressure vessel application, fracture toughness, fatigue crack growth rate and neutron irradiation embrittlement resistance plus tensile strength were considered the influencing properties in the evaluation of three types of A508 steels [10]. A steel presented an excellent combination of strength and fracture toughness based on a tempered martensitic microstructure, however, due to its nickel content, which is prone to neutron irradiation, required further evaluation. In other case of a pipeline application, a good balance between high strength, low temperature toughness and good weldability were highlighted in the analysis of two manufacturing concepts on X100 pipeline steel [11].

The above examples show a sensitive interdependence between the process parameters, the chemical composition and the microstructure of the steels, which determines the desired properties in each application.

In general, the high strength of HSLA steels can be achieved with microstructures such as martensite and bainite, however, the balance between tensile strength and toughness has been reported due to microstructures such as acicular ferrite, bainites or combinations between phases [12, 13]. On the other hand, good weldability in steels mainly refers to the minimal risk of cold cracking with normal welding practices, the use of filler metals with low hydrogen content and no need for temperature control in welding. This property in HSLA steels is due to the very low carbon content and the low carbon equivalent (CE) and in the case of thin plates avoids the use of pre- and post-weld treatments as well as reduces costs and increases productivity.

2.2. Strenx® 700MCE steel

According to the steel producer, Strenx® 700 MCE steel is a hot rolled structural steel for cold forming. The chemical composition (max %) and tensile mechanical properties are shown in Table 2.1 and Table 2.2, respectively. This steel is produced in thicknesses from 2 to 10 mm, covering the requirements of S700MC in EN 10149-2 and the E letter corresponds to a minimum energy impact of 27 J/-40°C [14].

Table 2.1 Chemical composition (%).

C	Mn	Si	P	S	V	Nb	Al	Ti	Fe
0.12	2.1	0.21	0.020	0.010	0.20	0.09	0.015	0.15	balance

Table 2.2 Tensile mechanical properties.

Yield strength (min MPa)	Tensile strength (MPa)	Elongation (min %)
700	750-950	10

S700MC steel is a HSLA steel, produced by TMCP whose mechanical properties are due to a ferritic-bainitic microstructure hardened through precipitation, solution, plastic deformation and grain refinement [15]. Various authors [16-18] agree with the previous microstructure. The role of the alloying elements such as Nb, V and Ti is reported according to the fine and coarse precipitates found in the microstructure. Górká and Stano [19] in the ferrite identified a hardening effect by (Ti, Nb) (C,N)-type dispersive precipitates of few nanometers in size; the reduction of the growth of recrystallized austenite grains by coarse

precipitates like the previous ones and carbides (Ti, Nb)C-type precipitates, while; Goritzki et al. [20] established an adverse effect on toughness by coarse inclusions of complex composition based on titanium carbonitride and aluminum oxide Al_2O_3 . The high strength of this grade of steels is due to various hardening mechanisms, although it has not been conclusively determined which is the mechanism that contributes the most to high strength, however, DeArdo et al. [12] point out that in the case of bainitic microstructure, the greatest effect is probably due to the density of dislocations and the solid -solution.

Due to properties as high strength, toughness and weldability, S700MC steel is used in various applications such as large cranes, earthmoving equipment, telescopic booms, truck trailers and agricultural machinery [14, 21].

The weldability attributed to S700MC steel can be judged based on the practical procedure given in [22]. Through this procedure the material is located by means of the carbon percent and CE in one of the three zones (Figure 2.2). The zones indicate the greater or lesser possibility of cold cracking (being higher in zone III) and temperature control requirements according to the thickness, filler material and joint restriction. Steels with carbon content less than 0.1%, although with a high CE, would be located in zone I where the risk of hydrogen cracking is lower. In relation to Strenx® 700 MCE steel, assuming the carbon content 0.1 %, the maximum percentages for the remaining chemical elements (Table 2.1) and by means of the relation (2.1) [22], the CE results 0.53, therefore it is located on the border between zone I and zone III. The steel manufacturer, for welding for this grade of steels up to 30 mm thick, does not prescribe preheating temperatures and between welding passes [14], thus indicating good weldability.

$$CE = C + \frac{Mn + Si}{6} + \frac{Cr + Mo + V}{5} + \frac{Ni + Cu}{15} \quad (2.1)$$

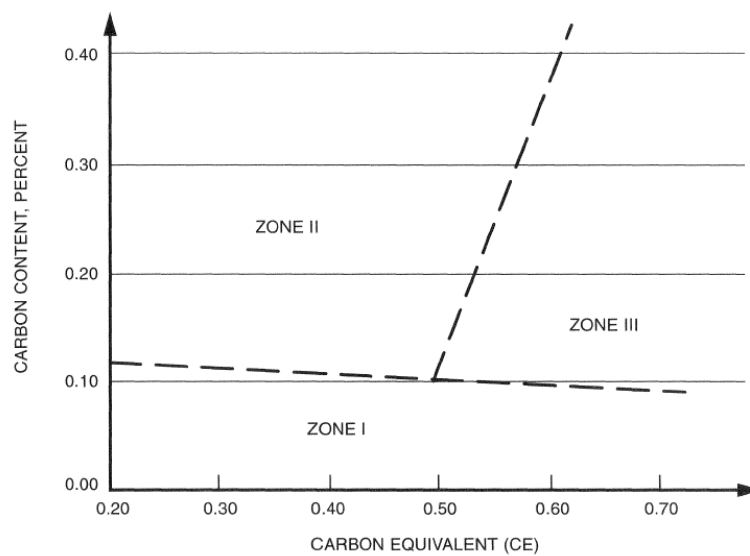


Figure 2.2 Diagram carbon-carbon equivalent [22].

2.3. Laser welding

The applications of laser welding are wide and varied. Sectors such as aerospace, automotive, biomedical, construction, railway, power generation and shipbuilding are among the most common; various types of steels, aluminum alloys, titanium alloys and dissimilar materials are some of the materials joined by laser welding [23]. The different modes of laser beam emission and interactions with the materials and the combinations with arc processes allow applications from very thin to thick thickness and in various types of welded joints. Autogenous laser welding (ALW), narrow gap laser welding (NGLW), pulsed laser, hybrid laser-arc are among others, types of laser welding that enrich the application alternatives in the field of welding.

A high power density is the significant feature of laser welding compared to conventional welding processes. Narrow and deep penetration, low heat input, small heat-affected zone (HAZ) and fusion zone (FZ), minimal distortion and other advantages such as flexibility and automation can be achieved by laser welding systems [24]. Characteristics like the previous ones have allowed laser welding to continue increasing the applications. Figure 2.3 illustrates an industrial application and a weld bead of laser welding.

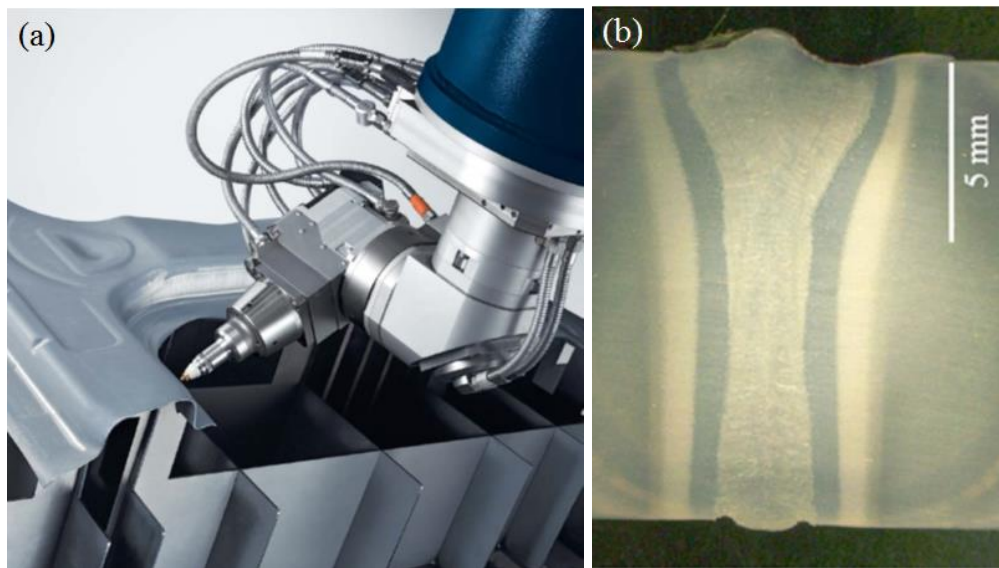


Figure 2.3 A laser welding application (a) [25] and ALW weld bead (b) [26].

2.3.1. Laser optics and beam quality

In laser welding, the coherent electromagnetic radiation emitted by the laser is conducted and focused on the welded joint. If the beam is delivered by optical fiber, the divergent beam is collimated and focused by lenses, see Figure 2.4a. Ideally at the welding site, high power concentrated in a small zone and constant throughout it is desirable; the diameter f_d (waist diameter, spot diameter or focus diameter) and the length f_l (focus depth) define this zone. Due to the laser optic system, a minimum beam diameter f_d is produced, the beam diverges beyond of the waist beam a certain angle ψ and a beam shape (Gaussian) where the power intensity varies in the space is formed, see Figure 2.4b. Through the characteristics and quality of the optical system and laser, the geometric parameters and the energy available at the welding site can be determined as indicated below.

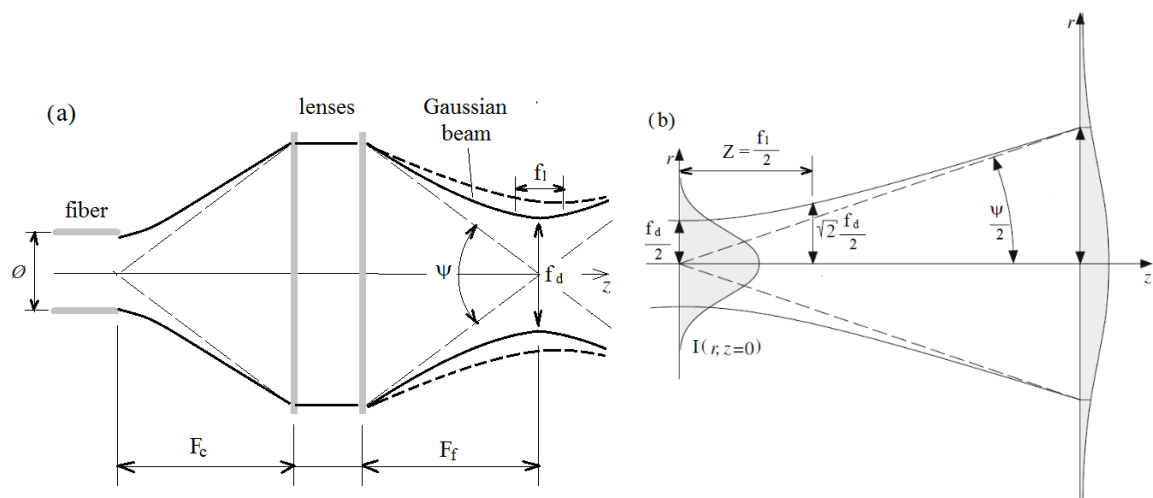


Figure 2.4 Schemes of the laser optical system a) and irradiance distribution in space b), adapted from [27]

The size of the focus diameter f_d is determined by the focal lengths F_f and F_c of the lenses and by of the optical fiber diameter \emptyset :

$$f_d = \frac{F_f \emptyset}{F_c} \quad (2.2)$$

The beam parameter product (BPP) which is a quality index of the laser establishes the angle of divergence ψ :

$$\psi = \frac{4 \text{ BPP}}{f_d} \quad (2.3)$$

The intensity of a laser beam is measured by the irradiance I , which is defined as the power of electromagnetic radiation per unit area (also named power density). For the fundamental transverse electromagnetic mode of any laser, the cross section of the beam is circular and the profile of the irradiance ($I(r, z)$) in this section is Gaussian [27]. Conventionally it is assumed that the waist radius is the radius value where the irradiance drops to $0.135I_0$, being I_0 the peak of irradiance on the beam waist center. In order to establish a distance in the direction z where the beam diameter is approximately constant ($2Z$ or f_l), the Rayleigh range it is generally used, in which the diameter increase to $\sqrt{2} f_d$, with this, the distance Z is:

$$Z = \frac{f_d}{\psi} \quad (2.4)$$

Therefore, the focus depth f_l can be determined in function of the focus diameter and the divergence angle ψ . In the Figure 2.4a, the schematic Non-Gaussian beam (dotted line) considers a laser output more real than a Gaussian beam. The decrease of the focusability for a beam more real can be evaluated by the beam factor M^2 which is the relation between BPP Non-Gaussian and Gaussian. The value of M^2 is always greater than one and depends of the laser type, its optics and the power [28].

In summary, the fiber diameter \varnothing and focal lengths determine the focus diameter f_d , while a low BPP value and an M^2 value close to one, allow a deep focal length for less power variation in the weld zone.

2.3.2. Disk Laser

Various types of laser are used in welding: CO₂, Nd: YAG, diode, fiber and disk. These lasers differ in power, wavelength, efficiency and in specific characteristics that allow them to compete as sources for welding, however, the current development focuses on the last three types [29]. A disk laser is a solid-state laser whose gain medium is a wafer-thin crystalline disk made of Yb: YAG pumped by a diode laser and the optical resonator composed of internal and external mirrors to the cavity containing the disk [30]. Figure 2.5 shows two diagrams of the disk laser. The principal advantages of disk lasers are: high output power, high electrical efficiency and high beam quality simultaneously [29, 31].

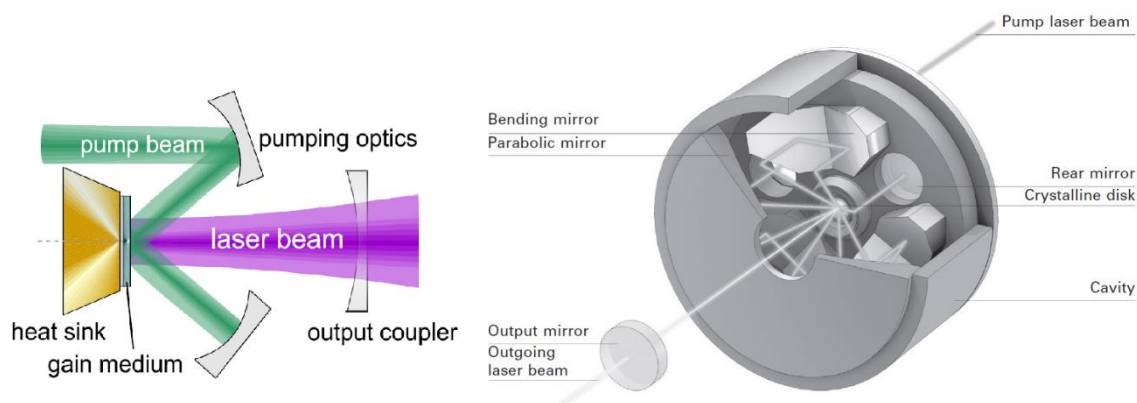


Figure 2.5 Schemes of disk laser systems [30, 32].

From the commercial information of a disk laser manufacturer [25], some technical characteristics of their models are the following: power at the workpiece: 1-16 kW, power constancy 1%, beam quality (BPP) 2-25 mm-mrad, laser light cable diameter: 50-600 μm and wavelength 1.03 μm . According to [31] the quality parameter M^2 can go from 1.2 to 20 for powers of 100 W to 8 kW, respectively.

The general characteristics of the laser equipment available for the research work can be seen in Table 2.3.

Table 2.3 General characteristics of available laser equipment.

Laser: Trumpf TruDisk 2000	
Laser maximum output (W)	2000
Beam wavelength (nm)	1030
Fiber diameters (μm)	50, 200
Beam parameter product (mm-mrad)	2

2.3.3. Operation modes

In laser welding two operation modes are distinguished from an irradiance level that produces a large increase in penetration. It is generally considered that on an irradiance of 10^6 W/cm^2 [33], the keyhole mode is produced, while below this level, the conduction mode occurs. In the keyhole mode, deep and narrow penetration, high welding speed and

low heat input (HI) can be achieved, however, certain disadvantages are present, such as close fitting due to small focused spot size, accurate beam-joint alignment and variety of weld bead defects can be produced. Although the conduction mode has a low penetration it also has advantages such as the process is stable, allows better control of the HI, the width beam reduces close fitting and not require high beam quality [34].

When a laser beam hits a metal surface, if the irradiance is not enough, the absorbed energy only forms a weld puddle and the heat is quickly dissipated by conduction, whereas, if the irradiance is enough the metal liquid rises the boiling temperature and a keyhole is formed due to the evaporation, see Figure 2.6. In conditions of stability the keyhole is maintained during the welding and a deep and narrow penetration is achieved. A characteristic aspect ratio of the weld bead (depth/width) has each mode [35], that according to Quintino et al. [33], a ratio greater than 1.5 identifies the keyhole mode.

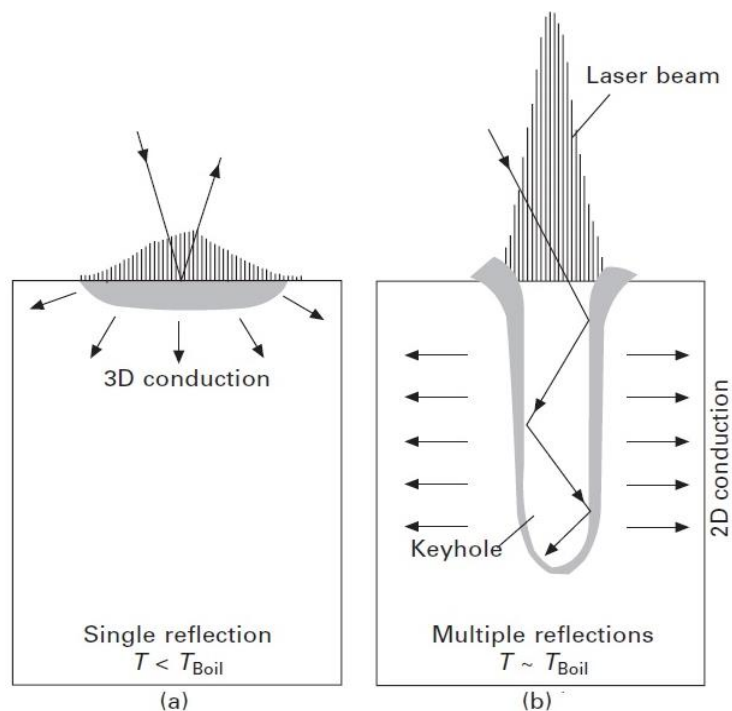


Figure 2.6 Scheme of laser welding operating modes, adapted from [36].

In a research of how laser welding affects the formability of a DP980 Double Phase steel [37], it was used two types of lasers with two different beam size, one much smaller than the other (600 μm and 12x0.5 mm). Characteristic weld beads were obtained

for each operating modes, thin and deep in the keyhole mode and wide and small penetration in conduction mode.

2.3.4. Laser Welding Parameters

For a base metal (BM), thickness, joint design and laser welding equipment, a set of welding parameters must be established for achieve a proper weld bead geometry, free of defects, adequate mechanical properties as well as the efficiency in the process. Considering that the high power density is the prominent characteristic of laser welding and the HI is a factor determinant for any welding process, the welding parameters could be grouped as main and secondary, as indicated below:

- Main: power (P), welding speed (v), focus diameter (f_d), focus position (f_p) and focus length (f_l).
- Secondary: shielded gas, surface condition, joint preparation, welding position and beam tilt.

In the case of thin materials, the focus position and focus length parameters may have less effect if the focal length is deep. Although some parameters have been called secondary, due to the sensitivity of laser welding they can affect the weldability and efficiency. In addition to the mentioned welding parameters, depending on the emission mode (continuous mode, pulsed mode) and the type of laser process, other parameters could influence in the weldability of the materials.

Unlike conventional welding processes, where knowledge and experience have allowed effective joint of the most of materials in industrial applications, in laser welding, achieving good weldability in a given application generally requires experimental work, several attempts and optimization, so that achieving a defect-free weld has become a challenge [38]. In the literature, several methods have been reported to determine the welding parameters for a satisfactory welding, these can include in: trial and error, design of experiments, use of analytical models, optimization methodologies and simulation by finite element method [39].

2.3.5. Effect of Laser Welding Parameters on Weld Geometry

The penetration and width of the weld bead are of primary importance in any welded joint, therefore the relationship with the laser welding parameters need to be known. In the work [33], using a 19mm thick API 5L: X100 steel plate, for a wide power range (2-8 kW), welding speed (0.3-3 m/min) and heat input (50-1200 J/mm) were established the respective functions in relation to penetration depth. Figure 2.7a and 2.7b show the relationship of penetration with power and speed, respectively. The welding parameters: beam diameter, 0.6 mm; BPP, 16 mm-mrad and focal position, 0 mm, were constant.

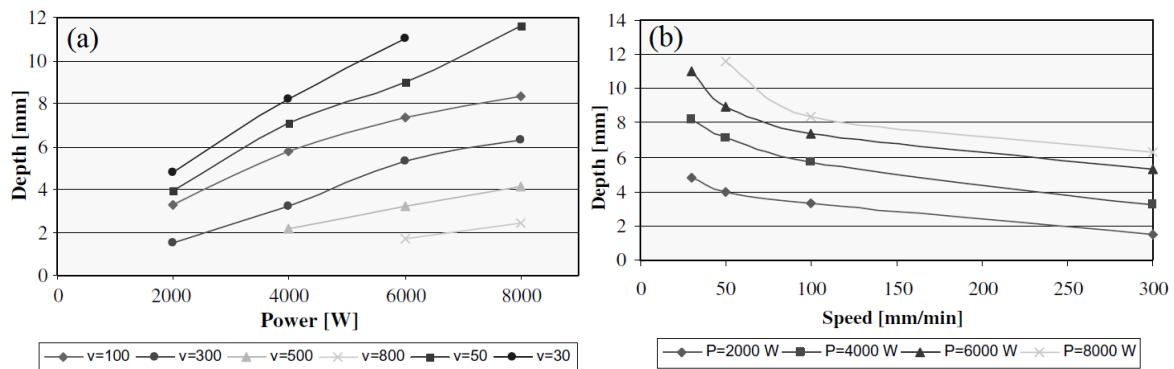


Figure 2.7 Penetration depth as function of power (a) and of welding speed (b) [33].

As seen in the two Figure 2.7, the relationships tend to be linear except for low values of the welding speed, where a large increase is observed as the welding speed is reduced.

The HI is an important welding parameter, represents the energy per unit length supplied to the welded joint, in laser welding the nominal heat input can be determined by the expression:

$$HI = 60 * \frac{P}{v} \quad (2.5)$$

where, with the power P in (kW) and the welding speed v in (m/min) results the HI in (J/mm). The value of the HI necessary for complete penetration in a given joint is very useful because it allows the variation of power and welding speed in order to modify the weld bead

geometry. The HI has been investigated in some works founding that the increase of the HI increase the penetration depth [33] as well as the width of the weld bead [40].

Sharma et al. [41], for combinations between steels: Dual Phase (DP), Transformation induced plasticity (TRIP), Boron alloyed and mild steels for butt welds in thicknesses ranged from 1 to 2 mm using Yb: YAG laser in keyhole mode, through of three series in which the power and welding speed varied between, 2-4.5 kW and 70-150 mm/s, respectively, developed an expression that allows to calculate the welding speed v (mm/s) as function of power P (kW) and thickness t (mm), thus:

$$v = 0.27 \exp\left[-0.886 \left(\frac{t}{P}\right) - 0.577\right] \quad (2.6)$$

For the previous relation was reported an error ranged -39 % to 27 %.

From an efficiency point of view, high powers, high speeds and small focus sizes are desired. When reviewing the literature, a wide range of these three factors is found for complete penetration in ALW of HSS. In Table 2.4 are presented data reported in various works with exception of the irradiance and the nominal HI that were calculated based in the focus diameter, power and welding speed.

Table 2.4 Welding parameters used in various works.

Type of Laser	Steel	Thickness (mm)	Focus diameter (μm)	Power (kW)	Welding speed (m/min)	Heat Input (J/mm)	Irradiance 10^6 (W/cm ²)	Mode	Reference
Fiber	S700	13.0	800	13.0	0.72	1083	2.6	keyhole	[26]
Fiber	S960	8.0	800	6.4	1.08	356	1.3	keyhole	[42]
Disk	Domex 960	5.0	200	3.3	1.00	198	10.5	keyhole	[43]
Fiber	S690QL	3.0	600	3.0	2.50	72	1.1	keyhole	[44]
Fiber	S700MC	5	200	2.5	0.50	300	2.0	keyhole	[45]
Fiber	TRIP	2.0	200	2.0	3.50	34	6.4	keyhole	[46]
Disk	Docol 1200M	1.8	300	2.5	6.00	25	3.5	keyhole	[47]
Disk	Docol 1200M	1.8	600	3.5	6.00	35	1.2	keyhole	[47]
Fiber	DP 980	1.2	600	6.0	16.00	23	2.1	keyhole	[48]
Diode	DP 980	1.2	6 mm ²	4.0	1.00	240	0.1	conduction	[48]

Some observations can be highlighted from the table above. The value of 10^6 W/cm² commonly assumed to differentiate the two modes agrees; in general, the HI necessary for a complete penetration increase when increase the thickness; the HI per mm of thickness varies between 14 to 80 J/mm² in keyhole mode; for a same thickness it is possible to achieve complete penetration with less HI if a focus of smaller diameter is used and even for relatively thin thicknesses, if small focus is not used, powers above 3 kW have allowed to reach full penetration. Expression (2.6) was tested for the data in Table 3.4, finding that it is valid for thin thicknesses.

For certain power, the beam size modifies the irradiance. Kawahito et al. [49], using four focus diameters: 130, 200, 360 and 560 μ m, investigated the effect of power density for a stainless steel SUS304, 8 mm thick. They found that at high welding speeds the penetration increase remarkable with the power density. Therefore, a small focus diameter increases the penetration. In relation to the effect of the focus position on the penetration in [50] was found that the penetration increase for negative focus positions.

Other factors than the main ones have also been studied in laser welding. Sokolov and Salminen [51], studied the effect of edge surface preparation in the penetration depth in a 20 mm thick butt welded joint in low alloy S355 steel. The edges of the plates were prepared by shot blasted or milling machine obtaining different roughness. They founded that penetration depth varied with de roughness and gap, it was also observed that the penetration had variation along of the weld axis. Maina et al. [52], found that the surface condition has a great influence on the laser micro-welding of copper. They established that the absorption ratio and the stability of the process increase by controlling the surface topology and therefore the penetration and the surface quality of the weld increase.

2.3.6. Effect of Laser Welding Parameters on Imperfections

Due to the laser welding comprises complex multidimensional mechanisms, the ensuring a high quality welded joint without defects is a major challenge [38]. The welding parameters must be chosen appropriately to avoid imperfections that can compromise the structural integrity of the welded joints. The ISO 13919-1 standard [53] presents three quality levels (B, C and D) and 18 imperfections for laser beam welds. In the literature there

are a variety of imperfections and denominations, the possible causes and their general prevention [54-56].

Imperfections such as undercuts, underfill, excess weld (humping), lack penetration, porosity, spatter and bad aspect of the weld seam are commonly reported in works [50, 57], where the effect of laser welding parameters on imperfections has been studied for ALW in thick steel plates. In the work [50] was studied principally the effect of welding speed and the focus position, it was established that high welding speeds tend to decrease the underfill and that the two mentioned welding parameters can serve to optimize the weld bead, see Figure 2.8.

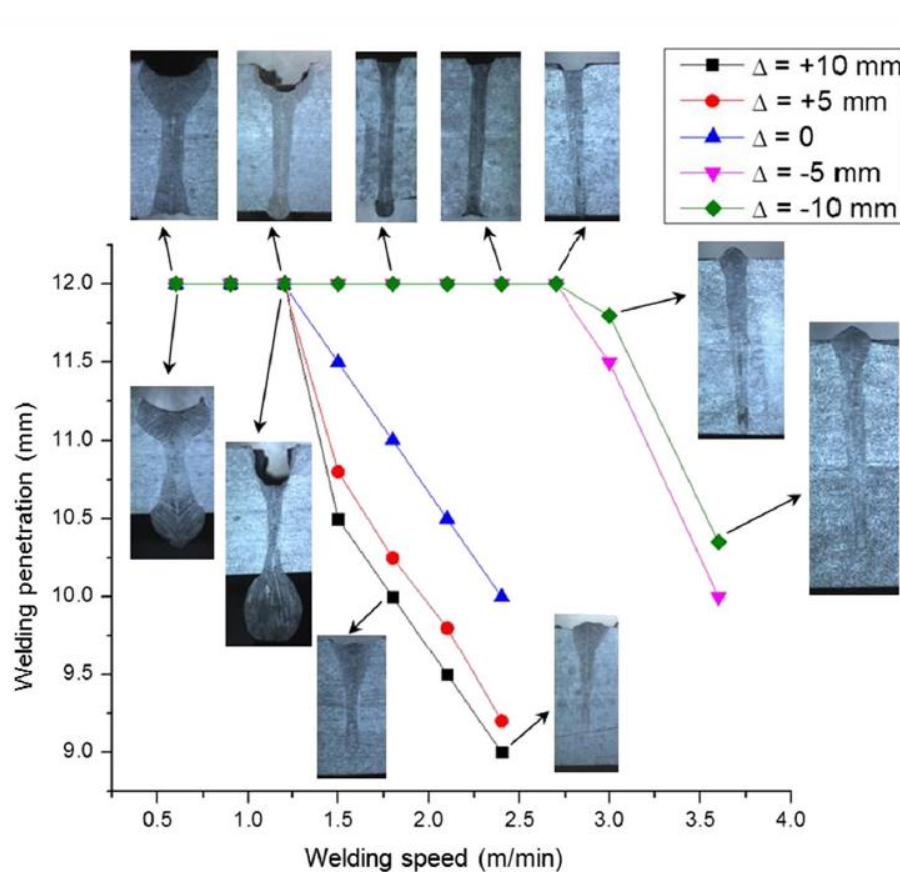


Figure 2.8 Welding speed and defocusing effects in the weld bead [50].

Meanwhile in [57] the effect of the laser focusing properties (f_d and f_l) on weld defects was investigated for a HSS. Two optics systems were used: system A ($f_d = 200 \mu\text{m}$, $f_l = 2 \text{ mm}$) and system B ($f_d = 270 \mu\text{m}$, $f_l = 4 \text{ mm}$). A variety of defects were observed

throughout the speed range in the system A, while in the system B the defects decrease and there is no porosity at low speeds. According to the authors the system B offers better weldability at low speeds that was attributed to the distribution of the power density along the keyhole, in the case of system B the power density was more balanced meanwhile, in the system A, there was a great variation. This study establishes that a stable keyhole for complete penetration is achieved with power density within 50-120 kW/mm². Figure 2.9 illustrates imperfections reported in the previous work for certain range of the welding speed.

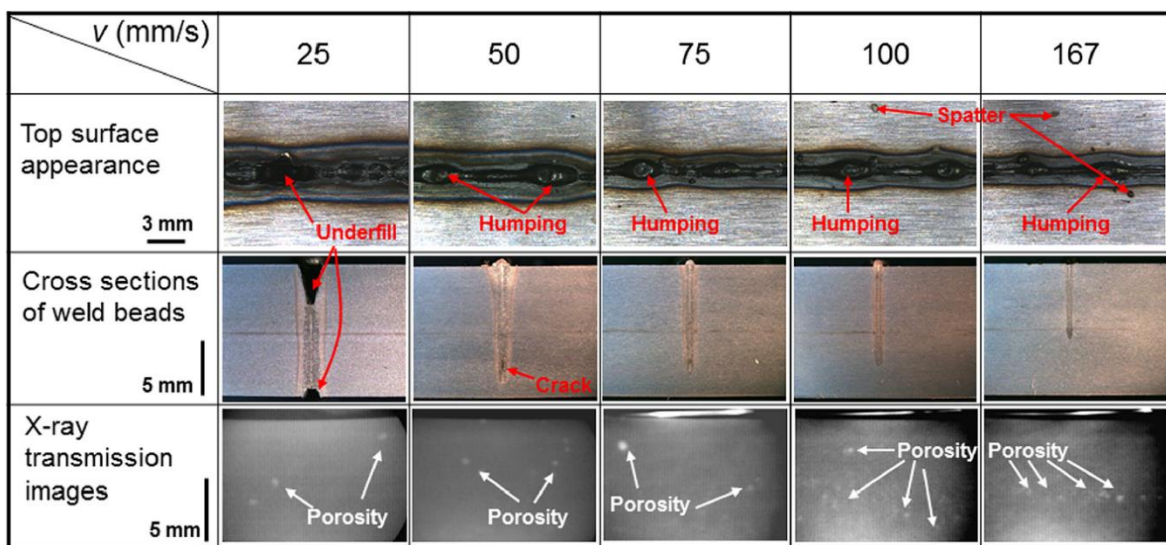


Figure 2.9 Defects of the system A produced as function of welding speed [57].

In the work [49], at 6 kW in a welding speed ranged 4.5 to 10 m/min and for the spots diameter of 360 and 560 μm , a window of sound welds between defects as porosity, humping and underfill was displayed, see Figure 2.10a. In this work, imperfections-free welds are attributed to the long molten pool that suppresses and accommodates the spattering and a stable keyhole without bubbles on the tip.

Lisiecky [45] investigated the effect of the HI in laser bead-on-plate welding of 5 mm thickness, determined the necessary HI for complete penetration and showed the influence of ranges of power and welding speed on the formation of imperfections, see Figure 2.10b.

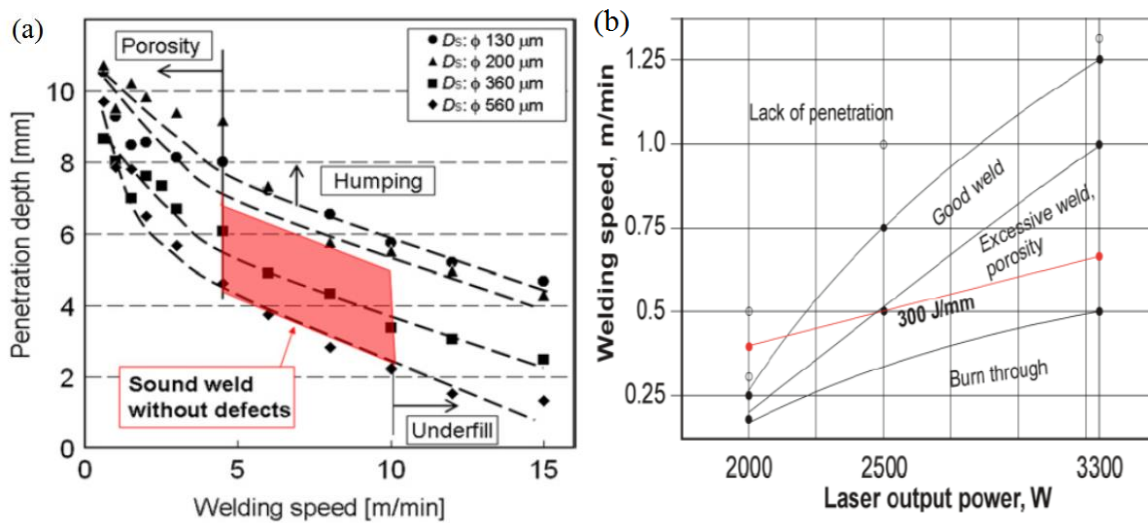


Figure 2.10 Sound welds windows in space depth-welding speed (a) [49] and welding speed-power (b) [45].

In two studies, [58] and [15], where the S700MC steel was laser welded, a quality level B according to the ISO 13919-1 standard and mainly imperfections such as undercuts, underfill, excess weld, porosity, misalignment, incomplete penetration, spatter, and bad appearance, were reported.

The stability of the keyhole appears as an important factor for a uniform penetration and to avoid defects as porosity in many materials [55, 59, 60]. In Zhao et al. [61] it is pointed out that for a range of defocusing the keyhole was stable and therefore porosity decrease significantly. In [62] the correlation between the keyhole oscillations and the frequency characteristics of the laser welding light emissions was studied. It was found that a significant oscillation of the keyhole results in variation of the penetration and rough surface of the weld bead therefore the welding process is unstable being the cause of the oscillation the inappropriate selection of the welding parameters. It was also determined for a carbon steel that the keyhole is more stable to high power, low speed and focus position below of workpiece surface. The instability of the keyhole also causes the variation of the weld bead section along of the weld axis as shown in some works [50, 63].

Other aspects have also been reported to cause imperfections, Lampa [64], investigated the effect of the separation between plates (gap) in butt joints formed with 2 mm thick stainless steel. It was observed that when the gap increases, underfill occurs.

As reviewed in these last two sections, there are several welding parameters influencing the weld bead geometry and imperfections, although there are general trends in the effects of each parameter, these are affected by the specific welding conditions of each case. On the other hand, there are conflicting criteria, for example productivity leads to the use of high speeds while low speeds are recommended for greater stability of the keyhole. Although it is possible to establish ranges of welding parameters in which there are welds without defects, these ranges are narrow or not applicable to low values of welding parameters such as power or welding speed. It has also been seen that despite keeping the welding parameters constant, there are always variations in the profile of the weld bead along the axis of the weld. Therefore, to achieve a suitable weld, a careful selection of the welding parameters and the evaluation of the variation of the section of the weld bead and imperfections in its length is required.

2.3.7. Modelling and Optimization in laser welding

The demands on the weld quality for a certain application may require minimizing the presence of imperfections, optimizing the weld bead profile or avoiding that the mechanical properties of the welded joint decrease excessively with respect to the BM. Several approaches are found in the literature for these purposes.

Guo et al. [42] reported in 8 mm thick S960 steel ALW that sound weld and complete penetration was achieved after of many trials. The cross sections of the weld beads obtained with different values of power are shown in Figure 2.11, the weld bead optimized corresponded to 6.5 kW (Figure 2.11d). It should be noted that the optimized weld bead has a slight excess weld at the weld root.

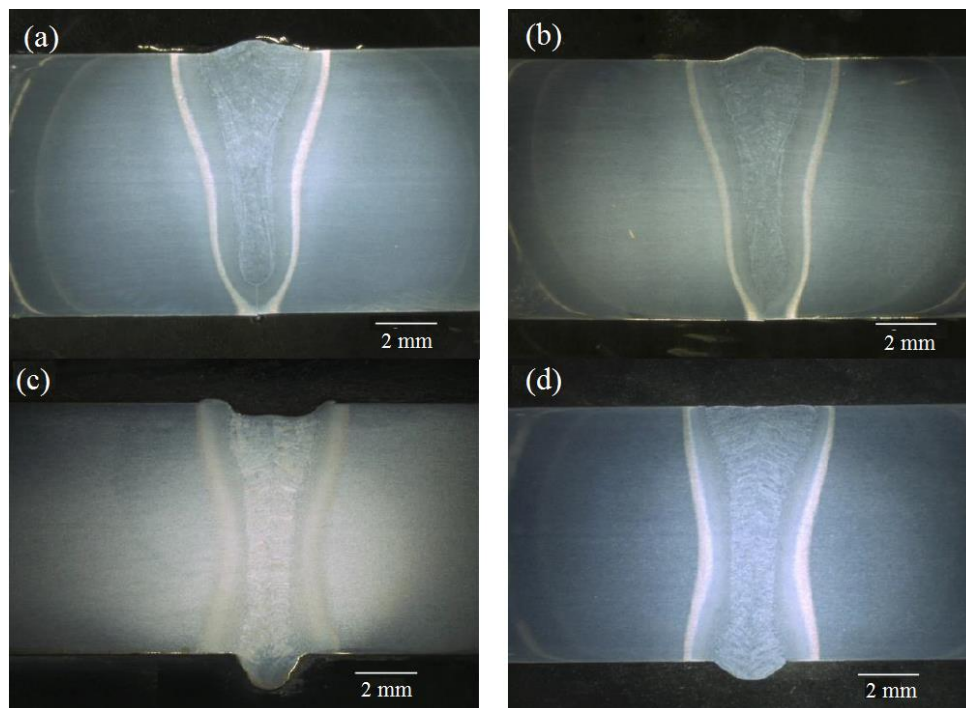


Figure 2.11 Wed bead cross sections for different power laser (kW), 6 (a), 6.2 (b), 6.7 (c) and 6.5 (d) [42].

The same author in another work [65] applied design of experiments (DoE) and optimization multi-variable at the NGLW process for find the better combination of parameters in order to achieve weld bead sound and efficiency. The laser power, welding speed and wire feed rate were the input variables while the weld integrity, weld bead width and de number of passes were the output variables. This approach was applied to S960 steel in 6 mm of thickness and after of the validation experimental, the relations of the optimization model were also applied to two steels with different thickness (8 and 13 mm). In the case of the 13 mm thickness, the optimization model results were modified slightly, indicating that the model has a limitation in the range of thicknesses it can cover.

Khan et al. [66] developed mathematical models to determine optimal laser welding parameters for minimization of weld bead width and maximization of penetration depth and shearing force of two stainless steels. They used a factorial design of three factors and three levels that allowed assessment the effect of each parameter, the solutions unlike other works, were validated for ranges of each parameter. This author highlighted that the conventionally the selection of laser welding parameters for new welded products depends of the skill of engineer or machine operator can lead a time consuming trial and error.

In [38] it is used an optimization method based in back-propagation neural network (BPNN) and genetic algorithm (GA) for welding defects reduction through the relationship between the welding parameters (power, welding speed and focal position) and the welding defects indexes for the weld bead. For 2 mm thick DP590 steel welded with fiber laser were founded porosity, incomplete penetration, drop-thru, humping and large fusion zone. The parameters that allowed to optimize the weld bead eliminating the defects as mentioned were: 2.14 kW, 2.73 m/min and -1.68 mm (Note the precision used in welding parameters).

Beyounis and Olabi [39], presented a review of the application of methods for the modelling and optimization in welding process using statistical and numerical approaches. Factorial design, artificial neural networks (ANN), GA, Taguchi and response surface methodology (RSM) are the principal methods reviewed in some applications to both weld bead defects and mechanical properties of the variety of welding processes.

According to the review from trial and error to various optimization methodologies they do not guarantee the elimination of defects and the variation of the weld profile along of the weld axis.

2.3.8. Laser welding of high strength steels

Although laser welding has characteristics that advantage over conventional welding processes, the heating and cooling cycles of welding differ considerably from the careful TMCP or Q&T used for the production of HSS. The hardening mechanisms and hard microstructures of the BM undergo changes in the welded zone due to the heat introduced for welding. The FZ and the HAZ produced by welding show microstructures different from that of the BM, these changes can affect the mechanical properties of the welded elements. On the other hand, the keyhole mode comprises vaporization that can also cause the loss of alloying elements.

Starting from the fact that mechanical properties are governed by the microstructure, understanding its evolution by effect of laser welding is of outstanding importance. The HI is the common measure of comparison of the heat effect in any welding

process, for the case of laser welding comprises the power and the welding speed according to the relation (2.5).

2.3.8.1. Effect on microstructure and hardness

Guo et al. [26], determined the microstructure evolution in three welding processes (GMAW, ALW and NGLW) of S700 steel in 13 mm thickness. The bainitic microstructure of the base metal was transformed into the HAZ and FZ in various microstructures according to HI of each welding process. For the ALW, with 13 kW of power, welding speed of 0.72 m/min ($HI=1083 \text{ J/mm}$) and focus diameter $800 \mu\text{m}$, the microstructure evolve to bainite and small quantities of martensite in the FZ and to martensite in the HAZ, see Figure 2.12. Consequently to microstructure changes, hardness profiles are produced in the welded area, such as those indicated in Figure 2.13.

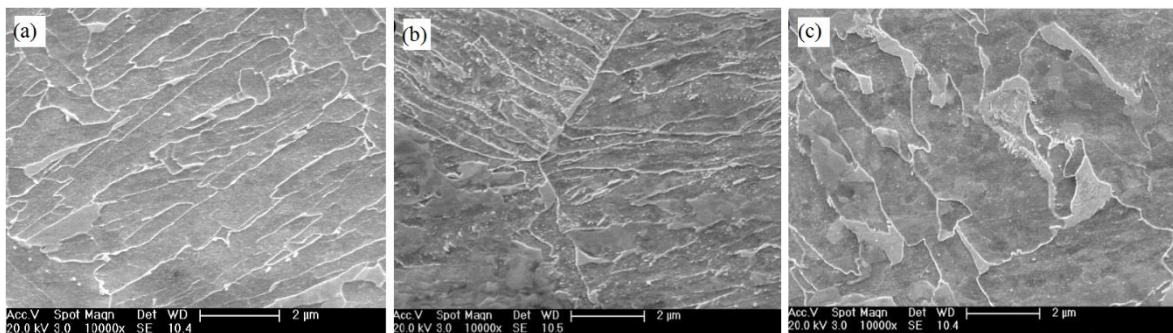


Figure 2.12 Microstructures of steel S700 in ALW, BM (a), HAZ (b) and FZ (c) adapted from [26].

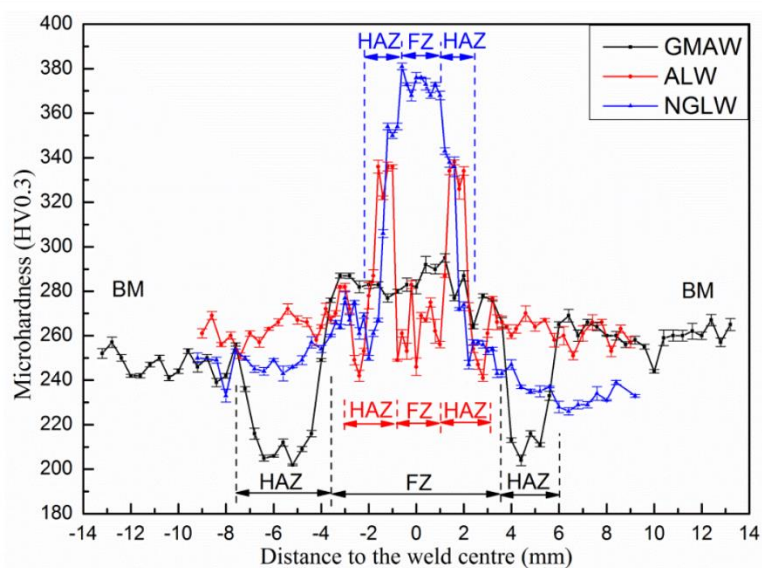


Figure 2.13 Micro-hardness of steels S700 [26].

As can be seen in previous Figure 2.13, the sizes of the HAZ and FZ of the laser processes are smaller than those the conventional process, the HAZ softening in the GMAW process is more greater than the laser process, the FZ hardness are greater than the BM for the laser processes and therefore the hardness in each zone is consistent with its microstructure.

Farabi et al. [67] analyzed the microstructures and hardness of two steels Dual Phase (DP600 and DP980, 1.2 mm thickness) welded by diode laser. It was used a power of 4kW, welding speed of 1 m/min (HI=240 J/mm) and beam dimension of 12x0.9 mm². The BM microstructure of these two steels consists mainly of ferrite and martensite in different proportions and shape. According to the authors, for the two steels in the HAZ, there were tempering of the martensite, affecting more to the DP980 steel because of its greater amount of martensite, and in the FZ of the two steels, the martensite formed is due to rapid cooling of the laser process. Figure 2.14a-c for DP 600 steel and Figure 2.14d-f for DP980 steel, illustrate the significant changes in BM microstructure in HAZ and FZ. In the hardness profiles that are shown in Figure 2.15, it is observed that the DP 600 steel suffers an increase in the FZ and a small softening in the HAZ, in contrast, the DP980 steel does not increase the hardness in the FZ and has a wide and sharp softening in the HAZ in which the hardness decreases considerably.

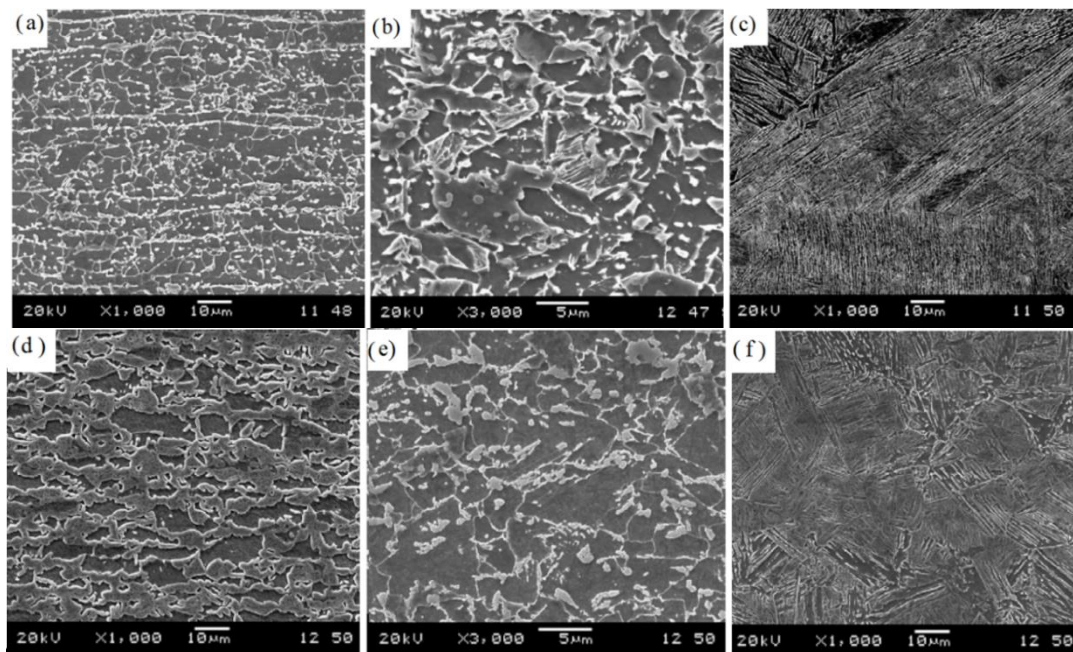


Figure 2.14 Evolution of microstructure in DP steels; BM (left)-HAZ (center)-FZ (right); (a)-(b)-(c) DP600 and (d)-(e)-(f) DP980 [67].

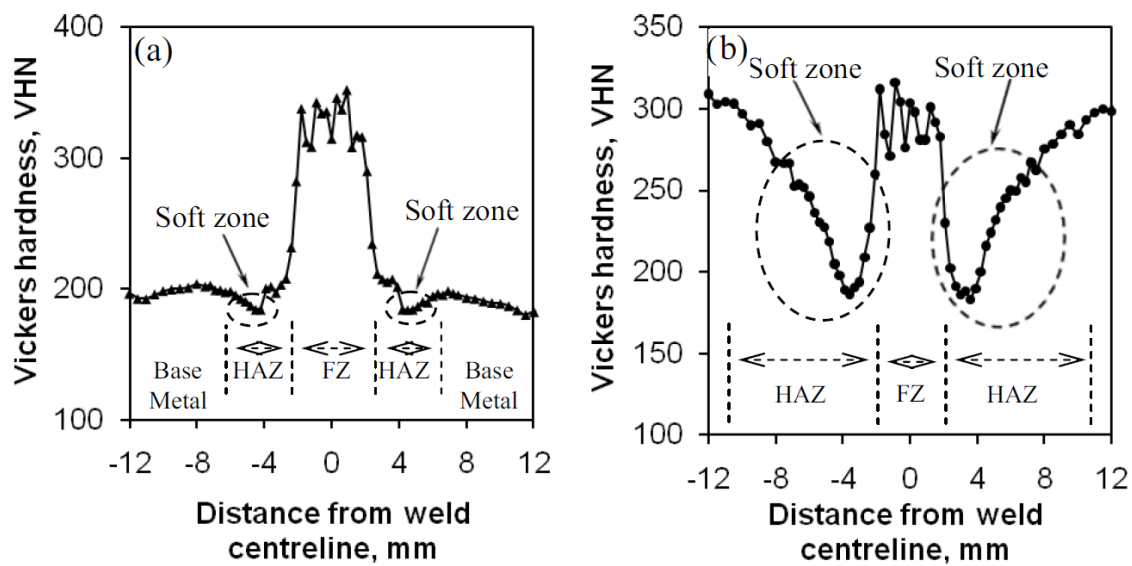


Figure 2.15 Hardness profiles of the dual phase steels DP600 (a) and DP980 (b) [67].

When comparing the width of the heat affected zones of the laser welds in Figure 2.13 and 2.15, it can be seen that there is an appreciable difference that may be mainly due to the larger size of focus used in the welding of the DP steels.

In two studies [68] and [15], the microstructure changes of S700MC steel due to different heat inputs were analyzed through the corresponding cooling rates expressed as $t_{8/5}$ cooling times. Lahtinen et al. [68] worked with four $t_{8/5}$ cooling times 5, 10, 15 and 20 s compared the S700MC-1 and S700MC-2 steels, where the difference was the addition of a micro-alloying element to a of the steels. They found a great effect on the mechanical properties that were related to the critical changes in the microstructure due to the cooling rates used. The recrystallized zone (CG-HAZ) was identified as the most problematic zone due to size, softening and microstructure. The microstructures found were composed by martensite and bainite and a greater tendency to form hard phases by low HI and due to the addition of the micro-alloying element. Figure 2.16 shows characteristic microstructures in HAZ for the two steels S700MC at $t_{8/5}$ cooling times of 5 and 20 s.

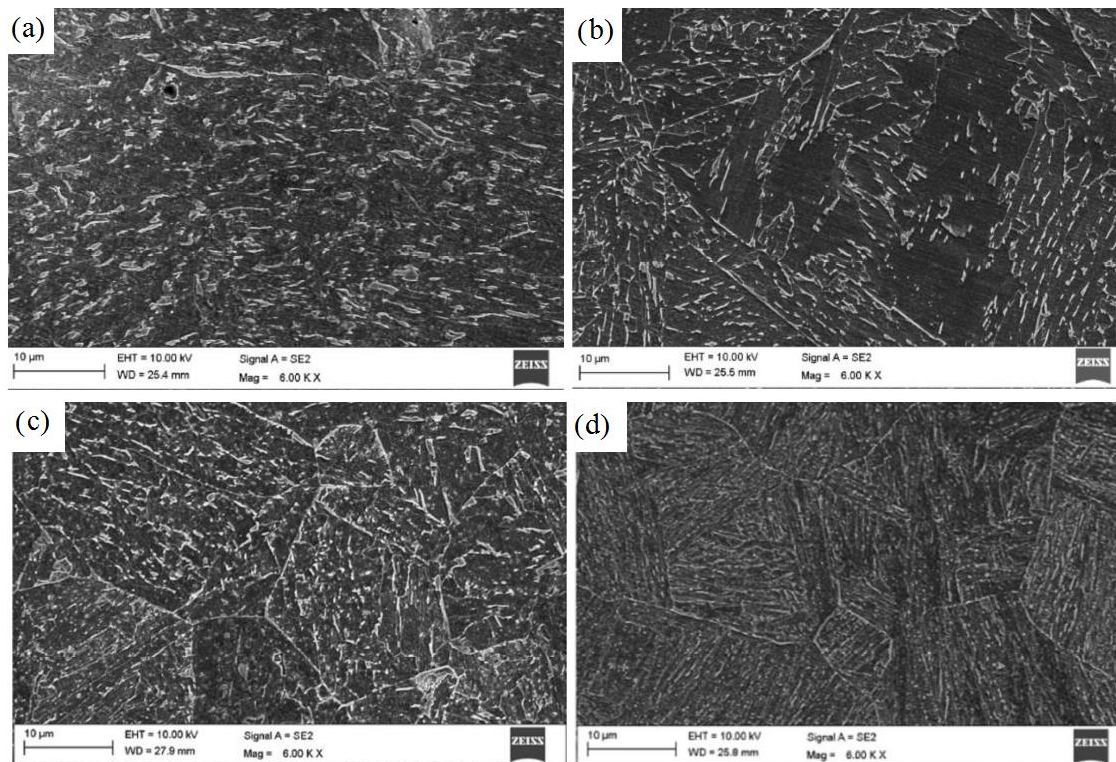


Figure 2.16 Microstructures in HAZ for high heat input ($t_{8/5} = 20$ s, left) and low heat input ($t_{8/5} = 5$ s, right) for S700MC-1 steel (a) and (b) and S700MC-2 steel (c) and (d), respectively.

Meanwhile, Górká [15] in a study of assessment to the weldability of a S700MC steel of 10 mm thickness, established that the microstructure can be from martensite for short times to a mixture of bainite and ferrite for big times. Figure 2.17 illustrates the microstructures found for cooling times $t_{8/5}$ of 3.4, 12.9 and 87.8 s. This author found that welding cycles can produce small precipitates (Ti, Nb) (C, N)-type together with large particles (Ti, Nb) N and TiC which lead to a higher density of dislocations and ductility reduction.

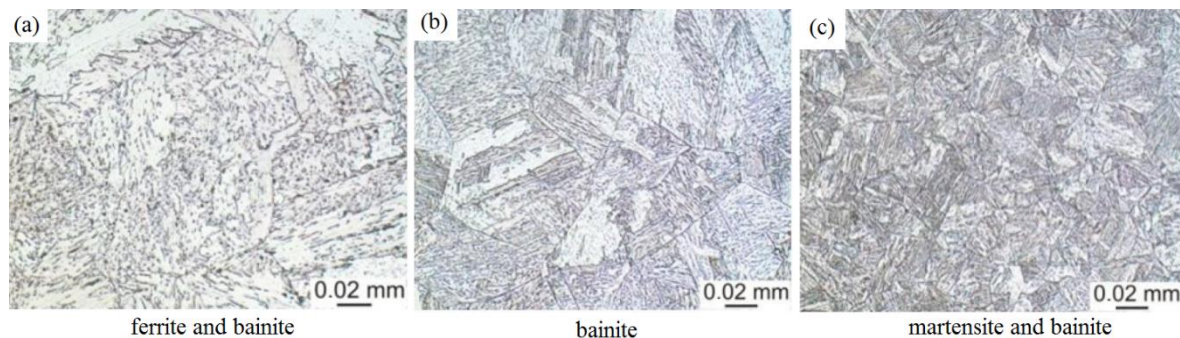


Figure 2.17 Microstructures of steel S700MC for three cooling times [15].

As can be seen in these last two works, small variations in the chemical composition of the steels and the different cooling times cause large changes in the microstructure. Being the HAZ of greatest interest in welding, as reviewed and additionally according to works [46] and [42] the hard bainite or martensite microstructures of the BM evolve into tempered microstructures, so this area was softened.

In summary, depending on the initial microstructure of the BM and the HI, different microstructures are produced in the HAZ and FZ that determine the distribution of the hardness. In general, in laser welding as low heat inputs and high cooling rates are provided, so in the FZ, hard microstructures are produced if the BM is soft and, conversely, a hard microstructure can be smoothed if the HI is not low enough. In the HAZ there is almost always softening, although its magnitude depends mainly on the HI value.

2.3.8.2. Effect on tensile strength and ductility

As is well known, tensile strength is positively correlated to hardness while the opposite occurs with the ductility. Since the detriment of the mechanical properties has been associated mainly due to the size and softening of the HAZ and in the previous section it was shown that this generally occurs although to a lesser degree in laser welding, therefore it is necessary to determine the effect on tensile strength and ductility in laser welded elements.

In the work [46] where two steels (Docol 1200M, 1 mm thick and TRIP, 2 mm thick) were welded with various conventional welding process (MAG and TIG) and with laser processes (DL and FL), the effects on HAZ width, hardness and tensile mechanical properties were reported. It is found that the HAZ width was much smaller in the laser processes (0.2 mm) than the conventional ones (2 mm). The HAZ hardness in the Docol 1200M steel was lower than the BM for welding laser (373 HV) but was much lower for the conventional process (236 HV). The tensile strength in all the joints welded in the Docol 1200M steel decreases with respect to the BM, however it decrease less for the laser process, see Table 2.5. Meanwhile for the weld joint on TRIP steel, the tensile strength decreased in relation to BM in the conventional process but increased for the laser processes, see Table 2.6. As can be seen, ductility (A %) in all cases decrease in relation to the BM being the largest decrease for conventional processes. This behaviour was explained by the effect of

the HI and the changes suffered by the microstructures by the heating and cooling cycles. In laser processes the HI is lower and the rate cooling is high unlike conventional processes.

Table 2.5 Mechanical properties of Docol 1200M welds [46].

	Rp0.2 [MPa]	Rm[MPa]	A [%]
Base material	1198	1307	4
Laser weld - I	1037	1080	0.8
Laser weld - T	800	837	1.5
MAG weld - I	652	796	-
MAG weld - T	514	714	3.7

Table 2.6 Mechanical properties of TRIP welds [46].

	Rp0.2 [MPa]	Rm [MPa]	A [%]
Base material	404	885	20.7
TIG	461.0	873.3	6.1
MAG	466.7	847.7	6.5
TIG HT	412.7	830.6	7.9
MAG HT	440.7	840.7	7.1
DL	487	1012	11.6
FL	486.7	997.2	10.7

From the review of two works [47, 48] where the effect of HI on the microstructure and mechanical properties in butt joints laser welded using thin HSS were studied, the following can be established: when the HI increase, the size of the HAZ and FZ grows, the tensile strength and the ductility decrease. According to the reported by the authors, although the tensile strength decreased, it was close to that of the base metal. In the second study [48] the two steels generated high efficiencies in the tensile strength (over 94%) in relation to the BM.

According to the effects observed in the previous studies the possibility to obtaining a tension strength in the welded joints equal to or greater than the base material can be summarized in the following features: small size and softening of the HAZ and equal or higher hardness in the FZ, for this the HI must be low as possible. In relation to the ductility always is less than the BM, however to lower HI the ductility decreases less.

Finally, Guo et al. [42] reported practically the same tensile strength and elongation between an S960 steel (HSLA) and butt joints in ALW. According to the authors, defect-free weld seam and adequate penetration were obtained, however, the hardness profile presented a slight softening at the HAZ and a high hardness in the FZ.

2.3.9. Laser welding of S700MC steel

A different behaviour in relation to the tensile strength and ductility of S700MC steels laser welded was reported in two works. In [58] for a Strenx® S700MC steel of 2 mm thick butt joints, the tensile strength was slightly greater while the ductility was little lower than the BM. These results were attributed to a precise adjustment of the laser parameters, an appropriate preparation and performance process. The microstructure obtained consisting of ferritic-bainitic in HAZ, bainite with slight amount of ferrite in fusion line and bainite with various types of ferrite in FZ. The failure of the specimens was in the BM near to the HAZ. Meanwhile, in the work [15], for a 10 mm thick S700MC steel plate, a lower tensile strength and very lower impact strength were found. The author attributes the results to changes in the microstructure by the presence of small precipitates together to big particles. Thus, despite the fact that the two works reported the same B weld quality level, there are differences in the mechanical properties that must be better investigated.

2.4. Residual stress in high strength steels laser welded

Residual stress is an important factor in the fatigue behaviour of the welded joints because they are added to stresses that produce the external loads being able to affect both the fatigue strength and the crack growth rate. Residual stress can be characterized experimentally, using mathematical models or finite element method (FEM) [69].

There are several experimental techniques such as neutron diffraction, X-ray diffraction, surface and deep hole drilling, boring, slicing and magnetic methods [70] for measure the residual stresses, however, the X-ray diffraction technique (XRD) is one of the most used. The XRD advantages and practical issues are described in [71], some are: it is considered a non-destructive test for measure the surface residual stress to depths of up to 30 μm , but with layer removal can be up to 1 mm; the measurement itself is relatively

straightforward, the equipment available, measurement speed fast-medium, accuracy 20 MPa in steel and biaxial residual stresses measurements. The principle to determine the residual stresses based in XRD consist in measure the change in the inter-planar spacing d of polycrystalline solid due to strains introduced for the welding, then the strains are related to residual stresses. With the XRD technique the angles at which the maximum diffracted intensities occur are measured and through of the Bragg's law is possible obtain the spacing d [72].

In welding processes, the residual stresses are due to the introduction of non-uniform plastic and elastic strains in the weld seam and the BM, these strains can be consequence of the contraction and dilatation not free of the melted and surrounding areas or by processes of phase transformations that involve changes of volumes during the weld cooling. As a result of the heating and cooling of the weld, there is a distribution of residual stresses in the direction parallel (longitudinal) to the weld, transverse to it and in the thickness direction. In a general way, the longitudinal residual stresses are greater than the transversal stresses, in the weld metal there are high tensile residual stress that can reach to yield strength, the magnitude and distribution of residual stresses depends de many factors such as the HI, the transformation temperature, the microstructure, thickness and the plate constrains [72].

Kumar et al. [73] investigated the effect of welding speed on the residual stresses that occur when was laser welded a 9 mm thick plate of steel ASTM A387 Grade 9. They used a power of 8 kW and speeds of 0.75 (plate A) and 1.5 (plate B) m/min corresponding to heat inputs of 640 and 320 J/mm, respectively. Among several results they found, the following stand out: the longitudinal and normal residual stresses are the most significant presenting an M-shape with peaks at tensile close to the edge of the HAZ and with low tensile or compressive stresses in the FZ, see Figure 2.18a; there was little difference in residual stresses due to HI; it was determined that in the cooling close to 400°C, there was a phase change from austenite to martensite producing a significant material expansion; the final residual stresses are the product of thermal contraction and the expansion of the phase transformation from austenite to martensite, the strains produced by the expansion of the martensite reduced the tensile residual stresses or may also cause compressive residual stresses.

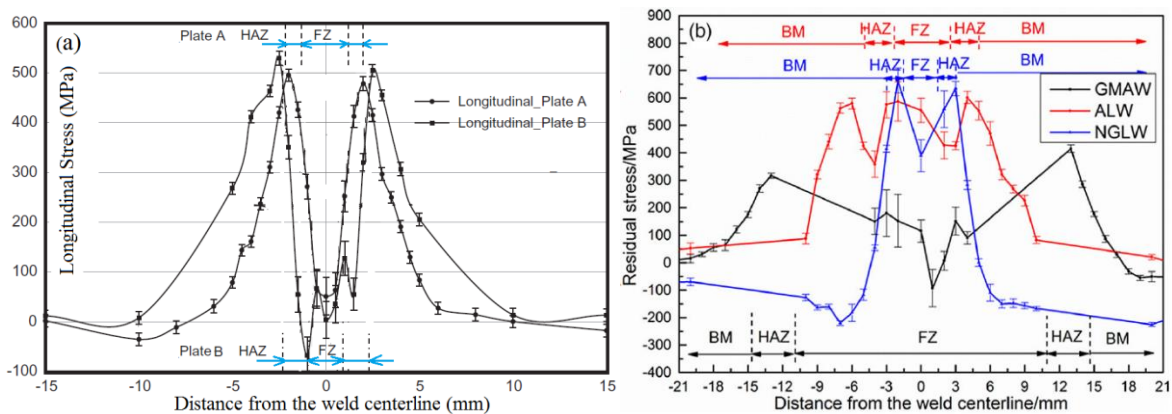


Figure 2.18 Residual stress distributions in laser welding (a) modified form [73], and in various welding processes (b) [26].

In another work similar distributions were also found in the investigation of the residual stresses caused on S700 steel plates by three welding processes: GMAW, ALW and NGLW [26]. XRD was used to measure the surface stresses and the contour method for the stresses along the 13 mm thickness of the steel plates. The residual stresses induced in each process on the surface can be observed in Figure 2.18b. It is established that the residual stress distributions are influenced by the thermal contraction and by the different phase changes that occur in the welded zones. It is pointed out that for this particular steel the transformation temperatures of martensite and bainite in FZ are relatively high (460°C and 540°C), so they do not have a greater compensating effect on the tensile residual stresses.

Rong et al. [69], using a finite element model, predicted the residual stresses of a 4 mm thick EH36 steel in a butt joint configuration, in the midplane of the plate close to the weld zone, they found a range of transversal residual stresses approximately between 250 and -200 MPa, these values had a good agreement with the experimental results. They argue that the transfer of the peak value of residual stresses from the FZ to the HAZ was due to the effect of the solid phase transformation of the material. Derakhshan et al. [74] using X-ray measurement and numerical simulation determined the residual stresses induced in a 4 mm thick butt joint in structural steel for four welding processes: three laser processes and a conventional arc process. For the ALW process in which a low heat input (88 J/mm) was used, the longitudinal residual stresses varied from approximately -50 MPa in the FZ to 250 MPa in the HAZ and presented the typical M-shape. These last two works presented residual tensile stresses lower than the first two works suggesting that the residual stress decreases

with thickness and therefore also decreases with lower heat inputs. Although there are no conclusive studies, for a same type of laser process, in the reference [75] for a lap joint with a STS301L it is suggested that the high residual stresses are due to higher HI.

According to above studies it is established that the residual stresses are product principally of two opposite effects: the deformation that prevent the thermal contraction inducing tensile residual stresses and the deformation due to the change of volume by the phase transformations producing residual compressive stresses. The importance of this last factor is confirmed in recent works with low transformation temperature welding consumables [76]. As already noted previously, the distribution and magnitude of residual stresses in welded joints is a phenomenon depending on the HI, the microstructure, the thickness, the cooling rate and the type of process therefore is a complex phenomenon depending of many factors.

2.5. Fatigue in Welded Joints

Fatigue is the process of accumulation of damage in a material due to cyclical loading. Even with cyclical loads less than the load corresponding to the elastic limit of the material in a certain number of cycles its fracture can occur. In the case of metals, the fatigue comprises three stages: initiation, propagation and final fracture of element. The crack initiation stage is due to a variety of microstructural inhomogeneities that cause local concentration of stresses which produce local plastic deformation or cracking and detachment of brittle precipitates. It has been pointed out that the crack initiation usually occurs on the surface in inhomogeneities such as surface roughness, notches, non-metallic inclusions, second phases, precipitates, pores and other flaws and even though in the case of metals ideally free of inhomogeneities, cracks can be initiated in the surface due to slip mechanism in crystallographic planes that creates microscopic extrusions and intrusions by the plastic deformation by the cyclic loads [77].

In the case of ductile materials, once a crack initiates can grow inside a grain and expand to other grains, join with other cracks to form a large crack in a way that a widespread damage occurs, while in materials of limited ductility such as high strength metals, the

damage is less widespread and tends to be concentrated at defects and the crack grows in a plane normal to the tensile stress until the failure. When the crack reaches a limit size the final fracture occurs in a way ductile or brittle [78].

Due to the welding process the features of welded joints are conducive to cracks initiation because they generally exhibit seam rough surfaces, flaws, section changes and residual stresses. In addition, the changes caused in the microstructure and in other properties can also promote the cracks initiation, affect the growth of cracks and the final fracture of the welded joint.

It is well known that the stress-concentrating effect causes a decrease in fatigue performance. In the case of welded joints, the weld bead profile produces high local stress concentrations reducing fatigue strength. When comparing the fatigue strength between a welded element and a non-welded element both with similar stress concentration factor, the fatigue strength of the welded element is lower, being the main causes for the lower fatigue performance of welded elements the presence of sharp discontinuities such as undercuts, cold laps and non-metallic inclusions that exert a combined effect with stress concentration due to the weld geometry [79]. These discontinuities are named crack-like imperfections. Figure 2.19 illustrates the increase in the remote stress σ applied to butt weld joint due to weld toe, σ_{k1} , and by the combined effect of the weld toe and undercut, σ_{k2} .

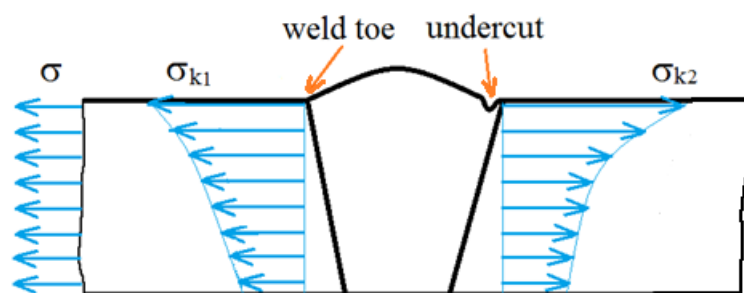


Figure 2.19 Sketch of remote stress (σ) and local stresses (σ_k) in imperfections.

The presence of crack-like imperfections has been judged to be unavoidable in welded joints due to welding processes [80]. The combined effect of weld geometry and crack-like imperfections facilitates the onset of fatigue, leading to the initiation period being neglected and therefore that the crack growth period is the dominant one in the fatigue

performance of the welded joints [79]. With the latter assumption agree various authors [81-83] and in practical terms it has led to the application of the fracture mechanics approach in determining the fatigue life at any level of stress.

For other hand the conventional S-N curve approach used to assessment the fatigue strength of elements with and without notches is widely applied in research work of welded specimens or components and in design standards to determine the fatigue strength of particular welded joints. The S-N curve is a global approach because does not distinguish between crack initiation and crack growth periods.

Maddox [84] and other researchers [83, 85] distinguish several factors that influence the fatigue strength of welded joints, these mainly converge on: geometrical notches or imperfections (weld quality), residual stress and material.

2.5.1. S-N curve of welded joints

The S-N diagram experimentally determines the relationship between the applied stress range, $\Delta\sigma$, and the fatigue life in cycles, N . The specimens or components are tested with constant amplitude, certain stress ratio R and frequency at various stress levels to define the fatigue life until fracture and the fatigue limit which supposes the stress level for infinite life. The results have shown that the S-N curve is generally a potential relationship, therefore on a double logarithmic scale it is a linear relationship. The two mentioned relationships are indicated below:

$$N = \frac{C}{(\Delta\sigma)^m} \quad (2.7)$$

$$\log(N) = \log(C) - m \log(\Delta\sigma) \quad (2.8)$$

where, C and m are parameters that characterized the curve and can be determined through linear regression and the linearity can be validated by appropriate statistical methods.

Figure 2.20 illustrates a typical S-N curve of a steel welded joint and those corresponding to similar non-welded elements. As has already been mentioned, the fatigue strength of welded joints suffers an appreciable decrease in relation to the BM.

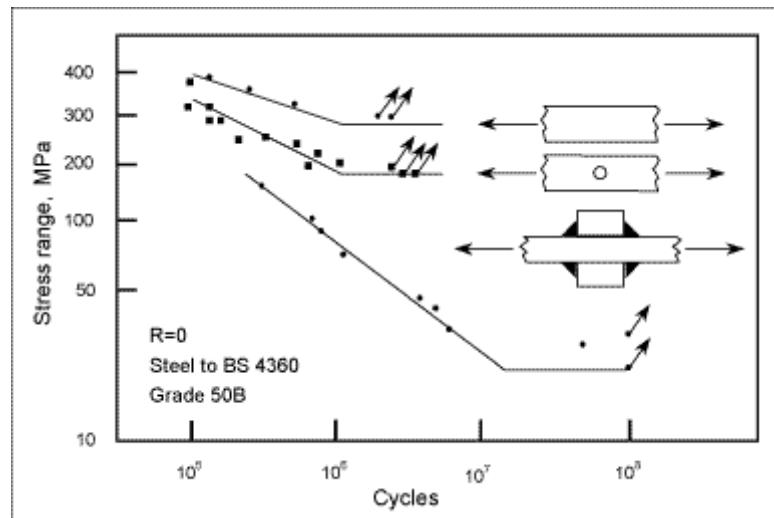


Figure 2.20 S-N curves for welded joint and similar non-welded elements [79].

Some results of S-N curves in welded joints with high strength steels show that the slope m of the linear relationship approaches a values 3.5-4 [83], while in the IIW recommendations it is assumed as 3 [81]. The stress level where the “knee point” is observed correspond to the fatigue limit and is conventionally assumed for a certain number of life cycles such as 2×10^6 or 10^7 , however, there is evidence that even at very low stress levels there is a finite life [86].

The experimental results in types of joints such as the one in the Figure 2.20 have served as the basis for establishing the S-N design curves in design standards or recommendations. For example, in the IIW recommendations [82], the S-N curves are called FAT class curves and are defined with a fatigue strength at two million cycles, the “knee point” at 10^7 cycles and two slopes, $m=3$ and $m=5$, down and up, respectively, from the “knee point”.

2.5.2. Fatigue strength of high strength steels

Regarding the fatigue behaviour of HSS, significant decreases in fatigue strength are generally reported in the welded joints. This can be illustrated with three studies on butt joints in 1.2-2.0 mm thick steels whose base materials covered a tensile strength range 440-1500 MPa. In the study [67], for two DP steels laser welded were reported fatigue limits of

175 MPa and 125 MPa for the DP600 and DP980 steels, respectively, and relations between the fatigue limits and tensile strength that resulted in 0.28 and 0.23 according to the same order. It is also reported that all welded joints failed in the HAZ for the DP980 steel while for the DP600 steel when the stress level was less than 250 MPa, the fracture was in the BM. Figure 2.21a shows S-N curves of the two steels.

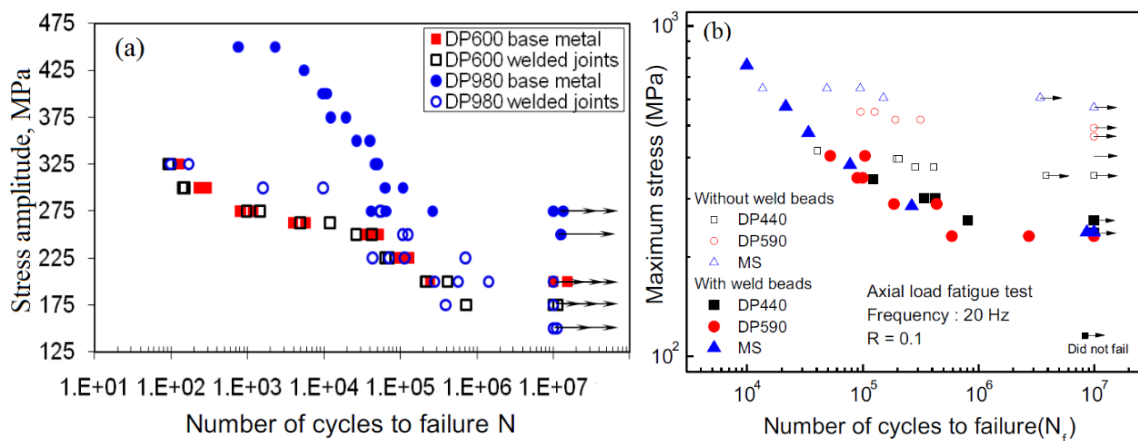


Figure 2.21 S-N curves for AHSS: DP600 and DP980 (a) [67] and DP440, DP590 and MS (b) [87].

Figure 2.21b shows the S-N curves of three AHSS welded with GMAW process [87]. As can be seen, the maximum stresses of fatigue limits are approximately in the range of 240 to 270 MPa, which corresponds in terms of stress amplitudes at 108 to 122 MPa. It is important to note in Figure 2.21b that the fatigue strength of the steel (DP440) with the lowest tensile strength was slightly higher than the other steels. Although the authors did not attribute this fact to the better hardness profile of DP440 steel, they did point out that this steel did not undergo softening in the HAZ and had a smooth transition increasing the hardness in the FZ, see Figure 2.22a. In this work the fatigue failure was reported in the circles marked in black.

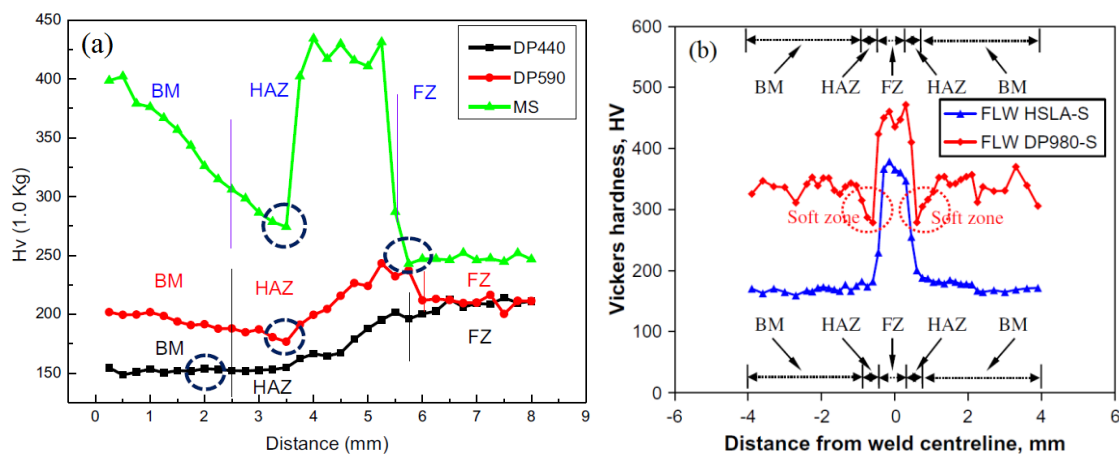


Figure 2.22 Hardness profiles obtained in processes: GMAW (a) [87] and in laser (b) [48].

Meanwhile in the work [48], the stress amplitudes corresponding to the fatigue limits of a HSLA (tensile strength 546 MPa) steel and DP980 steel laser welded resulted 125 and 150 MPa, respectively. In this study the welding parameters were chosen for cause a low HI (22.5 J/mm) and widths of the HAZ and FZ very small, see Figure 2.22b.

In the three cases considered, the fatigue limits are within a narrow range (108-175 MPa) despite the wide range in tensile strength of the steels considered and other differences related to the welding processes. In other words, the high strength of the steels does not seem to have a great influence on the fatigue limit. On the other hand, according to the sites where fatigue failure was reported, lower hardness in the hardness profile seems to have some influence on fatigue strength.

2.5.3. Effect of the weld quality.

In general terms, the weld quality refers to the presence of imperfections in the welded joints that decrease their fatigue strength. Avoiding certain imperfections or minimizing their size or quantity according to the detrimental effect on fatigue strength is expected a better performance of the welded joints. This effectively occurs as shown in several studies where post-welding techniques and treatments modifying the severity of imperfections increase the fatigue strength [88-90], in studies where a high weld quality level according to a standard meant greater fatigue strength of the welded joints [91] or as

evidenced in design recommendations, where the fatigue strength for a welded joint can be increased, if the size of a certain imperfection is under an established limit [82].

In welding quality standards such as ISO 5817 [92] (does not cover laser welding) or ISO 13919-1 (covers laser welding) [53], three quality levels are distinguished: B, C and D, being the B level of higher quality. In these standards, which are of a general application, additional requirements are given for fatigue welded joints. In the case of the first standard, that mainly refer to adjusting the limits of imperfections to FAT fatigue class curves, while in the second standard, it is pointed out that if higher requirements are necessary in the case of dynamic loads, the welds can be machined or grounded to eliminate imperfections.

On other hand, it should be noted that in guidelines and recommendations for the design of welded joints [82], the fatigue strength does not differ according to the tensile strength of the steel, that is, under the same conditions, a low-strength steel has the same fatigue strength as a high-strength steel. The reason for this fact has been explained in [79] due to the fact that in the welded joints due to the presence of imperfections, the crack growth stage predominates, which is not strongly affected by the tensile strength of steels. However in [93], it has been shown that in high quality welded joints, fatigue strength is positively correlated to tensile strength.

The ISO 13919-1 standard identifies eighteen imperfections, but can be summarized in the following: cracks, incomplete penetration, lack of fusion, porosity, inclusions, undercuts, underfill, excess weld, misalignment and weld spatter. The cracks are not allowed at any quality level while others imperfections can be tolerated within certain sizes and quantities.

The widely studied stress concentration approach in notched elements has also been applied to weld imperfections such as undercuts, weld toe, underfill, pores, among the others, in order to assess how they affect the fatigue strength of welded joints. Through the stress concentration factor (SCF) calculated analytically but especially with the finite element method (FEM), the geometry of the weld bead and imperfections are defined in more and more detail in parametric studies in order to define the effect on fatigue strength. Actually some imperfections are 3D modelled for evaluate the SCF [94]. Approaches based

on fracture mechanics are also used to study the effect of weld profile and imperfections on fatigue strength [95].

The weld toe geometry and undercuts are identified as common imperfections in welding processes with greater negative effect on fatigue strength [96, 97]. On the relative effect of the geometrical parameters of these two imperfections in the fatigue strength there are several studies [95, 98, 99], although there may be a discrepancy in which one is more influential.

Particularly in the case of pores, their quantity and location are of particular importance in the fatigue performance of aluminum welded joints due to the sensitivity of this material to presenting this type of defects [100, 101]. However, that, in steels this problem is considered less, in ALW, pores can also be of consideration.

Others imperfections as the ripples have also been reported affecting the fatigue strength and as fatigue starts [102], however its effect has not been duly studied. Another aspect that deserves attention is the variation of the geometry of the weld bead along its axis with statistical treatments to evaluate the effect on the fatigue strength [103]. The effect of imperfections according to the thickness of the welded joints is another aspect to be clarified, as reported in [95], where a greater effect on fatigue strength due to the presence of undercuts in thin plates (3 mm) than in thick plates (20 mm).

As has been pointed out in other sections, in relation to laser welding in thin plates, regarding the weld quality and its effect on the fatigue strength, there are also few studies and, on the other hand, as previously noted, the quality level according to the ISO 13919-1 standard does not seem to be correlated with the fatigue strength.

2.5.4. Effect of the weld bead geometry and residual stresses

Due to the importance of the weld profile and residual stresses in fatigue performance, some studies are reviewed in this section.

In two studies [104, 105], with welded joints in high strength steels and conventional welding processes, where, on the one hand, the weld bead geometry at weld

toe was modified by machining or hammer peening to obtain different radii, and on the other hand, with the use of thermal treatments the residual stresses were relieved, it was shown that in the case of the welded joints with low residual tensile stresses (150 MPa) the modified radius had a greater influence on the fatigue strength while in the case of the welded joints in which high residual compressive stresses (near to -400 MPa) were induced, these had a greater influence than the modified radius at weld toe. Figure 2.23 illustrates the effect on fatigue strength of the modified radius in weld toe. As can be seen, significant decreases occur due to small radii in the weld toe.

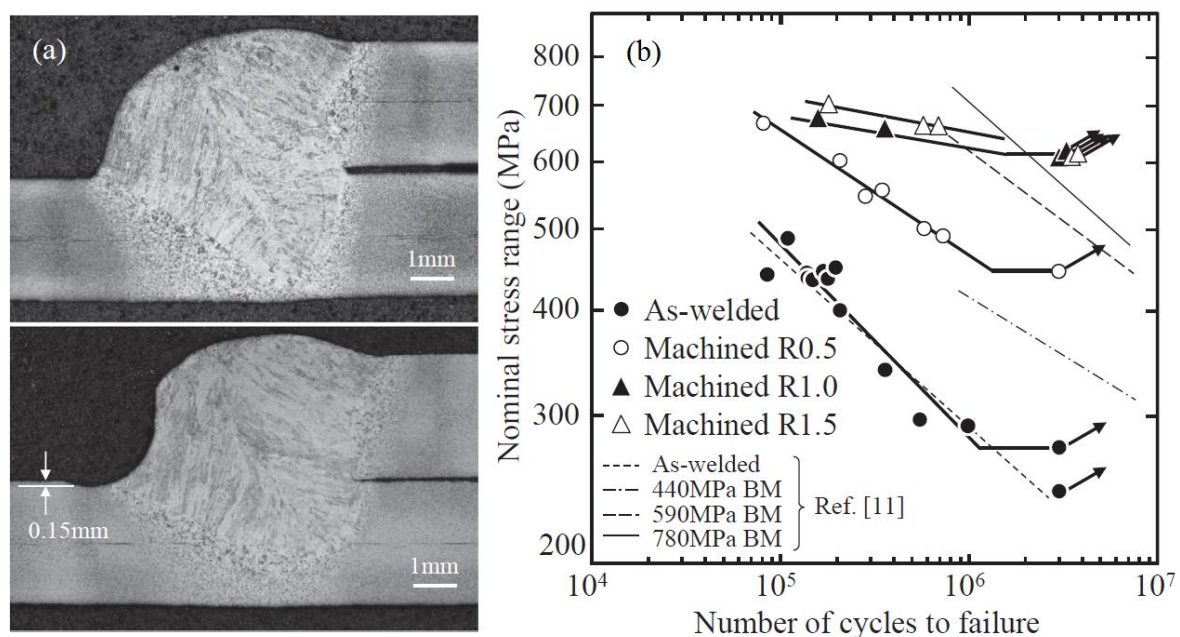


Figure 2.23 Aspect of the machined and non-machined weld toe (a) and fatigue strength (b) [104].

Harati et al. [106] in fillet welds compared welds with different toe radii and residual stress levels, concluding that residual stresses had a relatively greater influence than the radius on fatigue strength.

It is well known that residual tensile stresses deteriorate fatigue behaviour as they contribute to the mechanism of initiation and grow of cracks and that add to the effects of external loads. On the other hand, there is a large amount of work [88, 89, 105, 109] that reports on the improvement of fatigue performance of welded joints by techniques that induce residual stresses to compression in the weld toe. It has been reported for example the

induction of residual stresses of -800 MPa [108] and 32% of improvement in fatigue at 10^7 cycles [90] due to technics of shot peening.

2.5.5. Fatigue of S700MC steels

There are few works in relation to the fatigue strength of S700MC steels. In [109] for specimens in non-welded condition, fatigue tests were development in rotational bending mode, polished specimens with stress ratio R -1 and frequency of 40 Hz. A fatigue limit of 440 MPa, crack initiation on the surface, without inclusions that decrease the fatigue strength were some of the relevant aspects, meanwhile, in [86] for similar conditions, but at high frequency and in the gigacycle region (3×10^5 - 10^{10} cycles) were reported that this steel does not present a “knee point”. This latter characteristic was also observed in the work [110], but for specimens laser welded and a decrease of approximately 33% of the fatigue strength in relation to BM in all fatigue life range was found.

2.6. Fatigue crack growth

As reviewed, the crack propagation stage predominates in the case of welded joints and because the initiation and growth of cracks generally occurs in the welded area, the local properties of crack propagation in these zones are relevant to describe the fatigue behaviour in welded joints.

Once a crack exists in a material, there is a stress distribution around the crack tip that can be described by the stress intensity factor (SIF) K , whose relationship is:

$$K = Y \sigma \sqrt{\pi a} \quad (2.9)$$

where, σ is the remote stress acting on an element containing a crack of size a and Y is a characteristic geometric parameter of the specimen or component. Noting that a certain fluctuating stress range $\Delta\sigma$ causes a range of stress intensity factor range (SIFR) ΔK on an element, the above concept can be applied to the growth of cracks through the Paris law for the crack growth rate [79]:

$$\frac{da}{dN} = A \Delta K^n \quad (2.10)$$

being, A and n , constants of the material which are determined experimentally. A schematic da/dN vs ΔK diagram in a scale log-log take a form as is shown in the Figure 2.24, where the effect of the stress ratio R is also presented.

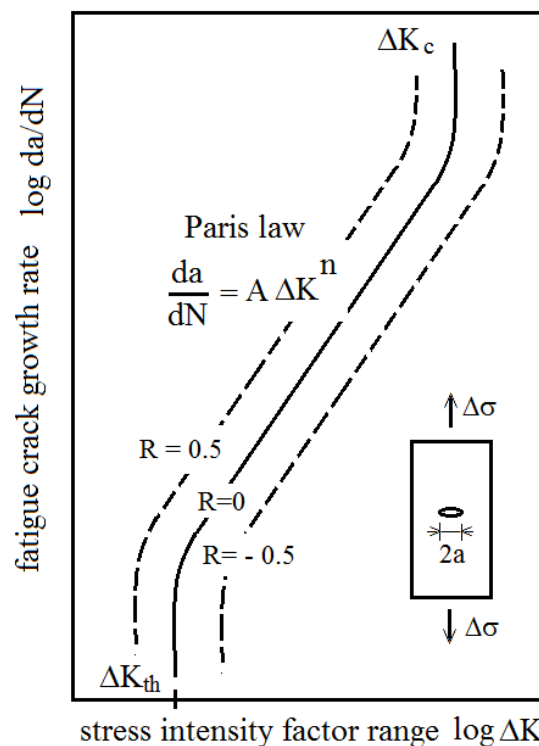


Figure 2.24 Sketch of fatigue crack growth rate diagram.

As seen in the Figure 2.24, in addition to the Paris law whose application is in the linear part of the diagram, the extreme values ΔK_{th} and ΔK_c are shown, where ΔK_{th} is a threshold value below which the crack does not grow and ΔK_c is the range where the fracture toughness of the material is exceeded and the crack growth rate is very high in the top of unstable region next to the fracture. The crack growth rate for a material can increase or decrease in function of stress ratio R as well as the value of ΔK_{th} . In [78, 111] can be found empirical relationships for consider the effect of stress ratio R on the curve crack growth rate versus stress intensity range.

As shown schematically in Figure 2.24, the fatigue crack growth rate (FCGR) is determined from a long crack. In the literature the growth of so-called small cracks is also studied [112, 113]. Although there may be different distinctions and disparities of criteria, those cracks that growth from locations to the left of the ΔK_{th} limit can be assumed to be small. The consideration that the radius of the plastic zone is smaller than the size of the crack has been an aspect to differentiate a crack as small and the adequate application of the SIF concept [114].

In [83] it is shown that for a certain welded joint the integration of Paris law determines that the S-N curve on a double logarithmic scale is a straight line, therefore it is specified that the fatigue life of the welded joints is completely due to crack propagation.

2.6.1. Crack closure phenomenon

An aspect the importance affecting the FCGR is the phenomenon named crack closure, which means that not all the tension range ΔK is effective to open the crack, that is, a part of the tension range ΔK the crack remains closed. Several mechanisms have been identified for crack closure, however crack tip plasticity is one of the most significant. According to this mechanism, due to the cyclic plastic deformation at the crack tip, an elongated area is created at the edges of the crack that causes the crack closure. The tension load range (ΔP) from which the crack opens can be determined through the graph of ΔP in function of crack opening displacement (COD). COD is the displacement between two points located at the crack centre, but on opposite edges of the crack. The tension load range from which the behaviour is linear between ΔP and COD, identifies the corresponding crack opening stress range ΔS_{op} that allows to determine the percentage of the stress range during which the crack is open. This leads to the FCGR being expressed in terms of ΔK_{eff} instead of ΔK . In [115], methods for determining the ΔS_{op} , are presented.

2.6.2. Factors that affect the fatigue crack propagation.

In the literature, several factors affecting the FCGR were found: microstructure, residual stress, crack closure, thickness and the stress ratio R . In two studies [116, 117] working with AHSS subjected to different heat treatments that modified the microstructure,

it was found that the FCGR varies due to this fact. In the first study the results show that the FCGR decreased and ΔK_{th} increased with increase martensite content. A retarding effect on the growth of cracks is attributed to martensite due to secondary cracks that consume energy at the crack tip. Figure 2.25 shows the curve $da/dN - \Delta K$ and microstructures of the steels used in the first work. Meanwhile in the second study, in addition to other mechanisms, the plasticity-induced crack closure was pointed out as an extrinsic factor and the higher ductility as an intrinsic factor, which caused the retardation of crack propagation.

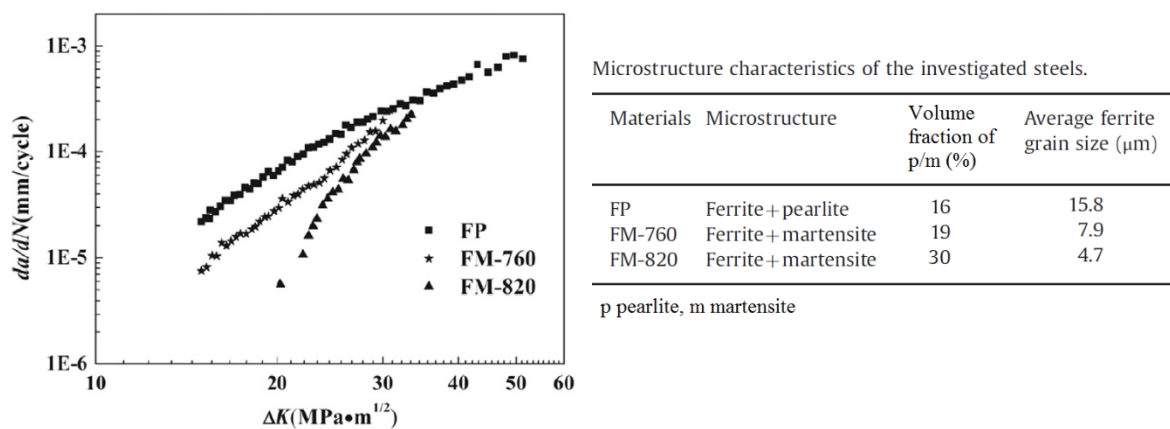


Figure 2.25 Curve $da/dN - \Delta K$ and microstructures characteristics, adapted from [116].

Wang et al. [118] investigated the effect of microstructure, thickness, residual stresses and stress ratio R on the FCGR in weld joint of a new HSS. They used four values for R : 0.1, 0.25, 0.4 and 0.7; specimens of 5 and 10 mm of thickness and three conditions: BM, as-welded (WM) and post-welding heat treated (PWHT). The results indicated that the weld metal has higher resistance to fatigue crack growth in relation of BM at every stress ratio R as consequence of lath martensite and basket-weave acicular ferrite produced in weld metal. There was a slight retardation in the FCGR due to a greater thickness and to a decrease in the residual stresses due to the effect of the PWHT.

In [119] the fatigue crack grow in a welded plate of JIS SPV490 steel with residual compressive stresses was investigated. The residual compressive stresses were created by low transformation temperature welding wire used unlike of the joint with conventional consumables that created residual tension stresses, see Figure 2.26a. The FCGR was improved and the fatigue threshold almost was doubled as shown in Figure 2.26b.

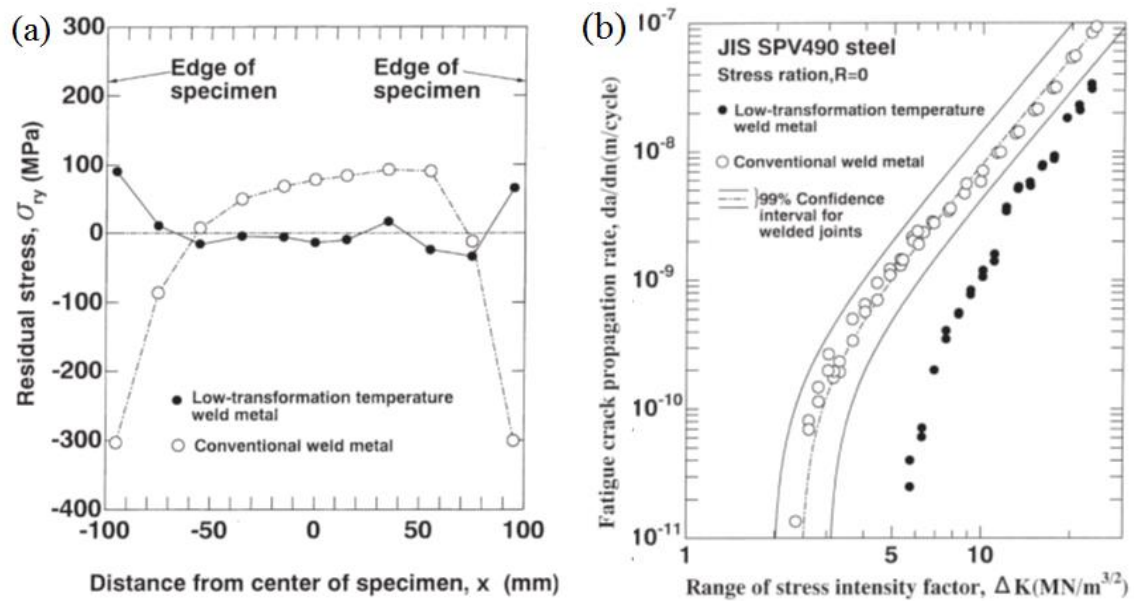


Figure 2.26 Residual stresses due to welding consumables (a) and FCGR for JIS SPV490 steel (b) [119].

In summary, due to the changes introduced by heat treatments or welding, given a certain stress ratio R and thickness, the hard microstructures and residual compressive stresses exert a greater retarding effect on the FCGR.

2.7. Fatigue strength assessment

In general, the assessment of fatigue strength in welded and non-welded components is based on two theories [120]: cumulative fatigue damage and fatigue crack propagation. In the first theory, approaches based on stress, strain, energy and continuum damage mechanics are named, while in the second theory approaches such as, long crack growth, physically small crack growth and microstructurally small crack growth, are indicated.

In [80, 81] various approaches are presented for the fatigue assessment for welded joints. They are classified as S-N approaches and crack propagation approaches. A complete distinction of the S-N approaches according to the type of stress and the method used can be found in [82].

In the literature there is variety of works on fatigue strength assessment of welded joints. The conventional local stress approach is applied mainly for the evaluation of the fatigue limit through the SCF K_f , however, it is also applied in the complete range of stress as in the work [121], where the weld toe geometry in as-welded and modified conditions of the welded joints was used for the assessment of the S-N curves.

In relation to crack propagations approaches, this approach is gaining more application and serving for the evaluation of various factors that influence fatigue strength. In [122] where was evaluated the effect of the weld bead geometry, residual stresses and misalignment on fatigue life using an analytical model based in Paris' law, the M_k factor, and the growth of a central superficial semi-elliptic crack. Wide ranges of the weld toe radius, flank angle, thickness (9 to 32 mm) and residual stress were analyzed. Chapetti et al. [123] incorporated small crack treatment into life predictions. In the so-called IBES approach [113] a complete treatment based on fracture mechanics is observed, where among other aspects, the determination of the fatigue strength are obtained statistically, the variation of the weld bead along the weld axis, the local properties of the FZ and HAZ and the small crack growth are considered.

Zhang and Maddox [124] applied a differentiated analysis for fatigue strength predictions of the weld toe burr grinding of non-load-carrying transverse fillet welded joints. In the low life regime ($<10^6$ cycles), they used fracture mechanics, meanwhile in the long life regime ($>10^6$) used a local stress approach proposed by Lawrence. They argued that in the low life regime, the fatigue life was dominated by crack propagation while in the long life regime crack initiation became significant.

Although the crack propagation approach seems to be the most indicated for welded joints, there are some observations for its application such as those mentioned in [83]. There is also evidence of a different behaviour of imperfections at high and low stresses, phenomena as the early onset of crack propagation, greater number of fatigue starts and less scatter have been noted occur at high stress [125]. The foregoing indicates that further study is necessary of the crack propagation approach at low stress levels close to the fatigue limit. In the same line with this, in [126], it is indicated that the fatigue limit is a matter of crack initiation only, being a surface phenomenon.

2.7.1. Fatigue limit assessment

The effect on the fatigue strength in elements with notches such as grooves, holes, section changes and others, has been widely studied considering the stress concentration and the stress distribution in the notch. The imperfections present in the welded joints can be considered severe notches.

Áman et al. [127] reviewed fatigue notch methods proposed by several authors (Isibasi, Peterson, Siebel&Stieler and Taylor) to estimate the fatigue limit, there the convenience of the use of effective stress concentration factor K_t is highlighted. This factor can be calculated through the relations with the notch sensitivity factor q and the stress concentration factor K_f . In the Peterson' method the notch sensitivity factor q is function of the notch radius ρ and the parameter a^* according to the tensile strength of the material. The two expressions mentioned above are shown below:

$$q = \frac{K_f - 1}{K_t - 1} \quad (2.11)$$

$$q = \frac{1}{1 + \frac{a^*}{\rho}} \quad (2.12)$$

When a mean stress σ_m acts in addition to the alternating stress σ_a , several relations exist in the literature for the evaluation of this effect [128]. One of these is the modified Goodman line which is easy to graphically represent and mathematically handle. Including the effective stress concentration factor K_t to account for local stress in a stress raiser and a factor n_G to evaluate the coincidence of a certain combination of applied stresses (σ_m, σ_a) with the mentioned modified Goodman line ($n_G = 1$ indicates that the stresses are on the line), the relationship takes the form:

$$\frac{K_f \sigma_a}{S_e} + \frac{K_f \sigma_m}{S_{ut}} = \frac{1}{n_G} \quad (2.13)$$

where, S_e and S_{ut} are the fatigue limit and tensile strength of the unnotched element, respectively.

Murakami [129], based on the fracture mechanics and a large number of experimental results, presented a proposal to determine the fatigue limit σ_w of small defects and nonmetallic inclusions as a function of the \sqrt{Area} parameter, the Vickers hardness HV , the stress ratio R and a dimensionless parameter α . Murakami's relationship has the form:

$$\sigma_w = \frac{1.43 (HV + 120)}{\sqrt{Area}^{1/6}} \left[\frac{1 - R}{2} \right]^\alpha \quad (2.14)$$

with, σ_w (in MPa) and \sqrt{Area} (in μm). The Area of the defect is the area projected in a normal plane to the applied stress. In the case of defects long and very shallow, the \sqrt{Area} parameter is calculated as $a\sqrt{10}$, where a , is the defect depth, according to Murakami's recommendation for this type of defect. In this work, the Vickers hardness is also used to estimate the fatigue limit and tensile strength as $1.6xHV$ and $3.2xHV$, respectively.

2.7.2. Crack propagation approach

Fracture mechanics is the basis for analysis for cracked materials. The practical application of crack propagation approach to welds with imperfections is summarized in the following steps: categorization of the imperfection or failure mode with a type of crack, definition of crack dimensions and estimation of the fatigue life according to the SIF and a propagation law.

Figure 2.27 presents three types of surface cracks. The semi-elliptical crack is commonly associated to various imperfections that develops its characteristic shape and can increase in size according to several factors; the continuous crack can be the product of the coalescence of multiple imperfections, of several semi-elliptic cracks that coalesce early or a continuous imperfection throughout the width of the element; while the border crack, it is produced by imperfections located on the edges of the element.

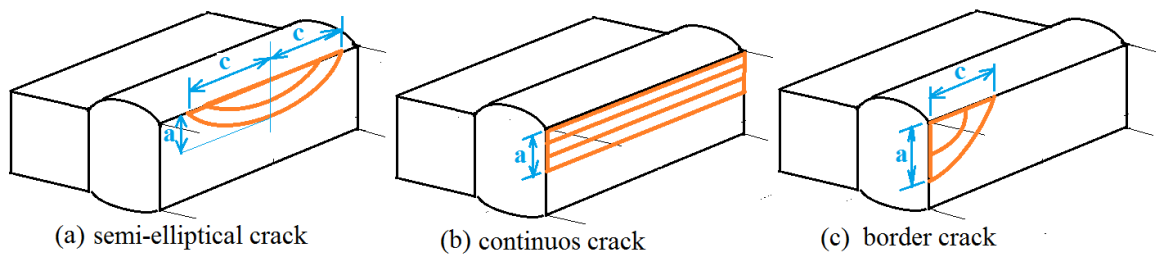


Figure 2.27 Scheme with three types of surface cracks.

The semi-elliptic surface crack has been studied in a large number of works in relation to the development of its aspect ratio a/c as it grows and its possible coalescence when there are nearby cracks [130, 131]. The aspect ratio a/c of a growing semi-elliptical crack is primarily a function of its initial size, the type of load applied, and its location on the surface, see Figure 2.28a. According to study [132] the elements cyclically loaded under tension load can develop the aspect ratios a/c as a function of a/t and initial sizes as illustrated schematically in Figure 2.28b. Thus a long and shallow crack presents an approximately linear relationship as in as shown in the lower part of the diagram in Figure 2.28b.

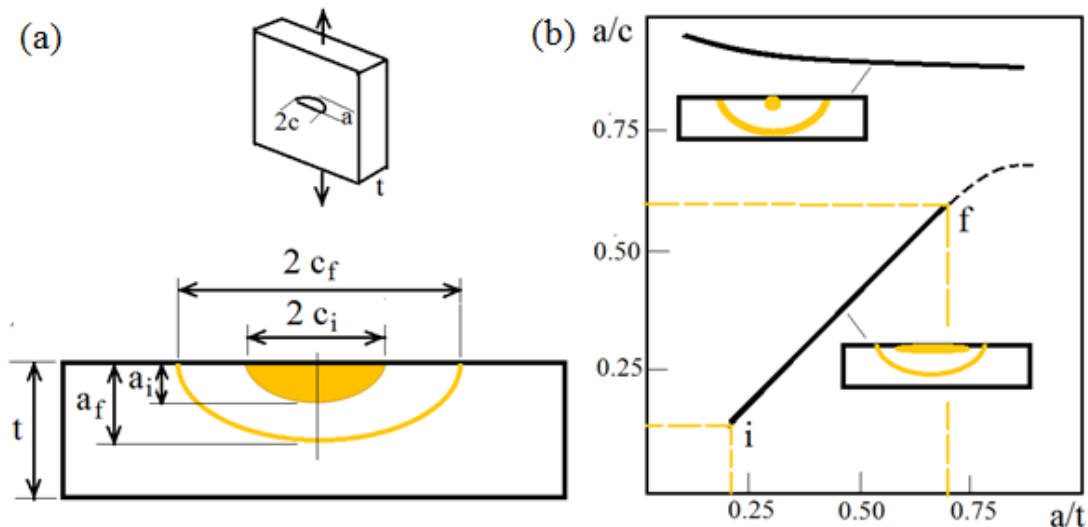


Figure 2.28 Scheme with sizes of semi-elliptical crack (a) and aspect ratio a/c - a/t for two types of cracks (b).

The initial and final crack sizes can be measured or assumed. In the International Institute of Welding (IIW) recommendations for fatigue design of welded joints, for cracks beginning at weld toe, crack sizes of 0.1 mm are suggested [82]. The initial cracks sizes can also be determined for fitting derived of experimental fatigue data of the Paris law, taken values from 0.05 to 0.15 mm [133]. The use of a certain initial crack size has been

highlighted more as a model parameter than a physical size itself [113]. The short crack behaviour is neglected because is covered by the fitting or size assumed. In relation to the final crack size, this can also be assumed, the typical value suggested for fatigue life calculations is half the thickness [82]. Because the results of calculating the number of fatigue cycles N is very sensitive to the initial crack size the value of the final crack size is the secondary importance.

Fatigue life estimation can be done by integrating the Paris propagation law and with the SIFR according to the following expressions:

$$N = \int_{a_i}^{a_f} \frac{da}{A \Delta K^n} \quad (2.15)$$

$$\Delta K = Y M_k \Delta \sigma \sqrt{\pi a} \quad (2.16)$$

The inclusion of the M_k factor in the SIFR, makes it possible to take into account the effect geometric features of the weld profile on crack. Relationships for the determination of Y and M_k are available from various sources for different types of cracks [82, 113, 134, 135].

For the determination of the number of cycles N , due to the M_k factor is function of aspect ratio a/c and of a/t , numerical integration or a direct integration can be used with stepwise integration considering M_k constant in small increments of crack size.

2.8. References

- [1] A. Ilić, L. Ivanović, D. Josifović and V. Lazić, "Advantages of High Strength Steels Applications in Mechanical Constructions," in *The 7th International Symposium KOD, Balantofured*, 2012.
- [2] World Auto Steel, "Advanced High-Strength Steels, Application Guidelines Version 6.0," April 2017. [Online]. Available: <https://www.worldautosteel.org/download-ahss-guidelines-6-0-free/>. [Accessed 1 February 2019].
- [3] K. Hulka, A. Kern and U. Schriever, "Application of Niobium in Quenched and Tempered High-Strength Steels," *Materials Science Forum*, Vols. 500-501, pp. 519-526, 2005.
- [4] J. Nowacki, A. Sajek and P. Matkowski, "The influence of welding heat input on the microstructure of joints of S1100QL steel in one-pass welding," *Archives of Civil and Mechanical Engineering*, vol. 16, pp. 777-783, 2016.
- [5] X. He, Y. Kim, T. Wallington, S. Zhang, W. Shen, R. De Kleine, G. Keoleian, R. Ma, Y. Zheng, B. Zhou and Y. Wu, "Cradle-to-gate greenhouse gas (GHG) burdens for aluminum and steel production and cradle-to-grave GHG benefits of vehicle lightweighting in China," *Resources, Conservation & Recycling*, vol. 152, pp. 1-10, 2020.
- [6] J. Zhao and Z. Jiang, "Thermomechanical processing of advanced high strength steels," *Progress in Materials Science* 94, pp. 174-242, 2018.
- [7] C. I. García, "High strength low alloyed (HSLA) steels," in *Automotive Steels*, London, Elsevier Ltd, 2017, pp. 145-166.
- [8] ASM International, *ASM Handbook*, Ohio: ASM, 1993, pp. 193-202.
- [9] D. Skobir, "High-Strength Low-Alloy (HSLA) Steels," *Materials and technology*, vol. 45, no. 4, pp. 295-301, 2011.
- [10] M. Kim, S. Park, K. Lee and B. Lee, "Comparison of fracture properties in SA508 Gr.3 and Gr.4N high strength low alloy steels for advanced pressure vessel materials," *International Journal of Pressure Vessels and Piping*, vol. 131, pp. 60-66, 2015.
- [11] L. Lan, Z. Chang, X. Kong, C. Qiu and D. Zhao, "Phase transformation, microstructure, and mechanical properties of X100 pipeline steels based on TMCP and HTP concepts," *Journal of Materials Science*, vol. 52, p. 1661-1678, 2017.
- [12] A. DeArdo, M. Hua, K. Cho and C. García, "On strength of microalloyed steels: an interpretive review," *Materials Science and Technology*, vol. 25, no. 9, pp. 1074-1082, 2009.
- [13] Y. Shao, C. Liu, Z. Yan, H. Li and Y. Liu, "Formation mechanism and control methods of acicular ferrite in HSLA steels: A Review," *Journal of Materials Science & Technology*, vol. 34, pp. 737-744, 2018.
- [14] SSAB, [Online]. Available: <https://www.ssab.com/products/brands/strenx/products/strenx-700-mc>. [Accessed 2019].
- [15] J. Górka, "Assessment of Steel Subjected to the Thermomechanical Control Process with Respect to Weldability," *Metals*, vol. 8, no. 169, pp. 1-17, 2018.
- [16] F. Bayock, P. Kah, B. Mvola and P. Layus, "Effect of Heat Input and Undermatched Filler Wire on the Microstructure and Mechanical Properties of Dissimilar S700MC/S960QC High-Strength Steels," *Metals*, vol. 9, no. 883, pp. 1-20, 2019.
- [17] X. Wang, H. Di, C. Zhang, L. Du and X. Dong, "Weldability of 780 MPa Super-High Strength Heavy-Duty Truck Crossbeam Steel," *Journal of Iron and Steel Research*, vol. 19, no. 6, pp. 64-69, 2012.
- [18] J. Moravec, I. Novakova, J. Sobotka and H. Neumann, "Determination of Grain Growth Kinetics and Assessment of Welding Effect on Properties of S700MC Steel in the HAZ of Welded Joints," *Metals*, vol. 9, no. 707, pp. 1-20, 2019.
- [19] J. Górka and S. Stano, "Microstructure and Properties of Hybrid Laser Arc Welded Joints (Laser Beam-MAG) in Thermo-Mechanical Control Processed S700MC Steel," *Metals*, vol. 8, no. 132, pp. 1-15, 2018.
- [20] V. Goritskii, G. Shneiderov and I. Guseva, "Study of Impact Toughness Anisotropy and Tendency Towards Lamination of Strenx 650MC and Strenx 700MC Steels after Thermomechanical Rolling," *Metallurgist*, vol. 62, no. 7-8, pp. 753-765, 2018.
- [21] M. Mazur and R. Ulewicz, "Analysis of strength and fatigue properties of construction materials for manufacturing the parts of semi-trailers," *Applied Engineering Letters*, vol. 2, no. 1, pp. 32-37, 2017.
- [22] American Welding Society, *Structural Welding Code -Steel AWS D1.1/D1.1 M:2010*, Miami: American Welding Society, 2010.
- [23] J. Ion, *Laser Processing of Engineering Materials: principles, procedure and industrial application*, Oxford: Elsevier Butterworth-Heinemann, 2005.

- [24] A. Jayanthi, K. Venkataramanan and K. Kumar, "Laser Beams A Novel Tool for Welding: A Review," *IOSR Journal of Applied Physics*, vol. 8, no. 6, pp. 8-26, 2016.
- [25] TRUMPF, 2019. [Online]. Available: http://www.trumpf.com/es_INT/productos/laser/.
- [26] W. Guo, J. Francis, L. Li, A. Vasileiou, D. Crowther and A. Thompson, "Residual stress distributions in laser and gas-metal-arc welded high-strength steel plates," *Materials Science and Technology*, vol. 32, no. 14, pp. 1449-1461, 2016.
- [27] R. Poprawe, D. Hoffman and K. Boucke, *Tailored Light 1 High Power Lasers for Production*, Aachen: Springer-Verlag GmbH, 2018.
- [28] A. Mahrle and E. Beyer, "Heat sources of hybrid laser-arc welding processes," in *Hybrid laser-arc welding*, Cambridge, Woodhead Publishing Limited, 2009, pp. 47-84.
- [29] S. Katayama, "Introduction: fundamentals of laser welding," in *Handbook of Laser welding technologies*, Cambridge, Woodhead Publishing Limited, 2013, pp. 1-16.
- [30] K. Löffler, "Developments in disk laser welding," in *Handbook of laser welding technologies*, Cambridge, Woodhead Publishing Limited, 2013, pp. 85-102.
- [31] A. Giesen and J. Speiser, "Fifteen Years of Work on Thin-Disk Lasers: Results and Scaling Laws," *IEEE Journal of Selected Topics in Quantum Electronics*, vol. 13, no. 13, 2007.
- [32] J. Mende, E. Schmid, J. Speiser, G. Spindler and A. Giesen, "Thin-disk laser – Power scaling to the kW regime in fundamental mode operation," *Proc. of SPIE*, vol. 7193, pp. 1-12, 2009.
- [33] L. Quintino, A. Costa, R. Miranda, D. Yapp, V. Kumar and C. Kong, "Welding with high power fiber lasers – A preliminary study," *Materials and Design*, vol. 28, p. 1231-1237, 2007.
- [34] L. Quintino and E. Assuncao, "Conduction laser welding," in *Handbook of laser welding technologies*, Cambridge, Woodhead Publishing Limited, 2013, pp. 139-162.
- [35] J. Ready, "Penetration Welding," in *Handbook of Laser Materials Processing*, Orlando, Magnolia Publishing, 2001, pp. 361-367.
- [36] I. Miyamoto, "Laser Welding of Glass," in *Handbook of laser welding technologies*, Woodhead Publishing Limited, 2013, pp. 301-331.
- [37] N. Sreenivasan, M. Xia, S. Lawson and Y. Zhou, "Effect of Laser Welding on Formability of DP980 steel," *Journal Engineering Materials and Technology*, vol. 130, pp. 1-9, 2008.
- [38] Y. Ai, P. Jiang, X. Shao, C. Wang, P. Li, G. Mi, Y. Liu and W. Liu, "An optimization method for defects reduction in fiber laser keyhole welding," *Applied Physics A*, vol. 122, no. 31, pp. 1-14, 2016.
- [39] K. Beyounis and A. Olabi, "Optimization of different welding processes using statistical and numerical approaches – A reference guide," *Advances in Engineering Software*, vol. 39, pp. 483-496, 2008.
- [40] A. Unt and A. Salminen, "Effect of welding parameters and the heat input on weld bead profile of laser welded T-joint in structural steel," *Journal of Laser applications*, vol. 27, no. S2, pp. 1-7, 2015.
- [41] R. Sharma and P. Molian, "Journal of Materials Processing Technology," Weldability of advanced high strength steels using an Yb:YAG disk laser, vol. 211, pp. 1888-1897, 2011.
- [42] W. Guo, D. Crowther, J. Francis, A. Thompson, Z. Liu and L. Li, "Microstructure and mechanical properties of autogenous laser welded S960 high strength steel," *Materials & Design*, vol. 85, p. 534-548, 2015.
- [43] A. Lisiecka and A. Lisiecki, "Laser welding of the new grade of advanced high-strength steel DOMEX 960," *Materials and Technology*, vol. 51, no. 2, pp. 199-204, 2017.
- [44] L. Tuz, "Evaluation of microstructure and selected mechanical properties of laser beam welded S690QL high-strength steel," *Advances in Materials Science*, vol. 18, no. 3, pp. 34-42, 2018.
- [45] A. Lisiecky, "Effect of heat input during disk laser bead-on-plate welding of thermomechanically rolled steel on penetration characteristics and porosity formation in the weld metal," *Archives of Metallurgy and Materials*, vol. 61, no. 1, pp. 93-102, 2016.
- [46] S. Němeček, T. Mužík and M. Míšek, "Differences between laser and arc welding of HSS steels," *Physics Procedia*, vol. 39, pp. 67-74, 2012.
- [47] J. Górká and A. Ozgowicz, "Structure and Properties of Laser-Beam-Welded Joints of Low-Alloy High-Strength Steel DOCOL 1200M with a Martensitic Structure," *Materials and Technology* 52, pp. 189-193, 2018.
- [48] W. Xu, D. Westerbaan, S. Nayak, D. Chen, F. Goodwin and y. Zhou, "Tensile and fatigue properties of fiber laser welded high strength low alloy," *Materials and Design*, vol. 43, pp. 373-383, 2013.
- [49] Y. Kawahito, M. Mizutami and S. Katayama, "Elucidation of high-power fibre laser welding phenomena of stainless steel and effect of factors on weld geometry," *Journal of Physics D: Applied Physics*, vol. 40, p. 5854/5859, 2017.

-
- [50] M. Zhang, K. Tang, J. Zhang, C. Mao, Y. Hu and G. Chen, "Effects of processing parameters on underfill defects in deep penetration laser welding of thick plates," *Advanced Manufacturing Technology*, vol. 96, pp. 491-501, 2018.
- [51] M. Sokolov and A. Salminen, "The effect of joint edge surface preparation on the efficiency of fiber laser welding of low-alloyed steels," *Mechanika*, vol. 21, no. 3, pp. 220-225, 2015.
- [52] M. Maina, Y. Okamoto, R. Inoue, S. Nakashiba, A. Okada and T. Sakagawa, "Influence of Surface State in Micro-Welding of Copper by Nd: YAG Laser," *Applied Sciences*, vol. 8, no. 2364, pp. 1-13, 2018.
- [53] International Organization for Standardization, *Welding - Electron and laser-beam welded joints - Guidance on quality levels for imperfections. Part 1: Steel*, Geneva: ISO, 1996.
- [54] C. Dawes, *Laser Welding A practical guide*, Cambridge: Abintong Publishing, 2008.
- [55] S. Katayama, "Defect formation mechanisms and preventive procedures in laser welding," in *Handbook of laser welding technologies*, Cambridge, Woodhead Publishing Limited, 2013, pp. 332-373.
- [56] K.-M. Hong and Y. Shin, "Prospects of laser welding technology in the automotive industry: A review," *Journal of Materials Processing Technology*, vol. 245, pp. 46-69, 2017.
- [57] N. Matsumoto, Y. Kawahito, K. Nishimoto and S. Katayama, "Effects of laser focusing properties on weldability in high-power fiber laser welding of thick high-strength steel plate," *Journal of Laser Applications*, vol. 29, no. 1, pp. 1-8, 2017.
- [58] P. Prochenka, K. Makowska and J. Janiszewski, "Assessment of Mechanical Properties of Laser Beam Welded Joints Made of Steel Strenx S700MC Subjected to High Impact Load," *Biuletyn Instytutu Spawalnictwa*, vol. 2, pp. 251-260, 2018.
- [59] B. Chang, C. Allen, J. Blackburn and P. Hilton, "Thermal and fluid flow characteristics and their relationships with porosity in laser welding of AA5083," *Physics Procedia*, vol. 41, pp. 478-487, 2013.
- [60] A. Matsunaga, "Problems and solutions in deep penetration laser welding," *Science and Technology of Welding and Joining*, vol. 6, no. 6, pp. 351-354, 2001.
- [61] H. Zhao, D. White and T. DebRoy, "Current issues and problems in laser welding of automotive aluminium alloys," *International Materials Reviews*, vol. 44, no. 6, pp. 238-266, 1999.
- [62] L. Mrna, M. Sarbort, S. Rerucha and P. Jedlicka, "Correlation between the keyhole depth and the frequency characteristics of light emissions in laser welding," *Physics Procedia*, vol. 41, pp. 469-477, 2013.
- [63] V. Alfieri, *Disk Laser Welding of Metals Alloys for Aerospace*, Universita Degli Studi Di Salerno: Doctoral Thesis, 2012.
- [64] C. Lampa, *Laser Welding Energy Redistribution and Weld Geometry*, Lulea University of Technology: Doctoral Thesis, 1997.
- [65] W. Guo, D. Crowther, J. Francis, A. Thompson and L. Li, "Process-parameter interactions in ultra-narrow gap laser welding of high strength steels," *International Journal of Advanced Manufacturing Technology*, pp. 1-20, 2015.
- [66] M. Khan, L. Romoli, M. Fiaschi, G. Dini and F. Sarri, "Experimental design approach to the process parameter optimization for laser welding of martensitic stainless steels in a constrained overlap configuration," *Optics & Laser Technology*, vol. 43, pp. 158-172, 2011.
- [67] N. Farabi, D. Chen and Y. Zhou, "Fatigue properties of laser welded dual-phase steel joints," *Procedia Engineering*, vol. 2, p. 835-843, 2010.
- [68] T. Lahtinen, P. Vilaça, P. Peura and S. Mehtonen, "MAG Welding Tests of Modern High Strength Steels with Minimum Yield Strength of 700 MPa," *Applied Sciences*, vol. 9, no. 1031, pp. 2-18, 2019.
- [69] Y. Rong, T. Lei, J. Xu, Y. Huang and C. Wang, "Residual stress modelling in laser welding marine steel EH36 considering a thermodynamics-based solid phase transformation," *International Journal of Mechanical Sciences*, Vols. 146-147, pp. 180-190, 2018.
- [70] G. Webster and A. Ezeilo, "Residual stress distributions and their influence on fatigue lifetimes," *International Journal of Fatigue*, vol. 23, pp. S375-S383, 2001.
- [71] F. Kandil, J. Lord, A. Fray and P. Grant, "A Review of Residual Stress Measurement Methods - A Guide to Technique Selection," NPL, Teddington, 2001.
- [72] ASM International, *Handbook of Residual Stress and Deformation of Steel*, Ohio: ASM International, 2002.
- [73] S. Kumar, A. Kundu, K. Venkata, A. Evans, C. Truman, J. Francis, K. Bhanumurthy, P. Bouchard and G. Dey, "Residual stresses in laser welded ASTM A387 Grade 91 steel plates," *Materials Science & Engineering A* 575, pp. 160-168, 2013.
- [74] E. Derakhshan, N. Yazdian, B. Craft, S. Smith and R. Kovacevic, "Numerical simulation and experimental validation of residual stress and welding distortion induced by laser-based welding
-

- processes of thin structural steel plates in butt joint configuration," *Optics and Laser Technology*, vol. 104, pp. 170-182, 2018.
- [75] R. Sindhu, M. Park, S. Lee and K. Lee, "Effects of Residual Stresses on the Static and Fatigue Strength of Laser-Welded Lap Joints with Different Welding Speeds," *International Journal of Automotive Technology*, vol. 11, no. 6, p. 857-863, 2010.
- [76] E. Harati, L. Karlsson, L. Svensson and K. Dalaei, "Applicability of low transformation temperature welding consumables to increase fatigue strength of welded high strength steels," *International Journal of Fatigue*, vol. 97, pp. 39-47, 2017.
- [77] U. Krupp, *Fatigue Crack Propagation in Metals and Alloys*, Weinheim: Wiley-VCH, 2007.
- [78] N. Dowling, *Mechanical Behaviour of Materials*, Harlow: Pearson, 2013.
- [79] S. Maddox, "Fatigue design rules for welded structures," in *Fracture and fatigue of welded joints and structures*, Cambridge, Woodhead Publishing, 2011, pp. 168-207.
- [80] B. Fustar, I. Lukacevic and D. Dujmovic, "Review of Fatigue Assessment Methods for Welded Steel Structures," *Advances in Civil Engineering*, pp. 1-16, 2018.
- [81] W. Fricke, "Fatigue strength assessment of local stresses in welded joints," in *Fracture and fatigue of welded joints and structures*, Cambridge, Woodhead Publishing, 2011, pp. 115-138.
- [82] A. F. Hobbacher, *Recommendations for Fatigue Design of Welded Joints and Components*, London: Springer, 2016.
- [83] T. Gurney, *Cumulative damage of welded joints*, Cambridge: Woodhead Publishing Ltd, 2006.
- [84] S. J. Maddox, *Fatigue strength of welded structures*, Cambridge: Abington Publishing, 2002.
- [85] D. Rajac, M. Sonsino and W. Fricke, *Fatigue assessment of welded joints by local approaches*, Cambridge: Woodhead Publishing Limited, 2006.
- [86] R. Ulewicz, P. Szataniak, F. Novy, L. Trsko and O. Bokuvka, "Fatigue characteristics of structural steels in the gigacycle region of loading," *Materials Today: Proceedings*, vol. 4, p. 5979-5984, 2017.
- [87] G. Ahiale and Y. Oh, "Microstructure and fatigue performance of butt-welded joints in advanced high-strength steels," *Materials Science & Engineering A* 597, pp. 342-348, 2014.
- [88] G. Marquis and Z. Barsoum, "A guideline for fatigue strength improvement of high strength steel welded structures using high frequency mechanical impact treatment," *Procedia Engineering* 66, pp. 98-107, 2013.
- [89] E. Harati, L. Svensson, L. Karlsson and M. Widmark, "Effect of high frequency mechanical impact treatment on fatigue strength of welded 1300 MPa yield strength steel," *International Journal of Fatigue*, no. 92, pp. 96-106, 2016.
- [90] J. Lago, M. Guagliano, O. Bokuvka, L. Trško, O. Řidký and F. Nový, "Improvement of fatigue endurance of welded S355 J2 structural steel by severe shot peening," *Surface Engineering*, vol. 33, no. 9, pp. 715-720, 2017.
- [91] H. P. Lieurade, I. Huther and F. Lefebvre, "Effect of Weld Quality and Postweld Improvement Techniques on the Fatigue Resistance of Extra High Strength Steels," *Welding in the World*, vol. 52, no. 7-8, pp. 106-115, 2008.
- [92] British Standards Institution, *Welding Fusion-welded joints in steel, nickel, titanium, and their alloys (beam welding excluded) - Quality levels for imperfections (ISO 5817:2014)*, Brussels: BIS Standards, 2014.
- [93] I. Lillemäe, H. Remes, S. Liinalampi and A. Itävuori, "Influence of weld quality on the fatigue strength of thin normal and high strength steel butt joints," *Welding in the Word*, vol. 60, no. 4, pp. 731-740, 2016.
- [94] S. Liinalampi, H. Remes and J. Romanoff, "Influence of three-dimensional weld undercut geometry on fatigue-effective stress," *Welding in the World*, vol. 63, pp. 277-291, 2019.
- [95] F. R. Mashiri, X. L. Zhao and P. Grundy, "Effects of weld profile and undercut on fatigue crack propagation life of thin-walled cruciform joint," *Thin-Walled Structures*, vol. 39, pp. 261-285, 2001.
- [96] R. Bell, O. Vosikovskiy and S. Bain, "The significance of weld toe undercuts in the fatigue of steel plate T-joints," *International Journal Fatigue*, vol. 11, no. 1, pp. 3-11, 1989.
- [97] M. Ottersböck, M. Leitner, M. Stoschka and W. Maurer, "Effect of weld defects on the fatigue strength of ultra high-strength steels," *Procedia Engineering*, vol. 160, pp. 214-222, 2016.
- [98] B. Schork, U. Zersbt, Y. Kiyak, M. Kaffenberger, M. Madia and M. Oechsner, "Effect of the parameters of weld toe geometry on the FAT class as obtained by means of fracture mechanics-based simulations," *Welding in the Word*, vol. 64, no. 6, pp. 925-936, 2020.
- [99] M. Cerit, O. Kokumer and K. Genel, "Stress concentration effects of undercut defect and reinforcement metal in butt welded joint," *Engineering Failure Analysis*, vol. 17, pp. 571-578, 2010.

-
- [100] X. Wang, Q. Meng and W. Hu, "Continuum damage mechanics-based model for the fatigue analysis of welded joints considering the effects of size and position of inner pores," *International Journal of Fatigue*, vol. 139, pp. 1-10, 2020.
- [101] F. Shen, B. Zhao, L. Li, C. Chua and K. Zhou, "Fatigue damage evolution and lifetime prediction of welded joints with the consideration of residual stresses and porosity," *International Journal of Fatigue*, vol. 103, pp. 272-279, 2017.
- [102] M. Alam, Z. Barsoum, P. Jonsén, A. Kaplan and H. Häggblad, "The influence of surface geometry and topography on the fatigue cracking behaviour of laser hybrid welded eccentric fillet joints," *Applied Surface Science*, vol. 256, pp. 1936-1945, 2010.
- [103] H. Remes and P. Varsta, "Statistics of weld geometry for laser-hybrid welded joints and its application within notch stress approach," *Welding in the World*, vol. 54, no. 7/8, pp. R189-R207, 2010.
- [104] T. Shiozaki, N. Yamaguchi, Y. Tamai, J. Hiramoto and K. Ogawa, "Effect of weld toe geometry on fatigue life of lap fillet welded ultra-high strength steels joints," *International Journal of Fatigue*, vol. 116, pp. 409-420, 2018.
- [105] F. Lefebvre, C. Peyrac, G. Elbel, C. Revilla-Gomez, C. Verdu and J. Buffière, "Understanding of fatigue strength improvement of steel structures by hammer peening treatment," *Procedia Engineering* 133, pp. 454-464, 2015.
- [106] E. Harati, L. Karlsson, L.-E. Svensson and K. Dalaei, "The relative effects of residual stresses and weld toe geometry on fatigue life of weldments," *International Journal of Fatigue*, vol. 77, pp. 160-165, 2015.
- [107] X. Cheng, J. Fisher, H. Prask, B. Yen, T. Graunapel-Herold and S. Roy, "Residual stress modification by post-weld treatment and its beneficial effect on fatigue strength of welded structures," *International Journal of Fatigue* 25, pp. 1259-1269, 2003.
- [108] D. Závodská, M. Guagliano, O. Bokůvka and L. Trško, "Fatigue resistance of low alloy steel after shot peening," *Materials Today: Proceedings* 3, pp. 1220-1225, 2016.
- [109] M. Mazur and R. Ulewicz, "Analysis of strength and fatigue properties of construction materials for manufacturing the parts of semi-trailers," *Applied Engineering Letters*, vol. 2, no. 1, pp. 32-37, 2017.
- [110] P. Kopas, Sága M, F. Nový and B. Leitner, "Low-cycle fatigue behaviour of laser welded high-strength steel DOMEX 700 MC," in *MATEC Wen of Conference* 157, 2018.
- [111] T. Anderson, *Fracture Mechanics Fundamentals and Applications*, Boca Raton: Taylor & Francis, 2005.
- [112] M. Chapetti, J. Belmonte, T. Tawada and T. Miyata, "Integrated fracture mechanics approach to analyse fatigue behaviour of welded joints," *Science and Technology of Welding and Joining*, vol. 9, no. 5, pp. 430-438, 2004.
- [113] U. Zerbst, M. Madia, B. Schork, J. Hensel, P. Kucharczyk, D. Ngoula, D. Tchuindjang, J. Bernhard and C. Beckmann, *Fatigue and Fracture of Weldments*, Basilea: Springer, 2019.
- [114] J. Schijve, *Fatigue of Structures and Materials*, New York: Springer, 2008.
- [115] W. Yisheng and J. Schijve, "Fatigue Crack Closure Measurements on 2024-T3 Sheet Specimens," *Fatigue & Fracture of Engineering Materials & Structures*, vol. 18, no. 9, pp. 917-921, 1995.
- [116] S. Li, Y. Khan and S. Kuang, "Effects of microstructure on fatigue crack growth behavior in cold-rolled dual phase steels," *Materials Science & Engineering A*, vol. 612, pp. 153-161, 2014.
- [117] M. Askari-Paykani, H. Reza and R. Miresmaeili, "Fatigue crack growth behavior of a type of novel advanced high-strength steel in a FeCrNiBSi alloy system: A comparison between heat-treated cast and hot-rolled specimens," *Materials Science & Engineering A*, vol. 673, pp. 280-287, 2016.
- [118] Q. Wang, S. Yang, X. Liu, Z. Dong and H. Fang, "Understanding of fatigue crack growth behavior in welded joint a new generation Ni-Cr-Mo-V high strength steel," *Engineering Fracture Mechanics*, vol. 194, pp. 224-239, 2018.
- [119] A. Ohta, N. Suzuki, Y. Maeda, K. Hiraoka and T. Nakamura, "Superior fatigue crack growth properties in newly developed weld metal," *International Journal of Fatigue*, vol. 21, pp. S113-S118, 1999.
- [120] W. Cui, "State-of-the-art review on fatigue life predictions methods for metals structures," *Journal of Marine Science and Technology*, vol. 7, pp. 43-56, 2002.
- [121] H. Yamamoto, Y. Danno, K. Ito, Y. Mikami and H. Fujii, "Weld toe modification using spherical-tip WC tool FSP in fatigue strength improvement of high-strength low-alloy steel joints," *Materials and Design*, Vols. 1019-1028, p. 160, 2018.
- [122] T. Nguyen and M. Wahab, "The effect of weld geometry and residual stresses on the fatigue of welded joints under combined loading," *Journal of Materials Processing Technology*, vol. 77, pp. 201-208, 1998.
- [123] M. Chapetti and F. Jaureguizar, "Fatigue behavior prediction of welded joints by using an integrated fracture mechanics approach," *International Journal of Fatigue*, vol. 43, pp. 43-53, 2012.
- [124] Y.-H. Zhang and S. Maddox, "Fatigue life prediction for toe ground welded joints," *International Journal of Fatigue*, vol. 31, pp. 1124-1136, 2009.
-

- [125] J. Schijve, "Fatigue Predictions and Scatter," *Fatigue & Fracture of Engineering Materials & Structures*, vol. 17, no. 4, pp. 381-393, 1994.
- [126] J. Schijve, "The significance of fatigue crack initiation for predictions of the fatigue limit of specimens and structures," *International Journal of Fatigue*, vol. 61, pp. 39-45, 2014.
- [127] M. Åman, Y. Tanaka, Y. Murakami, H. Remes and G. Marquis, "Fatigue strength evaluation of small defect at stress concentration," *Structural Integrity Procedia*, vol. 7, pp. 351-358, 2017.
- [128] N. Douling, C. Calhoun and A. Arcari, "Mean stress effects in stress-life fatigue and the Walker equation," *Fatigue & Fracture of Engineering Materials & Structures*, vol. 32, pp. 163-179, 2008.
- [129] y. Murakami, *Metal Fatigue: Effects of Small Defects and Nonmetallic Inclusions*, Oxford: Elsevier Science Ltd, 2002.
- [130] C. Liu and S. Chu, "Prediction of shape change of semi-elliptical surface crack by fatigue crack growth circles parameter," *Journal of Mechanical Science and Technology*, vol. 28, no. 12, p. 4921~4928, 2014.
- [131] P. Yu and W. Guo, "An equivalent thickness conception for prediction of surface fatigue crack growth life and shape evolution," *Engineering Fracture Mechanics*, Vols. 65-74, p. 93, 2012.
- [132] P. Nair, "Fatigue Crack Growth Model for Part-Through Flaws in Plates and Pipes," *Journal of Engineering Materials and Technology*, vol. 101, pp. 53-58, 1979.
- [133] A. Hobbacher, "The use of fracture mechanics in the fatigue analysis of welded joints," in *Fracture and fatigue of welded joints and structures*, Cambridge, Woodhead Publishing, 2011, pp. 91-111.
- [134] FITNET, *FITNET Fitness-for-Service. Vol. II Annex*, Geesthacht: FITNET, 2008.
- [135] S. Lie, S. Vipin and H. Zhao, "New weld toe magnification factors for semi-elliptical cracks in plate-to-plate butt-welded joints," *Fatigue & Fracture of Engineering Materials & Structures*, vol. 40, pp. 207-220, 2016.

Chapter 3: Interactions of the process parameters and mechanical properties of laser butt welds in thin high strength low alloy steel plates

Patricio Gustavo Riofrío^{a*}, Carlos Alexandre Capela^b, José AM Ferreira^c and Amilcar Ramalho^c

^aDepartamento de Ciencias de la Energía y Mecánica, Universidad de las Fuerzas Armadas, Sangolqui, Ecuador

^bSchool of Technology and Management, Polytechnic Institute of Leiria, Leiria, Portugal

^cFaculty of Sciences and Technology, University of Coimbra, Coimbra, Portugal

Published in **Proc. Inst. Mech. Eng. Part L: J. Materials: Design and Applications**. 234(5) (2020) 665-680, [doi:11.1177/1464420720910442](https://doi.org/10.1177/1464420720910442).

Abstract

High strength low alloy steels subjected to the thermomechanical control process present excellent strength–toughness combination, high strength/weight ratio, and weldability. Therefore, they are widely used in structural components, such as pressure vessels, oil/gas transportation pipes, lifting equipment, vehicles, shipbuilding and offshore industries, and in the automotive industry where low thickness (0.8–3mm thickness) is of great importance. Usually, these steels are welded by conventional gas metal arc welding, which creates wide heat-affected zones, large residual stresses, and distortion in the welded parts. Laser welding is nowadays an alternative process to weld high strength low alloy steel parts due to its advantages. The aim of this work is to understand the effect of process parameters on defects, weld bead geometry, microstructure, and mechanical properties, namely hardness and tensile strength. We identify the main laser welding parameters and their influence on the weld bead geometry and defects, for a 3mm thick high strength low alloy steel welded under a maximum power of 2 kW. A cross section of the weld seam was optimized achieving a good geometry without porosity. The threshold value of the heat input to achieve complete penetration was determined for different focus diameters. The

microstructure, size, and hardness of the heat-affected zone and of the fusion zone are strongly influenced by the heat input. The values of the tensile strength achieved in butt welds were close to the base metal by an appropriate selection of the laser welding parameters and the heat input.

Keywords: Laser welding parameters, high strength low alloy steels, welding defects, mechanical properties, heat input

3.1. Introduction

The laser welding of high strength low alloy (HSLA) steels is a promising technology since it allows to reduce the weight and to increase the efficiency of the weld, when comparing with other existing techniques. HSLA steels have several applications in diverse areas such as automotive, structural, pipeline, lifting, shipbuilding, among others [1-3]. Due to the improvement of laser technology and to its advantages over conventional welding processes, laser welding is also being used in alloys of aluminum, magnesium, titanium, dissimilar materials [4] and in advanced engineering materials, such as NiTi, being for the latter the most used joining process [5]. The key feature of laser welding is its high-power density, which allows a lower heat input (HI), high cooling rate, and a narrower heat-affected zone (HAZ) [6].

Although these characteristics may be conducive to the welding of HSLA steels and other materials, establishing the laser welding parameters that allows achieving sound welds and similar mechanical properties between the base metal (BM) and the welded joint is not trivial.

Since laser welding comprises complex multidimensional mechanisms, ensuring a high-quality welded joint without defects is a major challenge [7]. While high-power density is the prominent feature of laser welding and HI is a determinant factor for any welding process; the power, the welding speed, the focus diameter, and the focus position are dominant parameters in laser welding. However, by the sensitivity of the laser welding there are other factors that can affect the weldability and efficiency, such as shielding gas,

preparation of the joint, surface condition, etc. Therefore, several parameters must be controlled to obtain a good weld bead. Many studies have established the effect of welding parameters on the weld bead geometry. Quintino et al. [8] studied the effect on the penetration of the power, welding speed, and HI for relatively high values of these variables. Sharma and Molian [9] developed an analytical relationship that allows to calculate the welding speed as a function of power and penetration for HSLA steels. Sreenivasan et al. [10] studied the effect of the beam size by using two types of lasers with two different beam sizes, one much smaller than the other, and found a thin and deep weld bead in the first case and a wide and small penetration in the second. Kawahito et al. [11] used four focus diameters to examine the effect of power density on 8-mm-thick stainless steel SUS304 in fiber laser welding, finding that high power density at high speeds exerts a marked effect, increasing the penetration. In two works [12, 13] in which the effect of the focus position on the penetration was studied, it was determined that for certain ranges of negative focus position the penetration increases. In the welding of thin plates of high-strength steels, in several reviewed works, [14-17] a large variation of the welding parameters is observed, particularly in the power, focus diameter, and welding speed. Other factors than the main ones have also been studied. Sokolov and Salminen [18] studied the effect of edge surface preparation on the efficiency of the fiber laser welding for low alloy steels. The results showed that no additional accurate machining of the edges is necessary and that a small gap can be used. Maina et al. [19] found that the surface condition (shape and roughness) influences the penetration and quality of the micro-welding of copper by laser. Lampa's research, [20] in 2-mm-thick stainless steel butt welded joints, showed that the absorbed power and the weld bead geometry are affected by the size of the gap.

There are many works that seek to avoid specific defects and optimize the shape of the weld bead. In Zhang et al., [13] when concerning the effect of various processing parameters on the underfill in autogenous laser welding of thick steel plates, it was established that high speed tends to decrease the underfill and that the negative defocusing and the welding speed are the parameters that can be used to optimize the weld bead. Ion [21] characterized (fine and coarse) the porosity presenting the sources for its generation: base material, filler additions, surface contaminants, and process gases for the fine porosity and keyhole instability for the coarse porosity. In several studies [12, 22, 23] where porosity is attributed to an unstable keyhole, the mechanisms for its formation are explained and

solutions are suggested to minimize or avoid porosity. In Matsumoto et al. [24], the effect of the laser focusing properties on weld defects was investigated for a high strength steel with 12 mm thickness. Two systems with different power density distributions were used, finding that the system with a more uniform distribution did not present porosity. In the work [11] previously cited, for four focus diameters and a wide range of speed it was established that there is a limited window of sound welds between defects such as porosity, humping, and underfill.

Although a sound weld bead can be achieved, the HI affects the microstructure of HSLA steels and their mechanical properties. It is well known that due to the HI and the respective cooling rate, the microstructure of the BM evolves significantly in the HAZ and fusion zone (FZ). After reviewing several works [25-28] of laser welding where the evolution of the BM microstructure of different HSLA steels was analyzed, it is possible to establish, in general lines the following: in the FZ if low HI are provided, a relatively soft microstructure evolves to a relatively hard (for example, bainite changes to martensite); and, conversely, a relatively hard microstructure evolves to a relatively soft, if the HI is not low enough. In the HAZ there is almost always softening.

The hardness and mechanical properties of welded joints are a consequence of microstructure evolution in the HAZ and FZ. According to the results obtained in the studies [10, 15, 16], the possibility of obtaining a tension strength in the welded joint equal to or greater than the BM can be summarized in the following features: small size and low softening of the HAZ and equal or higher hardness in the FZ. In order to achieve it, the HI must be as low as possible. Regarding the ductility, it is always lower than the BM. However, Guo et al. [29] reported that the strength and ductility of autogenous laser welds matched of the BM due to the elimination of defects, a small HAZ and a minimum softening.

The aim of this work is to understand the effect of laser welding parameters and HI on defects, weld bead geometry, microstructure, and mechanical properties such as hardness and tensile strength. An experimental design, one-factor-at-a-time (OFAT) and additional runs are used for investigating the effect of four parameters and the condition of the edges and surface on the 3-mm-thick HSLA Strenx[®] 700MCE steel. Unlike other works that use high powers to perform the welding, in this study the maximum available power

was 2 kW, meaning that the range of welding speeds is reduced and therefore it limits the search for solutions to the defects' problem. The current work identifies the main welding parameters and their influence. A cross section of the weld bead without porosity and with good geometry was achieved. The HI showed be a relevant parameter instead the separate values of the power and welding speed. The threshold value of the HI to achieve the full penetration was determined for different focus diameters. The effect of the HI on the microstructure, microhardness, and size of HAZ and FZ was also established. In spite of the differences in the weld bead geometry and HI of the butt welded joints, a tensile strength close to the BM was achieved.

3.2. Material and experimental procedures

3.2.1. Material

The HSLA steel Strenx[®] 700MCE used in this study is a hot-rolled structural steel made for cold forming and designed for stronger and lighter structures, covering the requirements of S700MC in EN 10149-2 [30]. The chemical composition presented in Table 3.1, was determined by X-ray fluorescence and carbon analysis by automatic direct combustion. The mechanical properties shown on Table 3.2 were determined according to the ASMT EM8 standard and are the average of three specimens cut in the rolling direction.

The microstructure of the base material is shown in Figure 3.1, where it is observed the presence of fine grains of two components and precipitates, which corresponds to a bainitic–ferritic microstructure. The same microstructure was reported in two works [31, 32] that used S700MC steel.

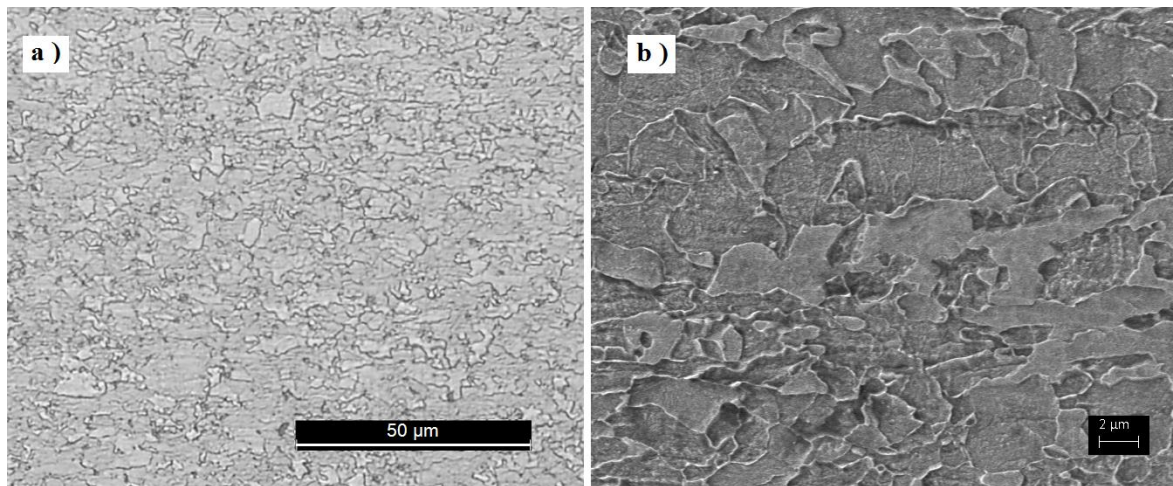


Figure 3.1 Microstructure of the base material: (a) optical microscopy; (b) SEM micrograph.

Table 3.1 Chemical composition of the base metal.

C	Mn	Si	P	S	Cr	V	Nb	Ni	Cu	Al	Mo	Ti	Co	Fe
0.07	1.69	0.01	0.012	0.006	0.03	0.02	0.046	0.04	0.011	0.044	0.016	0.117	0.016	balance

Table 3.2 Tensile mechanical properties of the base metal.

Yield Strength (MPa)	Tensile Strength (MPa)	Elongation %
807.63	838.26	15.04

3.2.2. Laser welding

The parameters and values used for the experimentation are shown in Table 3.3. The parameters were chosen because they are the most influential in laser welding and the values allow complete and partial penetrations. In the experimental design one-factor-at-a-time, welding was done on the surface of the sheets in their delivery state and the edges were milled after laser cutting (surface-edge condition C1). Additionally, to establish trends, to study the effect of the surface edge condition and for optimization, other parameter values and three more surface edge conditions were used (see Table 3.3 and Table 3.5). Due to the number of factors and to be able to make inferences about its effects and estimate the experimental error, for sample numbers: 2, 4, 7, 9, 15, 16, and 17, two replicates were used, while one replica was used for the rest of the samples (see Table 3.5).

Table 3.3 Welding parameters used in the experimental work.

Parameters	Units	Notation	Values			
Laser power	kW	P	1.50	1.75	1.25	2.00
Welding speed	m/min	v	2.00	2.50	1.50	3.00,2.10,1.65,1.60
Focus diameter	μm	f_d	350	500	150	
Focus position	Mm	f_p	0	2	-2	
Surface-edge condition	-	S-E	-	CI	-	C2, C3, C4

Table 3.4 Laser equipment characteristics.

Laser: Trump TruDisk 2000	
Laser maximum output (W)	2000
Beam wavelength (nm)	1030
Fiber diameters (μm)	50, 200
Beam parameter product (mm-mrad)	2

A disk laser equipment with the characteristics present in Table 3.4 was used. Several focus diameters are possible by the combining of one of its two fibers with the focal length, which is adjusted by the optical system. The operation was taken in the continuous mode at 6000 Hz.

The butt welded samples were formed with two sheets of 185×110×3 mm cut by laser. Fixing slots were placed in the sheets Figure 3.2a. The surface of the sheets for the second condition (C2) was in the state of delivery. In the third condition (C3), the surface close to the weld was sanded by means of two sandpapers #80 and #120, while in the fourth condition (C4), the surface was prepared by sand blasting. In the three conditions C2, C3, and C4, the edges were rectified to achieve a uniform and practically null gap clearance between the sheets. Before performing the welding, the surfaces and edges were cleaned with acetone, the welding line was aligned to the trajectory of the laser beam and the sheets were fastened in the slots by means of screws. During the welding, argon shielding gas was used at a flow rate of 20 L/min. The axis of the weld bead was arranged transversely to the rolling direction.

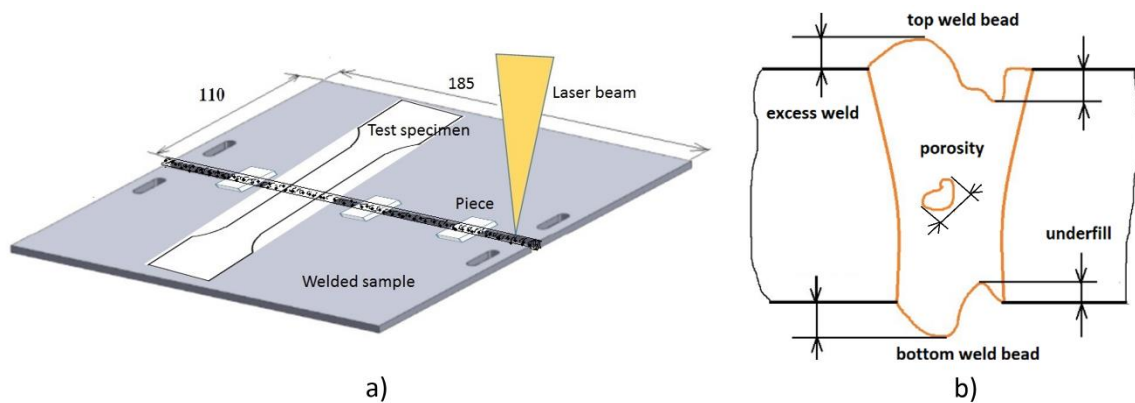


Figure 3.2 Schemes of (a) location of specimens and pieces in the weld sample and (b) measurements made on the cross section of the weld bead

3.2.3. Weld bead geometry, microstructure, and mechanical properties

For the measurement and analysis of the cross-section, microhardness, and the microstructure of the weld bead, pieces were extracted from the center and near to the ends of the butt welded samples Figure 3.2a. The pieces were sanded, polished, and etched with nital at 2%. In the case of samples that have two replicas, two pieces (one from the center and the other near the end) were extracted for each replica, while for samples with one replica, three pieces were extracted (one from the center and the other two of the ends).

The penetration depth (D), width (W) of the FZ and HAZ and defects were measured through the Mitutoyo Toolmaker's Microscope equipped with digital micrometers. In the present work, the width W of HAZ and FZ instead of the individual size of each zone was used as an indicative of the HI effect and the measurement was made on the top weld bead.

The scheme in Figure 3.2b shows the measurements used to characterize defects in terms of underfill (–), excess weld (+), misalignment, and porosity. All the results of the measurements made with the microscope are the average of four and three pieces according to the number of replicas as explained above. The microhardness Vickers' profile (HV, 0.5 kg, 10 s) was determined in a piece at a depth of 50 mm from the top weld bead and it is the average of two indentations made with a Struers' Duramin equipment. A Leica DM4000M LED optical microscope and a Zeiss scanning electron microscope were used for the

microstructure observation and photomicrographs, while the macrostructure and appearance of the weld seam was characterized by photomacrographs made with Nikon' SMZ-10 optical microscope.

The tensile mechanical properties of the welded samples were determined according to the ASTM E8M standard. The specimens were cut by electrical discharge machining and tested on an Instron 4206 machine, the results are the average of two specimens.

3.3. Results and discussion

3.3.1. Appearance, section geometry, and defects of the weld bead

Table 3.5 shows the results for penetration P, width W and their respective standard deviations in conjunction with the welding parameters and HI for all samples. Table 3.5 discriminates four groups of samples, which were used for the following purposes: # 1–9 correspond to the design one-factor-at-a-time; # 10–14 to complete trends; # 15–17 for the effect of the surface-edge condition; and # 18–20 for optimization.

The following points stand out from the results shown in Table 3.5. Without considering the samples that had complete penetration, each sample (with different welding parameters) produced a different result in penetration P and width W, and those differences are greater in penetration P than in the width W.

Table 3.5 Sample set results.

Sample #	P (kW)	v (m/min)	fd (μm)	fp (mm)	S-E condition	HI (J/mm)	D (mm)	SD (mm)	W (mm)	SD (mm)
1	1.50	1.50	350	0		60.0	3.00	0.00	2.04	0.03
2	1.50	2.00	350	0		45.0	2.54	0.06	1.71	0.05
3	1.50	2.50	350	0		36.0	2.33	0.05	1.46	0.02
4	1.50	2.00	150	0		45.0	2.96	0.08	1.67	0.13
5	1.50	2.00	500	0	C1	45.0	2.29	0.09	1.58	0.01
6	1.50	2.00	350	2		45.0	2.41	0.04	1.80	0.05
7	1.50	2.00	350	-2		45.0	2.67	0.03	1.75	0.06
8	1.25	2.00	350	0		37.5	2.20	0.02	1.59	0.04
9	1.75	2.00	350	0		52.5	3.00	0.00	1.77	0.05
10	1.75	2.00	500	0		52.5	2.55	0.08	1.78	0.01
11	1.00	3.00	150	0		20.0	2.34	0.26	1.11	0.14
12	2.00	2.00	350	0	C1	60.0	3.00	0.00	1.81	0.05
13	2.00	2.00	500	0		60.0	3.00	0.00	1.94	0.05
14	2.00	1.50	350	0		80.0	3.00	0.00	2.14	0.05
15	1.75	2.10	350	-2	C2	50.0	3.00	0.00	1.68	0.05
16	1.75	2.10	350	-2	C3	50.0	2.68	0.09	2.10	0.10
17	1.75	2.10	350	-2	C4	50.0	2.66	0.03	2.03	0.02
18	2.00	1.50	350	-2		80.0	3.00	0.00	2.60	0.05
19	2.00	1.60	350	-2	C3	75.0	3.00	0.00	2.35	0.09
20	2.00	1.65	350	-2		72.7	3.00	0.00	2.36	0.02

The standard deviations for both penetration D and width W are small and similar with the exception of the samples with small focus diameter (150 μm). For the penetration D, considering the samples with two replicas (# 2, 4, 7, 9, and 15–17) but not counting the samples that reached complete penetration (# 9 and # 15), the average of standard deviations is close to 0.06 mm, this value is an estimate of the experimental error. All of the above validate the results and confirm that the differences in the results are due to the combination of welding parameters of each sample.

Figure 3.3 to 3.5 show the appearance of the weld seam: top and bottom, the cross section, and the quantification of defects of the weld bead for the samples in surface-edge condition C1.

Several defects are shown in Figure 3.3, 3.4, and 3.5. In general, all samples have irregular weld seams, porosity, excess weld metal, and underfill. Other defects observed in a few samples were misalignment, undercut, spatter, and beam deviation. The underfill and the excess weld metal are greater in the samples that had complete penetration, while in those

that had partial penetration the porosity is greater. The latter result is in line with what was found by Chang et al. [33], who observed a decrease in the porosity levels, both in quantity and size, in full penetration welds in relation to the partial penetration welds. The underfilling may be explained by the evaporation of the base material, excessive joint gap, or bad preparation of the border plates [34], while the porosity may result mainly from surface contaminants and keyhole instability [12, 21, 23].

Considering the samples with full penetration, the results show that sample # 14 has fewer defects, a regular appearance, and wide weld seam. These characteristics may be due to a good combination of welding parameters: high power, low speed, medium focus diameter, and long focus depth (small beam parameter product (BPP)), which lead to a more stable keyhole. The previous analysis is consistent with two works [11, 24] in which the effect of laser welding parameters on defects formation was studied. In the first study, there was no defects at low speeds, long focus depth and for the largest focus diameter, which according to the authors, is due to a balanced power density in the keyhole, which causes a stable molten pool. Meanwhile, in the second study, the sound weld bead formed is attributed to the long molten pool as well as a stable keyhole, which occurs for larger focus diameters (350 and 500 μm) and certain range of speeds, but outside this window, for small focus diameters (150 and 200 μm) humping occurs, while with high speeds, underfill occurs. In the present work, for the focus diameter 150 μm , there was an irregular weld seam and a variable penetration, while the underfill increased slightly when the welding speed increased (samples #13 and #9).

Sample number	14	1	13	12	9
Parameters: P, v, fd, fp (kW, m/min, μm, mm)	2.00, 1.50, 350, 0	1.50, 1.50, 350, 0	2.00, 2.00, 500, 0	2.00, 2.00, 350, 0	1.75, 2.00, 350, 0
Top weld seam					
Bottom weld seam					
Weld bead section					
Porosity: #, size (mm)	0, 0	1, 0.12	1, 0.06	1, 0.04	1, 0.04
Underfill: top, bottom (mm)	- 0.19, - 0.06	- 0.16, 0.00	- 0.34, - 0.03	- 0.14, - 0.04	- 0.25, - 0.12
Excess weld: top, bottom (mm)	0.00, 0.13	0.00, 0.22	0.00, 0.15	0.00, 0.11	0.00, 0.27
Misalignment (mm)	x	x	0.17	x	0.19
Other	x	spatter	x	x	x

Figure 3.3 Appearance, section geometry, and defects of weld beads for samples 14, 1, 13, 12, and 9.

Sample number	4	7	10	2	6
Parameters: P, v, fd, fp (kW, m/min, μm, mm)	1.50, 2.00, 150, 0	1.50, 2.00, 350, -2	1.75, 2.00, 500, 0	1.50, 2.00, 350, 0	1.50, 2.00, 350, 2
Top weld seam					
Weld bead section					
Porosity: #, size (mm)	1, 0.09	2, 0.18	2, 0.17	2, 0.12	2, 0.16
Underfill: top, bottom (mm)	- 0.18, x	- 0.08, x	- 0.10, x	- 0.11, x	- 0.12, x
Excess weld: top, bottom (mm)	0.00, x	0.03, x	0.02, x	0.03, x	0.00, x
Misalignment (mm)	x	0.17	x	0.10	x
Other	irregular penetration	undercut	x	spatter	x

Figure 3.4 Appearance, section geometry, and defects of weld beads for samples 4, 7, 10, 2, and 6.





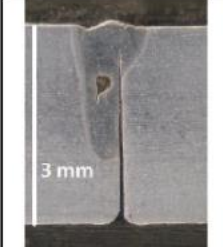
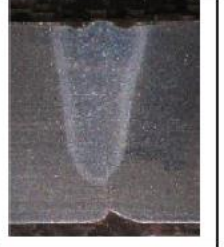
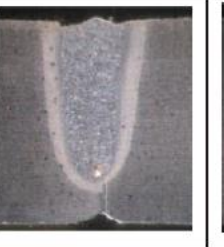
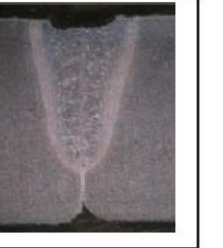
Sample number	11	3	5	8
Parameters: P, v, fd, fp (kW, m/min, μ m, mm)	1.00, 3.00, 150, 0	1.50, 2.50, 350, 0	1.50, 2.00, 500, 0	1.25, 2.00, 350, 0
Top weld seam				
Weld bead section				
Porosity: #, size (mm)	1, 0.09	1, 0.11	1, 0.13	1, 0.05
Underfill: top, bottom (mm)	- 0.12, x	- 0.10, x	- 0.05, x	- 0.19, x
Excess weld: top, bottom (mm)	0.04, x	0.00, x	0.07, x	0.00,x
Misalignment (mm)	x	0.05	x	x
Other	beam deviation	spatter	x	x

Figure 3.5 Appearance, section geometry, and defects of weld beads for samples 11, 3, 5, and 8.

3.3.2. Effects of the laser parameters on the penetration and width of HAZ and FZ

Effect of the power, welding speed, focus diameter and focus position. Figure 3.6 reveals the effect of four laser weld parameters and their importance in the penetration D and width W. As it is possible to observe, the welding speed, power, and focus diameter have a strong effect on the penetration D, while the effect of the focus position is slight. However, the change to a negative focus position can make the difference between obtaining complete or partial penetration in thin sheets. Regarding the width W, only the welding speed produces a considerable effect.

Although the relationships for W and D as functions of the four parameters shown in Figure 3.6 are generally known, it is important to establish the magnitude of variation produced by each parameter in the specific conditions of low power, thin thickness, and for material used in this study. The relative lower effect of the focus position is explained by the characteristics of the laser equipment optical system.

This system's BPP is small, so the focus depth is long and therefore there is a more uniform distribution of power density in the focus depth.

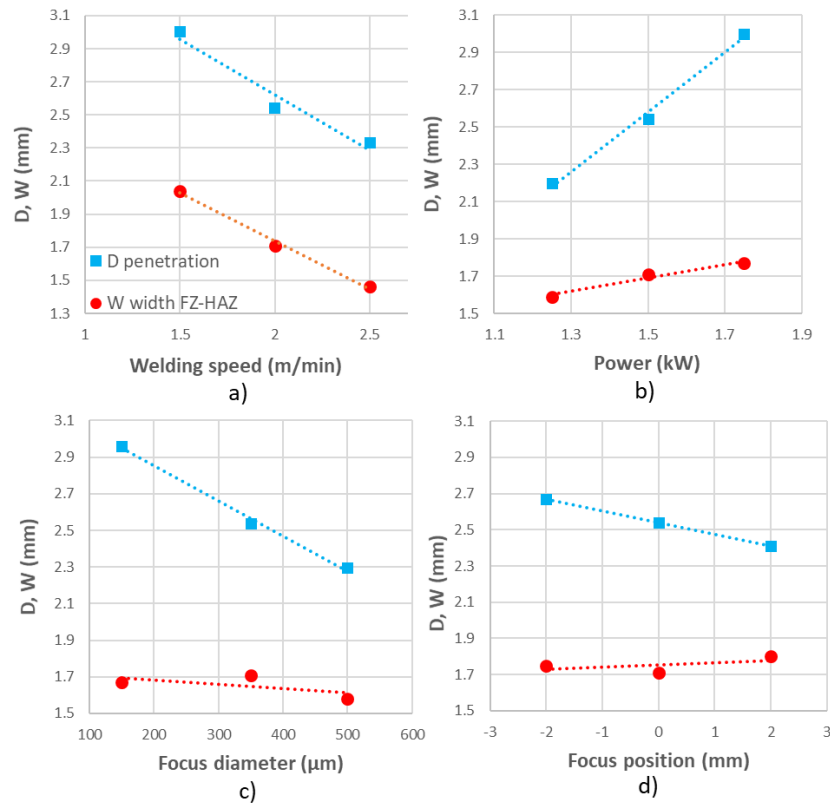


Figure 3.6 Penetration depth D and width W in function of: (a) welding speed, (b) power, (c) focus diameter, and (d) focus position.

3.3.2.1. Effect of surface and edge condition.

The state of the surfaces, edges, and the groove gap are factors that affect the appearance and shape of the weld bead as well as the stability of the keyhole. When observing the photographs of the samples present in Figure 3.4 and 3.5, it is found that most of the top weld seams have an irregular appearance and chamfers in the bottom edges. Examining the joint gap clearance allowed observing an irregular and light gap in condition C1 Figure 3.7a. Consequently, and according to the literature reviewed, these factors may have influenced the geometry and appearance of the weld bead as well as the stability of the keyhole mode. To study the effect of the surface-edge condition, samples #15, #16, and #17 were prepared under conditions C2, C3, and C4 as already detailed in an earlier section, obtaining a regular and practically null gap for the three conditions as illustrated by condition C3 Figure 3.7a. The results in penetration D , width W , and appearance of the weld seam can

be observed in Figure 3.7b and c. There is a clear difference in the results between the surface-edge conditions C2 versus the other two conditions: C3 and C4. These last two have very similar results. Comparatively, in condition C2 the penetration D increases, the width W decreases, and the top weld seam appearance is irregular.

The greater penetration observed in surface-edge condition C2, when comparing with conditions C3 and C4, is explained due to the absorption phenomenon, since the surface is less bright and rougher, it reflects less energy from the incident beam. The best appearance of the weld seam of conditions C3 and C4 can also be consequence of the roughness effect.

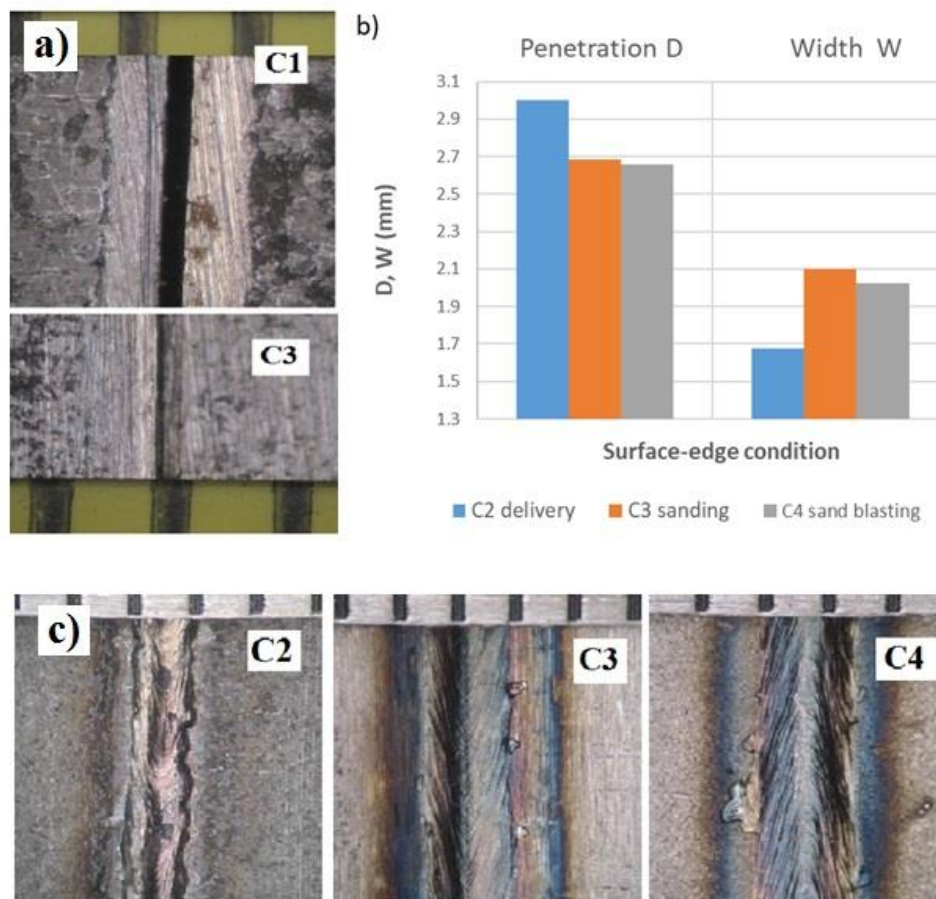


Figure 3.7 Effect of the surface-edge condition: (a) gap difference between conditions C1 and C3 (C2, C4); (b) penetration depth D

3.3.2.2. Effect of the heat input.

The HI is an important parameter for any welding process. It is the heat supplied per unit length and results from the division of power by the welding speed. Figure 3.8 shows the effect of the HI on penetration D and width W for all the samples with the surface-edge

condition C1. In Figure 3.8a, it is seen that while a minimum value of HI is necessary to achieve the complete penetration (3 mm) of the butt joint, this minimum value varies according to the focus diameter. The trend lines determine that the minimum HI values are approximately 47, 53, and 60 J/mm for the focus diameters 150, 350, and 500 mm, respectively. The effect of the focus position on the penetration for the conditions, HI of 45 J/mm and focus diameter of 350 μm , is also highlighted in Figure 3.8a. The penetration increases as it passes from the positive to negative values as it can be seen in Figure 3.6d. In Figure 3.8b, it is possible to observe that the relationship between the width W and the HI is approximately linear for all the focus diameters and that there are small differences for the same HI due to the effects of focus position, power, and welding speed. Since the HI is a linear relationship between the power and speed.

$$HI = 60 * \frac{P}{v} \quad (3.1)$$

The results of a graph like the one in Figure 3.8a can be very useful for two purposes. First, for a certain focus diameter and a certain focus position knowing the minimum value of the HI to achieve complete penetration, for a given speed allows determining the necessary power, or vice versa. And second, it is possible to draw a line that divides the speed power space, so as to differentiate the combinations of speed-power values that cause a complete penetration of those combinations which produce partial penetration.

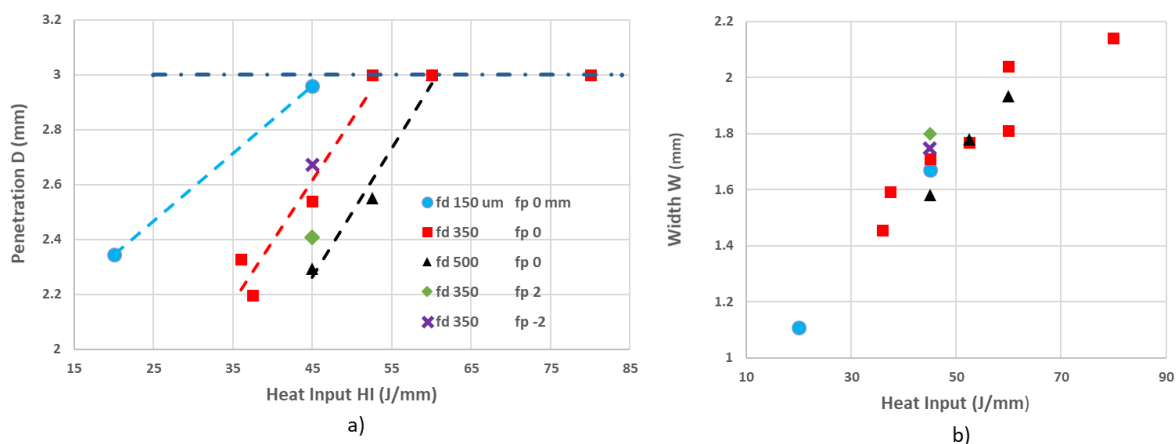


Figure 3.8 Penetration depth D (a), and width W (b), in function of heat input (HI).

3.3.3. Weld bead optimization

Considering the sample section # 14, which presents low porosity and where excess weld metal is greater than the underfill, the geometry of the section was optimized keeping constant the parameters: 2 kW, 350 μm , -2 mm, and C3 condition, while the welding speed varies in three values: 1.50, 1.60, and 1.65 m/min. The results correspond to samples number 18, 19, and 20, as shown in Figure 3.9.

According to the results, there is a slight improvement in the cross-section geometry, the excess weld decreases and there is no porosity due to increase of the welding speed. Sample #19 shows a better section because there is no tendency to undercut, unlike the other two samples. However, it is necessary to perform a better examination of this last aspect along the welding axis.




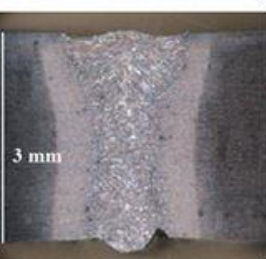


Sample number	18	19	20
Parameters: P, v, fd, fp (kW, m/min, μm , mm)	2.00, 1.50, 350, -2	2.00, 1.60, 350, -2	2.00, 1.65, 350, -2
Top weld seam			
Weld bead section			
Porosity: #, size (mm)	0, 0.00	0, 0.00	0, 0.00
Underfill: top, bottom (mm)	- 0.08, - 0.09	- 0.07, - 0.09	- 0.07, - 0.10
Excess weld: top, bottom (mm)	0.03, 0.17	0.03, 0.16	0.00, 0.17
Misalignment (mm)	x	x	x
Other	x	x	x

Figure 3.9 Appearance, section geometry, and defects of weld beads for samples 18, 19, and 20.

3.3.4. Macrostructure and microstructure

A typical macrostructure of the samples is presented in Figure 3.10a. The FZ and HAZ are clearly differentiated. Large columnar grains grown in the cooling direction are observed in the FZ. In the HAZ, two subzones are distinguished, one of fine grain (FG) and another of coarse grain (CG). The changes that the BM microstructure underwent in the FZ and HAZ are illustrated in the SEM micrographs of Figure 3.10b, c, and d: a softened bainitic–ferritic microstructure in the HAZ (FG) and the presence of bainite and martensite in different proportions and morphology in the HAZ (CG) and in the FZ.

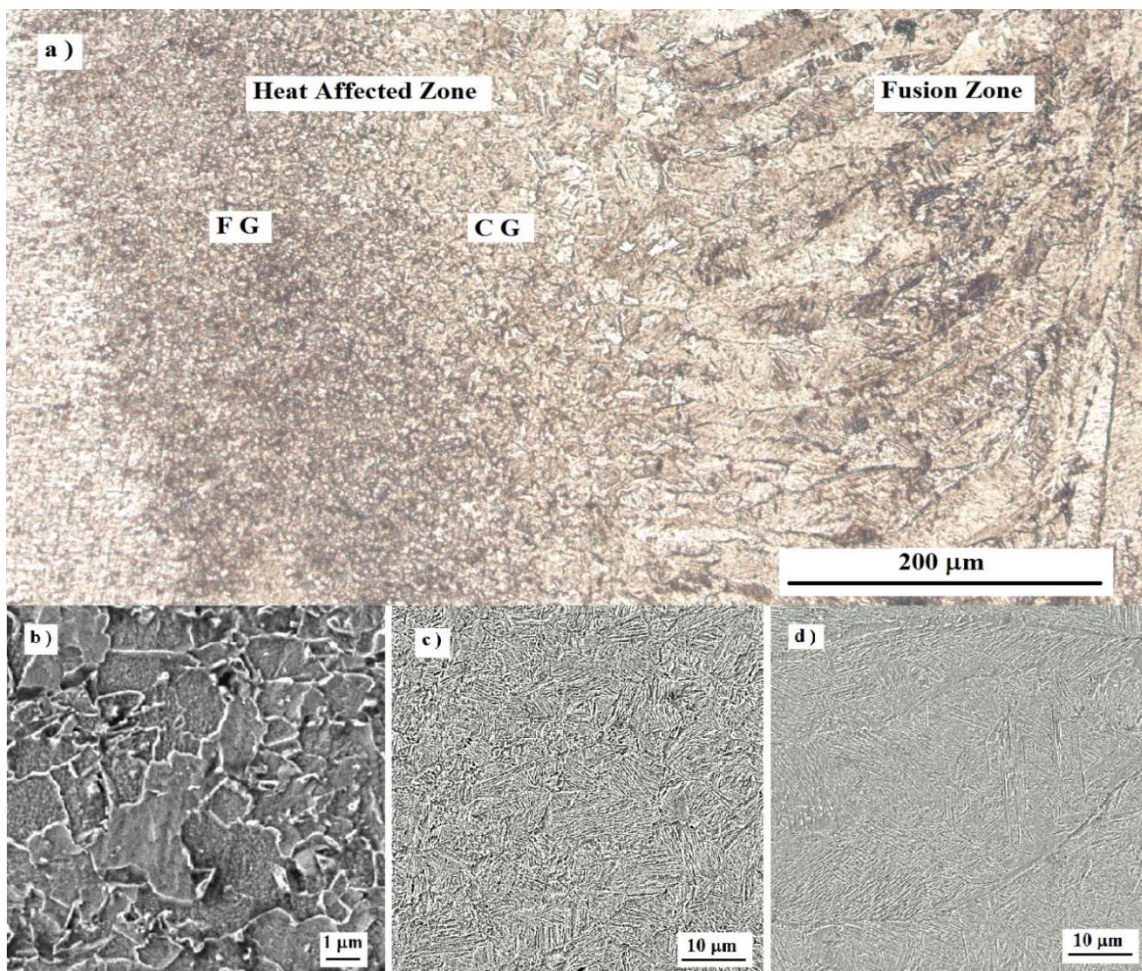


Figure 3.10 Macrostructure and microstructure of the welded sample # 4: (a) optical microscopy and SEM micrographs of: (b) FG-HAZ, (c) CG-HAZ, and (d) FZ.

Figure 3.11 shows characteristic microstructures found in the FZ of the samples. A progressive change in the microstructure was observed, from one composed mainly of a

mixture of bainite and martensite (sample #11, 20 J/mm) to the one in which appreciable amounts of bainite appear (sample #14, 80 J/mm). This illustrates the evolution that can occur in the microstructure due to the HI.

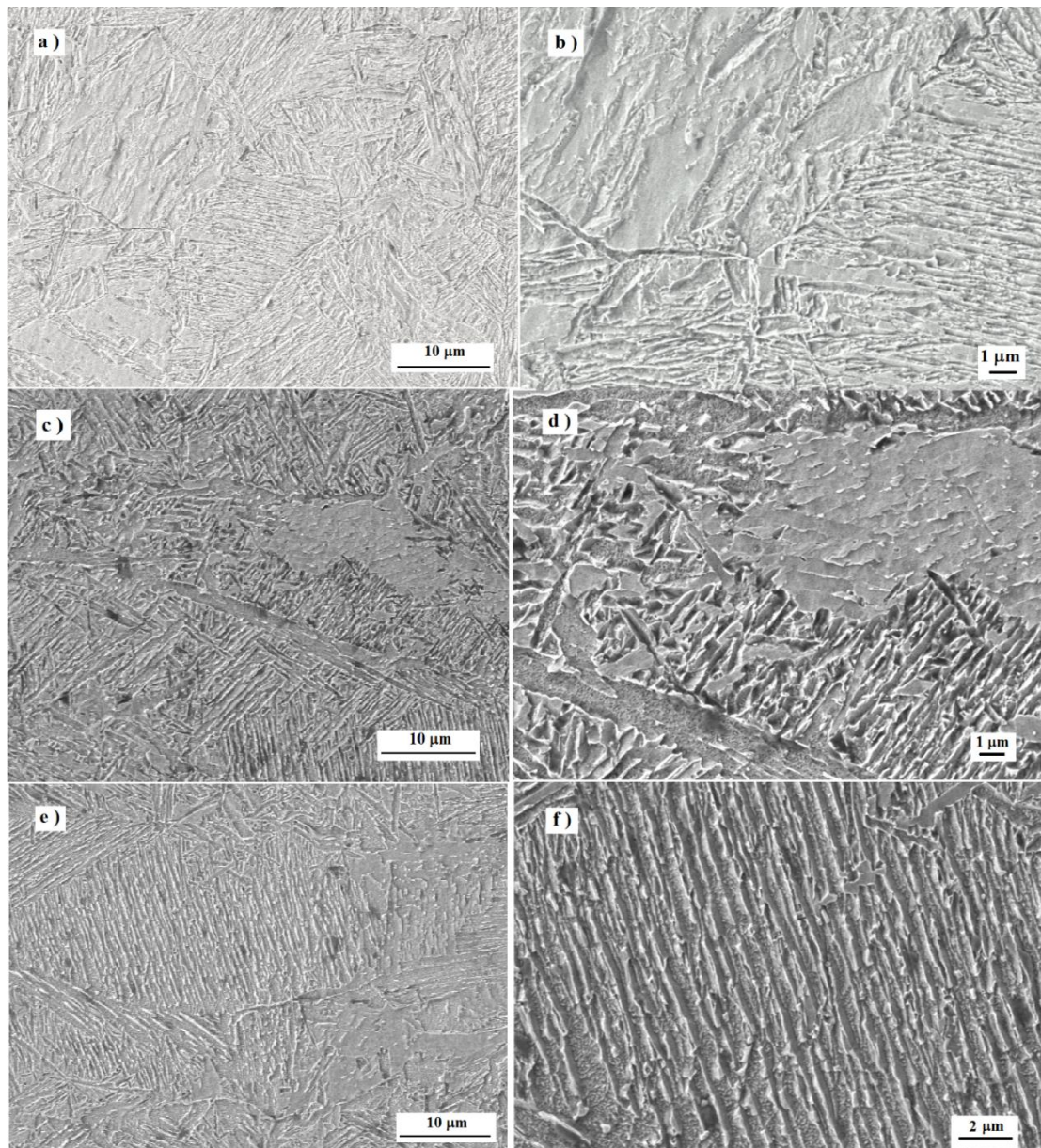


Figure 3.11 SEM micrographs of the FZ showing microstructures for the samples: # 11 (a)–(b); #12 (c)–(d); and # 14 (e)–(f).

The aforementioned transition is consistent with the work of Górká [32] regarding the assessment of weldability of a 10-mm-thick S700MC steel welded with different welding processes and HI. In that work, a continuous cooling temperature (CCT)

diagram was determined under welding conditions and, simulations tests of cooling times $t_{8/5}$ showed that the microstructure can result in: martensite for short times (<3 s), mixture of bainite and martensite for 3–10 s, bainite for 10–14 s, and a mixture of bainite and ferrite for large times (60–200 s). Photomicrographs of the present work are similar to those presented in the work of Górká, so that the microstructure of sample #14 looks like the one that cooled at $t_{8/5}$ of 12.96 s, while sample # 11 looks like the one that cooled at $t_{8/5}$ of 3.40 s. The microstructure present in the HAZ and FZ of the welded samples can be determined more accurately by combining several techniques. Thus, in Bayock et al. [31], it was reported that the use of scanning electron microscopy (SEM) and image processing detected small amounts of retained austenite together with the main microstructural components in a S700MC steel, or in Rodriguez et al. [35], for an HSLA steel, the use of SEM and electron backscattered diffraction allowed to identify microconstituents that were not possible with optical microscopy.

3.3.5. Microhardness

Figure 3.12 presents the microhardness Vickers' profiles (HV, 0.5 kg, 10 s) for several samples. There is a progressive variation of the hardness and size of the FZ and HAZ when the HI varies from 20 to 80 J/mm. In the FZ, the hardness increases for all samples except for the sample with a HI of 80 J/mm. Conversely, in the HAZ, all the samples suffer softening with the exception of the sample with a HI of 20 J/mm where hardness is slightly increased. The ranges of microhardness variation in the FZ and HAZ are approximately +100 and -35, respectively. It is also possible to observe that the hardness is similar for the same HI value even though the power and welding speed were different, as were the case of samples #4 and #2. Figure 3.12 shows two samples (# 1 and # 18) with lower hardness in the BM in comparison with the other samples. This may be due to an excessive softening caused by the cut when the pieces and tensile specimens were removed from the samples. The sizes of the HAZ and FZ (W), which can be estimated in Figure 3.12, are smaller than the results shown in Table 3.5 since the microhardness measurements were taken below the top surface.

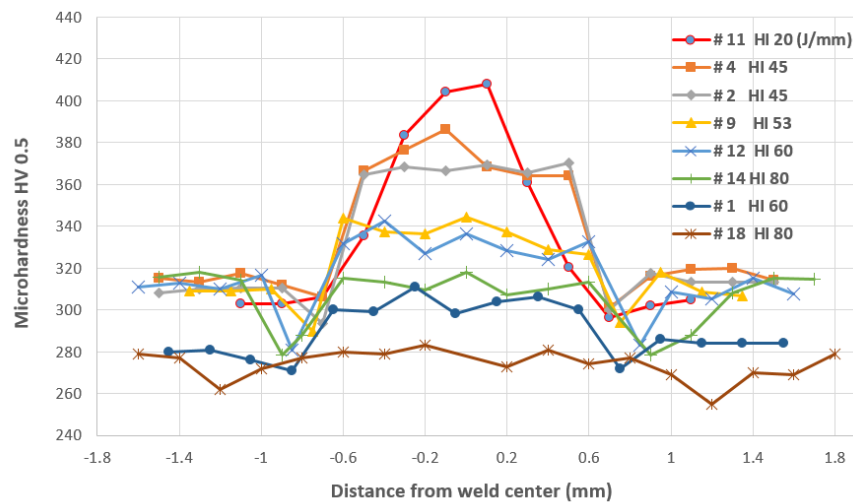


Figure 3.12 Microhardness of several samples.

3.3.6. Mechanical properties and fracture analysis

Table 3.6 shows the tensile mechanical properties of several samples that had complete penetration, including the HI, the BM microhardness close to the weld bead, the HAZ softening, and the width W , for analysis purposes. Also, it includes the samples (# 18 and # 1) that presented low microhardness in the BM. Stress–strain curves representative of BM and welded samples specimens are shown in Figure 3.13.

Considering Table 3.6, the tensile strength of the all samples is in general very close to that of the BM but in particular for those that have high hardness. Even in the case of sample #9, it exceeds the tensile strength of the BM. In terms of the yield strength and elongation percentage, all samples present lower values than the BM and the values are not as close as in the case of tensile strength, except for sample # 1 whose elongation percentage is greater than the BM. All specimens failed in the BM with the exception of one of the two specimens of samples #14 and #18 that failed in the weld. The behaviour described above is similar, in general, with the one reported in the work [14] where the effect of the fiber laser welding on the tensile strength and ductility for a Strenx[®] S700MC steel of 2mm thick was analyzed.

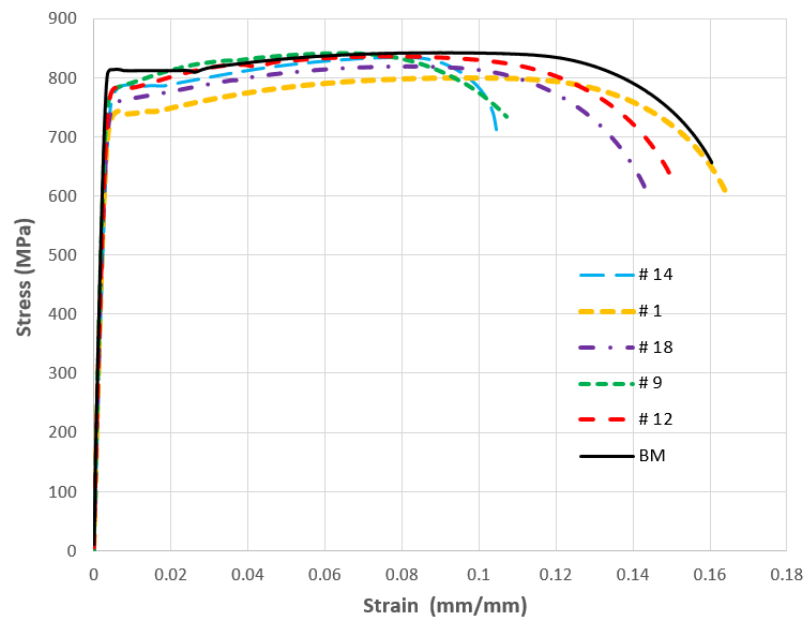


Figure 3.13 Stress–strain curves of several samples and base metal (BM).

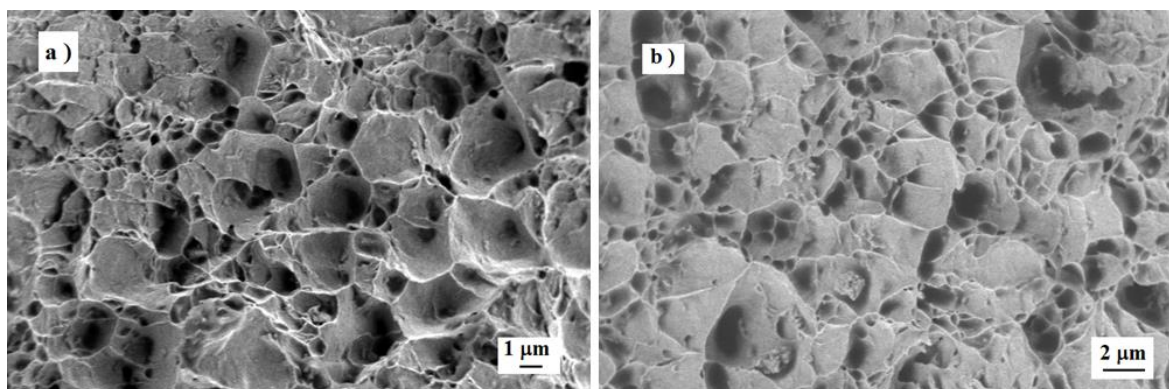
In Table 3.6, two behaviors can be highlighted: sample #12 that presented both good tensile strength and ductility; and, the specimens that failed in the weld (samples #14 and #18). In the first case, the behaviour may be due to a balance between the HI and the medium hardness reached in the FZ. In the second case, the failure in the welds may be explained by HAZ softening, the low hardness in the FZ that barely equals the BM, and the presence of defects that can increase the applied loads. For both samples, the HI was 80 J/mm.

According to the previously reviewed literature about the factors that allow obtaining in welded joints a tensile strength and ductility close to or equal to the BM, in the present work, the HI is more determining than the weld bead geometry or defects. The results are consistent with the aforementioned, especially for the first three samples, because the tensile strength decreases as the HAZ softens and the width W increases when HI increases.

Table 3.6 Mechanical properties, microhardness, width, and heat input of samples.

Sample #	Yield Strength (MPa)	Tensile Strength (MPa)	Elongation %	Site of failure	Microhardness (HV 0.5)		W (mm)	Heat Input (J/mm)
					BM	Softening HAZ		
BM	807.63	838.26	15.04	-	-	-	-	-
9	778.42	841.15	12.20	BM, BM	307	-16	1.77	52.50
12	784.07	831.99	14.50	BM, BM	311	-29	1.81	60.00
14	776.58	830.93	10.19	BM, weld	313	-34	2.34	80.00
18	763.42	824.70	12.40	BM, weld	279	-20	2.60	80.00
13	766.49	820.06	9.59	BM, BM	294	-6	1.94	60.00
19	740.51	799.28	15.87	BM, BM	291	-22	2.35	75.00
1	737.99	798.88	17.18	BM, BM	279	-7	2.04	60.00

The appearance of the fracture surface of the two samples that failed in the BM is shown in Figure 3.14. In both samples, a mixture of ductile and brittle fracture composed by areas of dimples and areas of tear planes is observed.

**Figure 3.14** Fracture surface of the tensile specimens: (a) sample # 9 and (b) sample #12.

3.4. Conclusions

- The effect of power, welding speed, focus position, focus diameter, surface-edge condition, and HI on the section geometry, defects, microstructure, hardness, and tensile strength of laser welded butt joints for a 3-mm-thick Strenx[®] 700MCE steel has been studied using a strategy of one-factor-at-a-time and additional runs with a disk laser equipment at power limit of 2 kW. Welding speed, power, and focus diameter have a similar and strong effect on the penetration, while in the width of the HAZ and FZ only the welding speed has a considerable effect. The relatively lower effect of focus position is due to the low BPP of the laser equipment that indicates a deep focal length. However, in thin sheets, this effect is not negligible. Negative values of focus position increase the penetration. The surface-edge condition also has a considerable effect in the weld bead geometry and appearance of the weld seam.

- The presence of porosity in the weld bead can be minimized due to a good combination of welding parameters, which causes a wide and regular appearance in the top weld seam. Starting from a weld bead that has underfill and excess weld metal in the top and bottom weld seam, respectively, the section can be optimized by slightly increasing the welding speed.

- To achieve complete penetration, each focus diameter has a well-defined HI threshold value. In the surface-edge condition C1, the values 47, 53, and 60 J/mm were found for the focus diameters 150, 350, and 500 μm , respectively. The typical macrostructure for the steel used consisted of FG and CG in the HAZ and large columnar grains in the FZ. The bainitic–ferritic microstructure of the BM changes to softened bainitic–ferritic in the fine-grained area of the HAZ and to mixtures of bainite and martensite in the coarse-grained area of HAZ and in the FZ. The mixture depends on the HI. In the FZ and HAZ, there is a progressive variation of the hardness when the HI varies from 80 to 20 J/mm. In the FZ, the hardness increases for all HI except for 80 J/mm, while in the HAZ there is softening for all HI, with the exception for 20 J/mm that slightly increases hardness. The mechanical properties obtained by the tensile test for the laser butt welds show values similar to the BM in relation to tensile strength and are somewhat lower in terms of ductility. It was verified that the factors that would allow similar mechanical properties between the BM and the

welded joints are low softening of the HAZ, high hardness in FZ, and small width of HAZ and FZ. For the above, an adequate selection of laser welding parameters and HI is important.

3.5. References

- [1] World Auto Steel. Advanced High-Strength Steels Application Guidelines Version 6.0, <https://www.worldautosteel.org/ahss-application-guidelines-update-begins/> (2017, accessed 1 February 2019).
- [2] Guo W. Laser Welding of High Strength Steels. PhD Thesis, University of Manchester, UK, 2015.
- [3] Mazur M and Ulewicz R. Analysis of strength and fatigue properties of construction materials for manufacturing the parts of semi-trailers. *Appl Eng Lett* 2017; 2: 32-37.
- [4] Hong Y and Shin Y. Prospects of laser welding technology in the automotive industry: A review. *J Mater Process Technol* 2017; 245: 46-69.
- [5] Oliveira J, Miranda R, Schell N, et al. High strain and long duration cycling behavior of laser welded NiTi sheets. *Int J Fatigue* 2015; 83: 195-200.
- [6] Jayanthi A, Venkataramanan K and Kumar K. Laser Beams A Novel Tool for Welding: A Review. *IOSR-JAP* 2016; 8(6-III): 8-26.
- [7] Ai Y, Jiang P, Shao X, et al. An optimization method for defects reduction in fiber laser keyhole welding. *Appl Phys A-Mater* 2016; 122(31): 1-14.
- [8] Quintino L, Costa A, Miranda R, et al. Welding with high power fiber lasers – A preliminary study. *Mater Des* 2007; 28: 1231–1237.
- [9] Sharma R and Molian P. Weldability of advanced high strength steels using an Yb:YAG disk laser. *J Mater Process Technol* 2011; 211: 1888-1897.
- [10] Sreenivasan N, Xia M, Lawson S, et al. Effect of Laser Welding on Formability of DP980 steel. *J Eng Mater Technol* 2008; 130(4): 1-9.
- [11] Kawahito Y, Mizutami M and Katayama S. Elucidation of high-power fibre laser welding phenomena of stainless steel and effect of factors on weld geometry. *J Phys D: Appl Phys* 2017; 40: 5854-5859.
- [12] Pástor M, Zhao H and DebRoy T. Pore formation during C.W. Nd: YAG laser welding of aluminum alloys for automotive applications. *Rev Metal* 2000; 36: 108-117.
- [13] Zhang M, Tang K, Zhang J, et al. Effects of processing parameters on underfill defects in deep penetration laser welding of thick plates. *Int J Adv Manuf Technol* 2018; 96: 491-501.
- [14] Prochenka P, Makowska K and Janiszewski J. Assessment of Mechanical Properties of Laser Beam Welded Joints Made of Steel Strenx S700MC Subjected to High Impact Load. *Biul Inst Spawal* 2018; 2: 251-260.
- [15] Němeček S, Mužík M and Míšek T. Differences between laser and arc welding of HSS steels. *Physics Procedia* 2012; 39: 67-74.
- [16] Górka J and Ozgowicz A. Structure and Properties of Laser-Beam-Welded Joints of Low-Alloy High-Strength Steel DOCOL 1200M with a Martensitic Structure. *Mater Technol* 2018; 52: 189-193.
- [17] Parkes D, Xu W, Westerbaan D, et al. Microstructure and fatigue properties of fiber laser welded dissimilar joints between high strength low alloy and dual-phase steels. *Mater Des* 2013; 51: 665-675.
- [18] Sokolov M and Salminen A. The effect of joint edge surface preparation on the efficiency of fiber laser welding of low-alloyed steels. *Mechanika* 2015; 21: 220-225.
- [19] Maina M, Okamoto Y, Inoue R, et al. Influence of Surface State in Micro-Welding of Copper by Nd: YAG Laser. *Appl Sci* 2018; 8: 1-13.
- [20] Lampa C. Laser Welding; Energy Redistribution and Weld Geometry. PhD Thesis, Luleå University of Technology, Sweden, 1997.
- [21] Ion J. Laser Processing of Engineering Materials: principles, procedure and industrial application. 1st ed. Oxford: Elsevier Butterworth-Heinemann, 2005, p. 419.
- [22] Zhao H, White D and DebRoy T. Current issues and problems in laser welding of automotive aluminium alloys. *Int Mater Rev* 1999; 44: 238-266.
- [23] Matsunaga A. Problems and solutions in deep penetration laser welding. *Sci Technol Weld Joining* 2001; 6: 351-354.

- [24] Matsumoto N, Kawahito Y, Nishimoto K, et al. Effects of laser focusing properties on weldability in high-power fiber laser welding of thick high-strength steel plate. *J Laser Appl* 2016; 29(1): 1-8.
- [25] Kumar S, Kundu A, Venkata K, et al. Residual stresses in laser welded ASTM A387 Grade 91 steel plates. *Mater Sci Eng A* 2013; 575: 160-168.
- [26] Farabi N, Chen D and Zhou Y. Fatigue properties of laser welded dual-phase steel joints. *Procedia Eng* 2010; 2:835–843.
- [27] Tuz L. Evaluation of microstructure and selected mechanical properties of laser beam welded S690QL high-strength steel. *Adv Mater Sci* 2018; 18: 34-42.
- [28] Guo W, Francis J, Li L, et al. Residual stress distributions in laser and gas-metal-arc welded high strength steel plates. *Mater Des* 2016; 32: 1449-1461.
- [29] Guo W, Crowther D, Francis J, et al. Microstructure and mechanical properties of autogenous laser welded S960 high strength steel. *Mater Des* 2015; 85: 534–548.
- [30] SSAB. Strenx® 700 MC, <https://www.ssab.com/products/brands/strenx/products/strenx-700-mc> (2008, accessed 1 February 2019).
- [31] Bayock F, Kah P, Mvola B, et al. Effect of Heat Input and Undermatched Filler Wire on the Microstructure and Mechanical Properties of Dissimilar S700MC/S960QC High-Strength Steels. *Metals* 2019; 9(883): 1-20.
- [32] Górká J. Assessment of Steel Subjected to the Thermomechanical Control Process with Respect to Weldability. *Metals (Basel, Switz.)* 2018; 8(169): 1-17.
- [33] Chang B, Allen C, Blackburn J, et al. Thermal and fluid flow characteristics and their relationships with porosity in laser welding of AA5083. *Physics Procedia* 2013; 41: 478-487.
- [34] Katayama S. Defect formation mechanisms and preventive procedures in laser welding. In: Katayama S (ed). *Handbook of laser welding technologies*. Cambridge: Woodhead Publishing Limited, 2013, pp. 332-373.
- [35] Rodriguez T, Duarte V, Avila J, et al. Wire and arc additive manufacturing of HSLA steel: Effect of thermal cycles on microstructure and mechanical properties. *Addit Manuf* 2019; 27: 440-450.

Chapter 4: Imperfections and Modelling of the Weld Bead Profile of Laser Butt Joints in HSLA Steel Thin Plate

Patricio G. Riofrío^{a*}, José A. M. Ferreira^b and Carlos A. Capela^c

^aDepartamento de Ciencias de la Energía y Mecánica, Universidad de las Fuerzas Armadas-ESPE, Av. General Rumiñahui S/N, 171103 Sangolquí, Ecuador

^bUniversity of Coimbra, Centre for Mechanical Engineering, Materials and Processes (CEMMPRE), Department of Mechanical Engineering, P-3004 516 Coimbra, Portugal.

^cPolytechnic Institute of Leiria, School Tech and Management, Department of Mechanical Engineering, Morro do Lena - Alto Vieiro, 2400-901 Leiria, Portugal

Published in **Metals**.11 (151) (2021), 1–19 [doi: 10.3390/met11010151](https://doi.org/10.3390/met11010151).

Abstract

In many applications that use high strength steels, structural integrity depends greatly on weld quality. Imperfections and the weld bead geometry are influencing factors on mechanical properties of the welded joints but, especially in the fatigue strength, they cause a great decrease. The proper knowledge of these two factors is important from the nominal stress approach to the fracture mechanics approaches. Studies concerning the profile and imperfections of the weld bead in laser welding for thin plates of high strength steels are scarce. In this work, these two aspects are covered for five series single and double-welded joints, butt joints in a 3 mm thick HSLA steel, welded in a small range of welding parameters. The actual profiles captured with profilometer were modeled with proposed geometric parameters achieving an adequate fit with values of the coefficient of determination R^2 greater than 0.900. Description of imperfections includes the distributions of porosity and undercuts. The evaluation of the weld quality, taking as guide the ISO 13919-1 standard determined B and D levels for the welded series while based on the stress-concentrating effect, showed a greater detriment in those series with undercuts and excessive penetration. The analysis of variance validated the results of the different combinations of laser welding

parameters and showed, for the factorial experimental design, a more significant effect of the welding speed.

Keywords: welding imperfections; modelling profile; laser butt joints; thin HSLA steel; heat input

4.1. Introduction

Despite the promising advantages for many applications, laser welding of high strength and low alloy (HSLA) steels still does not overcome the deterioration suffered in the mechanical properties of the base material, there being an appreciable reduction especially in fatigue strength. In two works [1, 2], where the fatigue strength of welded joints formed with steels of high and low tensile strength is compared, it is found that at high-stress levels the difference is small, when the stress level decreases the difference is reduced and the welded joints can have a similar fatigue limit. One of the principal factors for behaviors like the above may be the weld quality, so that the high strength of the steels cannot be exploited due to the weld quality as showed in [3] and [4]. The weld quality is associated mainly with the imperfections of the weld bead. However, the heat input (HI) from the welding process also produces changes in the microstructure and residual stresses that may influence fatigue strength. If the objective is to understand the reduction of the fatigue strength in welded joints it is important to have complete knowledge of the imperfections and weld profile, as well as the type of joint, the materials, the welding process and a detailed analysis of the site, start and path of the fatigue failure; otherwise, partial or biased conclusions could be drawn.

Imperfections such as undercuts, excess weld metal, excessive penetration, underfill, porosity and misalignment occur frequently in laser welding and may affect the fatigue strength of welded joints. The notch effect exerted by the undercuts and excess weld at weld toe is well known. In studies, more parameters of these two imperfections are being incorporated into the relationships that evaluate their effect, although there is disagreement regarding which parameters are the most influential. Mashiri et al. reported a greater effect of the depth over the width and the radius of the undercuts, the influence of the fillet weld

profile on the undercut depth and a relatively major loss of fatigue crack propagation life for thin plate than for thick plate [5]. In Cerit et al. [6], the stress concentration factor (SCF) for undercuts and weld toe reinforcement for butt joints were determined by means of finite element method (FEM), six parameters were used (three for each one) and it was established that the highest stresses were produced from the combination of a high ratio of depth to radius with a low reinforcement angle. Lillimäe et al. evaluated the correlation between two analytical expressions for the SCF and experimental results of fatigue strength, they found a better fit for the five-parameter formula than the three-parameter expression and also reported that the results agreed better with the mean values of weld height and flank angle than with the mean values of transition radius and the undercut depth [4]. In Liinalampi et al., the length of the undercuts has been incorporated to evaluate the effective stresses due to this factor and the results showed that the effective notch stress is overestimated in the 2D analysis if the notch is short and deep [7]. Finally, in simulations based on the fracture mechanics approach, Schork et al. [8] showed that the notch (or undercut) depth is the most influential parameter, whether considered individually or in conjunction with other parameters of the weld toe.

When reviewing the literature regarding the effect of porosity on the fatigue behaviour in joints of steels and aluminum alloys, it is found that pores can decrease the load-bearing area and exert a stress-concentrating effect that reduces the fatigue strength. In [9], was reported for lap joints with pores, that these imperfections did not initiate fatigue and the fatigue strength was proportional to the actual area of the welds, while for butt joints, which were removed the excess weld and other imperfections, pores can initiate fatigue, in large pores [10, 11], in small pores near to the surface [12, 13], as also in small or big internal pores [14]. According to what is proposed in Wang et al. [15], fatigue life is more affected by the size than by the pore's position. Biswal et al. [16], for titanium alloys, showed that sub-surface pores have high SCF while for isolated inner pores, the increase in SCF is small. In the literature, other imperfections are also reported as affecting the fatigue strength: linear [17] and angular [18] misalignment, especially in slender elements and thin plates increasing the local stresses; weld ripples as sites where the fatigue can initiate when the weld toe radius is large enough [19], while in [20], the period of toe waves and the local toe geometry were designated as features that strongly influenced the fatigue crack initiation and propagation lives. However, the weld ripples are not usually part of the weld quality standards and have

not been explicitly characterized by any parameter to evaluate the effect on fatigue strength, although their effect was indirectly taken into account in the study [21]. From the above revision, it is observed that the size, shape, localization, combinations and interactions between imperfections are influential and should be considered for proper analysis. For the measurement and capture of imperfections and weld profile along the weld axis various techniques and procedures with variable complexity and resolutions from 1 to 100 μm are found: mechanical profilometer [3], rubber replicas [22], non-destructive replica and design software [23], laser scanner and optical 3D scans [21] and laser scanner and optical system with cameras [4].

On the other hand, avoiding imperfections in laser welding in keyhole mode via the proper setting of welding parameters has shown limitations due to the sensitivity of the welding process and even more under certain restrictions, this purpose can require a large number of trials and consumption of time. Particularly for medium and high ranges of welding parameters, e.g., for power and welding speeds from 3 to 15 kW and m/min, there are studies that show zones where there are no imperfections [24], or maps where the effect on a certain imperfection is analyzed [25]. Other studies with optimization methodologies find specific combinations of welding parameters that optimize the weld bead under an established criterion [26, 27]. However, there are few studies that validate the solutions optimized within a range of parameters [28], that evaluate imperfections along the weld axis or that cover ranges of small values of the welding parameters (e.g., <3 kW and m/min). Particularly in works where notch stress and fracture mechanics approaches are applied for the assessment of the fatigue strength of welded joints [18, 21, 23, 29], aspects such as knowledge of the variation of the weld bead profile along the weld axis, the statistical distribution of imperfections and the use of more realistic geometries and microstructures are highlighted in order to achieve a scientific approach and effective response to the concept “fitness for purpose”; therefore, it is necessary to carry out studies that cover those aspects.

This work was developed in view of overcoming the deficiencies observed in the previous review, and therefore reports in detail the weld profile and the imperfections for five series of laser butt joints welded in thin plates under a small range of welding parameters. The weld profile and various imperfections were captured by a profilometer showing that for small weld beads it is very useful and may be more advantageous compared

to other methods and equipment. For all of the welded series, a simple graphic model consisting of arcs of circles and straight lines is proposed in order to model the profile of the weld beads. The distributions of porosity and undercuts are reported. The quality of the welded series was evaluated, taking as a guide the ISO 13919-1 standard [30]. Additionally, to assess the effect of the weld profile and the undercuts on fatigue strength, their corresponding stress concentrating factors were determined. The analysis of variance (ANOVA) was performed for validation of results and evaluation of the effect of the welding parameters and HI on the weld bead geometry.

4.2. Materials and Methods

4.2.1. Material and Laser Welding

Butt joints of 3 mm thickness were manufactured with the high strength low alloy steel Strenx[®] 700MCE. This metal is hot-rolled steel under the requirements of S700MC in EN 10149-2 [31], with the chemical composition Table 4.1, tensile mechanical properties Table 4.2 and microstructure fine-grained mainly composed by ferrite and bainite as reported in [32].

Table 4.1 Chemical composition of the base metal.

C	Mn	Si	P	S	Cr	V	Nb	Ni	Cu	Al	Mo	Ti	Co	Fe
0.07	1.69	0.01	0.012	0.006	0.03	0.02	0.046	0.04	0.011	0.044	0.016	0.117	0.016	balance

Table 4.2 Tensile mechanical properties of the base metal.

Yield Strength (MPa)	Tensile Strength (MPa)	Elongation %
807.63	838.26	15.04

According to the results of the previous work on the same type of joints [32], low heat inputs (less than 80 J/mm) produced small sizes and less softening of the heat-affected zone (HAZ) and tensile mechanical properties similar to the base metal, although there were some imperfections in the weld beads. Therefore, for the present study, the welding parameters shown in Table 4.3 were chosen, on the one hand, to form a factorial

design in a narrow range of welding speed and power for single-welded joints that allow partial and complete penetration with HI less than 80 J/mm, and on the other hand, to achieve complete penetration with double-welded joints of low HI (each weld pass less than to 60 J/mm) without increasing the size and softening of the HAZ, although it could increase the level of porosity. Thus, the first four series (S1, S2, S3 and S4) form a 2^2 factorial design, where the factors welding speed and power varied on two levels Table 4.3, and for the fifth series (S5) welded from both sides, on the top side, the welding speed was varied within the range of 2.0 to 1.75 m/min with the constant power (1.75 kW) and, on the bottom side, the welding parameters were constant Table 4.3. For all series, the welding parameters-focus diameter, focus position and the beam inclination-were constant in the values: 350 μm , -2 mm and 9 degrees respectively. A disk laser equipment Trumpf TruDisk 2000 with laser maximum output of 2000 W; beam wavelength, 1020 nm; beam parameter product, 2 mm-mrad; and fiber diameter 200 μm was used in continuous mode.

Table 4.3 Welding parameters used in the experimental work.

Series	Samples	Laser Power (kW)	Welding Speed (m/min)	Heat Input (J/mm)
S1	F1, F2, F6, F10, F20, F22	2.00	1.60	75.0
S2	F5, F8, F16, F17, F19	1.75	1.60	65.6
S3	F4, F7, F12, F13, F18	2.00	2.00	60.0
S4	F21, F23	1.75	2.00	52.5
Top Side Weld Pass				
	F15	1.75	1.75	60.0
	F14	1.75	1.80	58.3
	F9	1.75	1.90	55.3
	F11	1.75	1.95	53.8
	F3	1.75	2.00	52.5
Bottom Side Weld Pass				
S5	F15, F14, F9, F11, F3	1.25	2.50	30.0

The butt joints were formed with two laser-cut 181 mm x 110 mm x 3 mm plates. To facilitate the operation and maintain the same welding clamping condition, fixing slots were machined in the plates and two small tack welds were welded at samples, ends Figure 4.1a. The surfaces close to the welds were prepared with sandpapers #80, #120 and #180

and the edges were rectified to achieve a uniform and practically null gap clearance between the plates. Before welding, the surfaces and edges were cleaned by acetone, the welding line aligned to the trajectory of the laser beam and the plates fastened in the slots by means of screws. Argon (99.996%) shielding gas was used at a flow rate of 20 L/min. The weld axis was arranged transversely to the rolling direction.

4.2.2. Measurement of Weld Bead Geometry and Imperfections

The measurement and capture of weld bead geometry and imperfections were performed with a microscope and profilometer on samples or pieces and test specimens that were extracted from the samples Figure 4.1a. The Mitutoyo Toolmaker's Microscope (Kawasaki, Japan) equipped with digital micro-meters was used for the measurements of the widths (near to the top side) of the heat-affected zones and for penetration depth on the macrographs of the pieces extracted from the samples. For S1 to S4 series, four macrographs were measured, each macrograph coming from different samples, except the S4 series for which two macrographs come from the same sample, while for the S5 series, two macrographs were measured for each sample. The features of the macrographs mentioned above and the designation of the typical imperfections that will be analyzed are presented in the scheme of Figure 4.1b.

The microscope was also used to measure porosity on a section cut along the weld axis, near to the center of the FZ, and successive polishing showed that the greatest amount of porosity occurred very close to the center of the FZ. For each series, the measured weld length was 54 mm (six pieces of 9 mm). Pores with sizes less than 0.05 mm were not considered due to the resolution of the equipment.

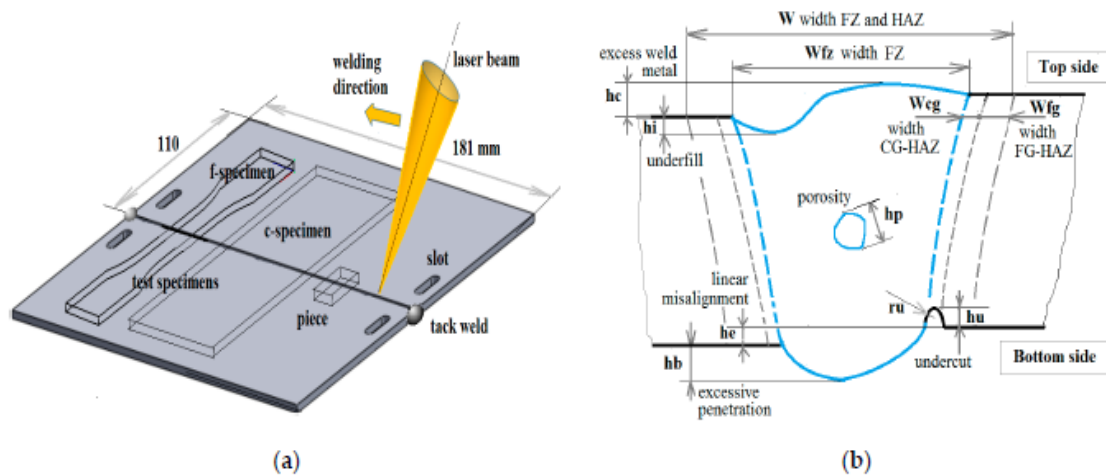


Figure 4.1 Schemes of: (a) the welded sample; (b) the weld bead with designations of typical imperfections and zones produced by welding.

The profile of each side (top and bottom) of the weld bead was captured through the Mitutoyo SURTEST SJ-5000 profilometer (Kawasaki, Japan) using a pitch of 1 μm . The data obtained by the profilometer were then inserted in an excel sheet to graphically represent the profile and to determine the geometrical parameters that define its shape and imperfections such as, excess weld metal, underfill, linear misalignment, excessive penetration and undercuts Figure 4.1b. Simple functions and relationships were used to establish parameters such as lengths, heights, angles and radii. Four profiles (in top and bottom sides) in each sample were captured for all of the series, however for series S1, S2 and S3, only four samples were used. Unlike the S4 series where the measurements were made on four sites distributed along the samples, for the other series, the measurements were made on the f-specimens. Therefore, for each one of the S1, S2 and S3 series, 16 measurements were made; for the S4 series, 8 measurements; and for the S5 series, 20 measurements.

Since no appreciable undercuts were observed at other sites, measurements for this imperfection were concentrated at the weld root of the S1, S2 and S3 series and were used four f-specimens and one c-specimen from different samples, completing 100 mm of examined length: 50 mm of the f-specimens and 50 mm of the c-specimen. To determine the size and distribution of the undercuts, the possible undercuts were first located under the microscope and with the help of light, once they were marked, they were verified and

measured with the profilometer, finally, the measurement of their length under the microscope was completed.

4.3. Results and discussion

4.3.1. Welding Bead Geometry

The weld bead geometry found for the welded series is illustrated in Figure 4.2 with profiles captured by the profilometer and with macrographs of the cross-section. As can be seen, in general, all series, weld bead profiles presented symmetry and are composed of rounded shapes, however, a more careful observation of Figure 4.2 and of the enlarged graphic representation that allows of the profilometer's data, showed that there are also straight parts. Small straight segments were observed especially in the weld face in the S3 series, as well in the bottom side (located in the middle part of the excessive penetration) in the S1, S2 and S3 series. It is also possible to observe, weld bead profiles with wide radii and smooth geometric transitions such as the top profiles of the S1, S4 and S5 series in contrast to more abrupt geometric transitions like the top profile of the S3 series or as the bottom profile of all series (without consider the S4 series).

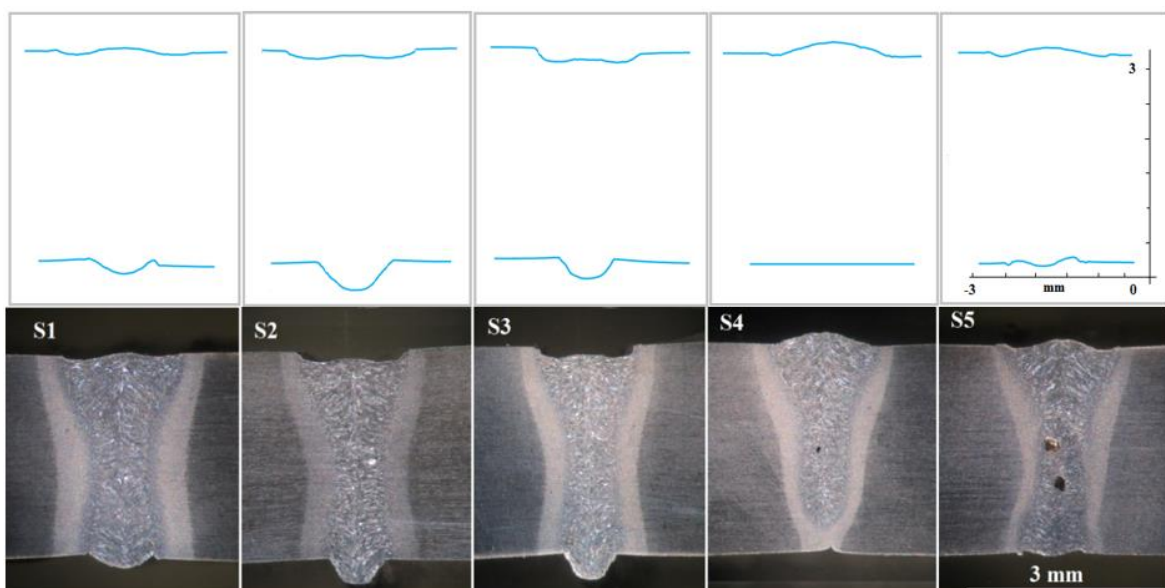


Figure 4.2 Appearance of the weld beads for welded series: profiles (above); macrographs (below).

Figure 4.3 proposes the geometric parameters that define two idealized profiles: t-profile and b-profile. Due to symmetry, only half of the profiles are shown. The combination of these two idealized profiles allows the modelling of any weld bead profile of the welded series. Therefore, the top and bottom profiles of the S1, S2 and S3 series can be reproduced by the idealized profiles t-profile and b-profile, respectively, for the S5 series contrary to the previous ones; and for the S4 series, only the top profile can be modeled with the b-profile.

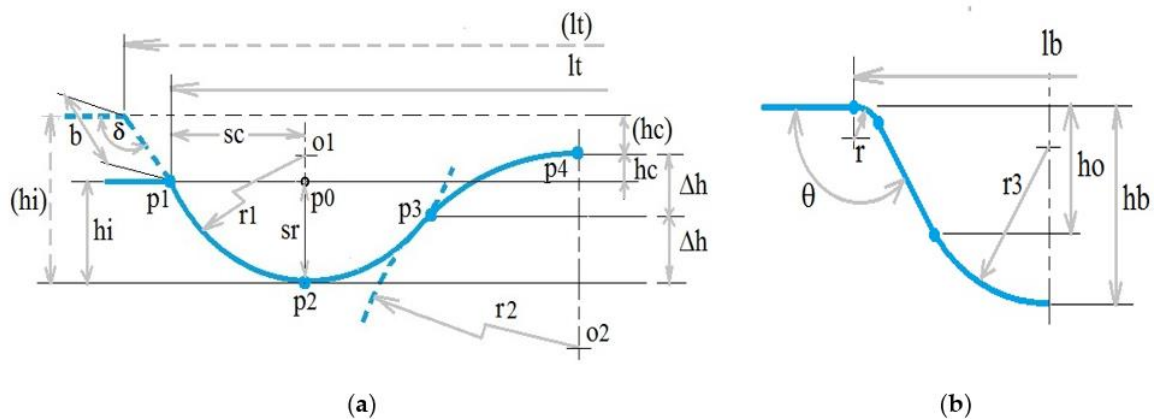


Figure 4.3 Sketch of the idealized profiles and their geometrical parameters: (a) t-profile; (b) b-profile.

The values for the geometric parameters proposed in Figure 4.3 which are shown in Table 4.4 were determined directly from the data and graphical representation of the profiles and through simple geometric functions, while the rest of the parameters (r_1 , r_2 , r_3 , h_o , Δh and sr) can be calculated as outlined in the profile modelling Section 3.2. As detailed in Section 2.2, various imperfections can also be evaluated from the results of Table 4.4. In this table, it should be noted that the hc values are positive for excess weld metal but due to the particular shape of the profiles they can also take negative values as in the case of underfill. In Table 4.4, the parameter he corresponding to the linear misalignment was also included.

Table 4.4 Geometrical parameters of the welded series.

Parameter		S1				S2				S3				S4				S5			
		Av ¹	SD ²	Max ³	Min ⁴	Av	SD	Max	Min	Av	SD	Max	Min	Av	SD	Max	Min	Av	SD	Max	Min
<i>hb</i>	(mm)	0.20	0.05	0.30	0.11	0.36	0.08	0.58	0.26	0.31	0.10	0.51	0.17	0.13	0.03	0.20	0.11	0.14	0.03	0.20	0.07
<i>lb</i>	(mm)	1.02	0.10	1.22	0.91	0.93	0.06	1.04	0.84	0.84	0.08	0.98	0.73	1.61	0.09	1.72	1.45	1.73	0.11	1.88	1.47
<i>r</i>	(mm)	0.16	0.07	0.32	0.06	0.06	0.04	0.14	0.02	0.07	0.05	0.21	0.01	0.54	0.26	0.85	0.17	0.54	0.38	1.50	0.25
θ	(°)	146	8	159	128	130	7	149	122	130	8	146	120	161	1	163	160	166	5	171	150
<i>he</i>	(mm)	0.03	0.02	0.08	0.00	0.06	0.05	0.12	0.00	0.05	0.03	0.10	0.01	0.05	0.02	0.07	0.01	0.05	0.03	0.09	0.00
<i>lt</i>	(mm)	1.86	0.06	1.97	1.76	1.65	0.06	1.76	1.55	1.51	0.08	1.68	1.36	-	-	-	-	1.02	0.10	1.23	0.87
<i>hc</i>	(mm)	0.02	0.05	0.09	-0.10	-0.05	0.03	0.00	-0.10	-0.08	0.07	-0.01	-0.26	-	-	-	-	0.00	0.04	0.06	-0.08
<i>hi</i>	(mm)	-0.08	0.03	-0.03	-0.15	-0.12	0.03	-0.07	-0.19	-0.15	0.06	-0.08	-0.32	-	-	-	-	-0.06	0.03	-0.01	-0.11
<i>sc</i>	(mm)	0.28	0.07	0.41	0.19	0.36	0.04	0.41	0.28	0.20	0.04	0.29	0.13	-	-	-	-	0.17	0.04	0.25	0.10
<i>b</i>	(mm)	-	-	-	-	-	-	-	-	0.15	0.04	0.22	0.09	-	-	-	-	-	-	-	-
δ	(°)	-	-	-	-	-	-	-	-	136	9	153	121	-	-	-	-	-	-	-	-

Some observations stand out in Table 4.4. The results show the variability of the profile features along the weld axis for all series which can be explained due to the sensibility of laser welding and the instability of keyhole mode as is well known [33]. Although the magnitudes are small (with the exception of the angular ones), clear differences and trends are observed between the welded series. For example, with respect to averages, the width *lt* decreases and the underfill *hi* increases for S1 to S3 series, however, there is closeness in some average values and overlap between the maximum and minimum values, especially between S2 and S3 series. It is also noteworthy that standard deviations, in general, are relatively small, and therefore it could be assumed that the weld beads of each series are characterized by their size and shape by the effect of the welding parameters, however, this issue will be analyzed in Section 3.5.

On the other hand, despite the variation of the welding speed used between its welded samples, the S5 series presented only in certain geometrical parameters (especially for the top profile) a slightly higher standard deviation than the other series, which justifies its grouping into a single series.

Table 4.5 shows the means of measurements in relation to the macrographs. The widths of the HAZ were measured near the top surface of the weld bead. The penetration depth of the S5 series corresponds to that achieved with two pass weld. The small difference between the values of the width of the FZ Table 4.5 and the values *lt* or *lb* (as appropriate in Table 4.4), indicate the reliability of the measurements made with the microscope and the

profilometer. Due to the S4 series, partial penetration joint, its details or discussion may be omitted in the following sections.

Table 4.5 Means of macrographs features

Series	Width of				Penetration Depth
	FZ ¹ and HAZ ¹	FZ	FZ – HAZ ³	CG – HAZ ⁴	
	(mm)	(mm)	(mm)	(mm)	(mm)
S1	2.47	1.82	0.22	0.09	3.00
S2	2.27	1.65	0.21	0.11	3.00
S3	2.11	1.55	0.21	0.10	3.00
S4	2.15	1.71	0.15	0.09	2.66
S5	2.23	1.71	0.19	0.08	3.00

¹ fusion zone (FZ); ² heat-affected zone (HAZ); ³ fine-grain heat-affected zone (FG-HAZ); ⁴ coarse- grain heat-affected zone (CG-HAZ).

4.3.2. Profile Modelling

The actual profile of the weld bead captured by the profilometer can be modeled through the combination of arcs of circles and straight lines as is proposed in Figure 4.3. For profiles that correspond to t-profile, the parameters $r1$, $r2$ and the location of their centers $o1$ and $o2$ are key elements for a good fit and were determined as described below. An arc of a circle is assumed to pass through points $p1$ and $p2$ so that the cut between the horizontal line that passes through $p1$ and the vertical line that passes through $p2$, define the semi-chord $p1p0$ (of length sc) and the segment-radius $p2p0$ (of length sr), allowing to determine both the radius $r1$ (through the geometric relationship between the semi-chord and the segment-radius) the center $o1$ of the circle. For the second circle that passes through $p4$ and $p3$, it is assumed that the inflection point $p3$ is located in the middle of the high between $p4$ and $p2$ (Δh) and therefore the radius $r2$ and the center $o2$ can be known in the same way as for the first arc of the circle. Specifically for the S3 series, the profile shown in segmented lines in the upper left of Figure 4.3 must be added to the profile formed by the two arcs of the circle and therefore the parameters b and δ should be used. The above procedure is appropriate given the range of the results, both for positive and negative values for hc being hi always negative. Even although the profiles that correspond to the lower part of the weld root surface can be modeled by the link between straight lines and arcs with tangential transitions, in this

work, to use the same modeling for profiles with both excess penetration and excess reinforcement, the arc corresponding to radius r_3 it will be graphed in a similar way to the arcs of the idealized t-profile, using as an approximation for all series a value of h_0 equal to $0.79 hb$. Figure 4.4 shows, for S1, S2, S3 and S5 series, examples with a real profile, its model and the average model (based on the mean parameters) according to the previous procedures.

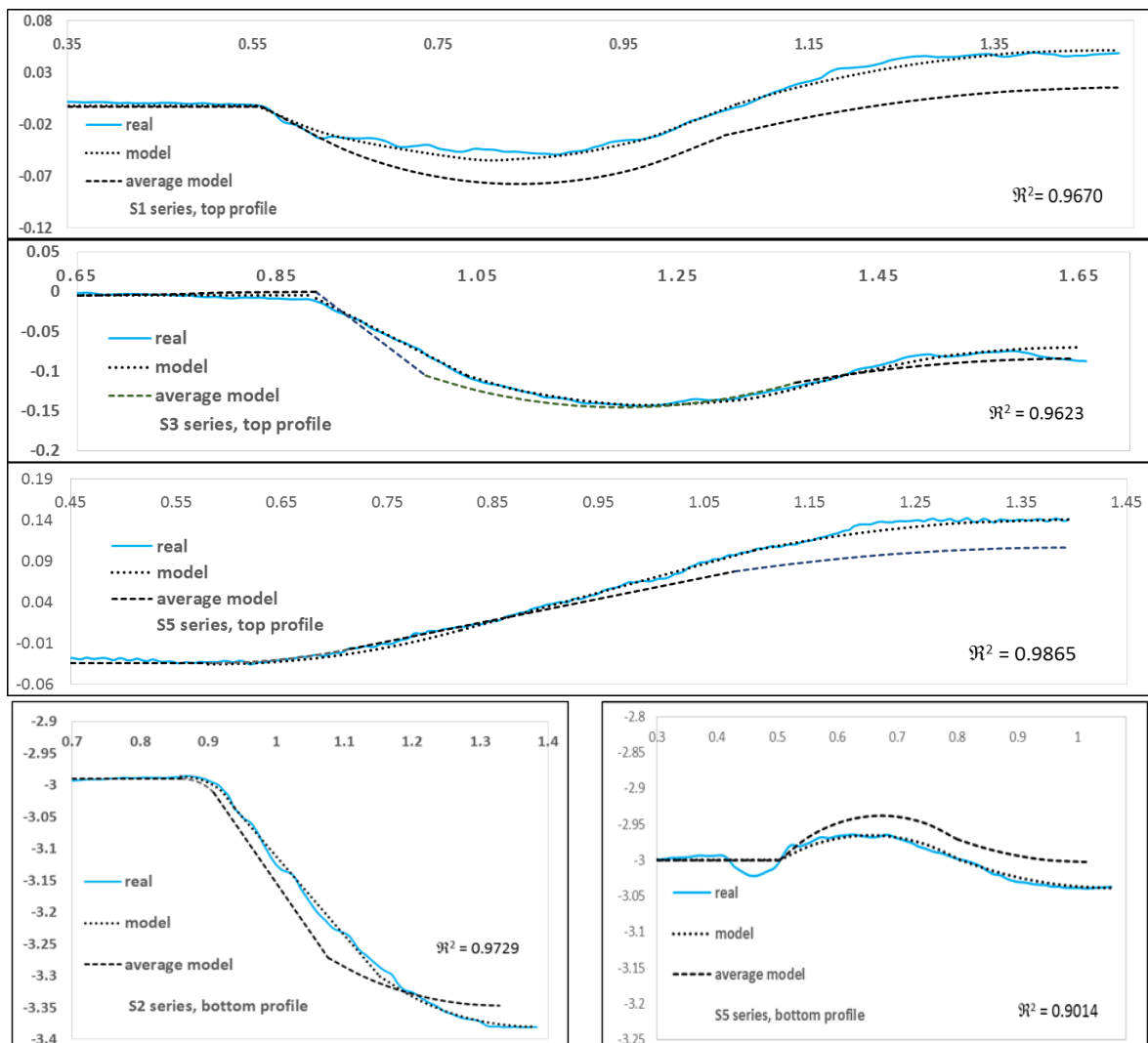


Figure 4.4 Examples of profiles: real, model and average model for S1, S2, S3 and S5 series (Y-axis and X-axis in mm).

Even though it is evident in Figure 4.4 that there is a good fit between the real profile and its model, for the five examples, the coefficient of determination R^2 was calculated in order to judge the goodness of the fit. The R^2 calculation was based on five

points taken along the profiles but especially in the places where there is a greater difference between the heights. The \mathfrak{R}^2 values (shown in the lower right part of the figures) obtained determine that the adjustment is adequate. On the other hand, regarding the small dimensions of the weld bead, it is possible to see minute details of the real profiles and it is possible to reproduce an average model for each welded series.

4.3.3. Imperfections

Since the cross-sections shown in Figure 4.2 represent the welded series, at first glance, at a certain level, all the series present multiple-imperfections. The S1, S2 and S3 series have especially underfill and excessive penetration, while the S4 and S5 series have excess weld metal and porosity. In particular, in the S1 and S3 series it is possible to observe undercuts in the weld root, while the S4 series show incomplete penetration and the S5 series underfill in the bottom side.

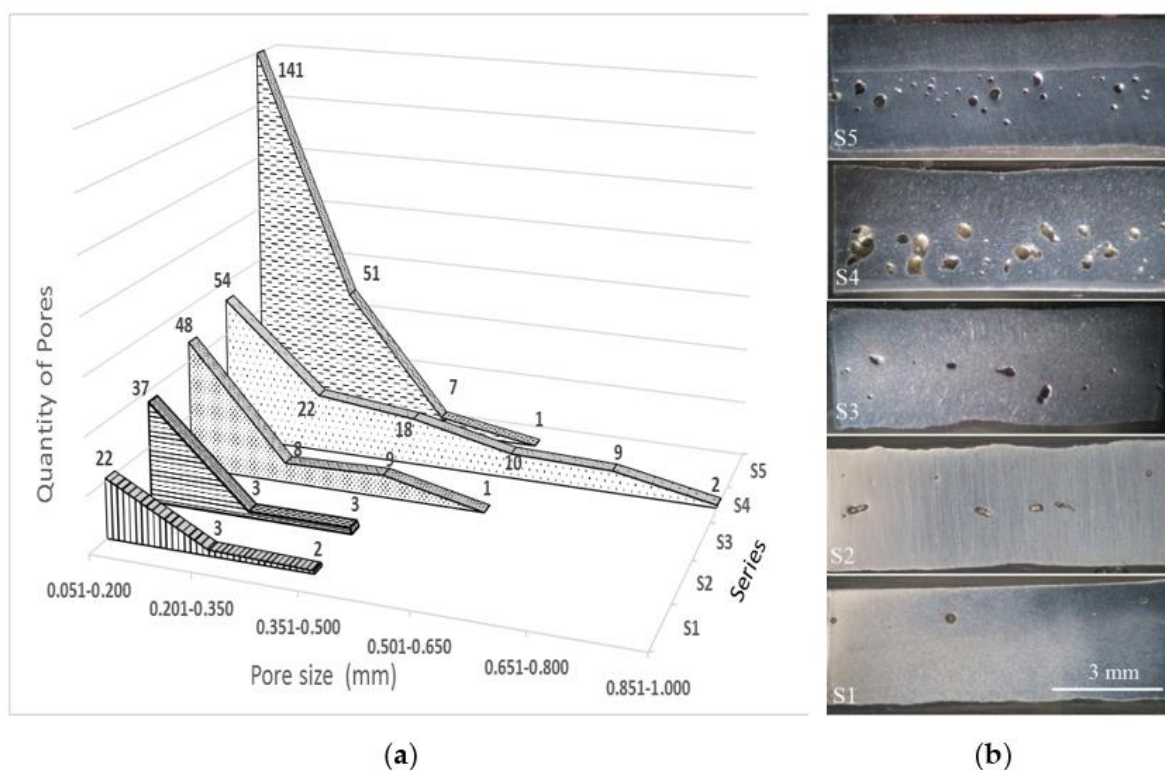
Some imperfections can be quantified through the parameters proposed in Figure 4.3 and the results of Table 4.4. Referring to the designations of the imperfections in Figure 4.1b, the excess weld metal is quantified with the positive parameter hc for the S1, S2, S3 and S5 series and by the hb parameter for the S4 series; the underfill with the negative parameter hi for all series; the excessive penetration with the hb parameter for the S1, S2 and S3 series and; the linear misalignment with the he parameter. In the next sections, we will present the porosity and undercuts distributions and the assessment of the level of imperfections according to the ISO 13919-1 welding quality standard and also focused on the effect of stress concentration.

4.3.3.1. Porosity

Table 4.6 and Figure 4.5 show the quantity, size, distribution and typical aspect of pores found in a section along the weld axis in the center of the FZ for each series. The measured weld length was 54 mm and the area projected was evaluated with the actual distribution of pores assuming round pores with a diameter equal to its size.

Table 4.6 Porosity features of welded series.

Series	Quantity of Pores	Average Size (mm)	Maximum Size (mm)	Minimum Size (mm)	Projected Area (%)
S1	27	0.12	0.46	0.05	0.32
S2	43	0.12	0.41	0.05	0.46
S3	66	0.18	0.53	0.06	1.58
S4	115	0.30	0.99	0.06	7.63
S5	200	0.17	0.51	0.05	3.51

**Figure 4.5** Distribution (a) and appearance (b) of porosity for the welded series.

In general, the results show that the increase in the quantity and size of pores is consistent with the decrease in the HI as was found in the work [34]. There was a significant increase in porosity in the S4 and S5 series as well as a tendency to linear porosity. In the S4 series, the number and size of pores increased while in the S5 series only the number of pores increased. The high porosity of the S4 and S5 series is explained by the instability of keyhole mode and the trapping of gases that is characteristic of partial penetration joints [33]. In the case of the S5 series, the weld pass in the bottom side (of low HI) reduced porosity that was produced by the weld pass on the top side. In relation to the pore sizes, in two studies on

welded joints in steel, maximum pore sizes of 0.5 mm [35] and 1 mm [36] were reported, which agrees with the maximum pore sizes found in the present work.

4.3.3.2. Undercuts

In [37], several types of undercuts are reported however some of those types can be similar to other imperfections as underfill or shrinkage groove according to the guidelines of the ISO 13919-1 welding quality standard [30]. In this study, the undercut will be identified as the groove with narrow width at the weld toe or at the weld root. According to the results, intermittent undercuts were localized in both sides in the weld root for S1, S2 and S3 series while for the S4 and S5 series imperfections with these characteristics practically were not observed.

Table 4.7 shows various parameters of the undercut geometry found for the three series, while in Figure 4.6a,b, the distributions of depth and radius respectively for the mentioned series are shown. Figure 4.7a illustrates the weld roots with and without undercuts captured by the profilometer and Figure 4.7b shows the appearance of undercuts in a photograph.

Table 4.7 Parameters of the undercut geometry.

Series	Quantity	Depth (μm)				Radius (μm)				Depth/Radius ($\mu\text{m}/\mu\text{m}$)			Length (mm)						
		Heading	Heading	Av ¹	SD ²	Max ³	Min ⁴	Av	SD	Max	Min	Av	SD	Max	Min	Av	SD	Max	Min
S1	38			40	22	105	15	56	33	147	5	1.36	2.00	9.00	0.17	1.11	0.63	2.84	0.35
S2	2			72	3	74	69	25	21	39	10	4.39	3.58	6.93	1.86	0.62	0.02	0.63	0.60
S3	28			52	24	114	23	32	24	87	6	3.33	3.74	15.17	0.28	0.59	0.23	1.17	0.21

¹ average (Av); ² standard deviation (SD); ³ maximum (Max); ⁴ minimum (Min).

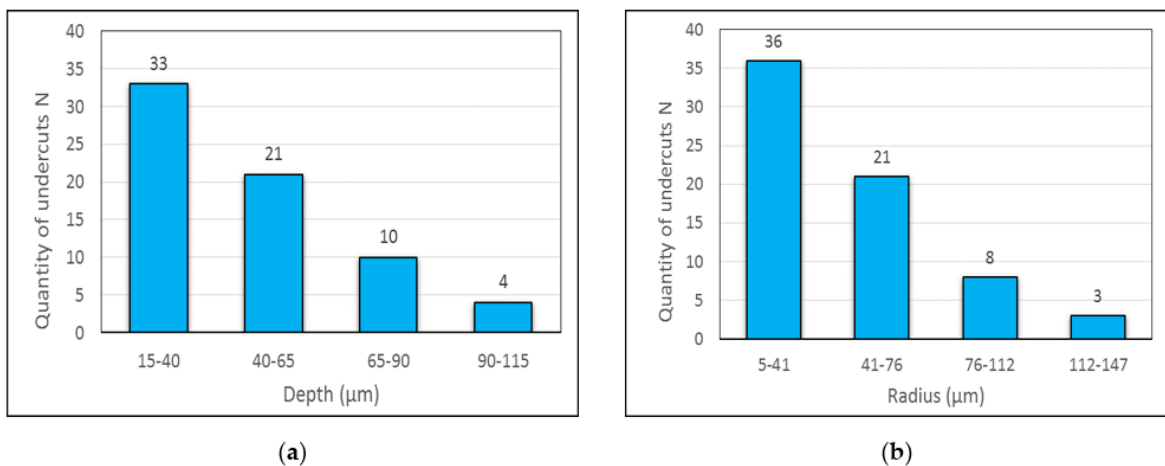


Figure 4.6 Distributions of undercut parameters for the set of series: (a) depth; (b) radius.

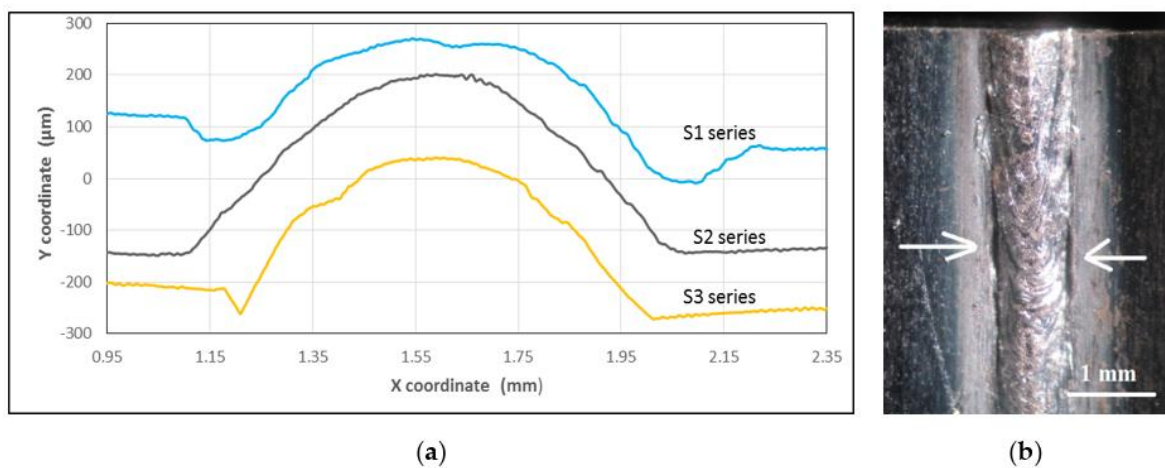


Figure 4.7 Appearance of weld roots and undercuts for S1, S2 and S3 series: (a) captured by profilometer; (b) photograph

From Table 4.7 and the distributions of Figure 4.6, the following can be highlighted: in general, the series have relatively shallow undercuts with very small radii and wide lengths; there is a tendency to increase the quantity, radius and length of the undercuts with increasing the HI, while the depth turned out to be similar for the three series and; the S2 series showed a considerable reduction in the number of undercuts. Due to this last fact, the root was examined with a higher magnification of the stereo-microscope finding micropores along the root of this series. The separation between undercuts was also determined in the base of the c-specimen, finding a great dispersion from 0.24 to 8.44 mm, with a mean of 2.68 mm.

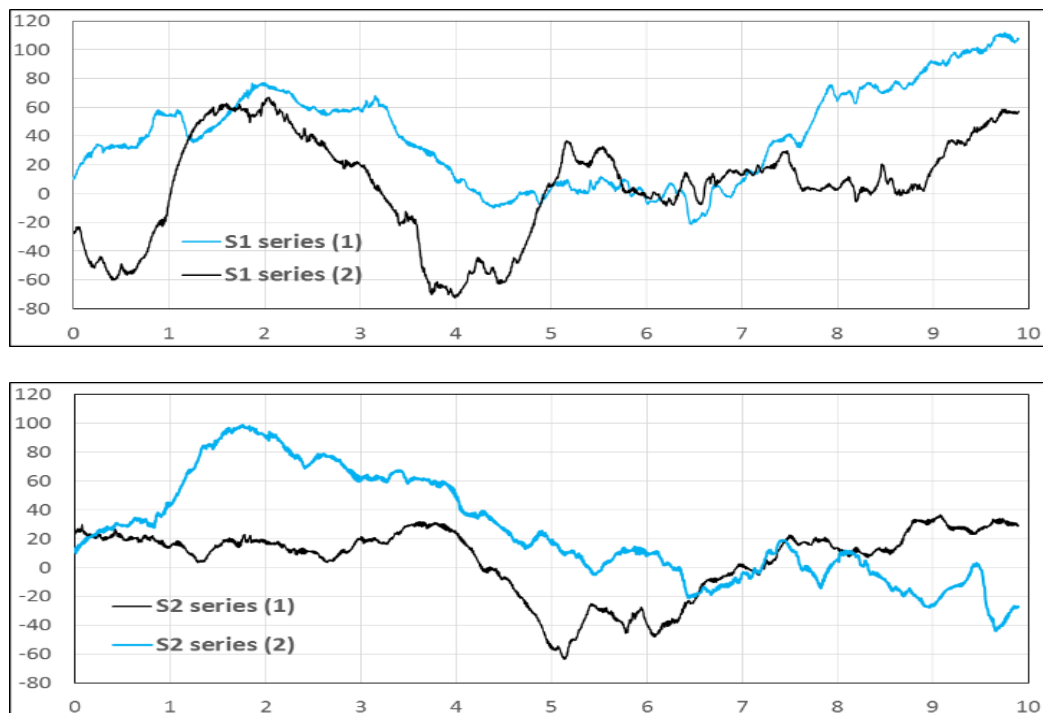
As illustrated in Figure 4.7a, relatively the undercuts may be wide and rounded but also narrow crack-like. From the point of view that considers the undercuts as cracks, these would have very low aspect ratios (a/c) [22]. It should also be noted in Table 4.7 that

the depth-to-radius ratios of the series are underestimated if they would be calculated through the corresponding mean values of depth and radius.

In the studies [25, 37], the causes and mechanisms of undercut formation in laser welding were analyzed: high welding speeds, a combination of high power and high welding speeds, surface oxides and process instability appear as some of the causes. In the present study, the significant decrease in undercuts in the S2 series suggests that may be due to the combination of low power and low welding speed.

4.3.3.3. Variation of the Underfill along the Weld Axis

As reviewed in the literature, the interaction of weld ripples and the weld toe can cause the initiation and reduction of life to fatigue. According to the results obtained in this work, there is a great variation of the weld profile along the weld axis and underfill in the S1, S2, S3 and S5 series. Therefore, it can be inferred that the underfill together with the weld ripples could be stress concentration sites where fatigue starts. For the aforementioned series, two weld profiles were captured along the sites where the underfill was observed, these two profiles (blue line and black line) are shown in Figure 4.8.



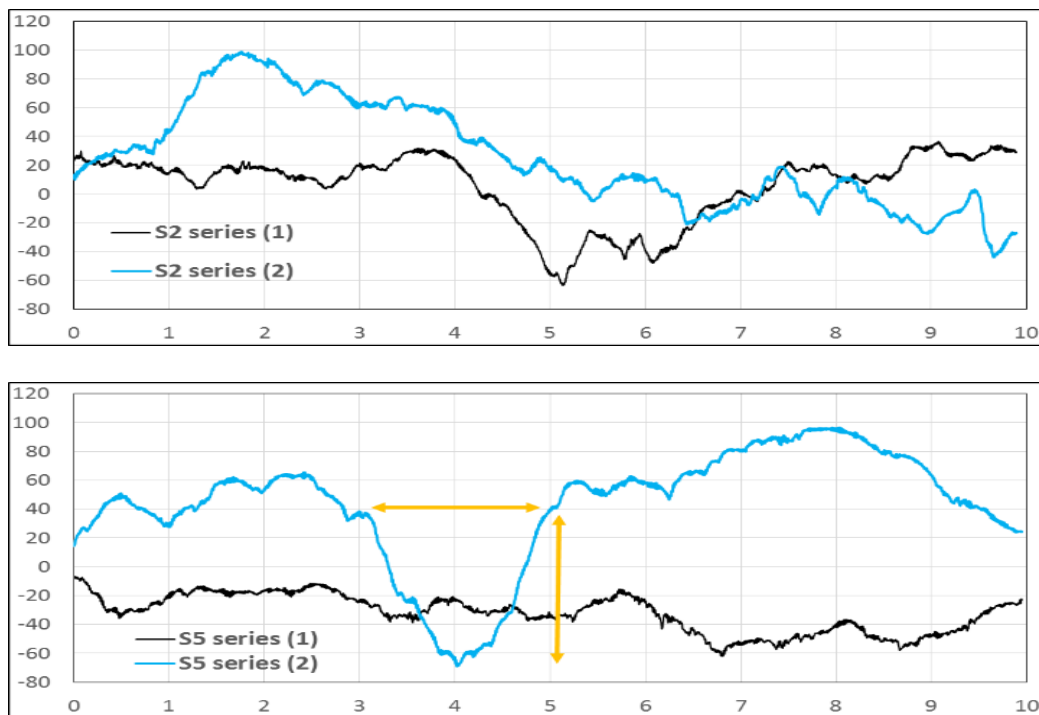


Figure 4.8 Variation of height of the profiles (Y-axis in μm) along the weld axis (X-axis in mm) in places of underfill for S1, S2, S3 and S5 series.

In Figure 4.8, the profiles present a high variation of the height along the weld axis, although for the S2 and S5 series it tends to decrease. The formation of deep (about $100 \mu\text{m}$) and long (2 to 4 mm) depressions (as the mark with arrow lines) that could have an effect similar to undercuts is also observed in all series. The height and length of depressions, as illustrated in Figure 4.8, could be parameters to consider in the combined effect between weld ripples and underfill.

4.3.4. Evaluation of Imperfections

Based on the results presented in the previous sections, for the complete penetration joints, Table 4.8 shows an evaluation of the imperfections found, taking, as a guide, the standard ISO 13919-1 [30]. This standard proposes three quality levels for steels: B stringent, C intermediate and D moderate. The quality levels for each imperfection in Table 4.8 are determined by comparing the maximum values found (Table 4.4, Table 4.6 and Table 4.7) with the limit values according to the quality standard for 3 mm thickness.

Table 4.8 Evaluation of the weld quality of the welded series.

Imperfection Designation	Parameter	Limits of Quality Levels			Quality Levels for Series			
		D	C	B	S1	S2	S3	S5
Porosity	-	-	-	-	-	-	-	-
maximum dimension for single pore	hp (mm) ≤	1.50	1.20	0.90	B	B	B	B
maximum projected area of pores	f (%) ≤	6.00	2.00	0.70	B	B	B	D
in cluster or linear porosity	-	-	-	-	-	-	-	-
two pores closer than	Δlp (mm)	0.75	1.50	1.50	B	D	B	D
shall be considered combined porosity	-	-	-	-	not	yes	yes	yes
if the affected weld length	lc (mm) ≤	6.00	3.00	3.00	-	-	-	-
combined porosity is permitted	-	-	-	-	-	yes	yes	not
Undercut	hu ≤	0.45	0.30	0.15	B	B	B	B
Excess weld metal (reinforcement)	hc (mm) ≤	1.10	0.80	0.65	B	B	B	B
Excessive penetration	hb (mm)	1.10	0.80	0.65	B	B	B	B
Linear misalignment	he (mm) ≤	0.75	0.45	0.30	B	B	B	B
Underfill	hi (mm) ≤	0.90	0.60	0.30	B	B	B	B

The quality level for the series, as shown in Table 4.8, generally speaking, is B, however by porosity, the S5 series is D level. It should also be noted that the linear porosity imperfection requires being measured in a greater length for a better evaluation and that the weld beads can present multiple-imperfections as shown in Figure 4.2.

Without considering porosity, according to the quality standard mentioned, the S1, S2, S3 and S5 series have practically the same quality level, however, the series can be evaluated taking into account the effect of imperfections and profile on fatigue behavior in terms of the SCF. For the determination of SCF values, two expressions proposed in [23] were used. Expression (4.1) for undercut and underfill and Expression (4.2) for excessive penetration or excess weld metal were modified to the nomenclature used in this work:

$$K_{tu} = 1 + 2 \left(1 - \left(\frac{\varphi}{180} \right)^{10} \left(\frac{hu}{ru} \right)^{0.25} \right) \left(\frac{hu}{ru} \right)^{0.54} \quad (4.1)$$

$$K_{tw} = 1 + \left(\frac{hb}{t} \right)^{0.30} \left(\frac{lb}{t} \right)^{0.30} \sin \left(\frac{180 - \theta}{2} \right)^{0.30} \left(\frac{t}{r} \right)^{0.33} \quad (4.2)$$

In Expression (4.1), hu , ru and φ are the depth, radius and groove angle of the undercut. For underfill as depth was assumed the value hi and as radius the corresponding radius $r1$. According to the results in [23], the variation of the angle φ within the range of 40

to 130 degrees caused a minimal change in K_{tu} , therefore in this work, a constant angle of 90 degrees was assumed for the calculation. In Expression (4.2), hb is the excessive penetration or excess weld metal, lb the width, r the transition radius, $(180 - \theta)$ the flank angle and t the thickness of the plate.

Figure 4.9 summarizes the SCF values found on both sides of the weld beads for all series. The values of the profiles correspond to underfill, excessive penetration or reinforcement as appropriate to each series, while for the S2 series, due to the fact that it had almost no undercuts, the corresponding SCF value is not shown. The values obtained were based on the means of Table 4.3 and Table 4.7. Figure 4.9 also shows the porosity percentage for each series.

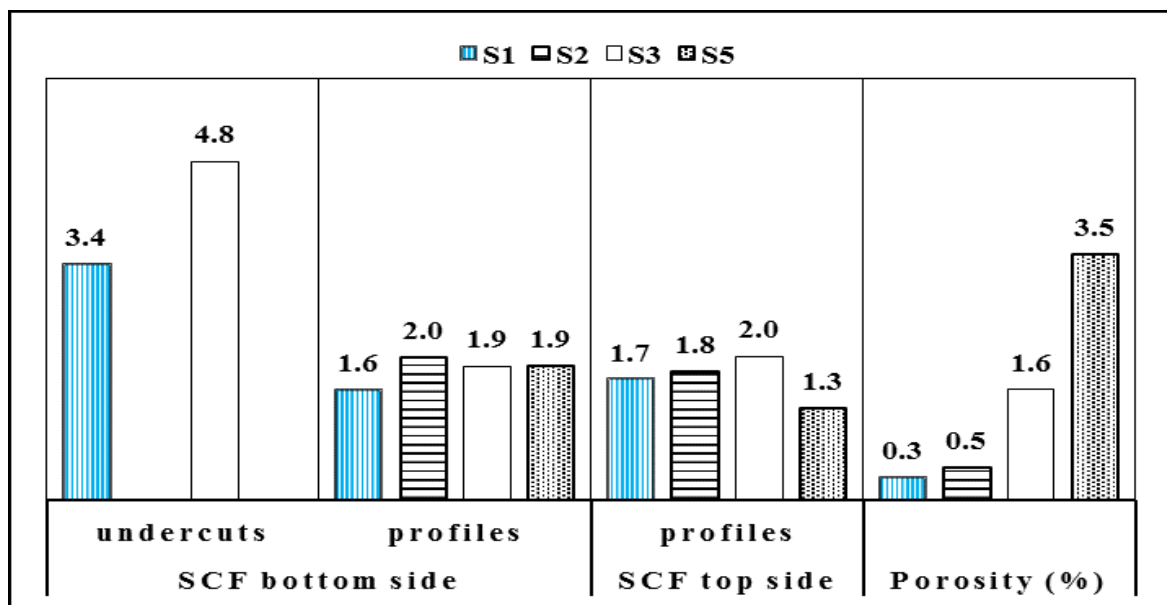


Figure 4.9 SCFs for undercuts and profiles and porosity percentage of S1, S2, S3 and S5 series.

The results of Figure 4.9 show a greater effect of undercuts than the profiles, that there are small differences between b-profiles and t-profiles and therefore a similar effect by excessive penetration, excess weld metal or by underfill, although a certain difference exists for the S5 series, and the least affected profile by underfilling corresponds to S1 series. Due to the interaction between the profile and the undercut, in the S3 and S1 series, the detriment to fatigue resistance could be further increased. In relation to porosity, the S5 series would be the most affected. When individually evaluating the series, considering a lesser effect by

porosity than by undercuts or profiles, the order of affectation in the fatigue strength, would be: S3, S1, S5 and S2.

4.3.5. Analysis of Variance

The ANOVA will be applied to confirm that the small differences observed between the means of the geometric parameters of the welded series Table 4.5 and Table 4.4 are the effect of the different laser welding parameters used for each series and not due to sampling fluctuation. On the other hand, given that the factorial design allows to separate the effects of the main factors (power and welding speed) of the interaction and since the HI is an important parameter in any welding process, it is convenient to evaluate the effect of these parameters on the weld bead geometry. Therefore, taking the width W as representative of weld bead geometry in order to validate the results two analyses are developed.

The first analysis focuses on proving that the HI is an influencing factor in the width W and that the differences between the means of width W respond to the different levels of HI, for the aforementioned, Table 4.9 shows the four observations for each level of HI, the means, the differences between means and the LSD value that allow the comparisons according to Fisher LSD method [38], while Table 4.10 is the ANOVA Table.

Table 4.9 Data for width W .

Series	Treatments	Observations				Means	Differences	LSD Value
Heading	(J/mm)	(mm)				(mm)	(mm)	(mm)
S1	75	2.465	2.440	2.420	2.566	2.473	W1-W2 = 0.207	0.087
S2	66	2.263	2.370	2.236	2.195	2.266	W2-W3 = 0.159	-
S3	60	2.077	2.055	2.171	2.126	2.107	W4-W3=0.045	-
S4	53	2.133	2.147	2.159	2.168	2.152	-	-

Table 4.10 ANOVA table for width W .

Source of Variation	Sum of Squares	Degrees of Freedom	Mean Square	F ₀	P-Value
Heat Input	0.080	3	0.027	8.383	0.0028
Error	0.038	12	0.003	-	-
Total	0.118	15	-	-	-

Following the common procedure, to test the hypothesis that the HI does not affect the mean of width W , using a level of significance of 0.05, with $f(0.05, 3, 12) = 3.490$, and observing that $3.490 < 8.383$ (F_0 value), the hypothesis is rejected, and therefore the HI significantly affects the mean of W . On the other hand, the P-value $0.0028 < 0.05$, confirms that the HI influences the width W . The previous analysis also implies that some means of the width W are different by the treatments HI, and according to the Fisher LSD method, the above is verified when the difference of means is greater than the LSD value 0.087 mm. Therefore, there are differences between the means for all series except for the difference W4-W3, however, this result is affected by the fact that the S4 series is a partial penetration joint.

Finally, the residuals analysis shows a small deviation of the normality assumption in the high values Figure 4.10a and a small range of variance in the S4 series Figure 4.10b compared to the other series. The latter may be due both to the fact that the S4 series is a partial penetration joint and that the four observations correspond to two samples.

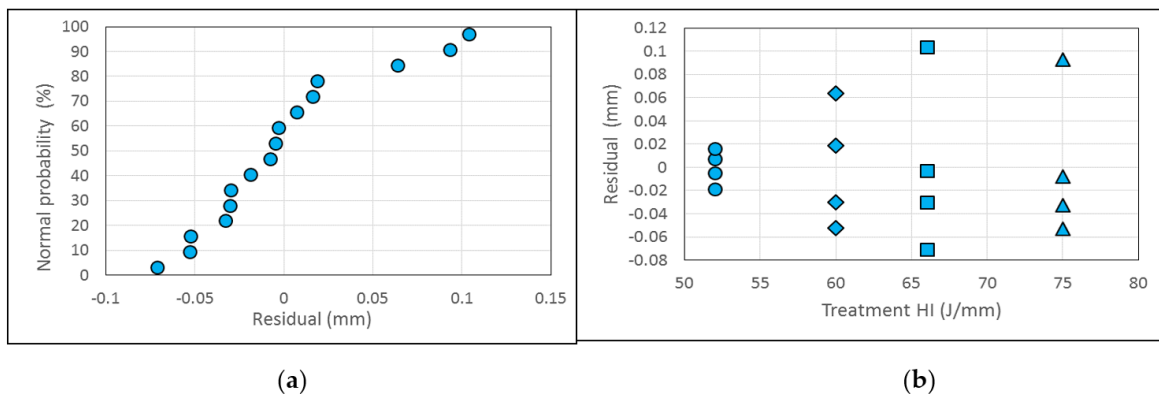


Figure 4.10 Plots of the residuals for width W : (a) normal probability; (b) residuals vs HI.

For the second analysis, Table 4.11 is the ANOVA table for factorial design also applied to width W and shows that all F_0 values exceed the value $f(0.05, 1, 12) = 4.747$, therefore the two main factors and their interaction affect the width W , however, the welding speed prevails over the interaction and the power. The small p-value for the welding speed confirms its strong influence. In concordance to Table 4.11, in Figure 4.11a, the interaction between factors is seen, however, it must be taken into account that this result is influenced by the partial penetration of the S4 series. For this last reason, in Figure 4.11b, which shows

the graph of width W as a function of the HI, the width W of the S4 series does not follow the same trend as the other series.

Table 4.11 ANOVA table for factorial design applied to width W .

Source of Variation	Sum of Squares	Degrees of Freedom	Mean Square	F ₀	P-Value
Power	0.026	1	0.026	8.29	1.39×10^{-2}
Welding speed	0.230	1	0.230	72.44	2×10^{-6}
Interaction	0.063	1	0.063	19.87	7.82×10^{-4}
Error	0.038	12	0.003	-	-
Total	0.358	15	-	-	-

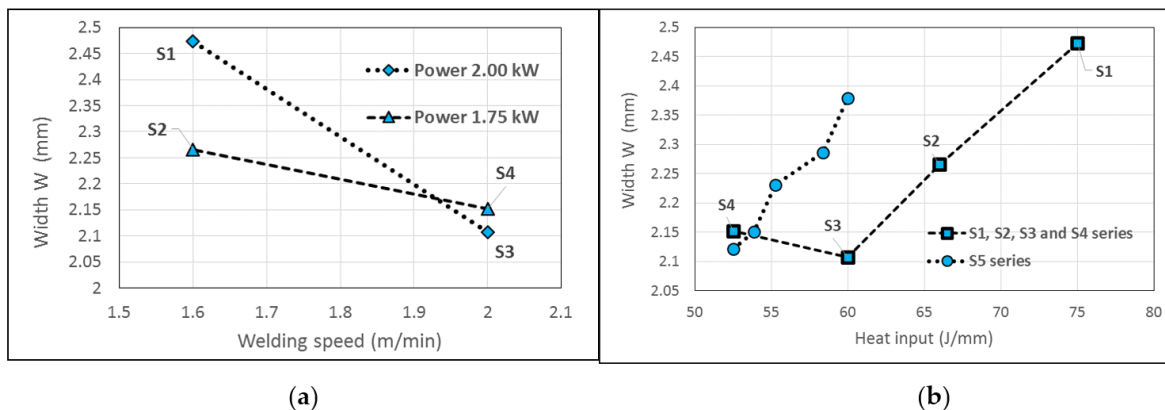


Figure 4.11 (a) Interaction in the factorial experiment; (b) width W in the function of the Heat Input

Figure 4.11b also includes the widths W corresponding to the five samples of the S5 series and considering the width W of the S4 series with the widths W of the S5 series due to the fact that the two series did not achieve full penetration with a single pass weld, it is verified that for both complete penetration and partial penetration there is an approximately linear relationship between width W and HI. Lastly, since it was tested that the different levels of HI generate different widths W , when noting that those levels of HI are combinations of different welding parameters, it is therefore verified that results are affected by the different laser welding parameters used for each series.

4.4. Conclusions

This study, emphasizing the effect of imperfections and weld bead geometry on fatigue strength, describes in detail these two factors for five series of butt joints in a thin HSLA steel plate welded within a small range of welding parameters. The following conclusions can be drawn:

- In the case of small weld beads, the profilometer proved to be a good alternative for capturing 2D profiles due to its accuracy, simplicity and speed in contrast to other techniques and procedures that may be more complex and expensive. Adding a few geometric parameters to those commonly needed to evaluate the main imperfections and with two proposed idealized profiles, the actual profile of the weld beads or those based on mean values of each welded series can be faithfully modeled, making it possible to use it in subsequent analyses, such as the stress-concentrating effect.
- The welded series showed multiple-imperfections. For single-welded joints, the most severe imperfections were concentrated at the weld root: intermittent undercuts, shallow (depth: 15-114 μm) but sharp (radius: 5-147 μm); high flank angles (60-21 degrees), high excessive penetration (0.11-0.53 mm) and small radius at the toe (0.01-0.32 mm). For all complete penetration joints: underfill (0.03-0.32 mm) and long depressions (similar to undercuts) on its surface along the weld axis. Particularly high porosity for partial penetration joint (7.6%) and double-welded joint (3.5%).
- The evaluation of the weld quality according to the ISO 13919-1 standard determined that all the evaluated series, in general, had a B level, however, the S5 series, due to porosity, had a D level. While focusing the evaluation on the stress-concentrating effect in fatigue strength, it was found that there may be a greater detriment due to undercuts than to profiles; that is more critical the weld side where there was excessive penetration and undercuts and that considering additionally the porosity but without taking into account the S4 series, the order of detriment of the fatigue strength in the series can be the following: S3, S1, S5 and S2.

- The ANOVA applied to geometric characteristics such as the width W showed that the effect of welding speed was the most significant; confirmed that the differences in the widths W between the welded series are due to the different levels of HI and therefore to the combinations of welding parameters used in each series and that there was an approximately linear relationship between the width W and the HI.

4.5. References

- [1] Ahiale, G.; Oh, Y. Microstructure and fatigue performance of butt-welded joints in advanced high strength steels. *Mater. Sci. Eng. A* **2014**, *597*, 342–348.
- [2] Xu, W.; Westerbaan, D.; Nayak, S.; Chen, D.; Goodwin, F.; Zhou, Y. Tensile and fatigue properties of fiber laser welded high strength low alloy. *Mater. Des.* **2013**, *43*, 373–383.
- [3] Lieurade, H.P.; Huther, I.; Lefebvre, F. Effect of Weld Quality and Postweld Improvement Techniques on the Fatigue Resistance of Extra High Strength Steels. *Weld. World* **2008**, *52*, 106–115.
- [4] Lillemäe, I.; Remes, H.; Liinalampi, S.; Itävuori, A. Influence of weld quality on the fatigue strength of thin normal and high strength steel butt joints. *Weld. World* **2016**, *60*, 731–740.
- [5] Mashiri, F.R.; Zhao, X.L.; Grundy, P. Effects of weld profile and undercut on fatigue crack propagation life of thin-walled cruciform joint. *Thin-Walled Struct.* **2001**, *39*, 261–285.
- [6] Cerit, M.; Kokumer, O.; Genel, K. Stress concentration effects of undercut defect and reinforcement metal in butt welded joint. *Eng. Fail. Anal.* **2010**, *17*, 571–578.
- [7] Liinalampi, S.; Remes, H.; Romanoff, J. Influence of three-dimensional weld undercut geometry on fatigue-effective stress. *Weld. World* **2019**, *63*, 277–291.
- [8] Schork, B.; Zerbst, U.; Kiyak, Y.; Kaffenberger, M.; Madia, M.; Oechsner, M. Effect of the parameters of weld toe geometry on the FAT class as obtained by means of fracture mechanics-based simulations. *Weld. World* **2020**, *64*, 925–936.
- [9] Kim, D.Y.; Hwang, I.; Jeong, G.; Kang, M.; Kim, D.; Seo, J.; Kim, Y. Effect of Porosity on the Fatigue Behavior of Gas Metal ArcWelding Lap Fillet Joint in GA 590 MPa Steel Sheets. *Metals* **2018**, *8*, 1–13.
- [10] Gou, G.; Zhang, M.; Chen, H.; Chen, J.; Li, P.; Yang, Y.P. Effect of humidity on porosity, microstructure, and fatigue strength of A7N01S-T5 aluminum alloy welded joints in high-speed trains. *Mater. Des.* **2015**, *85*, 309–317.
- [11] Hu, Y.N.; Wu, S.C.; Song, Z.; Fu, Y.N.; Yuang, Q.X.; Zhang, L.L. Effect of microstructural features on the failure behavior of hybrid laser welded AA7020. *Fatigue Fract. Eng. Mater. Struct.* **2018**, *41*, 2010–2023.
- [12] Han, X.; Yang, Z.; Ma, Y.; Shi, C.; Xin, Z. Porosity distribution and mechanical response of laser-MIG hybrid butt welded 6082-T6 aluminum alloy joint. *Opt. Laser Technol.* **2020**, *132*, 1–11.
- [13] Yan, S.; Zhu, Z.; Ma, C.; Qin, Q.; Chen, H.; Fu, Y.N. Porosity formation and its effect on the properties of hybrid laser welded Al alloy joints. *Int. J. Adv. Manuf. Technol.* **2019**, *104*, 2645–2656.
- [14] Leiner, M.; Murakami, Y.; Farajian, M.; Remes, H.; Stoschka, M. Fatigue Strength Assessment of Welded Mild Steel Joints Containing Bulk Imperfections. *Metals* **2018**, *8*, 1–15.
- [15] Wang, X.; Meng, Q.; Hu, W. Continuum damage mechanics-based model for the fatigue analysis of welded joints considering the effects of size and position of inner pores. *Int. J. Fatigue* **2020**, *139*, 1–10.
- [16] Biswal, R.; Syed, A.; Zhang, X. Assessment of the effect of isolated porosity defects on the fatigue performance of additive manufactured titanium alloy. *Addit. Manuf.* **2018**, *23*, 433–442.
- [17] Nguyen, N.; Wahab, M. The Effect of Undercut and Residual Stresses on Fatigue Behaviour of Misaligned Butt Joints. *Eng. Fract. Mech.* **1996**, *55*, 453–469.
- [18] Lillemäe, I.; Lammi, H.; Molter, L.; Remes, H. Fatigue strength of welded butt joints in thin and slender specimens. *Int. J. Fatigue* **2012**, *44*, 98–106.
- [19] Alam, M.; Barsoum, Z.; Jonsén, P.; Kaplan, A.; Häggblad, H. The influence of surface geometry and topography on the fatigue cracking behaviour of laser hybrid welded eccentric fillet joints. *Appl. Surf. Sci.* **2010**, *256*, 1936–1945.
- [20] Chapetti, M.D.; Otegui, J.L. Importance of toe irregularity for fatigue resistance of automatic welds. *Int. J. Fatigue* **1995**, *17*, 531–538.

-
- [21] Schork, B.; Kucharczyk, P.; Madia, M.; Zerbst, U.; Hensel, J.; Bernhard, J.; Tchuindjang, D.; Kaffenberger, M.; Oechsner, M. The effect of the local and global weld geometry as well as material defects on crack initiation and fatigue strength. *Eng. Fract. Mech.* **2018**, *198*, 103–122.
- [22] Otegui, J.; Kerr, H.; Burns, D.; Mohaupt, U. Fatigue Crack Initiation from Defects at Weld Toes in Steel. *Int. J. Press. Vessel. Pip.* **1989**, *38*, 385–417.
- [23] Remes, H.; Varsta, P. Statistics of weld geometry for laser-hybrid welded joints and its application within notch stress approach. *Weld. World* **2010**, *54*, R189–R207.
- [24] Kawahito, Y.; Mizutami, M.; Katayama, S. Elucidation of high-power fibre laser welding phenomena of stainless steel and effect of factors on weld geometry. *J. Phys. D Appl. Phys.* **2007**, *40*, 5854–5859.
- [25] Eriksson, I.; Powell, J.; Kaplan, A.F. Measurements of fluid flow on keyhole front during laser welding. *Sci. Technol. Weld. Join.* **2011**, *16*, 636–641.
- [26] Guo, W.; Crowther, D.; Francis, J.; Thompson, A.; Liu, Z.; Li, L. Microstructure and mechanical properties of autogenous laser welded S960 high strength steel. *Mater. Des.* **2015**, *85*, 534–548.
- [27] Ai, Y.; Jiang, P.; Shao, X.; Wang, C.; Li, P.; Mi, G.; Liu, Y.; Liu, W. An optimization method for defects reduction in fiber laser keyhole welding. *Appl. Phys. A Mater.* **2016**, *122*, 1–14.
- [28] Khan, M.; Romoli, L.; Fiaschi, M.; Dini, G.; Sarri, F. Experimental design approach to the process parameter optimization for laser welding of martensitic stainless steels in a constrained overlap configuration. *Opt. Laser Technol.* **2011**, *43*, 158–172.
- [29] Fricke, W. *IIW Recommendations for the Fatigue Assessment of Welded Structures by Notch Stress Analysis*; Woodhead Publishing Limited: Cambridge, UK, 2012.
- [30] ISO. *Welding-Electron and Laser-Beam Welded Joints-Guidance on Quality Levels for Imperfections. Part 1: Steel*; ISO 13919-1(1996); ISO: Geneve, Switzerland, 1996.
- [31] Strenx® 700 MC. Available online. <https://www.ssab.com/products/brands/strenx/products/strenx-700-mc> (accessed on 1 February 2019).
- [32] Riofrío, P.; Capela, C.; Ferreira, J.; Ramalho, A. Interactions of the process parameters and mechanical properties of laser butt welds in thin high strength low alloy steel plates. *Proc. Inst. Mech. Eng. Part L J. Mater. Des. Appl.* **2020**, *234*, 665–680.
- [33] Matsunaga, A. Problems and solutions in deep penetration laser welding. *Sci. Technol. Weld. Join.* **2001**, *6*, 351–354.
- [34] Bo, C.; Hong, Z.; Fengde, L. Effect of Heat Input on Porosity in High Nitrogen Steel Composite Welds. *MATEC Web Conf.* **2018**, *175*, 1–4.
- [35] Górká, J. Assessment of the Weldability of T-Welded Joints in 10 mm Thick TMCP Steel Using Laser Beam. *Materials* **2018**, *11*, 1–16.
- [36] Pańcikiewicz, K.; Świerczyńska, A.; Hućko, P.; Tumidajewicz, M. Laser Dissimilar Welding of AISI 430F and AISI 304 Stainless Steels. *Materials* **2020**, *13*, 1–15.
- [37] Frostevarg, J.; Kaplan, A. Undercuts in Laser Arc Hybrid Welding. *Phys. Procedia* **2014**, *56*, 663–672.
- [38] Montgomery, D.C. *Design and Analysis of Experiments*, 9th ed.; John Wiley & Sons: Hoboken, NJ, USA, 2017; pp: 96-97.

Chapter 5: Fatigue performance of thin laser butt welds in HSLA steel

P.G. Riofrío^{a,b}, F.V. Antunes^b, J. A. M. Ferreira^b, C. Capela^{b,c} A.C. Batista.

^aDECEM, Departamento de Ciencias de la Energía y Mecánica, Universidad de las Fuerzas Armadas-ESPE, Av. General Rumiñahui S/N, 171103 Sangolquí, Ecuador.

^bCEMMPRE, Department of Mechanical Engineering, University of Coimbra, P-3004 516 Coimbra, Portugal.

^cESTG, Department of Mechanical Engineering, Instituto Politécnico de Leiria, Morro do Lena - Alto Vieiro, 2400-901 Leiria, Portugal.

Submitted to **Metals** journal.

Abstract

This work is focused on understanding the significant factors on the fatigue strength of laser-welded butt joints in thin high-strength low-alloy (HSLA) steel. The effects of the weld profile, imperfections, hardness and residual stresses were considered to explain the results found in the S-N curves of four welded series. The results showed acceptable fatigue strength even though the welded series presented multiple-imperfections. The analysis of fatigue behavior at low stress levels through the stress-concentrating effect explained the influence of each factor on the S-N curves of the welded series. The fatigue limits of the welded series predicted through the stress-concentrating effect and by the relationship proposed by Murakami showed good agreement with the experimental results.

Keywords: Fatigue strength, Laser butt weld, HSLA steel, Fatigue limit prediction.

5.1. Introduction

The high-strength steels have high fatigue resistance, since this damage mechanism decreases with the increase of material's tensile strength. The welding of these materials may be done using laser welding due to lower heat inputs, smaller heat-affected zones and less softening of the material. However, reductions of up to 40% in the fatigue limit, low ratios of the fatigue limit to the ultimate strength of the base metal (BM) and fatigue limits that do not exceed 175 MPa are reported in [1-3] when thin high strength steels and laser welding were used in welded specimens.

The relevant facts that make the difference between welded joints and elements with notches or other defects, is the presence of crack-like imperfections and the changes introduced by the heat input (HI) into the BM. This has led to the fatigue initiation period being neglected [4, 5] and the application of the fracture mechanics approach considering only the period of crack growth for the assessment of the fatigue life [6], however, due to the small size of cracks or for low stress level, the initiation stage can be taken into account [7, 8].

The conventional approach used to predict the fatigue limit in notched elements based on stress concentration and stress gradient models is also used in welded joints [9]. In [10, 11] several traditional models of sensitivity to notches and new models were analyzed for the prediction of the fatigue limit of elements with small imperfections and for the applicability in welded joints. Based in fracture mechanics, Murakami [12] proposed an expression for fatigue limit predictions of materials containing small defects or cracks in function of the hardness and the size of small defects and Åman et al. [13] modified the mentioned expression for take in account the effect on the small defects at the notch root and suggested the application to the welded joints.

Several factors affecting fatigue strength in weldments are highlighted in [14, 6, 14], however they can be summarized in the following: weld quality, residual stress, material and size effects.

Although it has been shown that the weld quality control [15] or the use of post-weld treatments [16-19] in welded joints with high strength steels increases the fatigue

strength by reducing the severity of its inherent imperfections and this fact are recognized in design guides, allowing to increase the fatigue class curve (FAT) when the imperfections have been verified with nondestructive testing (NDT) or when an improvement method has been used [5]; there is no differentiation in the increase according to the mechanical strength of the materials. The foregoing has been explained in [20], due to the fact that the growth of cracks dominates the fatigue life of the welded joints and because the fatigue crack growth rate (FCGR) is insensitive to the mechanical strength of the material, however, as counterpart it was shown that when the weld quality is high, for high strength steels, the fatigue strength is positively correlated to the mechanical strength [21].

Microstructural features as phases and hardness are factors influencing the fatigue behavior of the welded joints. Due to welding process, the microstructures of the heat-affect zone (HAZ), fusion zone (FZ) and BM are different and since in most cases the fatigue starts and paths are in the HAZ or FZ, the properties of these zones are important. Thus, the hardness when is used instead of those of the BM improve the results or fatigue predictions as shown by Kucharczyk et al. [22]. Meanwhile, in [23], it showed that the increase of the proportion of martensite in the microstructure decreases the FCGR and increases the crack growth threshold. In welded joints, the size effects refer to the decrease in fatigue strength due to the increase in thickness plates [4], for example, in [5], fatigue reduction factors are applied when 25 mm of thickness is exceeded, however, although there is evidence that the opposite effect occurs for thin thicknesses [7], it is not taken into account in the design guides.

The general effect of notches and residual stresses on fatigue strength of welded joints is well known. In various studies their combined effect has been studied, determining that there is a relative effect between these two factors. Watanabe et al. [24] reported that the fatigue strength is dominated by stress concentration factor (SCF) when is high and by the residual stresses when the SCF is small, Harati et al. [25] concluded that the residual stress had larger influence than the weld toe geometry, meanwhile, Nguyen et al. [26] established that for residual tensile stresses of low magnitude or for residual compressive stresses the effect of undercut is dominant and Shiozaki et al. [27] reported that that due to the equality of results between the as-welded and heat-treated specimens, the effect of residual stress should not be considered for assessment the effect of weld toe geometry. In

almost all previous works, relatively thick plates and conventional welding processes were used.

As reviewed, there are few studies on the main factors influencing fatigue strength and on the application of the fracture mechanics approach to evaluation of fatigue limits to thin steel plates in laser welded joints. Therefore, in this study, starting from a previous work [28] in which the weld bead geometry, imperfections and the weld quality level of the welds according to the ISO13919-1 standard [29] were determined, considering in a more real way and accurate various factors as the local properties as hardness in HAZ and FZ, the actual profile of weld beads completely modeled to determine the SCFs, the sizes of imperfections found in the welds, the residual stress measurement by X-ray technique; through of failure analysis of fractured surfaces and with base on stress-concentrating effect, the influence of the main factors on fatigue behavior at low stress levels is explained. Predictions of the fatigue limits of the welded series are also made both by the stress-concentrating effect and by the relationship proposed by Murakami.

5.2. Material and procedures

5.2.1. Material and laser welding

Butt-welded joints were made with 3 mm thick high-strength low-alloy (HSLA) steel plate Strenx® 700MCE [30]. This steel has the chemical composition and tensile mechanical properties shown in Table 5.1 and Table 5.2 [31], respectively. It presents a fine-grain ferritic-bainitic microstructure. Note that the yield stress is close the tensile strength, which means that this material keeps the elastic behavior almost until final fracture.

Table 5.1 Chemical composition of the base metal.

C	Mn	Si	P	S	Cr	V	Nb	Ni	Cu	Al	Mo	Ti	Co	Fe
0.07	1.69	0.01	0.012	0.006	0.03	0.02	0.046	0.04	0.011	0.044	0.016	0.117	0.016	balance

Table 5.2 Tensile mechanical properties of the base metal.

Yield Strength (MPa)	Tensile Strength (MPa)	Elongation %
807.63	838.26	15.04

Five series were welded considering the welding parameters shown in Table 5.3. The S1, S2, S3 and S4 series are single-welded joints while the S5 series is double-welded joint. For this last series, the welding speed of the weld pass on the top side was different for each sample (1.75, 1.80, 1.90, 1.95 and 2.00 m/min), while the weld pass on the bottom side was constant for all samples (2.50 m/min). These parameters were selected based on a previous study of the effect of parameters on imperfections and tensile properties [31]. The heat inputs used in welding were defined in order to achieve different values of hardness in the welded series, but maintaining at the same time small HAZs, low softening and tensile mechanical properties similar to the BM, as was shown in [31]. A disk laser equipment Trumpf TruDisk 2000 with: laser maximum output, 2000 W; beam wavelength, 1020 nm; beam parameter product, 2 mm-mrad and fiber diameter, 200 μm , was used in continuous mode. Argon (99.996%) shielding gas was supplied only on the top side of the weld at a flow rate of 20 L/min. Figure 5.1a shows the size of plates used in the welding process.

Table 5.3 Welding parameters used in the experimental work.

Series	Laser power (kW)	Welding speed (m/min)	Heat input (J/mm)
S1	2.00	1.60	75.0
S2	1.75	1.60	65.6
S3	2.00	2.00	60.0
S4	1.75	2.00	52.5
S5	1.75	top side weld pass	52.5-60.0
		bottom side weld pass	
	1.25	2.50	30.0

In [28] were reported B (for S1, S2 and S3 series) and D (for S5 series) quality levels according to the ISO 13919-1 standard for the welded series and by the imperfection sizes these can be consider as crack-like imperfections (see the imperfections sizes in Table 5.6). Due to the S4 series did not reach full penetration it will be omitted in the next sections. Therefore, this series defines the lower boundary of the heat inputs in order to obtain full penetration of the welding in the 3 mm thick specimens.

5.2.2. Fatigue testing and analysis

The fatigue specimens were prepared and testing according the guidelines of the ASTM E466-15 standard [32]. Figure 5.1a illustrates the location of the welded specimens, which were obtained by laser cut, meanwhile, Figure 5.1b shows the specimen dimensions. The fatigue specimens were tested in three conditions: no-welded (BM), as-welded and bottom side-removed. For this last condition, the excess weld metal and undercuts were progressively eliminated until to create a smooth transition between the weld and the plate thus minimizing the stress concentration. The specimens were carefully grinded to a final polish with sandpaper # 220, particularly the edges and the welding surfaces. The total elimination of the undercuts was verified under the microscope with 20 magnification power.

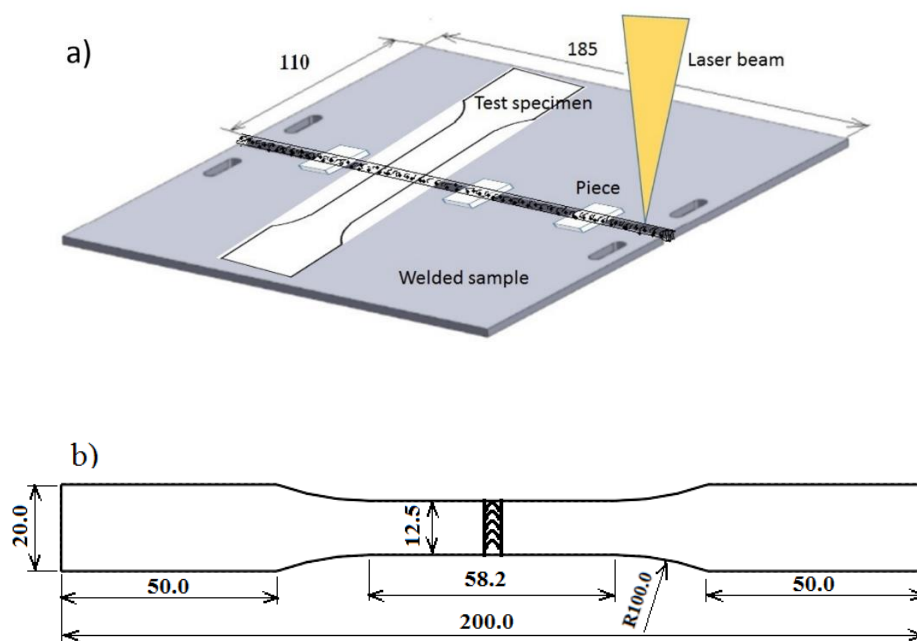


Figure 5.1 a) Sketch of plates for the welding and location of specimens, b) dimensions of specimens used in fatigue tests.

The testing was done on DARTEC INSTRON servo-hydraulic machine. The fatigue specimens were loaded axially with constant amplitude at a stress ratio $R=0$ and at a frequency of 15 Hz. The specimens were tested at various stress levels up to the final fracture, however, when at a certain stress level, the life of the specimens exceeded 2×10^6 cycles the tests were stopped (run-outs). After the fracture of the specimens, their surfaces

were analyzed with a stereo-microscope in order to determine the site, start, imperfection, path and shape of the fatigue surface.

A power law relationship was assumed for the S-N curves:

$$\log(N) = \log(C) - m \log(\Delta\sigma) \quad (5.1)$$

where, the nominal stress range $\Delta\sigma$ is the independent variable, the number of cycles N at which the failure occurs is the dependent variable and C , m are parameters that characterize the curves. Through linear regression, the S-N data were analyzed according to the ASTM E739-10 standard [33] to determine the C and m parameters of the S-N relationships, the median S-N curve and its 95% confidence band. The testing of adequacy of the linear model was also verified according to the mentioned standard. For comparison, the FAT100 curve (slope $m = 3$, $\Delta\sigma = 100$ MPa at two million cycles) was also plotted in the S-N graphs. This FAT100 curve, suggested in the fatigue design recommendations of the International Institute of Welding (IIW) for butt joints when imperfections (undercuts and porosity) are evaluated [5], was chosen because its requirements are close matching (differs in the thickness and the porosity of one of the series) to imperfection sizes and quality level found for welded series as reported in [28].

5.2.3. Measurement of residual stresses

The residual stress analysis was performed by X-ray diffraction using a Proto iXRD equipment, in the longitudinal and transverse directions of the laser welds, and on both sides (top and bottom surfaces) of the specimens. Lattice deformations of the $\{211\}$ diffraction planes ($2\theta \approx 156^\circ$) were measured using Cr- K_α X-ray radiation, with 11 β angles in the range $\pm 30^\circ$ (22 ψ angles in the range $\pm 42^\circ$), an acquisition time of 30 seconds by peak and $\pm 2^\circ$ oscillations in ψ . An aperture length of 0.5 mm \times 3 mm in the transverse and longitudinal directions, respectively, was used. The residual stresses were evaluated with an elliptical regression of $\sin^2\psi$, using the X-ray elastic constants values of 5.83×10^{-6} MPa $^{-1}$ for $(1/2) S_2$ and -1.28×10^{-6} MPa $^{-1}$ for S_1 . For the analyzed material and considering the radiation used, the average penetration depth of the X-rays was about 5 μm .

5.3. Results and discussion

5.3.1. S-N curves

Figure 5.2 shows the S-N experimental results of both the welded series and the BM. The mean and the 95% confidence band curves of the BM are also presented, along with FAT100 curve, which is a reference for welded joints. The BM shows a linear behavior in log-log scale with small scatter. The nominal stress ranged varied between 600 and 800 MPa, which correspond to 74 and 99% of material's yield stress, respectively. The modification introduced by laser welding on microstructure changed significantly the position of the S-N curves. A significant decrease of stress range for the same fatigue life is evident, namely for lower load ranges, i.e., for longer fatigue lives. The scatter increased significantly, comparatively to the BM. Both the S-N curves of the BM and of the welded joints present the characteristic "knee point" that identifies the stress level of the fatigue limit, that in this work will be assumed as the fatigue strength of run-outs at two million cycles. Eventually the series S2 may be considered to have better a higher limit. The FAT100 curve is clearly below the experimental results obtained for the welded series, which is a good indication for the quality of laser welding.

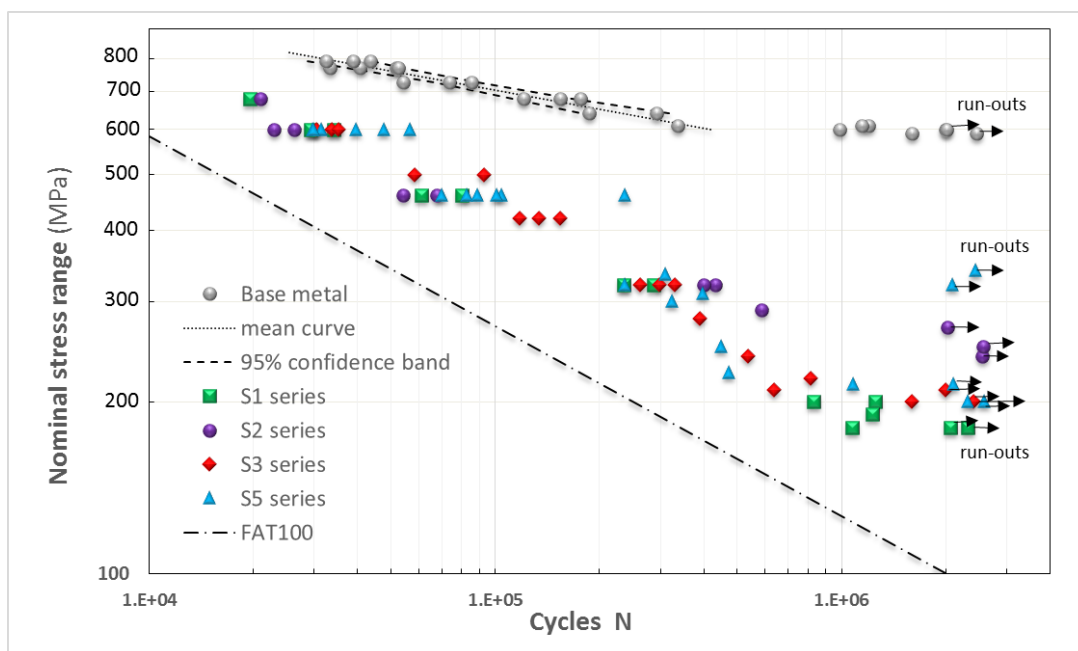


Figure 5.2 S-N data for all welded series and BM.

Figure 5.3 presents the results for each series and a photo-macrograph showing the cross-section of the weld bead. The stress levels corresponding to the fatigue limit are also indicated. The dispersion of the entire data set is reduced when each series is considered separately and that the dispersion of each series is similar than that of the BM. In the case of the S5 series, because two specimens (named as S5-F9) showed a considerably higher fatigue strength than the rest of specimens, they were not considered within the S5 series. The FAT100 is clearly below the experimental results in all the series.

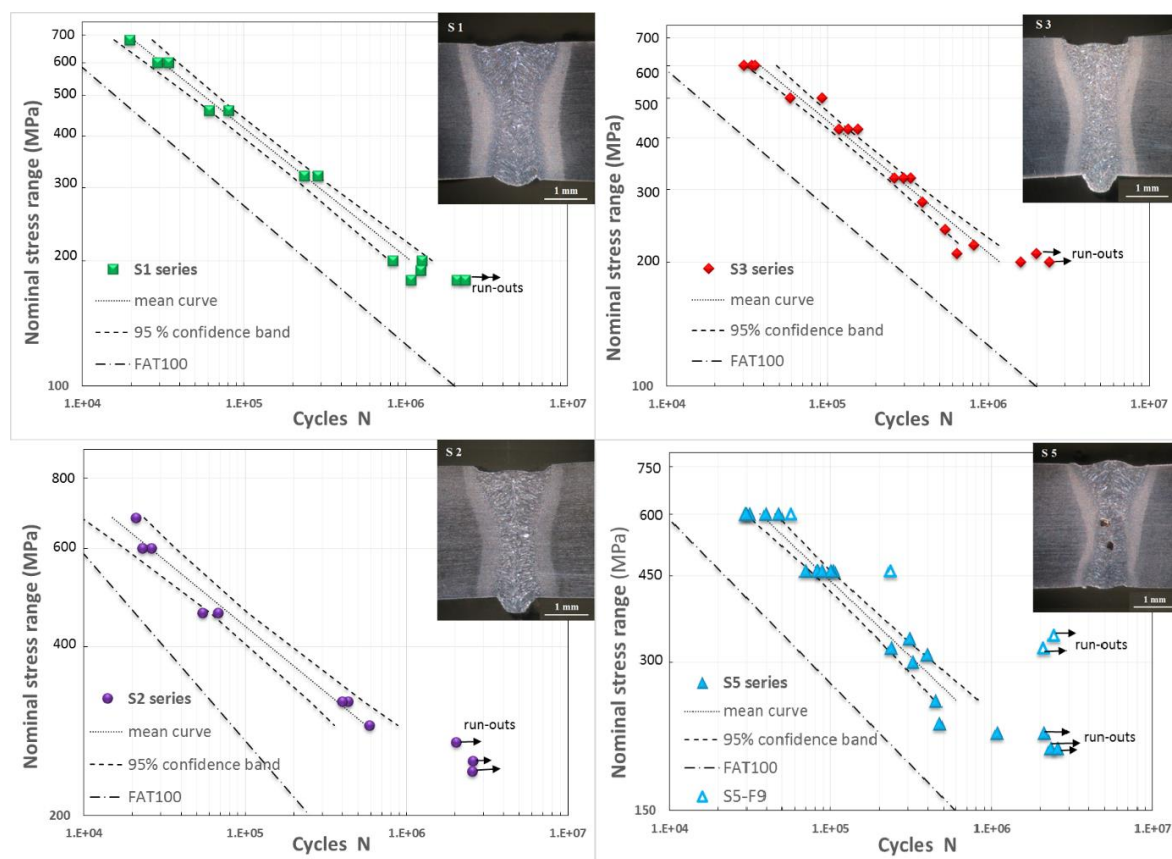


Figure 5.3 S-N curves of each series.

Table 5.4 presents $\log C$ and m parameters of S-N curves. There is a limited influence of welded series on these values, with the exception of S2 series. Besides, the m values are very close to FAT100 curve slope. The relatively high value m for the BM indicates that the initiation is dominant over the propagation. On the other hand, the relatively low value of m for the welded joints indicates the predominance of propagation over initiation. The fatigue limits shown in Table 5.4, which were assumed to be the maximum stress range values reached by the specimens that exceeded two million cycles,

are between 30% and 57% of the fatigue limit of the BM. As can be seen in Figure 5.3, all series had a fatigue life over the FAT100 curve.

An additional aspect should be noted from the results obtained; although the confidence F-test for all welded series and BM did not reject the hypothesis of linear model, for the S2 and S3 series, observing the mean curves and the results points, these change from one side to the other when going from a low stress levels to a high ones and in the case of the S2 series, at high stresses, it has the shortest fatigue life, while at low stresses it tends to have the longest life of the set of results (without consider S5-F9 specimens), see Figure 5.2 and 5.3.

Table 5.4 S-N curves parameters and fatigue limits.

Series	linear model	log C	m	Fatigue limits (MPa)
S1	not rejected	13.455	3.226	180
S2	not rejected	16.206	4.247	270
S3	not rejected	13.248	3.118	210
S5	not rejected	13.469	3.206	215 (340)*
BM	not rejected	30.642	9.004	600

*The value 340 MPa corresponds to S5-F9 specimens.

5.3.2. Fatigue failure modes

Table 5.5 presents the principal features of each failure mode (designated as FM) and representative photographs that show the fracture surfaces, details of the starts, imperfections and paths of the fatigue. Based on the analysis of the fractured surfaces of all the specimens, mainly four failure modes were found in the welded series. The FM1 failure mode was due to the undercuts at weld root of the S1 and S3 series, there was generally more than one that generated semi-elliptical cracks. In the FM2 failure mode, multiple imperfections along the root caused failures, especially in the S2 series, in these cases the presence of semi-elliptical cracks was not evident. The FM3 failure mode was present in practically all the series, the fatigue starts in the underfill occurred in the ripples, these being smaller in the S5 series, see Table 5.5.

Table 5.5 Failure modes features.

Failure Mode (series)	Fatigue start: site-imperfection (side)	Details	Approximate shape of fractured surface	Remarks
FM1 (S1, S3)	root-undercuts (bottom side)	a) long and deep undercuts, one or two very close b) several undercuts across the width	a) big semi-elliptical b) tending to rectangular by coalescence of small semi-elliptical	in some cases, microdefects close to undercuts
FM2 (S2, S1, S3)	root-excess weld (bottom side)	multiple starts in micro-imperfections (pores, cavities, shallow crack-like) across the width	tending to a rectangular stripe across the width	semi-elliptical forms were not observed

Failure Mode (series)	Fatigue start: site-imperfection (side)	Details	Approximate shape of fractured surface	Remarks
FM3 (S5) (S1,S2,S3)	face-underfill (bottom side) (top side)	multiple starts in waves and sharp ripples with microdefects	small semi-ellipses or tending to a big semi-ellipse by coalescence	in many cases, underfill at border
FM4 (S5, S1, S2, S3)	center-porosity (lateral side)	single pore or several on or near the surface	approaching the middle of a semi-elliptical	in some cases influenced by underfill close to corner

The FM4 failure mode refers to failure due to the presence of pores, it was present in all series but in greater numbers in the S5 series. The pores caused fatigue failures at the lateral side of the specimens generally when they were located near or on the surface, this failure can also be influenced by the underfill at the border of the element, as illustrated in Table 5.5.

It should be noted that in approximately 44% of the fractured specimens, at least two failure modes were observed (as illustrated in FM2 mode, S3 series in Table 5.5), however, in most cases, only one mode was decisive to fatigue failure. The fatigue path was

generally straight from the weld root through thickness to the underfill or vice versa, however, in certain cases the path had inclined parts due to the starts of fatigue from different planes, by the presence of porosity or in the final stages of the fracture due to deviations to the soft material where greater deformations were presented.

Figure 5.4 highlights that each series had a main failure mode that prevailed over the others and that all series presented at least two main and two additional failure modes. Also illustrates, in the sketches on the cross-sections of the weld beads, the starts and paths followed by the four failure modes and the fact that all the fractures in the specimens occurred within the FZ and HAZ. As can be seen, in S1 and S3 series the FM1 mode prevailed, in S2 series the FM2 mode, while in S5 series the FM3 mode. The above is strongly related to the corresponding presence of imperfections in each weld bead, see Table 5.5.

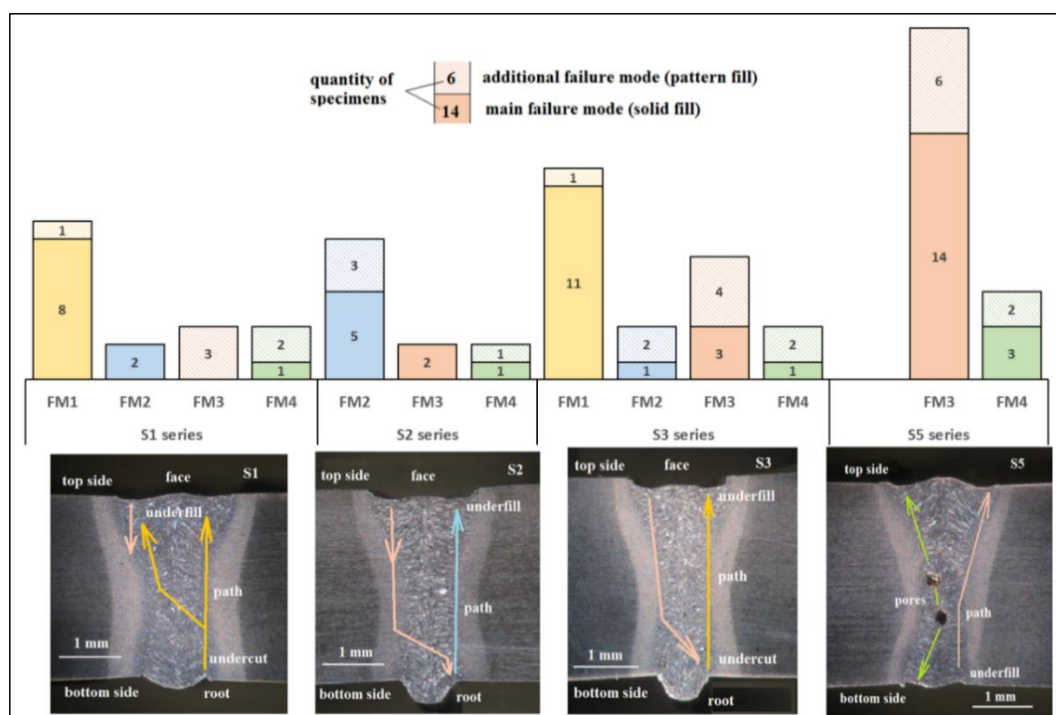


Figure 5.4 Failure modes distributions found in the specimens of the welded series and sketches of starts and paths on their cross-sections.

Considering the starts on underfill and the starts on excess weld and undercuts, it is observed that the last dominated in S1, S2 and S3 series while the first dominated in S5

series. The FM4 mode that corresponds to porosity caused few starts in all series, however, in S5 series, it increased as a consequence of its highest percentage of porosity (3.5%) [28].

5.3.3. Effect of weld bead geometry and imperfections

In order to evaluate the effect exerted by the weld profile and geometrical imperfections on the fatigue behaviour; the stress concentration factor (SCF), K_t , corresponding to the top and bottom sides of each welded series were determined by Finite Element Method (FEM) and with expressions from the literature. For the latter case, SCF values shown in Table 5.6 were calculated with semi-analytical expressions proposed in [34] for the weld profile, notches and their interaction, considering the mean values of the geometric parameters presented in Table 5.6. The ANSYS commercial code was used for the FEM. Siles models (0.2 mm in thickness) with meshes composed of quadrilateral elements with quadratic displacement function, were generated according the recommendations about the number of elements in notches and weld toes given in [35], i.e.: element size ≤ 0.012 mm (for radius 0.05 mm); number of elements over 45° arc, ≥ 3 and for 360° arc, ≥ 24 . Previous to the FEM, the weld profiles (top and bottom sides) of the four welded series were completely modelled according to the procedure and the mean geometrical parameters given in [28]. The models are presented in Figure 5.5, which also shows the fine mesh used in the models and in the imperfections of the weld root (toe), undercut and underfill. Therefore, the number of elements were exceeded and the sizes (approximately 0.010-0.015 mm) are close to the recommendations mentioned.

Table 5.6 SCFs and mean geometric parameters of imperfections.

			Welded series			
			S1	S2	S3	S5
excess weld (toe)	radius	(mm)	0.16	0.06	0.07	0.54
	width	(mm)	1.02	0.93	0.84	1.73
	high	(mm)	0.20	0.36	0.31	0.14
	flank angle	(degrees)	34	50	50	14
	SCF analytical		1.54	1.95	1.83	1.30
	SCF by FEM		1.71	2.25	1.98	1.36
Undercut	depth	(mm)	0.04	-	0.05	-
	radius	(mm)	0.06	-	0.03	-
	SCF analytical		3.56	-	4.89	-
	SCF by FEM		3.29	-	4.41	-
Underfill	depth	(mm)	0.08	0.12	0.15	0.06
	radius	(mm)	0.53	0.60	0.50	0.27
	SCF analytical		1.72	1.84	2.05	1.91
	SCF by FEM		1.75	1.77	1.94	1.95

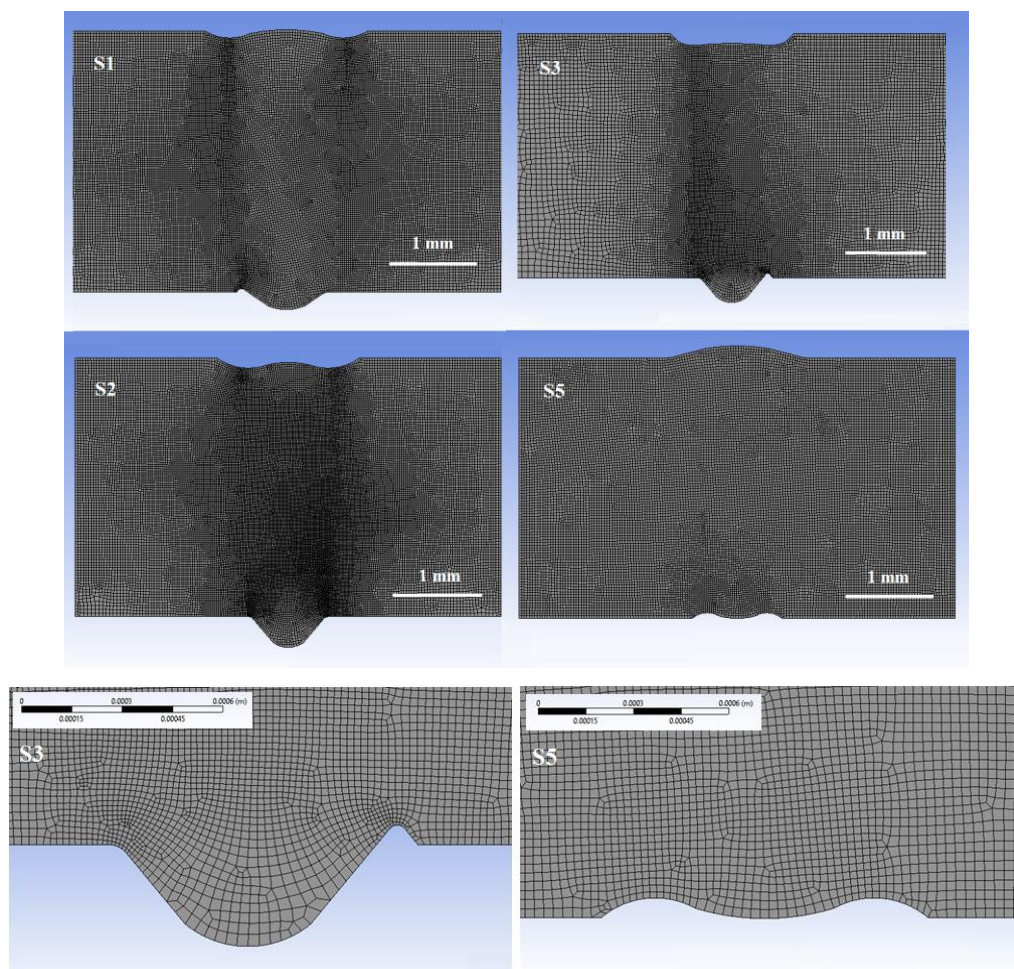
**Figure 5.5** Weld profile models of the welded series and details of meshing used in FEM.

Figure 5.6a and 5.6b plot the maximum principal stress for the bottom side of the welded series S3 and S5, respectively. The root of the weld is a point of stress concentration, as could be expected. The SCF obtained numerically are also presented in Table 5.6. In general, there is a difference of less than 10% between the SCFs determined with the semi-analytical expressions and by FEM. On the other hand, the SCFs corresponding to the undercuts are almost the double of the SCFs for the underfill or excess weld (toe), and there is some closeness between all the SCFs due to underfill and excess weld with exception of the value of the S5 series ($K_t=1.36$). It is also important to note, as shown in Figure 5.6, that the stress distribution on the imperfections are different, being more concentrated and with major gradient for the undercut while on the underfill is more wide and small gradient, as expected due to the difference in notch radii.

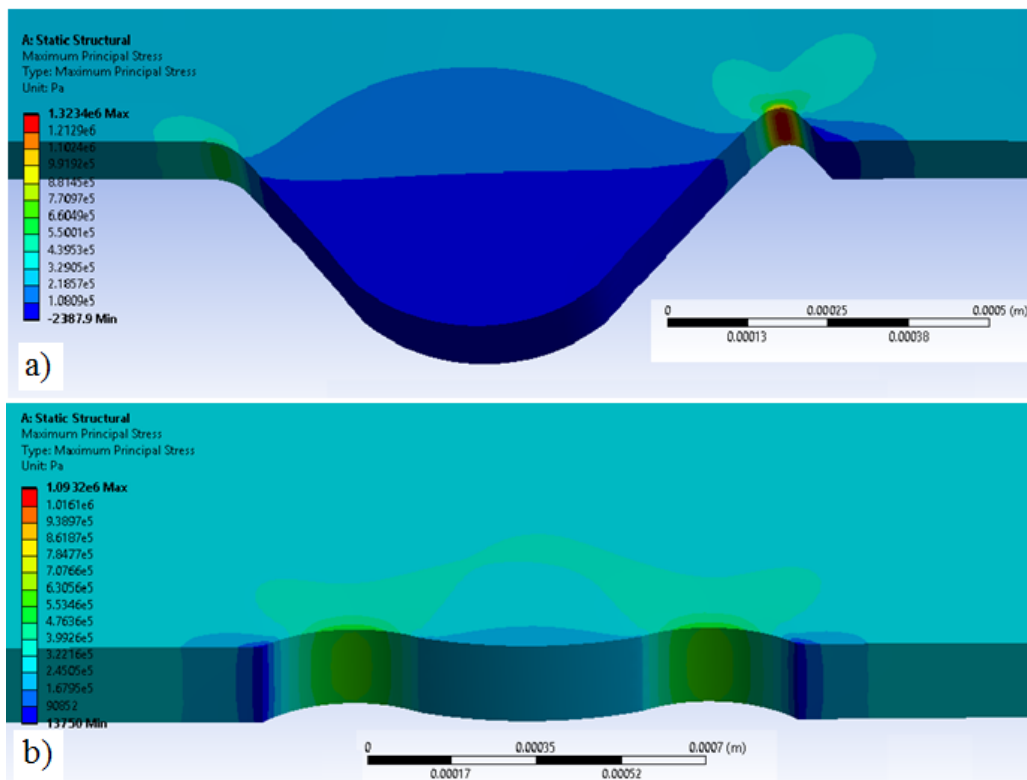


Figure 5.6 Stress distribution in bottom side of the welded series: **a)** S3 and **b)** S5.

When considering the SCFs of the imperfections in Table 5.6 and the failure modes in Figure 5.4, it can be noted that, the highest SCFs in each welded series are correlated to their major main failure mode and the respective imperfection, thus: 3.27-

undercut-S1, 2.25-excess weld-S2, 4.41-undercut-S3 and 1.95-underfill-S5. The foregoing highlights the known fact that, fatigue cracks starts commonly in sites of stress raisers.

5.3.4. Effect of top side and bottom side in the fatigue strength

Because the weld beads of the welded series showed fatigue starts on both sides, to examine better the effect of weld profile and imperfections on fatigue behaviour, various specimens were tested once the bottom side was removed from their weld beads. Figure 5.7 shows the S-N results for specimens of the S1 and S2 series in two conditions: as-welded and bottom side-removed. In S1 series (Figure 5.7a) the elimination of the bottom side increases significantly the fatigue strength for all stress ranges. Therefore, the slope of S-N curve is not significantly affected. Besides, the fatigue limit increased from 180 to 380 MPa.

In S2 series (Figure 5.7b) there is a significant effect of $\Delta\sigma$. At high stress range, the change of geometry does not affect significantly the fatigue life. On the other hand, at low stress range there is a significant effect on fatigue life. Therefore, there is a great reduction in the slope of S-N curve. The smoothing of geometry also increases fatigue limit from 270 to 390 MPa.

These results could be expected since the main imperfections (excess weld and undercuts) were eliminated, which reduces significantly the SCF. Therefore, the fatigue initiation changed to the top sides where the stress raisers are less severe.

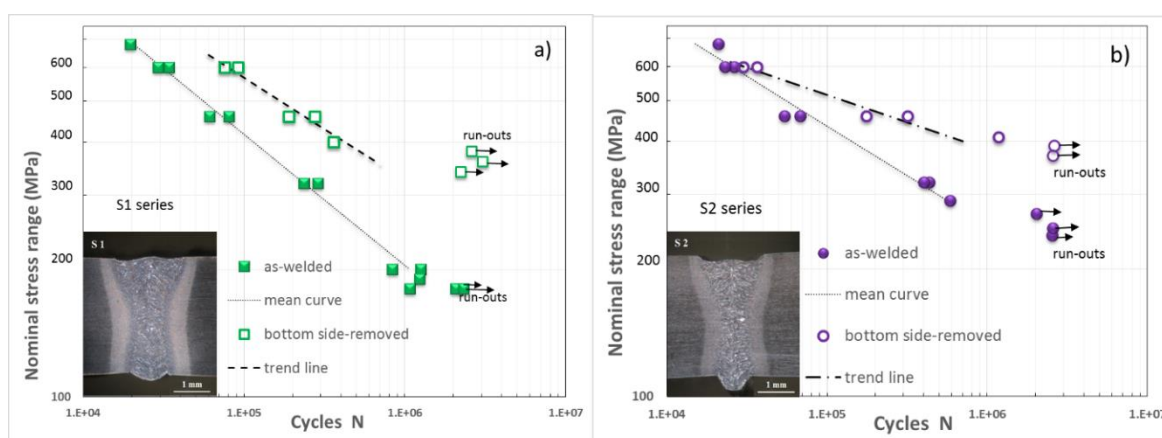


Figure 5.7 S-N curves for S1 and S2 series in two conditions: as-welded and bottom side-removed.

Table 5.7 presents the fatigue limits and the corresponding SCFs for series S1 and S2, as welded and with bottom-side removed. The fatigue strength at two million cycles can be substantially improved by eliminating defects from the bottom side of the weld beads. In average the increase of two welded series reached 64% in relation to the fatigue limit of the BM. However, at high stress levels the increase of the fatigue life is small for the S2 series. This could be due to the deep underfill reducing the load bearing area, due to the variation of the underfill along weld axis or due to the interaction between underfill and the weld ripples that would increase the stress concentration at those sites, as stated in [36].

Table 5.7 Correlation between ratios of SCFs and fatigue strengths.

Series	Fatigue limits (MPa)(imperfection)		SCFs (imperfection)		Ratios	
	as-welded	bottom side-removed	as-welded	bottom side-removed	strengths	SCFs
S1	180 (undercut)	380 (underfill)	3.29 (undercut)	1.75 (underfill)	2.11	1.88
S2	270 (excess weld)	390 (underfill)	2.25 (excess weld)	1.77 (underfill)	1.44	1.27

For a better understanding of the behavior at relatively high stress levels, in addition to the as-welded condition, several specimens with bottom side-removed and two side-removed conditions were tested at 600 MPa. The fatigue lives of almost all samples at that stress level are shown in Figure 5.8.

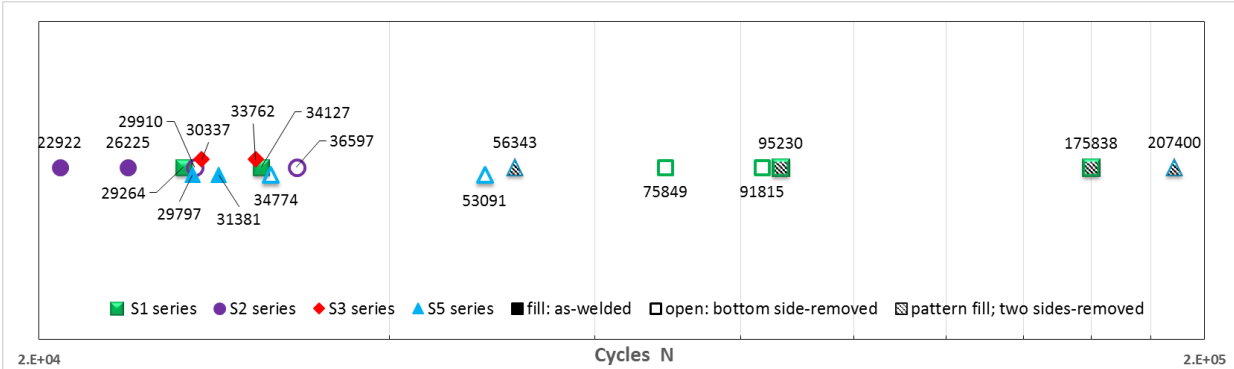


Figure 5.8 Fatigue lives of specimens at 600 MPa in various conditions.

The results reaffirm, as expected, the increase in fatigue life due to the elimination of imperfections of weld beads, however, the following should be noted: the lowest life of the specimens of the S2 series in the as-welded condition was due to the multiple small imperfections, practically presented a continuous crack along the width; for

the group of specimens of all series in as-welded and bottom side removed conditions with similar fatigue lives in the range of 29000 to 35000 cycles, semi-elliptical cracks that grew and covered the entire width or border of the specimens; from the specimen with a fatigue life of 36587 cycles, all specimens presented a single semi-elliptic crack, where the smallest starts had a longer life than the largest ones. The exceptions were the specimens with starts in pores, so the fatigue life of 56343 cycles corresponded to pores in the lateral side meanwhile the fatigue life of 207400 cycles correspond to internal pores. These results show the important effect of the quantity, size and position of the imperfections in the fatigue life at high stresses and therefore the greater influence of the coalescence and crack growth at high stress levels.

5.3.5. Fatigue limit assessment

5.3.5.1. Local Properties: microstructure and hardness

According to the fracture analysis, the fatigue starts at the weld root and undercuts were located at the boundary between the columnar grains of the FZ and the CG-HAZ, those in the underfill were located on the columnar grains of the FZ but very close to the HAZ (as shown in Figure 5.9), the fatigue paths were through the FZ and HAZ and due to the series were welded with different heat inputs; the actual microstructures, hardness, and residual stresses are important factors in the fatigue strength. Due to the heat input range used in the present work is similar to the range in a previous work [31], softened ferritic-bainitic in FG-HAZ and bainitic-martensitic in CG-HAZ and in FZ can be present in the microstructures.

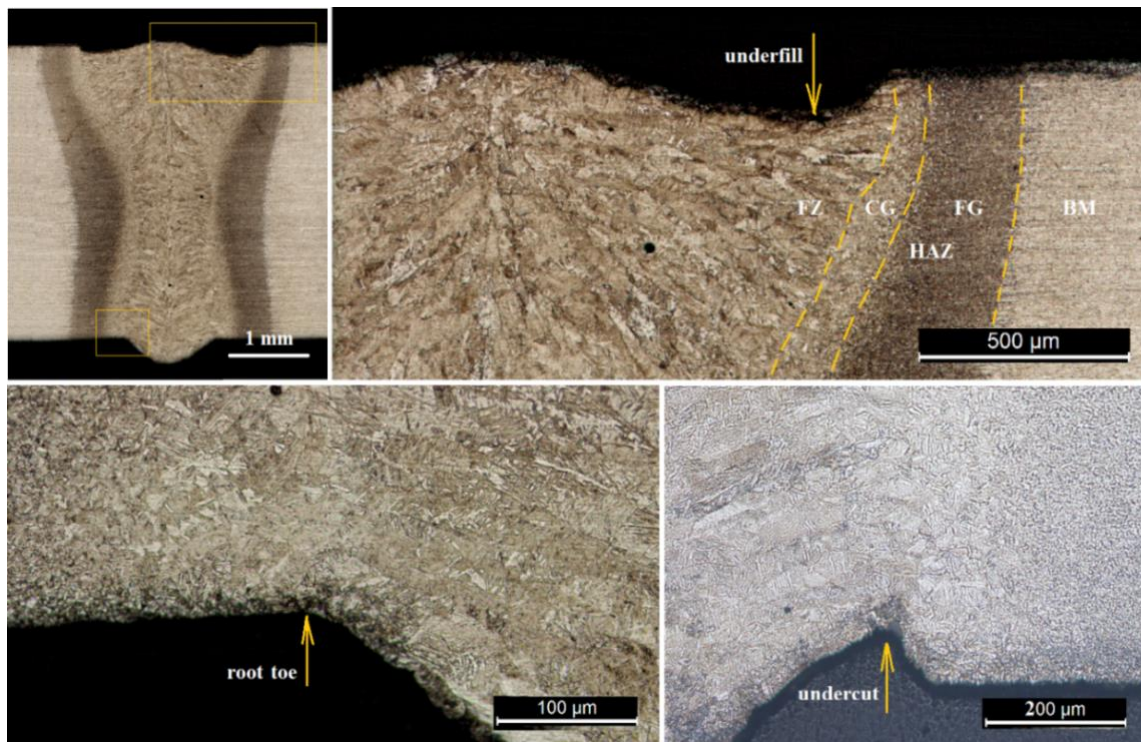


Figure 5.9 Fatigue initiation sites in the microstructure for underfill, undercuts and weld toe.

The microhardness (HV, 0.5 kg, 10 s) profiles were determined near to the surface on the cross-section of the weld beads for all welded series. Figure 5.10 shows two examples of the hardness profile found for the S1 and S5 series. As can be seen from the hardness profile, in the FZ the hardness is high and roughly the same for both sides of the weld bead at the fatigue sites, meanwhile in the HAZ, the S1 series had softening unlike the S5 series which practically did not have it. According to the results at the fatigue initiation sites, the hardness ranges for the welded series were 335 to 370 HV. Although small differences were distinguished between each welded series, the local properties of hardness assumed at the sites where the cracks started and propagated for the fatigue strength assessment are shown in Table 5.8.

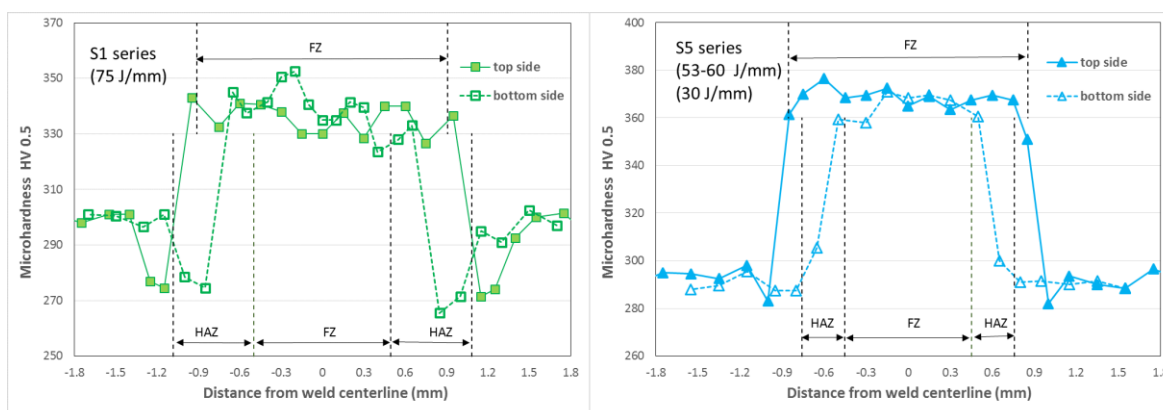


Figure 5.10 Microhardness profiles in S1 and S5 series.

5.3.5.2. Residual Stresses

The residual stresses induced by the welding are one of the main factors affecting the fatigue strength. Figure 5.11 shows the results of residual stresses measured with X-ray diffraction technique in three fatigue specimens. Because initial measurements of the transverse and longitudinal residual stresses made in one specimen (S1 series) showed similar distributions between transversal and longitudinal stresses, and to consider conservatively the effect of residual stresses, in the two additional fatigue specimens (S3 and S5 series) only the longitudinal residual stresses were measured. As can be seen in Figure 5.11, there were an M-shape close to the HAZ and FZ with residual tensile stresses at the HAZ and tending to zero or residual compressive stresses at the weld centerline. These results found about the shape, trend and the similar distribution between longitudinal and transverse residual stresses, agree with those reported in [35], where the residual stresses of a laser-welded 4 mm high strength low alloy HSLA steel plate were measured and simulated by FEM. There the residual stresses varied approximately from -200 MPa in the FZ to 250 MPa in the HAZ.

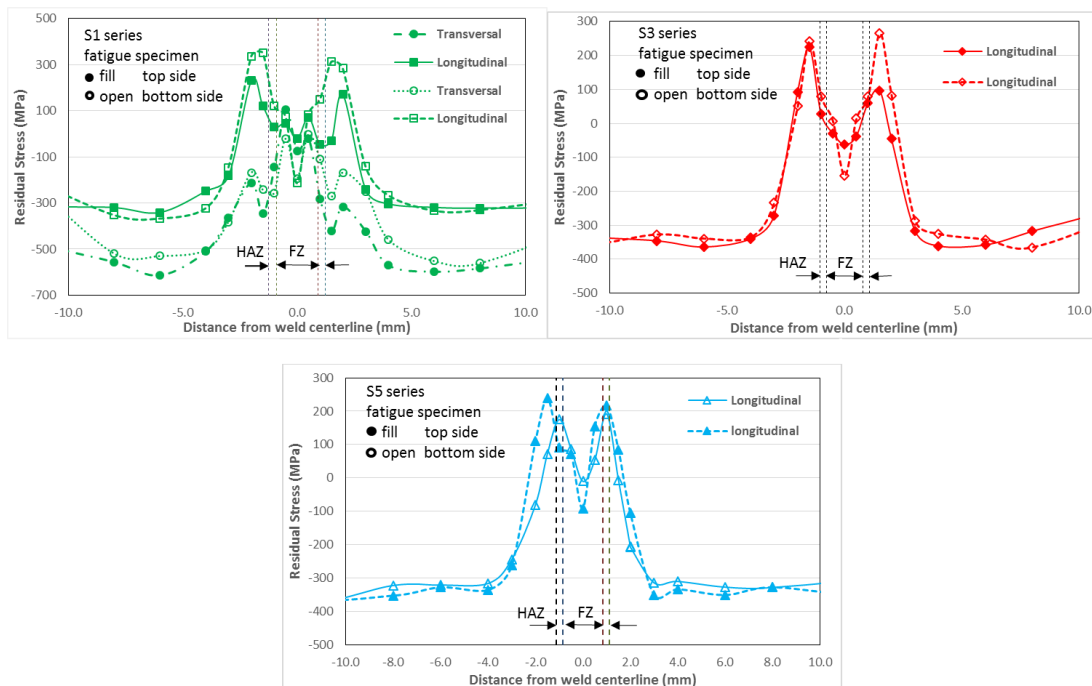


Figure 5.11 Residual stresses profiles in fatigue specimens.

Focusing attention on the sites where the starts of fatigue occurred: in the inner border of the HAZ (for excess weld and undercuts) and in FZ, but near to HAZ (the lowest point of the underfill); approximately residual stresses in the range of 200 to -40 MPa are observed in the graphs and although the differences in the values of the residual stresses between the welded series are small, it is worth noting that are approximately: 200 to 80 MPa, for S5 series; 130 to 50 MPa, for S1 series; 50 to -40 MPa, for S3 series. The results suggest that as the heat input decreases and therefore the cooling rate increases, the residual tensile stress progressively changes to residual compressive stresses, these results may be due to the effect of strains by the bainite and martensite transformation [36] since the proportion of these microstructures increases as the heat input decreases. Table 5.8 shows the residual stresses assumed for each series.

5.3.5.3. Fatigue limit evaluation

In previous sections it was shown that for low stress levels the approach of reducing fatigue strength through stress-concentrating effect can be used. To take in account the effect of the mean stress in the analysis of the fatigue strength at two million cycles of

the welded series, due to its simplicity, the modified Goodman line will be used according to the expression.

$$\frac{K_f \sigma_a}{S_e} + \frac{K_f \sigma_m}{S_{ut}} = \frac{1}{n_G} \quad (5.2)$$

where σ_a and σ_m are the nominal alternating (amplitude) and mean stresses applied and both are equal to $\Delta\sigma/2$ (according to $R=0$); K_f is the effective stress concentration factor calculated using the relationship of sensitivity to notch proposed by Peterson [37]; S_{ut} and S_e are the ultimate strength and the fatigue limit of the materials, that will be estimated for each welded series and BM through of the hardness HV, as $3.0xHV$ and $1.5xHV$, respectively, and n_G is the factor that evaluate the proximity to the mentioned failure criteria of the local stresses at imperfections of the specimens. When the residual stresses are considered, they will be added to the mean applied stress σ_m .

Table 5.8 shows the data used for the determination of the n_G factors for both, with residual stresses and without residual stresses for the welded series, conditions and imperfections indicated there, meanwhile, Figure 5.12 illustrates the position of the fatigue failure points of the specimens according to the mean and alternating local stresses in relation to respective modified Goodman lines.

Table 5.8 Data for fatigue strength assessment based on the modified Goodman line.

Case	Condition	Series-imperfection	Kt	ρ	Kf	Hardness (HV)	Residual stress (MPa)	Fatigue limits (MPa)	n_G factor	
				(mm)					with residual stress	without residual stress
1	as-welded	S1-undercut	3.29	0.06	2.33	335	130	180	1.08	1.60
2	bottom side-removed	S1-underfill	1.75	0.53	1.60	335	130	380	0.90	1.10
3	as-welded	S2-excess weld	2.25	0.06	1.74	345	90	270	1.20	1.47
4	bottom side-removed	S2-underfill	1.77	0.60	1.63	345	90	390	0.94	1.09
5	as-welded	S3-undercut	4.41	0.03	2.74	350	50	210	1.05	1.22
6	as-welded	S5-underfill	1.95	0.27	1.74	370	200	215	1.17	1.90
7	no-welded	Base metal	-	-	-	295	-	600	-	0.98

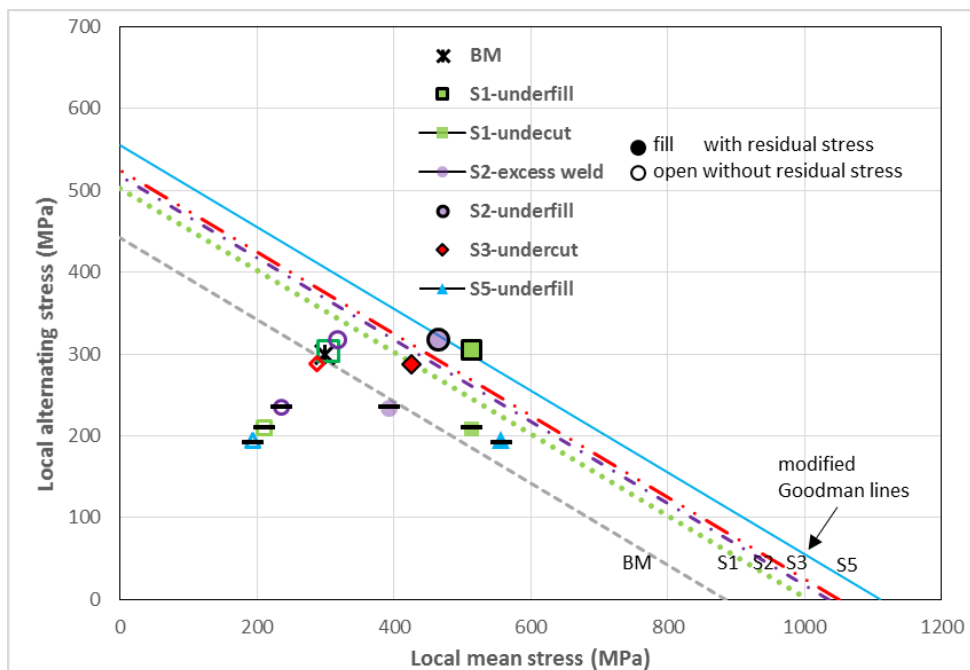


Figure 5.12 Fatigue failure points of specimens and modified Goodman lines.

When examining the concordance between the assumed failure criterion and the cases considered, it is found that it is excellent in the case of the BM, generally very good for all cases of the welded series when residual stresses were included and underestimated when they were not included, see Table 5.8 and Figure 5.12. It can also be noted that there is a good agreement considering with and without residual stress when the K_f values are low for underfill (cases 2 and 4), and on the contrary for the highest values of K_f (cases 1 and 5). Particularly even though when the residual stresses are considered, for the excess weld and the underfill of the S2 and S5 series respectively, there is the greatest discrepancy (close to 20%) between the experimental results and the assumed criterion (cases 3 and 6).

The effects of hardness, residual stresses and stress concentration on each welded series in the as-welded condition can be described as follows: the S1 series presented the lowest fatigue strength due to the combination of a high SCF at the undercut, a medium value of residual stress and a relatively lower hardness. The S5 series despite having the highest hardness and although the SCF was medium, due to the high value of the residual stresses it also presented low fatigue strength. The S3 series, with a low value of residual stresses and a high hardness, did not achieve a greater strength to fatigue because it had the highest SCF due to the sharp undercut in the weld root. The S2 series achieved the highest

fatigue strength of all series with medium SCF and hardness values and a relatively low residual stress value. It can be inferred that this series could achieve greater fatigue strength if the multiple small imperfections present along the weld root decrease. In other works the adverse effect of many small imperfections in addition to the weld bead profile on fatigue strength has also been reported [38, 39].

Regarding the fatigue limits achieved by the S1 (380 MPa) and S2 series (390 MPa) in the bottom side-removed condition, although the fatigue limit of the S2 series would be expected to be a little higher because its hardness is greater and the residual stresses are lower, the slight difference may be due, as already pointed out in a previous section, to the greater depth of the underfill and to the effect combined with the weld ripples.

In the case of the particular behaviour of the S5-F9 specimens which showed considerable greater fatigue strength than the other specimens of the S5 series, the weld profile in the bottom side were examined with more detailed finding that the underfill values were below the average of the series and the variation along to the axis weld were small as illustrated in other work [28]. The latter implies that the SCF of this series is lower and therefore its fatigue strength is higher.

The previous analysis showed that the SCF is a good predictor of fatigue limit in absence of multiple small imperfections such as those the S2 series that were not easily detected or when the SCF it is properly calculated (which was not the case of the S5 series). On the other hand, it shows a great effect of the residual stresses that is magnified by the SCF and by the mean applied stress. In summary, although the residual stresses found can be considered small, they adversely affect the fatigue strength of the welded specimens, as well as, the high SCFs due to the weld bead geometry and the small associated imperfections, meanwhile, the high hardness in the FZ and CG-HAZ it allows to improve the strength of the welded series.

5.3.6. Fatigue limit predictions

The estimates at low stresses showed that the fatigue strength can be predicted if the hardness, residual stresses, weld geometry and imperfections of the welded joints are known. Therefore using the expression (5.2), with $n_G = 1$ and the data in Table 5.8, the

fatigue strength at two million cycles in terms of stress range were predicted and the corresponding results for each welded series and conditions are showed in Table 5.9 together with the experimental results and the relation that compares both results.

Table 5.9 Fatigue limit predictions.

Series- Imperfection	Condition	Fatigue limits		
		experimental (MPa)	predicted (MPa)	ratio
S1-undercut	as-welded	180	201	0.90
S1-underfill	bottom side-removed	380	332	1.14
S2-excess weld	as-welded	270	336	0.80
S2-underfill	bottom side-removed	390	363	1.07
S3-undercut	as-welded	210	222	0.95
S5-underfill	as-welded	215	292	0.74

In previous Table 5.9, considering all results there are a good agreement between the experimental and predicted values. However a difference greater than 15 percent is found for the S2 and S5 series, these differences could be attributed for the S2 series, as already noted, to imperfections in the weld root that the stress concentration factor does not take into account and for the S5 series, to the results of a welding speed range (1.75 to 2.00 m/min) were unified in that series and therefore the value of the SCF can actually be higher than the one used (K_f , 1.95) since the latter was determined based on the average dimensions of the weld beads and on the other hand at small imperfections in the weld ripples.

Additionally, to the above predictions, to explain the effect of the imperfections present in the weld root of the S2 series and due to the small size of the undercuts present in the S1 series, the Murakami's relations proposed to predict the fatigue limit were applied to mentioned series, the relations have the form.

$$\sigma_w = \frac{1.43 (HV + 120)}{\sqrt{Area}^{1/6}} \left[\frac{1 - R}{2} \right]^\alpha \quad (5.3)$$

$$\alpha = 0.226 + \frac{HV}{10000} \quad (5.4)$$

where, σ_w (in MPa) is the fatigue limit, HV the hardness Vickers, R the stress ratio and \sqrt{Area} (in μm) the size parameter of the imperfection. The data shown in Table 5.10 correspond in the case of the S1 series to the average size of undercuts, while in the case of the S2 series, to the average depth of 10 measurements made on the long and narrow imperfections practically continuous in the weld root. In both cases the \sqrt{Area} parameter was calculated as $\sqrt{Area} = a\sqrt{10}$, where a , is the crack depth, according to Murakami's recommendation for this type of imperfection (very shallow surface crack) [12]. In the stress ratio R was considered the residual stresses of Table 5.8 and through an iterative process, in which fatigue limit values are assumed until equality in expression (5.3) is reached, were predicted the fatigue limits that are shown in Table 5.10 as well as the respective comparisons with the experimental results.

Table 5.10 Data and parameters for prediction of fatigue limits.

Series- Imperfection	Crack sizes length, depth (mm, μm)	\sqrt{Area} (μm)	Fatigue limits		
			experimental	predicted	ratio
			(MPa)	(MPa)	
S1-undercut	1.11, 40	126	180	214	0.84
S2-shallow crack-like	>0.23, 22	70	270	254	1.06

The results of Table 5.10 show that adequate predictions can be achieved through the approach proposed by Murakami, that in the case of the S2 series the prediction is better adjusted to the experimental value while in the case of the S1 series similar result was obtained as by the focus on the stress concentration. However, it should be noted that in the predictions according to this last approach it is necessary to know the imperfection and its size, which may not be evident, as in the case of the S2 series, where only once the specimens were fractured could they be observed and on the other hand, there may be variation in the sizes of the imperfections, which requires measurements and the application of some criterion, that in the present case was the average size. It should also be noted that in the case of undercuts (for series S1), a better prediction can be achieved if it is considered that approximately 4 to 5 undercuts were presented in each specimen, therefore it is more likely that the size of some of them is greater than the average size (40 μm). Taking into account that the depth of the undercuts varied from 15 to 105 μm [28], considering for example an

undercut depth of 90 μm , the fatigue limit would be 180 MPa, which is the same as the experimental result.

5.4. Conclusions

For four laser butt welded joints in thin HSLA steel plate, the effects of the weld profile, imperfections, hardness and residual stresses were considered to explain the experimental S-N curves and to predictions at low stress levels applying approaches based on both stress-concentrating effect and Murakami's relationship, the main conclusions drawn are:

- The fatigue strength of the welded series exceeded the FAT100 reference curve with fatigue limits in the range of 180 to 340 MPa, presenting multiple-imperfections shallow but sharp considered as crack-like imperfections and with B and D quality levels according to the ISO13919-1 standard.
- Although each series presented several fatigue failure modes due to the presence of different imperfections in the weld bead, a dominant failure mode strongly related to the imperfection with the highest SCF was observed for each series: 3.29-undercut-S1, 2.25-excess weld-S2; 4.41-undercut-S3; 1.95-underfill-S5.
- At low stress levels, the local properties of each welded series: hardness, residual stress and weld bead geometry, determined the fatigue limits and their influence was in very good agreement with the experimental results. Both high SCF and relatively low (< 200 MPa) residual tensile stresses affected the fatigue limits, only when SCFs are low (< 2.0) could the level (< 130 MPa) of residual tensile stresses not be considered, while the local hardness increased the fatigue limits of the welded series although its influence is less than the other two factors.
- The predictions of the fatigue limits were acceptable by the stress-concentrating effect when there were no small imperfections associated to excess weld, undercut or underfill, while when they were present or for small undercuts the relationship proposed by Murakami was appropriate.

5.5. References

- [1] W. Guo, Z. Wan, P. Peng, Q. Jia, G. Zou and Y. Peng, "Microstructure and mechanical properties of fiber laser welded QP980 steel," *Journal of Materials Processing Tech*, vol. 256, pp. 229-238, 2018.
- [2] N. Farabi, D. Chen and Y. Zhou, "Fatigue properties of laser welded dual-phase steel joints," *Procedia Engineering*, vol. 2, p. 835-843, 2010.
- [3] W. Xu, D. Westerbaan, S. Nayak, D. Chen, F. Goodwin and Y. Zhou, "Tensile and fatigue properties of fiber laser welded high strength low alloy," *Materials and Design*, vol. 43, pp. 373-383, 2013.
- [4] T. Gurney, *Cumulative damage of welded joints*, Cambridge: Woodhead Publishing Ltd, 2006.
- [5] A. F. Hobbacher, *Recommendations for Fatigue Design of Welded Joints and Components*, London: Springer, 2016.
- [6] S. J. Maddox, *Fatigue strength of welded structures*, Cambridge: Abington Publishing, 2002.
- [7] M. Chapetti and L. Jaureguizar, "Fatigue behavior prediction of welded joints by using an integrated fracture mechanics approach," *International Journal of Fatigue*, vol. 43, pp. 43-53, 2012.
- [8] Y.-H. Zhang and S. Maddox, "Fatigue life prediction for toe ground welded joints," *International Journal of Fatigue*, vol. 31, pp. 1124-1136, 2009.
- [9] H. Yamamoto, Y. Danno, K. Ito, Y. Mikami and H. Fujii, "Weld toe modification using spherical-tip WC tool FSP in fatigue strength improvement of high-strength low-alloy steel joints," *Materials and Design*, Vols. 1019-1028, p. 160, 2018.
- [10] J. Mei, S. Xiang, A. Vasu, J. Chung, R. Desai and P. Dong, "The fatigue limit prediction of notched components – A critical review and modified stress gradient based approach," *International Journal of Fatigue*, vol. 135, no. 105531, pp. 1-15, 2020.
- [11] J. Schijve, "The significance of fatigue crack initiation for predictions of the fatigue limit of specimens and structures," *International Journal of Fatigue*, vol. 61, pp. 39-45, 2014.
- [12] Y. Murakami, *Metal Fatigue: Effects of Small Defects and Nonmetallic Inclusions*, Oxford: Elsevier Science Ltd, 2002.
- [13] M. Åman, Y. Tanaka, Y. Murakami, H. Remes and G. Marquis, "Fatigue strength evaluation of small defect at stress concentration," *Structural Integrity Procedia*, vol. 7, pp. 351-358, 2017.
- [14] T. Lassen and N. Récho, *Fatigue Life Analyses of Welded Structures*, London: ISTE Ltda, 2006.
- [15] H. P. Lieurade, I. Huther and F. Lefebvre, "Effect of Weld Quality and Postweld Improvement Techniques on the Fatigue Resistance of Extra High Strength Steels," *Welding in the World*, vol. 52, no. 7-8, pp. 106-115, 2008.
- [16] C. Gerritsen, S. Vanrostenberghe and M. Doré, "Diode laser weld toe re-melting as a means of fatigue strength improvement in high strength steels," *Procedia Engineering*, vol. 66, pp. 171-180, 2013.
- [17] X. Cheng, J. Fisher, H. Prask, B. Yen, T. Graunapel-Herold and S. Roy, "Residual stress modification by post-weld treatment and its beneficial effect on fatigue strength of welded structures," *International Journal of Fatigue*, vol. 25, pp. 1259-1269, 2003.
- [18] F. Lefebvre, C. Peyrac, G. Elbel, C. Revilla-Gomez, C. Verdu and J. Buffière, "Understanding of fatigue strength improvement of steel structures by hammer peening treatment," *Procedia Engineering*, vol. 133, pp. 454-464, 2015.
- [19] G. Marquis and Z. Barsoum, "A guideline for fatigue strength improvement of high strength steel welded structures using high frequency mechanical impact treatment," *Procedia Engineering*, vol. 66, pp. 98-107, 2013.
- [20] S. Maddox, "Fatigue design rules for welded structures," in *Fracture and fatigue of welded joints and structures*, Cambridge, Woodhead Publishing, 2011, pp. 168-207.
- [21] I. Lillemäe, H. Remes, S. Liinalampi and A. Itävuo, "Influence of weld quality on the fatigue strength of thin normal and high strength steel butt joints," *Welding in the Word*, vol. 60, no. 4, pp. 731-740, 2016.
- [22] P. Kucharczyk, M. Madia, U. Zerbst, B. Schork, P. Gerwien and S. Münstermann, "Fracture-mechanics based prediction of the fatigue strength of weldments. Material aspects," *Engineering Fracture Mechanics*, vol. 198, pp. 79-102, 2018.
- [23] S. Li, Y. Khan and S. Kuang, "Effects of microstructure on fatigue crackgrowth behavior in cold-rolled dual phase steels," *Materials Science & Engineering A*, vol. 612, pp. 153-161, 2014.
- [24] O. Watanabe, S. Matsumoto, Y. Nakano and Y. Saito, "Fatigue strength of welded joints in high strength steel Effects of stress concentration factor and welding residual stress," *Welding International*, vol. 10, no. 3, pp. 201-206, 1996.

- [25] E. Harati, L. Karlsson, L.-E. Svensson and K. Dalaei, "The relative effects of residual stresses and weld toe geometry on fatigue life of weldments," *International Journal of Fatigue*, vol. 77, pp. 160-165, 2015.
- [26] N. Nguyen and M. Wahab, "The Effect of Undercut and Residual Stresses on Fatigue Behaviour of Misaligned Butt Joints," *Engineering Fracture Mechanics*, vol. 55, no. 3, pp. 453-469, 1996.
- [27] T. Shiozaki, N. Yamaguchi, Y. Tamai, J. Hiramoto and K. Ogawa, "Effect of weld toe geometry on fatigue life of lap fillet welded ultra-high strength steels joints," *International Journal of Fatigue*, vol. 116, pp. 409-420, 2018.
- [28] P. Riofrío, C. Capela and J. Ferreira, "Imperfections and Modelling of the Weld Bead Profile of Laser Butt Joints in HSLA Steel Thin Plate," *Metals*, vol. 11, no. 151, pp. 1-19, 2021.
- [29] ISO, *Welding - Electron and laser-beam welded joints - Guidance on quality levels for imperfections. Part 1: Steel; ISO 13919-1(1996)*, Geneva: ISO, 1996.
- [30] "Data Sheet S700MC," 2017. [Online]. Available: <http://www.saltgutter-flachsthal.de>.
- [31] P. Riofrío, C. Capela, J. Ferreira and A. Ramalho, "Interactions of the process parameters and mechanical properties of laser butt welds in thin high strength low alloy steel plates," *Journal of Materials: Design and Applications*, vol. 234, no. 5, pp. 665-680, 2020.
- [32] ASTM International, *Standard Practice for Conducting Force Controlled Constant Amplitude Axial Fatigue Tests of Metallic Materials. E466-15 (2015)*, West Conshohocken: ASTM International.
- [33] ASTM International, *Standard Practice for Statistical Analysis of Linear or Linearized Stress-Life (S-N) and Strain-Life (ϵ -N) Fatigue Data. E739-10(Reapproved 2015)*, West Conshohocken: ASTM International.
- [34] H. Remes and P. Varsta, "Statistics of weld geometry for laser-hybrid welded joints and its application within notch stress approach," *Welding in the World*, vol. 54, no. 7/8, pp. R189-R207, 2010.
- [35] W. Fricke, *IW Recommendations for the Fatigue Assessment of Welded Structures by Notch Stress Analysis*, Oxford: Woodhead Publishing Limited, 2012.
- [36] M. Alam, Z. Barsoum, P. Jonsén, A. Kaplan and H. Haggblad, "The influence of surface geometry and topography on the fatigue cracking behaviour of laser hybrid welded eccentric fillet joints," *Applied Surface Science*, vol. 256, pp. 1936-1945, 2010.
- [37] W. Pilkey, *Peterson's stress concentration factors*, New York: John Wiley & Sons, 1997.
- [38] B. Schork, U. Zersbt, Y. Kiyak, M. Kaffenberger, M. Madia and M. Oechsner, "Effect of the parameters of weld toe geometry on the FAT class as obtained by means of fracture mechanics-based simulations," *Welding in the Word*, vol. 64, no. 6, pp. 925-936, 2020.
- [39] J. Otegui, H. Kerr, D. Burns and U. Mohaupt, "Fatigue Crack Initiation from Defects at Weld Toes in Steel," *International Journal Pressure Vessels & Piping*, vol. 38, pp. 385-417, 1989.

Chapter 6: Influence of local properties on fatigue crack growth of laser butt welds in thin plates of high-strength low-alloy steel

P.G. Riofrío^{a,b}, Joel de Jesus^{b*}, José A. M. Ferreira^b, Carlos Capela^{b,c}

^aDECEM, Departamento de Ciencias de la Energía y Mecánica, Universidad de las Fuerzas Armadas-ESPE, Av. General Rumiñahui S/N, 171103 Sangolquí, Ecuador.

^bDepartment of Mechanical Engineering, Centre for Mechanical Engineering, (CEMMPRE) University of Coimbra, P-3004 516 Coimbra, Portugal.

^cESTG, Department of Mechanical Engineering, Instituto Politécnico de Leiria, School Tech and Management, Morro do Lena - Alto Vieiro, 2400-901 Leiria, Portugal.

Submitted to **Applied Sciences** journal.

Abstract

In this work, local properties as hardness and fatigue crack grow rate in the heat-affected zone for four laser-welded butt joints in thin high-strength low-alloy steel were examined, so as to explain and predict fatigue lives at high stress levels through the fracture mechanics approach. The different welded series presented a similar fatigue crack growth rate in the heat-affected and fusion zones, but lower than base metal due to the higher hardness of the bainitic-martensitic microstructure verified in the welded series. The results showed that at high stress levels in the as-welded condition, the fatigue initiation stage can be neglected and assume types of cracks, an initial crack of 0.07 mm and appropriate fatigue crack growth rates, estimates of fatigue life close to the experimental results were obtained.

Keywords: Fatigue crack growth, laser welding, high-strength low-alloy steel, fatigue life.

6.1. Introduction

The fatigue behaviour of steel welds has been widely studied, but there are still gaps in the knowledge of this complex subject due to several factors that affect the fatigue strength and even more so in what concerns to thin thicknesses and unconventional welding processes. The weld quality, the residual stresses and the material, among others, are pointed out as the main factors that affect the fatigue strength [1, 2]. Although it has been shown that the weld quality control [3] or the use of post-weld treatments [4-7] in welded joints with high strength steels increases the fatigue strength by reducing the severity of its inherent imperfections and this fact is recognized in design guides, allowing to increase the strength curve (FAT class) of welded joints when the imperfections have been verified with nondestructive testing (NDT) or when an improvement method has been used [8]; there is no differentiation in the increase according to the tensile strength of the materials. The foregoing has been explained in [9], due to the fact that the crack growth dominates the fatigue life of the welded joints and because the fatigue crack growth rate (FCGR) is insensitive to the mechanical strength of the material, however, as counterpart in [10], it was shown that when the weld quality is high, for high-strength steels, the fatigue strength is positively correlated to tensile strength.

The general effect of notches and residual stresses on fatigue strength of welded joints is well known as their combined effect was analyzed in various studies. However, in almost all works, thick plates and conventional welding processes were used [11-14]. Microstructural details such as grain size, phases and hardness also affect the fatigue behaviour of the welded joints. The crack propagation generally occurs in the heat affect zone (HAZ) and in the fusion zone (FZ) because the properties of these zones are usually different from base metal (BM), the use of local properties such as hardness and fatigue crack growth parameters can be useful to improve the analyzes and predictions of fatigue strength [15-17].

In welded joints the increase of plates thickness decreases the fatigue strength. For the same nominal stress, thicker welded plates have lower fatigue strengths than thinner welded plates. In thicker geometrically similar plates, the stress concentration field due to the weld toe extends over a larger volume so that small microcracks that form are driven by higher stresses [18]. A reduction factor is applied to the fatigue strength if the thickness

plates exceeds 25 mm [8], however if the plates' thickness is lower, there is no rule for the fatigue strength increase. In [19] a rule was estimated for the fatigue strength increase due to thickness plate decrease for thicknesses lower than 25 mm, which depends of the initial crack size. Nevertheless, these authors highlighted that for thickness less than 6 mm where observed an opposite effect when the initial crack size is higher than 0.3 mm was observed.

The presence of defects acting as a fatigue pre-crack are the main reason to a substantial reduction of the fatigue strength in welded joints. This determines that the initiation period can be neglected [8, 18] and that the fracture mechanics seems to be the appropriate approach to determine the fatigue life [9]. In various works where the assessment and prediction of the fatigue life are based in fracture mechanics, the basic procedure takes as base the Paris law and the stress intensity factor (SIF) applied to imperfections in all range of stress levels. However, due to the small size of cracks or in low stress levels also the initiation stage is considered [19, 20]. Additionally, refinements or variants to the Paris law are applied to predict or analyze the fatigue life of welded joints [21, 22]. Based in fracture mechanics, Murakami [23] proposed an expression for fatigue limit predictions of materials containing small defects or cracks in function of the hardness and the size of small defects; and Åman et al. [24], in a recent work, modified the aforementioned expression in order to analyze the consequence of a small defect at the notch root.

To define the welded joints imperfections previously described as a semi-elliptical crack, corner crack, and extended crack is a common practice whereby the guides and standards that use the fracture mechanics approach contain information of crack growth parameters, recommendations about the crack sizes and the appropriate expressions for calculation of SIFs and other factors [8, 25]. In the so-called IBES approach [26] based on fracture mechanics, it is observed that, where among other aspects, the determination of the fatigue strength is obtained statistically, considering the variation of weld bead along of weld axis and local properties of the fused zone (FZ) and heat affected zone (HAZ).

As was previously mentioned, the influence of the main factors on fatigue strength and application of fracture mechanics for welded joints with thin elements is a topic that lacks information. This study starting from a previous work [27] where the the weld bead geometry, imperfections and the weld quality level of welds were determined

according to the ISO13919-1 standard [28]. In the present study the influence of welding parameters on fatigue crack growth rate (FCGR) of laser butt welds in thin plates of high-strength low-alloy steel were analyzed. The local properties for the FCGR were determined and used them in order to predict the fatigue life through the failure analysis and fracture mechanics approach disregarding the fatigue initiation period for fatigue life at high stress levels. The FCGR parameters were obtained through of fatigue crack growth tests and complementary tests and analysis such as metallographic, hardness, crack closure and fractography were also performed.

6.2. Materials and Methods

HSLA steel plate Strenx® 700MCE with 3 mm thick were used in order to perform the butt-welded joints. This steel is composed by a fine-grain ferritic-bainitic microstructure. The chemical composition can be consulted in Table 6.1 and this material showed a yield strength of 808 MPa, a tensile strength of 838 MPa and 15 % of elongation at failure [29].

Table 6.1 Chemical composition of the base metal.

C	Mn	Si	P	S	Cr	V	Nb	Ni	Cu	Al	Mo	Ti	Co	Fe
0.07	1.69	0.01	0.012	0.006	0.03	0.02	0.046	0.04	0.011	0.044	0.016	0.117	0.016	balance

Five series were welded using the parameters presented in Table 6.1. The series S1-S4 were welded with a single pass in one side of the plates (top side) while the S5 series was welded applying two passes: one in each plates' side (top and bottom side). The welding equipment used was a disk laser Trumpf TruDisk 2000 with: laser maximum output of 2000 W, beam wavelength of 1020 nm, beam parameter product of 2 mm-mrad and fiber diameter of 200 μm. The equipment was used in continuous mode and did not used filler material.

Table 6.2 Welding parameters used in the experimental work.

Series	Laser power (kW)	Welding speed (m/min)	Heat input (J/mm)
S1	2.00	1.60	75.0
S2	1.75	1.60	65.6
S3	2.00	2.00	60.0
S4	1.75	2.00	52.5
top side weld pass			
S5	1.75	1.75-2.00	52.5-60.0
	bottom side weld pass		
	1.25	2.50	30.0

It is important to mention that in the S5 series the welding speed on the top side was different for each sample (1.75, 1.80, 1.90, 1.95 and 2.00 m/min) while the weld pass on the bottom side was constant for all samples (2.50 m/min). The heat inputs used in welding were chosen to achieve different hardness in the welded series, but maintaining at the same time a low heat input to achieved small HAZs, low softening and similar tensile mechanical properties to the BM as shown in [29].

The fatigue crack growth tests were carried out in a Dartec hydraulic machine using the ASTM E647-13a standard [30] as guideline. The FCGR rate determination for the BM and welded series was achieved with constant load range ΔP tests (ΔK increasing) and were used M (T) specimens' geometry. The samples' geometry used in the FCGR test can be consulted in Figure 6.1. As is possible to see in Figure 6.1, pre-cracks were machined by electrical discharge machining (EDM) and were localized on the underfill (see Figure 6.3). The specimens were loaded perpendicularly to the weld direction at stress ratio $R=0$, at room temperature and with 15 Hz of frequency. The FCGR tests were performed in three conditions: not-welded (BM), excess weld-removed and both sides-removed.

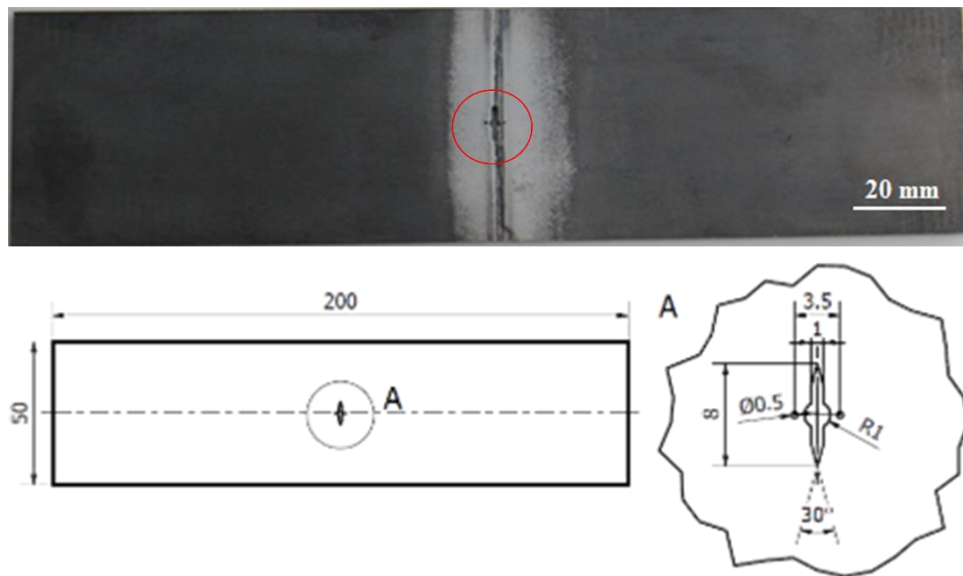


Figure 6.1 Specimens geometry used in FCGR tests, dimensions in mm.

The crack length was measured by optical observation through of a travelling micro-scope (45x) with digital micrometers and the crack growth rates were calculated according to the 5-points incremental polynomial method, following the ASTM E647-13a standard [30]. Once the specimen was cracked until a minimum crack size of 1 mm, at intervals with crack size increments (Δa) of 0.25 mm, the number of cycles was registered. During the test, it was verified that the measurements of the lengths of the two cracks do not differ more than 1.25 mm. The stress intensity factor range (SIFR) was calculated according the expression that corresponds to M (T) specimen given in [30]. The results were displayed as da/dN vs ΔK curves, only for the regime II of the Paris law for each condition.

In order to consider the crack closure effect on the FCGR, at regular intervals during the crack growth, the crack opening displacement (COD) between the two holes localized in the centerline of the specimen (see Figure 6.1) was recorded using a pin microgauge extensometer. These results were plotted in load vs COD and the tangent point method were applied for determinate the load for which the crack remains fully open, P_{op} [31].

S-N curves were obtained from dogbone-like shape specimens with a rectangular cross section with 12.5x3 mm. The fatigue tests were performed in the same machine and with the same conditions where were done the FCGR tests were done.

The metallographic analysis was completed through polishing and etching the cross section of the samples. Afterwards, the samples were observed through an optical micro-scope Leica DM4000 M LED. The reagent used for the etching process was Nital at 2%. The hardness Vickers tests were performed using a Struers Type Duramin-1 microhardness tester, applying 0.5 kg during 10 s. Finally, the fatigue fracture surfaces were observed using a stereo microscope and the defects measurement was achieved using x and y micrometers.

6.3. Results and discussion

6.3.1.1. Welded defects and hardness

Figure 6.2 illustrates the macrographs analysis of the welded series, were obtained a different morphology in each series was obtained. The principal imperfections noted there were: excess weld in the bottom side of the S1, S2 and S3 series and in the top side of S4 and S5 series; undercuts at the weld root in the bottom side of the S1 and S3 series and underfill and porosity in all series. In [27] it was reported that the series presented quality levels B and D according to the ISO 13919-1 welding quality standard and the imperfection sizes and morphology can be consider as crack-like imperfections. More details about the weld pro-file and imperfections of the welded series can be found in the previous reference. Due to the S4 series not reaching full penetration it will be omitted in the next sections.

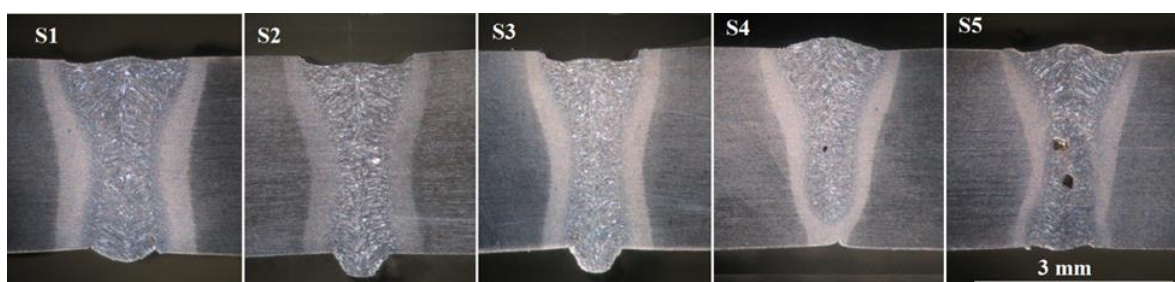


Figure 6.2 Cross-sections macrographs of the welded series.

Because the fatigue started on both sides of the weld bead and the fatigue trajectories occurred through the FZ and HAZ, the microstructure and hardness at these sites must be examined because they are factors that affect fatigue behaviour. Figure 6.3 presents a representative example of metallographic analysis were Figure 6.3b corresponds to the

megalographic analysis and underfill defect, Figure 3c shows the toe of weld root and Figure 6.3d illustrates an undercut defect. For the heat input range used in the present work, Figure 6.3b showed that the HAZ zone was divided in two important zones: softened ferritic-bainitic with fine grain (FG) and bainitic-martensitic with coarse grain (CG) as was found [29], can be also observed the FZ and BM.

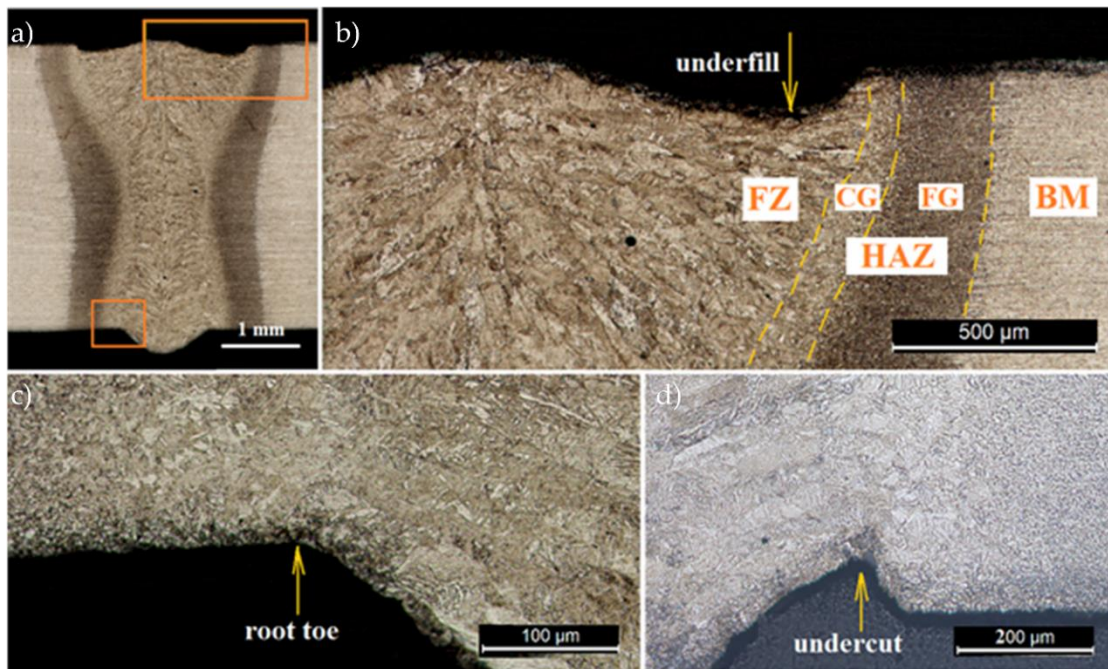


Figure 6.3 Metallographic and morphologic analyses. **a)** S1 series macrograph, **b)** Metallographic analysis and underfill defect, **c)** toe of weld root, **d)** un-dercut defect.

According to the fracture analysis, the fatigue starts in the weld root and undercuts located in the boundary between the columnar grains of the FZ and the CG, in the underfill located in the columnar grains of the FZ but very close to the HAZ and in pores located in the FZ. If fatigue crack paths depart from defects as underfill, undercuts and weld root (toe), they could enter to the FG that is generally a soft zone. The microhardness presents similar profiles for the different series, a very small softening in FG was verified. The hardness increases with the heat input decrease at the FZ and CG, but the difference in hardness is minimal in the sites where the fatigue started. For the fatigue starts locations, the approximated hardness values were: 335, 345, 350, and 370 HV for the welded series S1, S2, S3 and S5 respectively and approximately 295 HV for the BM. This increase of hardness can be explained by the quick cooling in the FZ and CG which allowed the bainitic-

martensitic microstructural transformation while the FG zone cool down slower modifying the BM microstructure to softened ferritic-bainitic microstructure.

6.3.2. S-N curves

The S-N curves obtained can be analyzed observing the Figure 6.4. The BM presented a higher fatigue strength than all welded series due to a free of defects condition and free of stress concentration points. Generally speaking, all series presented a similar fatigue behaviour, although the scatter is high and there is some difference in the fatigue limits of the welded series. In Table 6.5, the S-N parameters, $\log C$ and m of the mean curves and the fatigue limits are shown. The fatigue limits were assumed as the maximum stress range values reached by the specimens that exceeded two million cycles (run-outs).

Although each series presented several fatigue failure modes due to the presence of different imperfections in the top and bottom sides, as well as on the lateral side and inside the weld bead due to the presence of pores, a dominant failure mode was strongly related to the imperfection with the highest stress concentration factor was observed for each series.

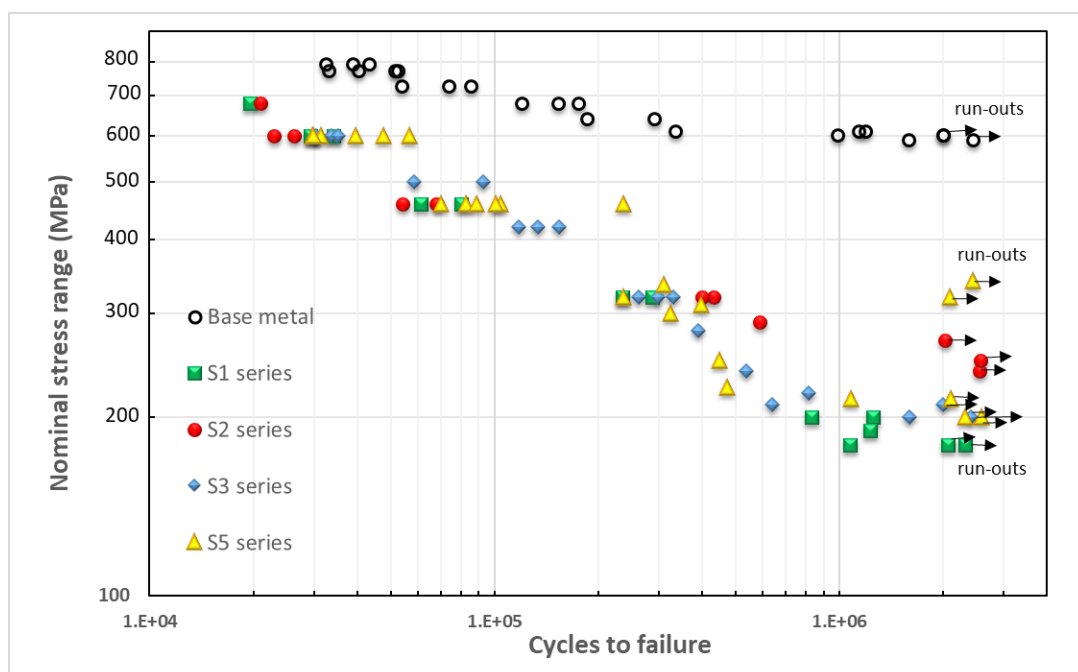


Figure 6.4 S-N curves

Table 6.3 S-N curves parameters and fatigue limits

Series	linear model	log C	m	Fatigue limits
S1	no rejected	13.455	3.226	180
S2	no rejected	16.206	4.247	270
S3	no rejected	13.248	3.118	210
S5	no rejected	13.469	3.206	215

6.3.3. Fatigue crack growth

Figure 6.5 shows the FCGR rate found for each series using two specimens in which the notches were cut on the underfill of the weld beads seeking to agree with the sites where the failure occurred in the fatigue testing. As can be seen for the S1, S2 and S3 series, the specimens that were smoothed on both sides (two sides-removed condition) showed a slightly slower crack growth rate than specimens smoothed only on one side (excess weld-removed condition).

In the case of the S5 series, even though the two specimens were prepared as the other series, the initial equality and subsequent greater difference (from the dotted line in S5 series) observed in the crack growth rates can be explained once the crack paths and fractured surfaces were examined. For the specimen with faster crack growth rate, it was found that the direction of the growth of the cracks gradually deviated from FZ towards the BM and therefore the crack growth rate of the upper part of the curve correspond to the BM. In the case of the specimen with a slower crack growth rate, the change in the slope was due to a large difference between the crack sizes (exceeding the limit for the test validity) as one of the crack fronts was affected by porosity while the other was not.

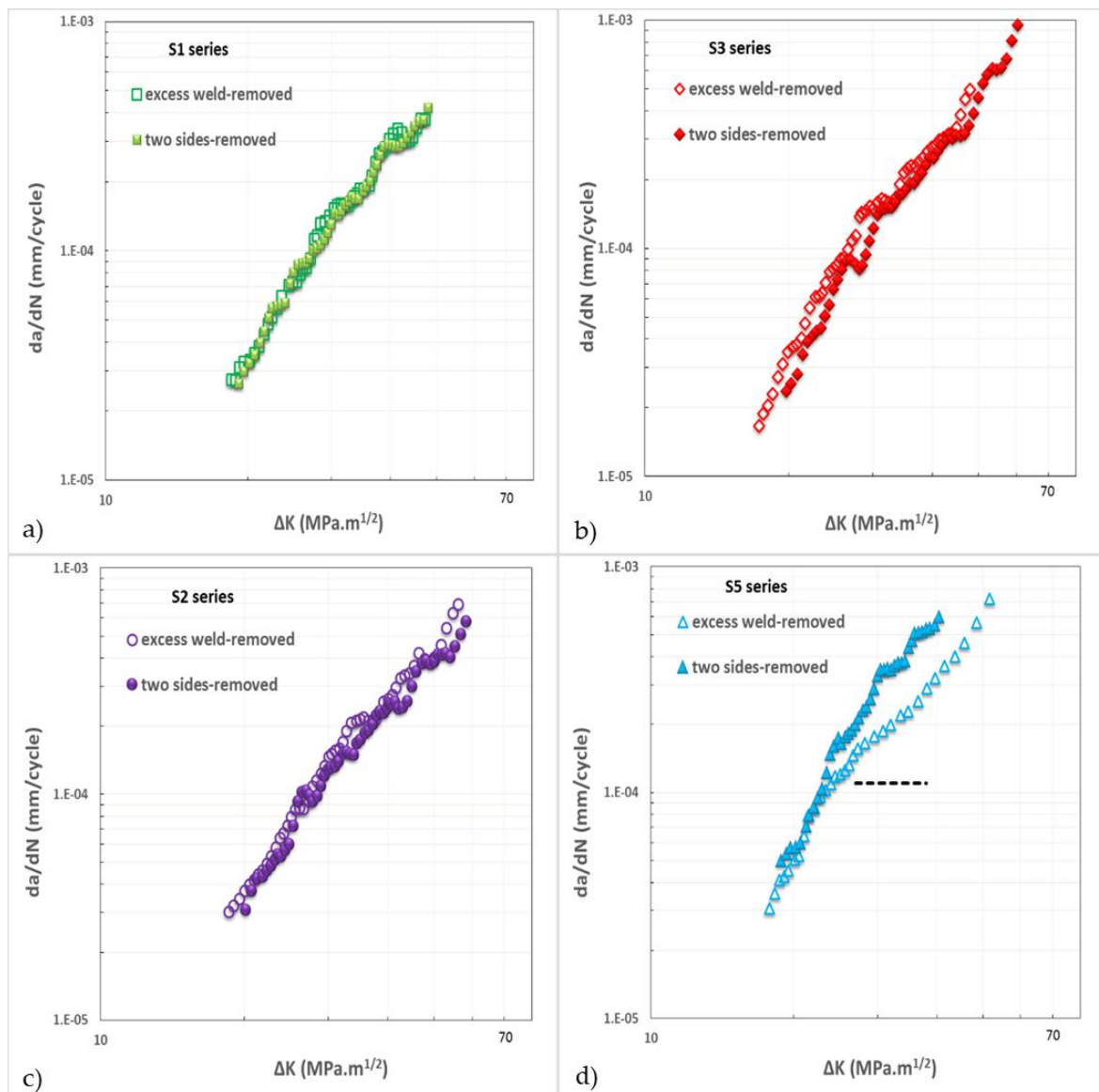


Figure 6.5 Fatigue crack growth rate at Paris regime. a) S1 series, b) S3 series, c) S2 series and d) S5 series.

6.3.4. Crack opening displacement and crack closure

The ΔP -COD example curves of the welded series and the BM plotted in Figure 6.6, where the non-linear part of the curves were marked by the tangent points, illustrating a different behaviour in relation to the crack closure phenomenon: the S1 and S5 series did not present crack closure, in the S2 series it was so minimal that in practice it can be considered null, while in the S3 series and in the BM this phenomenon was presented but in a different way. In the crack size range of 1-12 mm, for the BM, the load range at which the point of

tangency occurred was approximately constant, meanwhile, for S3 series, the load range increased and subsequently decreased.

Should the crack tip plasticity be assumed as the main cause of the crack closure, the behaviour observed could be explained considering the hardness and ductility of microstructures. The BM has low hardness and good ductility while the welded series the propagation paths had in the HAZ and FZ where the hardness is high and therefore low ductility. On other hand, it has been explained in [32] that due to the presence of residual tensile stresses, there is no crack closure. The particular behaviour of the S3 series could be caused by the crack path that also crossed the FG-HAZ (which is softer) since the its weld bead size is smaller than in the other series, and there could be residual compressive stresses presents in this series that contribute to the crack closure as reported in [32].

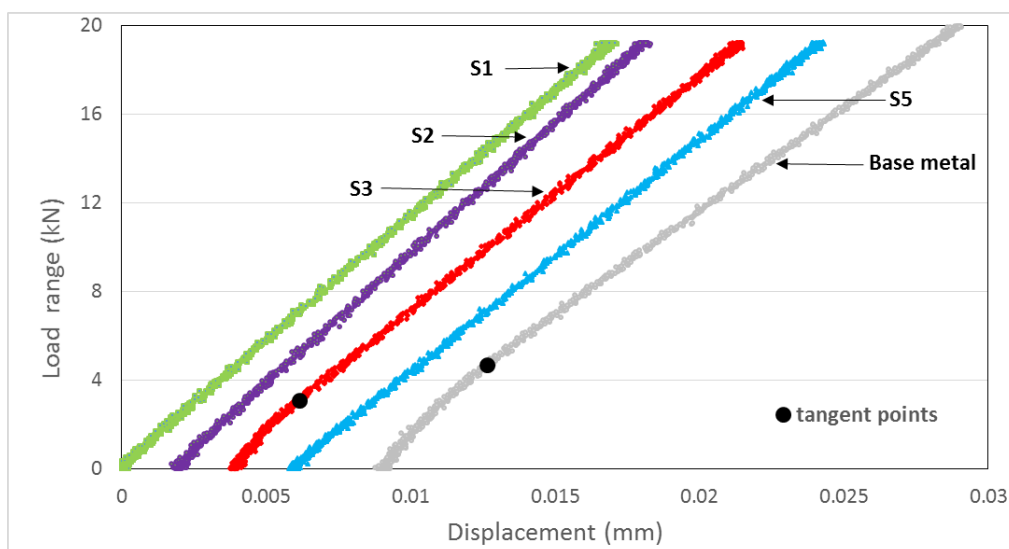


Figure 6.6 ΔP -COD example curves of each welded series and BM.

According to the above results and assuming the average of the load ranges values ΔP where the tangent points were observed for the crack sizes from 1 to 12 mm, the crack opening stress range ΔS_{op} and the $\Delta K_{eff}/\Delta K$ ratio were calculated for the BM and the S3 series, the results are respectively: 24.43 MPa, 0.82 and 15.94 MPa, 0.89; meanwhile for the series S1, S2 and S5, the values of ΔS_{op} were assumed equal to zero and therefore the $\Delta K_{eff}/\Delta K$ ratio equal to one.

The crack growth rates in function of the stress intensity factor range (SIFR) of the specimens from which the excess weld was removed and of BM are shown in Figure 6.7 and as can be seen, the S1, S2 and S3 series had practically the same crack growth rate, the S5 series had a slightly higher than the previous ones, while the BM has the highest crack growth rate due to having a lower hardness as was described previously. With the $\Delta K_{eff}/\Delta K$ ratio already obtained, for the BM and welded series, the effective SIFR, ΔK_{eff} , was determined, the $da/dN-\Delta K_{eff}$ curves were redrawn (Figure 6.7b). Table 6.4 shows the parameters A and n of the Paris law for the welded series and BM

The results found for the welded series suggest that the weld ripples, porosity, residual stress and the microstructure were factors that influenced on the crack growth rate. In relation to weld ripples even though the effect was very small, their size and shape can modify a more or less straight path to a zigzag one and therefore the propagation life [33]. Since the BM microstructure was constituted by ferrite-bainite while for the welded series by basically mixtures of bainite-martensite [29], there is a clear effect of decrease in the crack growth rate that can be attributed to the microstructure by the higher proportion of bainite and the presence of martensite. This agrees with the works [34, 35] where a retarding effect was reported in the growth of cracks due to the presence of hard phases such as martensite and bainite. Regarding porosity, this factor requires a better study since, as noted only one of the cracks was affected by this factor. In summary, since it is recognized that the phenomenon of crack growth is more influenced by the bulk properties than by the surface properties, the microstructure, the hardness and residual stresses could affect the crack growth rate to a greater degree while the effect of weld ripples was minimal.

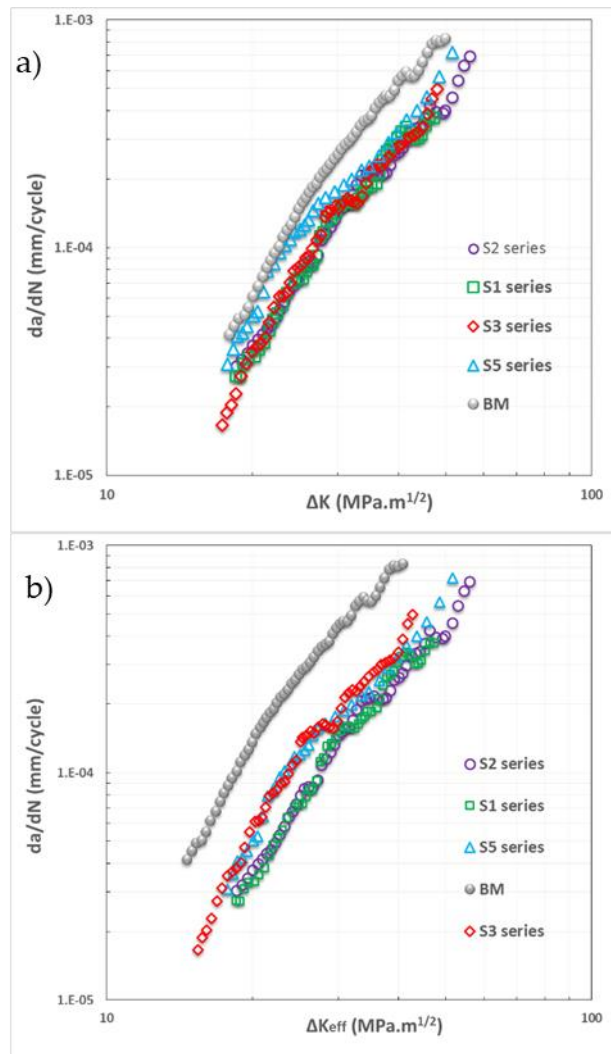


Figure 6.7 Fatigue crack growth rate at Paris regime. **a)** da/dN - ΔK and **b)** da/dN - ΔK_{eff} .

Table 6.4 A, n parameters of the FCGR¹ curves in function of ΔK_{eff}

Series	A	n
S1	6.00E-09	2.9147
S2	1.00E-08	2.7374
S3	4.00E-09	3.0276
S5	2.00E-08	2.6565
BM	2.00E-08	2.9556

¹ (da/dN in mm/cycle and ΔK_{eff} in MPa m^{1/2})

6.3.5. Effect of Imperfections at high stress levels

According to the fracture analysis, the fatigue starts in the weld root and undercuts located at the boundary between the columnar grains of the FZ and the CG, while those in the underfill are located on the columnar grains of the FZ but very close to the HAZ. In pores the starts were located in the FZ. If fatigue straight paths are considered from underfill, undercuts and weld root (toe), they could enter to the FG-HAZ that is generally a soft zone, this is most likely when the crack depth is large, start from underfill and in the S3 and S5 series in which the FZ sizes are narrower. Another aspect that is interesting to be noted is the defect size in relation to the grain size, so for example in the case of the undercut shown, in the direction of thickness, the undercut depth is greater than the size of the grains of the FZ or HAZ, however, when considering approximately the undercut radius or the small imperfection above the undercut, they would be similar to the CG grain size, see Figure 6.3. These last observations give account of the imperfections' character as crack-like imperfections.

The fractured surfaces of all specimens at the stress level of 600 MPa were examined and it was found that the size, quantity, and the location of imperfections are important to explain their fatigue lives, as described below with the specimens shown in Figure 6.8.

In Figure 6.8a to 6.8d, the specimens of all series in the as-welded condition show as principal characteristic that the fatigue failure occurred covering the entire width of the specimens and the fatigue lives were similar with the exception of specimens of the S2 series, which had a shorter life. The latter is due to the fact that unlike the other series where several fatigue cracks started were observed in cracks that grew semi-elliptical, in the S2 series, the growth of this type of cracks was not evident and there was practically only one crack front growing in depth along of width of the specimens. Similar failure mode was reported in [36] where by the high density of undercuts, one straight-fronted crack was the cause of the great reduction of fatigue strength.

In Figure 6.8e and Figure 6.8f, the factor that seems to influence the shorter life (29910 cycles) of the one of the two specimens of the S2 series in the bottom side-removed

condition, is the location of the failure starts towards the corner and the principal fracture surface on the lateral side of the specimen, meanwhile, although the specimen with the longest life (36597 cycles), presents fatigue starts that cover almost the entire width of the specimen, it was possible to observe a small growth until it coalesce and then a single semi-elliptical crack grew to the fracture. This last fact marks the difference of this specimen with the others of lesser lives, see Figure 6.4.

In Figure 6.8g to Figure 6.8j, the fatigue lives of these specimens increased considerably in relation to the previous specimens presenting large and semi-elliptical fatigue cracks located centrally. The differences observed in the fatigue lives between the two specimens in bot-tom side-removed condition are: the size and number of fatigue starts. The specimen with the longest life (91815 cycles) had a single large visible start while the one with the shortest life (75849 cycles) had several starts smaller that coalesced, however, it can be seen that the width after coalescence is greater than the width of the start of specimen with the longest life and there is also a little difference in the final aspect ratios (depth/length). The increase in the fatigue lives of the specimens presented in Figure 6.8i and Figure 6.8j and the differences between them, are explained in a similar way to the previous specimens: they are due to the fact that the size of the fatigue starts decreased significantly, which, as seen in the photographs, are a bit more difficult to identify despite the higher magnification. For these specimens it should be clarified that although the elimination of imperfections on both sides of the weld beads was verified through the microscope, the small imperfections that appear in the photographs may correspond to subsurface imperfections that did not dis-appear through the grinding applied to the specimens. In the work [20] this issue also was reported.

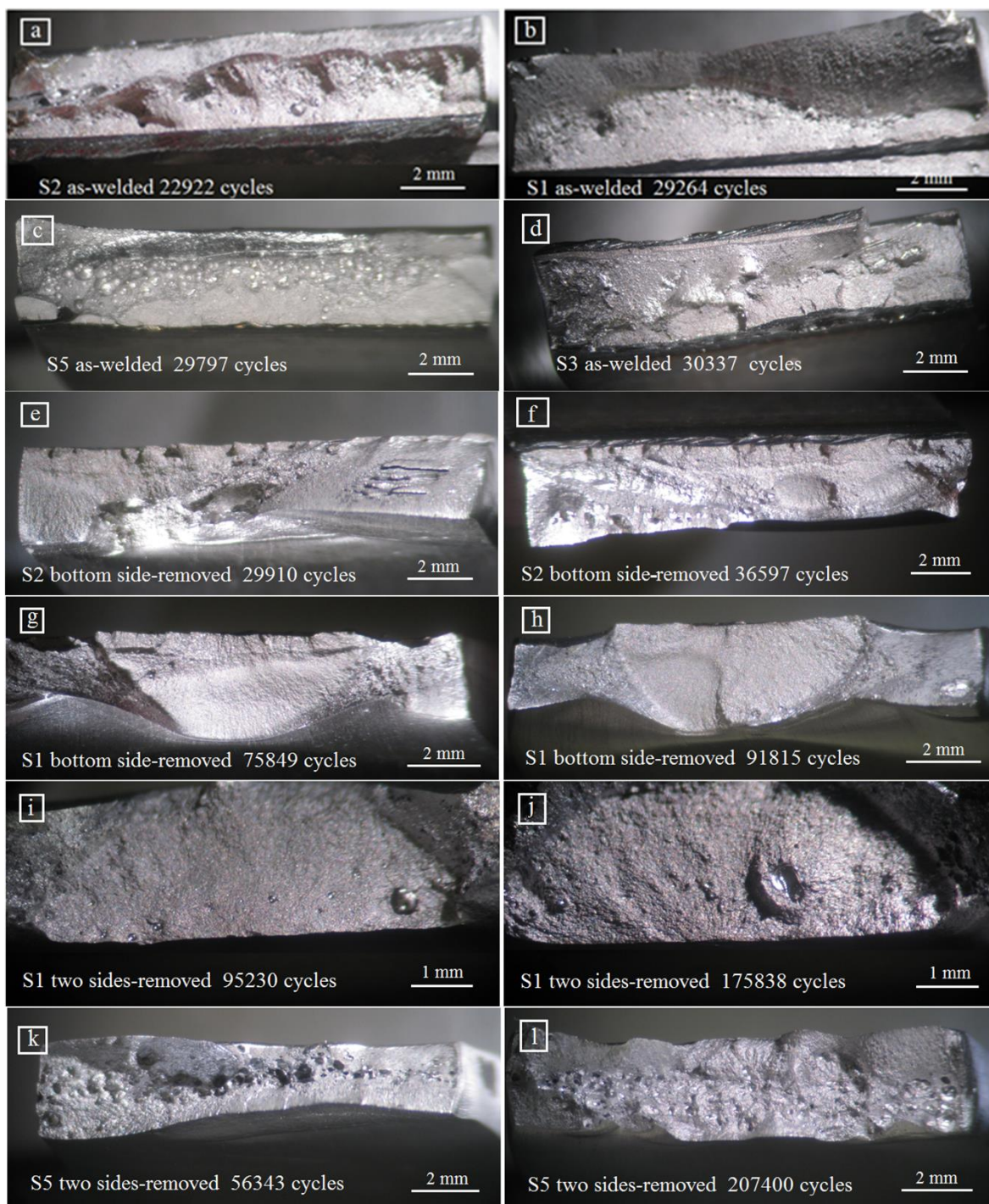


Figure 6.8 Fractured surfaces of specimens at 600 MPa.

In the last specimens of the S5 series shown in Figure 6.8k and Figure 6.8l, it is relevant that once the imperfections on both sides of the weld beads were removed, the fatigue failure corresponds to pores, surface pores located on the lateral side for the specimen with shorter life (56343 cycles) and internal pores for the specimen with longer life (207400

cycles). The apparent scatter previously mentioned for these specimens is actually the effect of the location of the pores in the specimens, as reported in the literature for pores near to the surface and for internal pores [37, 38]. From the previous review on the fractured surfaces, for the stress level examined, it can be inferred that in the fatigue life, the type and shape of the imperfections are less important than the size, quantity and location and there was a certain order in the fatigue lives of the specimens, from the lowest to the highest: a continuous very small surface imperfection along of the width of specimen; various surface imperfections covering the width of the specimens or imperfections near to the border that produce fatigue in the lateral side, but growing semi-elliptical; surface pores or near at surface in the lateral side; one big or few small surface imperfections that no cover the width of specimen that growth as one semi-elliptical crack; a condition similar to the previous one but with very small imperfections and one or various internal imperfections (pores). It should also be noted that specimens from all welded series, conditions and type of imperfections (undercuts, underfill, excess weld and pores) were included in the analysis carried out.

In summary, for the as-welded condition due to the as crack-like imperfections present in the top and bottom sides of weld beads at high stress levels increased the fatigue starts as reported in [36, 39, 40] and the phenomena of coalescence and growth of cracks have a greater influence on the fatigue life of the welded series and therefore also the local stress concentration at underfill or excess weld can to influence in the crack propagation.

6.3.6. Fatigue lives predictions

The previous analysis showed for the specimens in the as-welded condition, that at high stress levels, due to the presence of small imperfections, several fatigue starts are activated and coalescence rapidly, presenting conditions to neglect the fatigue initiation stage and therefore for the application of the fracture mechanics approach. The general procedure consists, first, in identifying the failure modes of the specimens with characteristic types of cracks and subsequently estimating the fatigue lives N according to well-known relation-ships of Paris law and SIFR, ΔK :

$$N = \int_{a_i}^{a_f} \frac{da}{A \Delta K^n} \quad (6.1)$$

$$\Delta K = Y M_k \Delta \sigma \sqrt{\pi a} \quad (6.2)$$

Figure 6.9a to 6.9d, show four fractured specimens of the as-welded condition with details of fatigue starts and schemes of crack types associated to the failure modes. Therefore, for the S2 series, a continuous surface crack corresponds to a failure due to multiple small imperfections along to the weld root; for the S1 series, semi-elliptical surface cracks correspond to the failure due to the undercuts, and; for the S3 series, a corner crack corresponds to a failure by the underfill near at the border of the specimen. Failure is assumed to occur when from an initial crack size to final crack size is reached that corresponds to a critical fracture condition. For the S1 series when the semi-elliptical cracks (in Figure 6.9b and 6.9c) growth from the initial aspect ratios, (a_i/c_i) , until when they coalesce and cover the entire width allows determine the fatigue lives of the specimens. In the case of the S3 series, when the initial crack depth grows to the thickness of the specimen (Figure 6.9d) and for the S2 series specimens, from a very small initial crack depth to the depth as observed in the fractured surface (Figure 6.9a).

Table 6.5 contains geometric data of the cracks for five specimens - the four shown in Figure 6.9 and an additional specimen similar to the one shown in Figure 6.9a -, parameters used to estimate the fatigue lives, the respective experimental results and the relations between the experimental lives and the corresponding estimated lives, meanwhile, Table 6.6 corresponds to predictions. It should be clarified how the crack sizes shown in Table 6.5 and Table 6.6 were established: the estimates were measured on the fractured surfaces of the specimens (as illustrated in the Figure 6.9c and Figure 6.9d), meanwhile, for predictions the same are based on sizes of the imperfections reported in [27]. In both cases, where applicable, the sizes are the mean values of the imperfections. The following observations point out aspects of the crack sizes of each series. For S2 series estimations, since there were multiple small imperfections along the width of the specimens, the width of the specimens, 12.5 mm, was assumed as the initial and final lengths. Meanwhile for predictions, the final crack sizes, a_f and c_f , were determined as described as follow. The crack depth a_f for the straight crack corresponding to the S2 series, it was assumed as half the plate

thickness (1.5 mm), as is recommended in [8] and the final crack length c_f was assumed, 12.5 mm, because corresponds to extended crack. The value, a_f , 3.00 mm in the S3 series, correspond to the failure critical condition assumed for the corner crack, meanwhile, the value 4.81 mm, correspond to the same aspect ratio a/c as in Table 6.5. The $a_f = 0.96$ mm, and $c_f = 1.56$ mm values, for S1 series, were set considering that the critical condition occurs when the semi-elliptical cracks grow until their crack length ends meet and cover the width of the specimen as observed in Figure 6.9b and Figure 6.9c. Therefore, based on the reported imperfections data [27]: number of undercuts 38 in 100 mm and undercut average length size, 1.11 mm; four undercuts were located evenly spaced across the width (12.5 mm) of the specimen, this allows to estimate the $2c_f$ value as 12.5/4 mm and assuming the same a/c relationship as in Table 6.5, the $a_f = 0.96$ values was obtained.

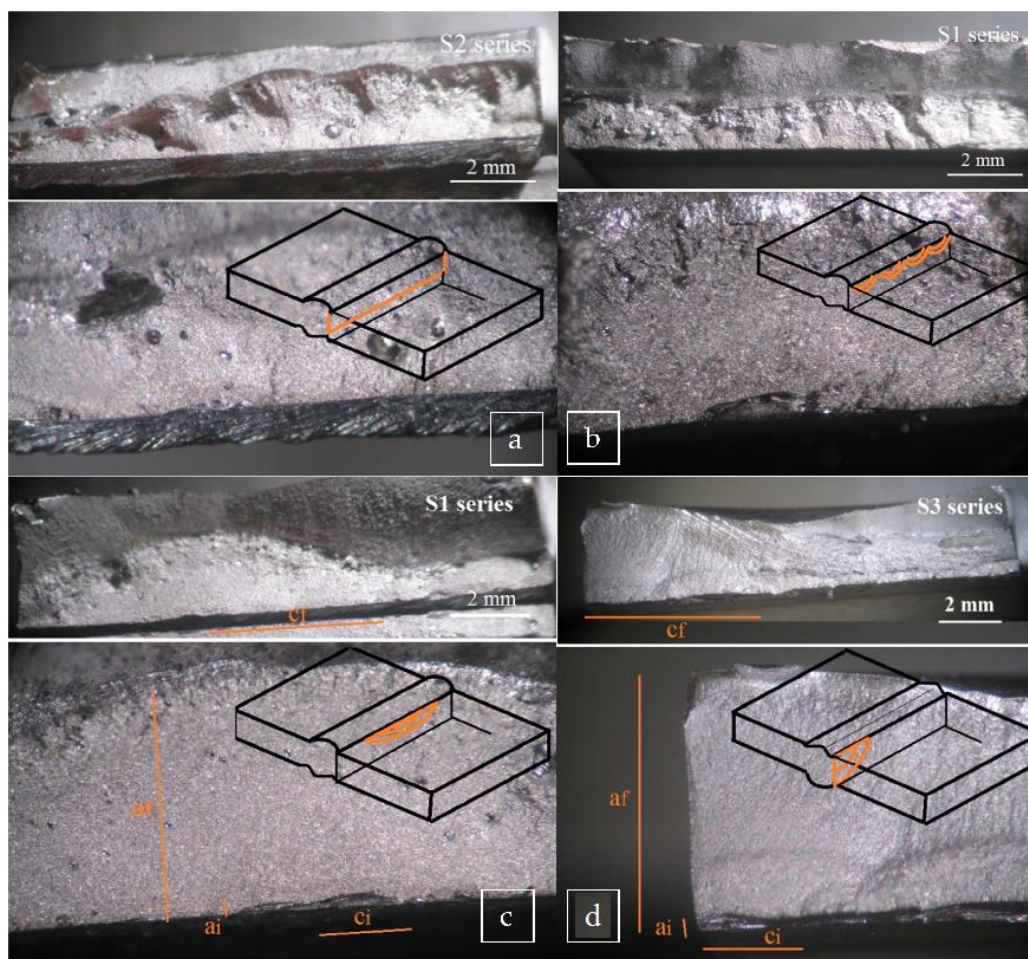


Figure 6.9 Fatigue failure modes with details and corresponding types of cracks. **a)** extended crack, **b)** semi-elliptical multicracks **c)** semi-elliptical crack and **d)** corner crack.

Due to the fact that the fatigue lives are calculated by means of the parameters A and n of the $da/dN-\Delta K$ curves and initial crack sizes a_i in Table 6.5 and Table 6.6 or, with $a_i = 0.1$ mm (for all specimens) according to the recommendation in [8] or also used in [13], generally underestimated the fatigue lives of the specimens, the initial crack size was slightly decreased to 0.07 mm (for all cases) and the parameters A^* , n^* were determined only with the first fifteen points using the same data of $da/dN-\Delta K$ curves. The previous adjustments are in line with the practical procedure that establishes the initial crack size adapted from the S-N data for its application with the $da/dN-\Delta K$ curve, as indicated in [26], there it is also pointed out that, the initial crack size rather than a physical size is a model parameter and this could lead to limits of transferability to other component geometries. The adjustments can be justified due to the small sizes of the fatigue starts and growing cracks and the thin thickness of the plate of the present work.

Due to the sensitivity of the initial crack value a_i , for a better estimation of the fatigue life to final crack size a_f , ten steps were used in the integration between a_i and a_f , with the first steps of less crack increase than the last steps and were also considered the effect of the variation of crack aspect ratios a/c and a/t assuming a linear relationship between these two. The previous assumption considers roughly what was reported in [41] for the growth of cracks with a large initial aspect ratio a/c as was the case of the crack aspect ratios found in the present work. The Y values and M_k factors displayed in Table 6.5 and Table 6.6 correspond to the average of the first five steps of the integration and were calculated with expressions from the literature, in [8, 25] was consulted the Y value and in [42] for the M_k factor. As can be seen in Table 6.5 and Table 6.6, the M_k factor that considers the effect of local stress concentration due to the excess weld on cracks starting from the undercuts had a small effect, mainly due to the small width of the weld beads and for the case of cracks start from underfill, the M_k factor were assumed equal to one. The M_k factor according to expression in [42], considers the weld bead features: flank angle, attachment, excess weld high and joint thickness.

As observed in Table 6.5, fatigue lives are generally underestimate being less than 25% and although the relation between the experimental results and the predictions of the fatigue lives achieved in Table 6.6 can be considered acceptable for the data, parameters

and assumptions done; the analysis showed that at high stress levels the appropriate values of parameters A , n and initial crack depth, a_i , must be used with a correct assignment of the type of crack to a given failure mode, as long as the initiation and coalescence stages can really be neglected. For specimens of the S5 series there were not predicted the fatigue life due to the FCGR was not appropriate as was described in section 6.3.3 and 6.3.4.

Table 6.5 Data and parameters for the estimation of the fatigue life.

Series-crack type (Figure)	Crack sizes		FCGR Parameters ¹	M_k factor	Y value	Fatigue life		
	a_i, c_i (mm)	a_f, c_f (mm)				A*, n*	experimental (cycles)	estimated (cycles)
S2-extended (Fig.6.9a)	0.02, 12.5	0.96, 12.5	2E-9, 3.2017	1.08	1.13	22922	20792	1.10
S2-extended (Fig.6.9a)	0.02, 12.5	1.22, 12.5	2E-9, 3.2017	1.08	1.13	26225	21043	1.25
S1-semi-elliptical (Fig.6.9b)	0.15, 0.46	1.62, 2.61	7E-10, 3.5965	1.05	1.10	29264	25485	1.15
S1-semi-elliptical (Fig. 6.9c)	0.10, 0.69	2.01, 4.83	7E-10, 3.5966	1.01	1.01	34127	38642	0.88
S3-corner crack (Fig. 6.9d)	0.21, 1.15	3.00, 4.81	6E-11, 4.4175	1.00	1.15	33762	35065	0.96

¹ (da/dN in mm/cycle and ΔK in MPa m^{1/2})

Table 6.6 Data and parameters for the predictions of the fatigue life.

Series-crack type	Crack sizes		M_k factor	Y value	Fatigue life at 600 MPa		
	a_i, c_i (mm)	a_f, c_f (mm)			experimental (cycles)	predicted (cycles)	ratio
S1-semi-elliptical crack	0.04, 0.56	0.96, 1.56	1.12	1.10	29264	23239	1.26
S2-extended crack	0.02, 12.5	1.5, 12.5	1.06	1.15	26225	21487	1.22
S3-corner crack	0.15, 1.58	3.00, 4.81	1.00	1.21	33762	29904	1.13

6.4. Conclusions

The effects of local properties, hardness and microstructure for four laser butt joints in thin HSLA steel plate were considered to explain fatigue crack growth behaviour. The main conclusions drawn are:

- Although the differences were small, each welded series presented at the crack start and propagation sites (CG-HAZ and FZ) higher hardness than the BM. The hardness range for the welded series was 335-370 HV and the hardness for BM was 295 HV;

- The welded series presented a similar FCGR rates in the HAZ-FZ, but lower than BM due to lower hardness presents in the BM because was verified a bainitic-ferritic microstructure in BM, while, in the welded series was observed a bainitic-martensitic microstructure in the CG-HAZ and FZ. Crack closure was observed only in the BM and in the S3 series, which can be attributed mainly to the crack tip plasticity for the BM and S3 series. The welding parameters did not influence in the FCGR rates;
- At high stress levels, fatigue life is strongly influenced by the quantity, size and location of the imperfections. The presence of crack-like imperfections located in critical positions such as near to lateral edge or several along the width of the specimen favor the initiation and coalescence of cracks so that the fatigue initiation period can be neglected;
- It has been shown that predictions of welded series' fatigue life are very sensitive to the adjustment of the initial crack size and the crack growth rates and to an adequate identification of imperfections and assumption of a type of superficial crack.

6.5. References

- [1] S. J. Maddox, *Fatigue strength of welded structures*, Cambridge: Abington Publishing, 2002.
- [2] W. Fricke, "Fatigue strength assessment of local stresses in welded joints," in *Fracture and fatigue of welded joints and structures*, Cambridge, Woodhead Publishing, 2011, pp. 115-138.
- [3] H. P. Lieurade, I. Huther and F. Lefebvre, "Effect of Weld Quality and Postweld Improvement Techniques on the Fatigue Resistance of Extra High Strength Steels," *Welding in the World*, vol. 52, no. 7-8, pp. 106-115, 2008.
- [4] C. Gerritsen, S. Vanrostenberghe and M. Doré, "Diode laser weld toe re-melting as a means of fatigue strength improvement in high strength steels," *Procedia Engineering*, vol. 66, pp. 171-180, 2013.
- [5] X. Cheng, J. Fisher, H. Prask, B. Yen, T. Graunapel-Herold and S. Roy, "Residual stress modification by post-weld treatment and its beneficial effect on fatigue strength of welded structures," *International Journal of Fatigue*, vol. 25, pp. 1259-1269, 2003.
- [6] F. Lefebvre, C. Peyrac, G. Elbel, C. Revilla-Gomez, C. Verdu and J. Buffière, "Understanding of fatigue strength improvement of steel structures by hammer peening treatment," *Procedia Engineering*, vol. 133, pp. 454-464, 2015.
- [7] G. Marquis and Z. Barsoum, "A guideline for fatigue strength improvement of high strength steel welded structures using high frequency mechanical impact treatment," *Procedia Engineering*, vol. 66, pp. 98-107, 2013.
- [8] A. F. Hobbacher, *Recommendations for Fatigue Design of Welded Joints and Components*, London: Springer, 2016.
- [9] S. Maddox, "Fatigue design rules for welded structures," in *Fracture and fatigue of welded joints and structures*, Cambridge, Woodhead Publishing, 2011, pp. 168-207.
- [10] I. Lillemäe, H. Remes, S. Liinalampi and A. Itävuori, "Influence of weld quality on the fatigue strength of thin normal and high strength steel butt joints," *Welding in the Word*, vol. 60, no. 4, pp. 731-740, 2016.

-
- [11] O. Watanabe, S. Matsumoto, Y. Nakano and Y. Saito, "Fatigue strength of welded joints in high strength steel Effects of stress concentration factor and welding residual stress," *Welding International*, vol. 10, no. 3, pp. 201-206, 1996.
- [12] E. Harati, L. Karlsson, L.-E. Svensson and K. Dalaei, "The relative effects of residual stresses and weld toe geometry on fatigue life of weldments," *International Journal of Fatigue*, vol. 77, pp. 160-165, 2015.
- [13] N. Nguyen and M. Wahab, "The Effect of Undercut and Residual Stresses on Fatigue Behaviour of Misaligned Butt Joints," *Engineering Fracture Mechanics*, vol. 55, no. 3, pp. 453-469, 1996.
- [14] T. Shiozaki, N. Yamaguchi, Y. Tamai, J. Hiramoto and K. Ogawa, "Effect of weld toe geometry on fatigue life of lap fil-let welded ultra-high strength steels joints," *International Journal of Fatigue*, vol. 116, pp. 409-420, 2018.
- [15] P. Kucharczyk, M. Madia, U. Zerbst, B. Schork, P. Gerwien and S. Münstermann, "Fracture-mechanics based prediction of the fatigue strength of weldments. Material aspects," *Engineering Fracture Mechanics*, vol. 198, pp. 79-102, 2018.
- [16] S. Ravi, V. Balasubramanian, S. Babu and S. Nemat Nasser, "Influences of MMR, PWHT and notch location on fatigue life of HSLA steel welds," *Engineering Failure Analysis*, vol. 11, p. 619-634, 2004.
- [17] Q. Wang, S. Yang, X. Liu, Z. Dong and H. Fang, "Understanding of fatigue crack growth behavior in welded joint a new generation Ni-Cr-Mo-V high strength steel," *Engineering Fracture Mechanics*, vol. 194, pp. 224-239, 2018.
- [18] T. Gurney, *Cumulative damage of welded joints*, Cambridge: Woodhead Publishing Ltd, 2006.
- [19] M. Chapetti and L. Jaureguizar, "Fatigue behavior prediction of welded joints by using an integrated fracture me-chanics approach," *International Journal of Fatigue*, vol. 43, pp. 43-53, 2012.
- [20] Y.-H. Zhang and S. Maddox, "Fatigue life prediction for toe ground welded joints," *International Journal of Fatigue*, vol. 31, pp. 1124-1136, 2009.
- [21] E. Javaheri, K. Hemmesi, P. Tempel and M. Farajian, "Fatigue assessment of the welded joints containing process rele-vant imperfections," *Welding in the World*, pp. 1-13, 2019.
- [22] R. Goyal, S. Bogdanov, M. El-zein and G. Glinka, "Fracture mechanics based estimation of fatigue lives of laser welded joints," *Engineering Failure Analysis*, vol. 93, pp. 340-355, 2018.
- [23] Y. Murakami, *Metal Fatigue: Effects of Small Defects and Nonmetallic Inclusions*, Oxford: Elsevier Science Ltd, 2002.
- [24] M. Åman, Y. Tanaka, Y. Murakami, H. Remes and G. Marquis, "Fatigue strength evaluation of small defect at stress concentration," *Structural Integrity Procedia*, vol. 7, pp. 351-358, 2017.
- [25] FITNET, FITNET Fitness-for-Service. Vol. II Annex, Geesthacht: FITNET, 2008.
- [26] U. Zerbst, M. Madia, B. Schork, J. Hensel, P. Kucharczyk, D. Ngoula, D. Tchuindjang, J. Bernhard and C. Beckmann, *Fa-tigue and Fracture of Weldments*, Basilea: Springer, 2019.
- [27] P. Riofrío, C. Capela and J. Ferreira, "Imperfections and Modelling of the Weld Bead Profile of Laser Butt Joints in HSLA Steel Thin Plate," *Metals*, vol. 11, no. 151, pp. 1-19, 2021.
- [28] ISO, *Welding - Electron and laser-beam welded joints - Guidance on quality levels for imperfections. Part 1: Steel; ISO 13919-1(1996)*, Geneva: ISO, 1996.
- [29] P. Riofrío, C. Capela, J. Ferreira and A. Ramalho, "Interactions of the process parameters and mechanical properties of laser butt welds in thin high strength low alloy steel plates," *Journal of Materials: Design and Applications*, vol. 234, no. 5, pp. 665-680, 2020
- [30] ASTM International, *Standard Test Method for Measurement of Fatigue Crack Growth Rates. E647-13a (2013)*, West Conshohocken: ASTM International.
- [31] W. Yisheng and J. Schijve, "Fatigue Crack Closure Measurements on 2024-T3 Sheet Specimens," *Fatigue & Fracture of Engineering Materials & Structures*, vol. 18, no. 9, pp. 917-921, 1995.
- [32] A. Ohta, N. Suzuki, Y. Maeda, K. Hiraoka and T. Nakamura, "Superior fatigue crack growth properties in newly devel-oped weld metal," *International Journal of Fatigue*, vol. 21, pp. S113-S118.
- [33] M. D. Chapetti and J. L. Otegui, "Importance of toe irregularity for fatigue resistance of automatic welds," *International Journal of Fatigue*, vol. 17, no. 8, pp. 531-538, 1995.
- [34] M. Guan and H. Yu, "Fatigue crack growth behaviors in hot-rolled low carbon steels: A comparison between ferrite-pearlite and ferrite-bainite microstructures," *Materials Science & Engineering A*, vol. 559, pp. 875-881, 2013.
- [35] S. Li, Y. Khan and S. Kuang, "Effects of microstructure on fatigue crack growth behavior in cold-rolled dual phase steels," *Materials Science & Engineering A*, vol. 612, pp. 153-161, 2014.
- [36] R. Bell, O. Vosikovskiy and S. Bain, "The significance of weld toe undercuts in the fatigue of steel plate T-joints," *Interna-tional Journal Fatigue*, vol. 11, no. 1, pp. 3-11, 1989.
-

- [37] D. Y. Kim, I. Hwang, G. Jeong, M. Kang, D. Kim, J. Seo and Y. Kim, "Effect of Porosity on the Fatigue Behavior of Gas Metal Arc Welding Lap Fillet Joint in GA 590 MPa Steel Sheets," *Metals*, vol. 8, no. 241, pp. 1-13, 2018.
- [38] R. Biswal, A. Syed and X. Zhang, "Assessment of the effect of isolated porosity defects on the fatigue performance of additive manufactured titanium alloy," *Additive Manufacturing*, Vols. 433-442, p. 23, 2018.
- [39] J. Schijve, "Fatigue Predictions and Scatter," *Fatigue & Fracture of Engineering Materials & Structures*, vol. 17, no. 4, pp. 381-393, 1994.
- [40] Y. Verreman and B. Nie, "Early Development of Fatigue Cracking at Manual Fillet Welds," *Fatigue & Fracture of Engineering Materials & Structures*, vol. 19, no. 6, pp. 669-681, 1996.
- [41] P. Nair, "Fatigue Crack Growth Model for Part-Through Flaws in Plates and Pipes," *Journal of Engineering Materials and Technology*, vol. 101, pp. 53-58, 1979.
- [42] S. Lie, S. Vipin and H. Zhao, "New weld toe magnification factors for semi-elliptical cracks in plate-to-plate butt-welded joints," *Fatigue & Fracture of Engineering Materials & Structures*, vol. 40, pp. 207-220, 2016.

Chapter 7: Conclusions and Future Work

7.1. Conclusions

An investigation was conducted on the fatigue behaviour and mechanical properties of a laser welded thin high-strength low-alloy (HSLA) steel. Single pass and double pass autogenous laser welding (ALW) of 3mm thick Strenx® S700MCE steel were developed subject to a maximum laser power of 2 kW. Said steel has a minimum yield strength at 700 MPa and an elongation percentage between 10-12%

The one-factor-at-a-time (OFAT) experimental design was applied to identify the main laser welding parameters and their influence on the weld bead geometry and imperfections in single-butt welded joints. For a range of heat input (HI), the microstructure in the heat-affected zone (HAZ) and fusion zone (FZ) and the mechanical properties – namely, micro-hardness and tensile strength – were determined.

In order to understand the factors that influence fatigue behaviour, a 2² factorial design based on welding speed and laser power was used to produce four single-butt welded joints. A double-butt welded joint was also used for the aforementioned purpose. Analysis of variance (ANOVA) was used to validate the effect of the welding parameters applied in each welded joint regarding the differences observed in the weld bead geometry as well as to establish the significance of each welding parameter.

For all four complete penetration welded joints (named S1, S2, S3 and S5 series): the weld quality was evaluated in accordance with the ISO 13919-1 standard, the undercut and porosity distributions were established, the sizes of the HAZ and FZ were determined and the weld bead profiles were captured and geometrically modeled for the assessment the stress concentration factor (SCF) with analytical expressions and by the finite element method (FEM).

The S-N curves and fatigue crack growth rates (FCGRs) of the four welded series and base metal (BM) were experimentally determined and analyzed. Through the analysis of the fatigue fractured surfaces, the failure modes were established. The hardness and residual stresses in HAZ and FZ were subject to measurement. These local properties, the modeled profiles, the imperfections and the fatigue failure modes were evaluated to explain fatigue behaviour and for making predictions at low and high stress levels based on the stress-concentrating effect as well as on the fracture mechanics approach. This research provides useful scientific data to support industrial applications of thin HSLA steel in low power and welding speed ranges. The main findings and conclusions presented in the present thesis may be summarized as follows:

7.1.1. Laser Welding, weld profile and imperfections

(1) While welding speed, power and focus diameter have a great effect on penetration, only welding speed has a considerable effect on weld bead width. Although the effects on the penetration of the focus position and the surface condition were minor, they are not negligible in thin thicknesses. In fact, the surface condition particularly affects the appearance of the weld seam. The HI also shows great influence on the weld bead geometry and is a convenient parameter because it encompasses the effect of parameters such as the previously mentioned ones.

(2) It was possible to weld a 3 mm thick Strenx® S700MCE steel plate with low laser power using a single pass ALW process. The three single-butt welded joints presented a B weld quality level according to the ISO 13919-1 welding standard, meanwhile, the double-butt welded joint also developed showed a lower weld quality level (D), due to high porosity.

(3) The actual weld bead profiles or those based on mean values of each welded series were faithfully modeled on the basis of proposed idealized profiles. The profiles modeled to reflect in greater detail the weld bead profiles allow for better results in SCFs determined with FEM.

(4) Considering the effect on fatigue strength through SCF, single-pass butt welded joints showed severe imperfections at the weld root: shallow but sharp intermittent undercuts (SCF: 3.3-4.4); weld toes with small radii, high flank angles and high excessive penetration (SCF: 1.7-2.3). All welded joints presented, on one side of the weld bead, underfill (SCF: 1.8-2.0) and variation of the weld bead profile along the weld axis. Particularly the welded joint made with two weld passes, presented a good weld profile in the top side (SCF: 1.4).

(5) The application of ANOVA to the weld bead widths in the factorial design showed a greater significance of the welding speed on the power and on its interaction, it also showed that the HI level is a factor in the differences found in the widths of the welded series. The differences observed in the geometry of each welded series result from the laser welding parameters.

(6) Heat input shows influence on various factors that affect the fatigue behaviour and mechanical strength of welded joints. The use of low HI is beneficial due to the smaller widths of the HAZ and FZ, greater hardness in the FZ, less softening in the HAZ, slower crack growth rates, lower residual tensile stresses and even residual compressive stresses in the fatigue initiation sites, however, it also exerts adverse effects such as increased porosity and increased underfill size.

7.1.2. Microstructure, hardness, residuals stresses and tensile strength

(1) The typical macrostructure of the welded joints consisted of fine grained (FG) and coarse grained (CG) in the heat-affected zone (HAZ) and large columnar grains in the fusion zone (FZ). The ferritic-bainitic microstructure of the base metal (BM) evolved to a softened ferritic-bainitic in the FG-HAZ and was predominantly bainite with small amounts of martensite in the CG-HAZ and in the FZ.

(2) In HAZ and FZ the hardness varies progressively when the HI decreases in the same way. From HI values lower than 80 J/mm, in the FZ and CG-HAZ, the hardness

increases from the hardness level of the MB, meanwhile, in the FG-HAZ, the softening is reduced until the hardness equals the hardness level of BM at 20 J/mm.

(3) Compared to the mechanical properties of the BM, the tensile strengths of the butt welded joints were practically the same while the yield strength and the elongation percentage were slightly lower. These results were obtained in the range of 80 to 53 J/mm, with the aforementioned properties showing a tendency to improve when the hardness increases in the FZ and the softening and the size of the HAZ are reduced.

(4) The longitudinal residual stresses in the fatigue specimens presented the typical M-shape near the HAZ and FZ, with residual tensile stresses at the HAZ and tending to zero or residual compressive stresses in the weld center line. At the sites where fatigue started, the residual stresses were approximately: 200 to 80 MPa, for S5 series; 130 to 50 MPa, for S1 series and; 50 to -40 MPa, for S3 series. The results suggest that as the HI decreases, the residual tensile stresses progressively change to residual compressive stresses. This is explained by the deformations due to phase transformations of microstructures such as bainite and martensite.

7.1.3 Fatigue behaviour

(1) The S-N curves of the four welded series (S1, S2, S3 and S5 series) showed linear models in logarithmic scales, results within 95% confidence bands, characteristic failure modes and different fatigue limits; indicating the effect of the welding parameters and HI in each series, despite the fact that the differences in the results and in the ranges of the welding parameters are small.

(2) The fatigue strengths of the welded series exceeded the FAT100 reference curve with fatigue limits in the range of 180 to 270 MPa, being 30 to 47% of the BM fatigue limit. Each series presented a dominant failure mode strongly related to the imperfection with the highest SCF, so: 3.29-undercut-S1 series, 2.25-weld toe-S2 series; 4.41-undercut-S3 series; 1.95-underfill-S5series. In particular, two specimens from the S5 series observed a high fatigue limit in relation to all series, due to the fact that they presented a lower SCF in the underfill and a lower variation of the weld bead profile along the weld axis.

(3) The evaluation of the welded series' fatigue limits, based on the stress-concentrating effect and the modified Goodman criterion, using the local properties (residual stresses and hardness) of fatigue initiation sites (HAZ and FZ) along with the local stresses determined through the effective stress concentration factor, showed a very good agreement with the experimental results. Good predictions of the fatigue limit were also achieved with the Murakami expression.

(4) The effect on fatigue limits of factors such as weld quality, residual stresses and material, quantified by the SCF, the magnitude of the residual stresses and the hardness, respectively, is established as follows: both high SCFs and relatively low residual tensile stresses (< 200 MPa) have a strong negative effect on fatigue limits; only when SCFs are low (< 2.0), the residual stresses less than 130 MPa could they be neglected. Meanwhile, greater local hardness increases the fatigue limits, however the effect is lesser in relation to SCF and residual stress.

(5) In the FZ and HAZ, the welded series presented similar FCGRs but lower than the FCGR of the BM due to the retarding effect of the predominant bainite present in these zones. Meanwhile, the crack closure present in the BM and in the S3 welded series can be attributed mainly to the crack tip plasticity for the BM and to the presence of residual compressive stresses, for the S3 welded series.

(6) At high stress levels, the fatigue life is strongly influenced by the quantity, size and location of the imperfections. The presence of crack-like imperfections located in critical positions such as near to lateral edge or several along the width of the specimen favor the initiation and coalescence of cracks, so that the fatigue initiation period can be neglected. For the as-welded condition, characteristic surface cracks were identified in each welded series: extended crack for the S2 series, semi-elliptical cracks for the S1, S3 and S5 series as well as corner crack for the S3 series

(7) At a stress level of 600 MPa, the crack propagation approach applied to estimate fatigue lives of fatigue specimens showing extended, semi-elliptical and border surface cracks was in good agreement with the experimental lives. For this, due to the thin thickness of the specimens, it became necessary to adopt a fitting procedure, assuming an

initial crack size of 0.07 mm and FCGRs determined with the initial section of the crack growth curves.

(8) It has been shown that good predictions of fatigue lives at high stress levels for welded series are possible through the approaches of crack growth and of fatigue limits with the stress-concentrating effect or with the Murakami expression, based on prior knowledge of imperfection sizes and local properties, therefore, S-N curves can be predicted based both on fatigue limits and fatigue lives at high stress level.

7.2. Future Work

This research focused on the fatigue behaviour and mechanical properties – namely hardness and tensile strength – of butt welded joints by ALW of a 3 mm thick S700® MCE HSLA steel. The local properties, weld bead geometry and imperfections were considered to evaluate fatigue strength and fatigue life at high and low stress levels by crack propagation approach and stress-concentrating effect. However, while those main aspects were investigated, there are still several areas in which further research can be developed. Some of the most important ones are included as follows.

7.2.1. Toughness and formability properties

According to the manufacturer, S700® MCE steel has a toughness of 20J/-40°C and is made for cold forming, so these two important mechanical properties must be evaluated in 3 mm thick laser welded joints, due to which a detriment in toughness and a reduction in the elongation percentage by laser welding it has been reported. This assessment should take into account current industrial applications and others that may expand its scope.

7.2.2. Comparative studies with conventional welding processes

Although conventional welding processes are considered more detrimental on fatigue strength than in comparison to laser welding, there are conventional processes that could compete with ALW for low thicknesses and due to the addition of filler materials. The

GTAW process is potentially suitable for low thickness and good weld quality, while the GMAW process adds chemical elements into the molten metal and the weld bead has less roughness. Therefore, a study comparing these two conventional welding processes with the ALW process could prove to be very useful.

7.2.3. Improvement of welding quality through laser welding parameters' optimization techniques

The ANOVA application to the factorial design showed the effect of welding parameters such as welding speed, power and heat input (HI) on the width of weld bead. It was also observed that two welded series presented undercuts while one series did not – this suggests that this defect is correlated to the welding parameters used. On the other hand, a large decrease in fatigue strength was found due to imperfections such as undercuts, weld toe, underfill, and the variation of the weld profile along to the weld axis. The technique response surface methodology can be implemented to establish a mathematical model that correlates welding parameters such as welding speed and power on the weld quality in terms of the minimization of imperfections. In this type of studies, the range of parameters used could be slightly extended, but without exceeding the established HI limits, so as to avoid excessive softening in the HAZ and achieve complete penetration.

7.2.4. Using conduction mode or increasing laser power to improve the weld profile

On the weld bead welded with two weld passes, the weld pass from the top side generated a profile with wide radii at the weld toe and without undercuts, however there was high porosity. The conduction mode can reduce porosity and present a profile similar to that previously mentioned, therefore an alternative to increase fatigue strength is to use two weld passes in conduction mode, although this solution may be less productive. On the other hand, the use of a power greater than 2 kW in keyhole mode would allow more options to find an improvement in the weld bead's profile.

7.2.5. Small crack behaviour

For a better understanding, experimental work can be oriented to the small crack growth. Literature approaches that take into account the effect of small cracks on the fatigue life of welded elements can also be considered. The two types of works can serve to provide greater prediction support both at low stress levels and at high stress levels.

7.2.6. Predictions of the S-N curves

It has been pointed out that different phenomena occur in finite-life and infinite-life behaviour. Acceptable predictions were made of the fatigue limit through stress-concentrating effect and at high stress levels through fracture mechanics. Predictions of the S-N curves can be made based on the fatigue strength at two stress levels: one close to the fatigue limit and the other close to the yield strength. Experimental studies or those based on data from existing works can serve for this purpose.